

1st Galapagos soft matter conference - research topic

Edited by

Frank Alexis, Raffaele Mezzenga and Ali Miserez

Published in

Frontiers in Soft Matter



FRONTIERS EBOOK COPYRIGHT STATEMENT

The copyright in the text of individual articles in this ebook is the property of their respective authors or their respective institutions or funders. The copyright in graphics and images within each article may be subject to copyright of other parties. In both cases this is subject to a license granted to Frontiers.

The compilation of articles constituting this ebook is the property of Frontiers.

Each article within this ebook, and the ebook itself, are published under the most recent version of the Creative Commons CC-BY licence. The version current at the date of publication of this ebook is CC-BY 4.0. If the CC-BY licence is updated, the licence granted by Frontiers is automatically updated to the new version.

When exercising any right under the CC-BY licence, Frontiers must be attributed as the original publisher of the article or ebook, as applicable.

Authors have the responsibility of ensuring that any graphics or other materials which are the property of others may be included in the CC-BY licence, but this should be checked before relying on the CC-BY licence to reproduce those materials. Any copyright notices relating to those materials must be complied with.

Copyright and source acknowledgement notices may not be removed and must be displayed in any copy, derivative work or partial copy which includes the elements in question.

All copyright, and all rights therein, are protected by national and international copyright laws. The above represents a summary only. For further information please read Frontiers' Conditions for Website Use and Copyright Statement, and the applicable CC-BY licence.

ISSN 1664-8714
ISBN 978-2-8325-5700-6
DOI 10.3389/978-2-8325-5700-6

About Frontiers

Frontiers is more than just an open access publisher of scholarly articles: it is a pioneering approach to the world of academia, radically improving the way scholarly research is managed. The grand vision of Frontiers is a world where all people have an equal opportunity to seek, share and generate knowledge. Frontiers provides immediate and permanent online open access to all its publications, but this alone is not enough to realize our grand goals.

Frontiers journal series

The Frontiers journal series is a multi-tier and interdisciplinary set of open-access, online journals, promising a paradigm shift from the current review, selection and dissemination processes in academic publishing. All Frontiers journals are driven by researchers for researchers; therefore, they constitute a service to the scholarly community. At the same time, the *Frontiers journal series* operates on a revolutionary invention, the tiered publishing system, initially addressing specific communities of scholars, and gradually climbing up to broader public understanding, thus serving the interests of the lay society, too.

Dedication to quality

Each Frontiers article is a landmark of the highest quality, thanks to genuinely collaborative interactions between authors and review editors, who include some of the world's best academicians. Research must be certified by peers before entering a stream of knowledge that may eventually reach the public - and shape society; therefore, Frontiers only applies the most rigorous and unbiased reviews. Frontiers revolutionizes research publishing by freely delivering the most outstanding research, evaluated with no bias from both the academic and social point of view. By applying the most advanced information technologies, Frontiers is catapulting scholarly publishing into a new generation.

What are Frontiers Research Topics?

Frontiers Research Topics are very popular trademarks of the *Frontiers journals series*: they are collections of at least ten articles, all centered on a particular subject. With their unique mix of varied contributions from Original Research to Review Articles, Frontiers Research Topics unify the most influential researchers, the latest key findings and historical advances in a hot research area.

Find out more on how to host your own Frontiers Research Topic or contribute to one as an author by contacting the Frontiers editorial office: frontiersin.org/about/contact

1st Galapagos soft matter conference - research topic

Topic editors

Frank Alexis — Universidad San Francisco de Quito, Ecuador

Raffaele Mezzenga — ETH Zürich, Switzerland

Ali Miserez — Nanyang Technological University, Singapore

Citation

Alexis, F., Mezzenga, R., Miserez, A., eds. (2024). *1st Galapagos soft matter conference - research topic*. Lausanne: Frontiers Media SA.

doi: 10.3389/978-2-8325-5700-6

Table of contents

- 04 **Challenges and opportunities from water under soft nanoconfinement**
Raffaele Mezzenga
- 11 **Mixture of fatty alcohols and alkyl polyglucosides stabilizing water-in-water emulsions**
Carolina Dari, Yuchen Si, Jean-Paul Douliez, Jean-François Tahon, Thierry Benezech, Paul S. Clegg and Anne-Laure Fameau
- 23 **Effect of sorbitan ester structure on the separation between tetrahydrofuran and water**
Bibiana Bartokova, Alejandro G. Marangoni, Thamara Laredo and Erica Pensini
- 37 **pH-dependent interactions of coacervate-forming histidine-rich peptide with model lipid membranes**
Sushanth Gudlur, Filipe Viana Ferreira, Javier Shu Ming Ting, Carmen Domene, Syed Maricar, Anton P. Le Brun, Nageshwar Yepuri, Michael Moir, Robert Russell, Tamim Darwish, Ali Miserez and Marité Cárdenas
- 50 **Phase behavior in multicomponent mixtures**
Luka Sturtewagen, Belinda P. C. Dewi, Arjen Bot, Paul Venema and Erik van der Linden
- 59 **Addressing the structural sophistication of meat via plant-based tissue engineering**
Daniel Dikovsky
- 68 **Antimicrobial cellulose hydrogels against gram-positive and gram-negative bacteria**
Karla Miño, Antonela Pérez, Tamia Xaymara Iza-García, Dayanna Gabriela Cabascango, Catalina Gordillo, Andrea Gordillo, Nelson Vispo, António Machado, Camilo Zamora-Ledezma and Frank Alexis
- 79 **Advancement in automation of co-extrusion collagen casings**
Shai Barbut
- 85 **To seal a wound, caterpillars transform blood from a viscous to a viscoelastic fluid in a few seconds**
Pavel Aprelev, Artis Brasovs, Terri F. Bruce, Charles E. Beard, Peter H. Adler and Konstantin G. Kornev
- 103 **Geometric modeling of phase ordering for the isotropic–smectic A phase transition**
David Uriel Zamora Cisneros, Ziheng Wang, Noémie-Manuelle Dorval Courchesne, Matthew J. Harrington and Alejandro D. Rey
- 123 **Using QSAR to predict polymer-drug interactions for drug delivery**
Alison W. Xin, Edgardo Rivera-Delgado and Horst A. von Recum



OPEN ACCESS

EDITED BY
Yuka Tabe,
Waseda University, Japan

REVIEWED BY
Yuri Gerelli,
National Research Council (CNR), Italy

*CORRESPONDENCE
Raffaele Mezzenga,
✉ raffaele.mezzenga@hest.ethz.ch

RECEIVED 19 October 2023
ACCEPTED 07 November 2023
PUBLISHED 23 November 2023

CITATION
Mezzenga R (2023), Challenges and opportunities from water under soft nanoconfinement.
Front. Soft Matter 3:1324589.
doi: 10.3389/frsfm.2023.1324589

COPYRIGHT
© 2023 Mezzenga. This is an open-access article distributed under the terms of the [Creative Commons Attribution License \(CC BY\)](https://creativecommons.org/licenses/by/4.0/). The use, distribution or reproduction in other forums is permitted, provided the original author(s) and the copyright owner(s) are credited and that the original publication in this journal is cited, in accordance with accepted academic practice. No use, distribution or reproduction is permitted which does not comply with these terms.

Challenges and opportunities from water under soft nanoconfinement

Raffaele Mezzenga^{1,2*}

¹Department of Health Sciences and Technology, ETH Zurich, Zurich, Switzerland, ²Department of Materials, ETH Zurich, Zurich, Switzerland

Nanoconfined water differs significantly from bulk water and challenges our common understanding of liquid water in both its most fundamental features, as well as in many applied aspects which stem out from its peculiar behavior. This brief perspective pinpoints both challenges associated with the study of water under soft nanoconfinement as well as some opportunities which arise from it, and which would not be at reach with standard bulk water. A special focus is given to the strong nanoconfinement (~1–10 nm) offered by inverse lipidic mesophases, viewed as a *natural* soft nanoconfinement environment for water.

KEYWORDS

nanoconfinement, supercooling, glass transition, glasses, lipid mesophases, lyotropic liquid crystals, cryo-enzymatic reactions

Introduction

From the cellular environment, to pharmaceutical applications, physics, chemistry and nanotechnology, interest in water under soft nanoconfinement has been constantly growing, mostly due to the fact that many real biological examples feature water in conditions which are far from bulk-like, and thus, do not meet our common stereotypes of water. However, there are precise reasons why nanoconfined water may offer a platform to study water under environmental conditions not possible or applicable to bulk water itself. The most notorious one is the capability of nanoconfined water to enter the so called *no man land* region of the phase diagram without the formation of ice, i.e., the range of temperature between $T_H = -41^\circ\text{C}$, at which homogeneous nucleation of ice occurs and roughly $T_X \approx -113^\circ\text{C}$, the so-called crystallization-onset temperature (Smart, 2017). This is a remarkable result in a temperature range within which even homogeneous nucleation of ice from bulk water cannot be avoided, neither upon cooling (ice formation from liquid water below T_H) nor upon heating (ice formation from supercooled glassy water above T_X). The only other known way to avoid ice formation in the no-man land region is to escape thermodynamics via cooling rates of the order of 10^5 – 10^6 K/s, so fast that only a handful of methods exist to realize this experimentally (Debenedetti and Stanley, 2003; Cervený et al., 2016). But nanoconfined water challenges our understanding of water in many other aspects, touching on relaxation dynamics, hydrogen bonding coordination, structure, solubility, reactivity, and many more. This short perspective aims, within the allowed limits of space, at briefly highlighting the challenges and opportunities arising from water under soft nanoconfinement, making a parallel among these two extremes and taking bulk water as benchmark reference. Given the limited allowed length, this perspective is by no means meant to comprehensively discuss the peculiarities of nanoconfined water, for which extensive literature already exists (Ortiz-Young et al., 2013; Huber, 2015; Knight et al., 2019). Instead, the main objective is to point at

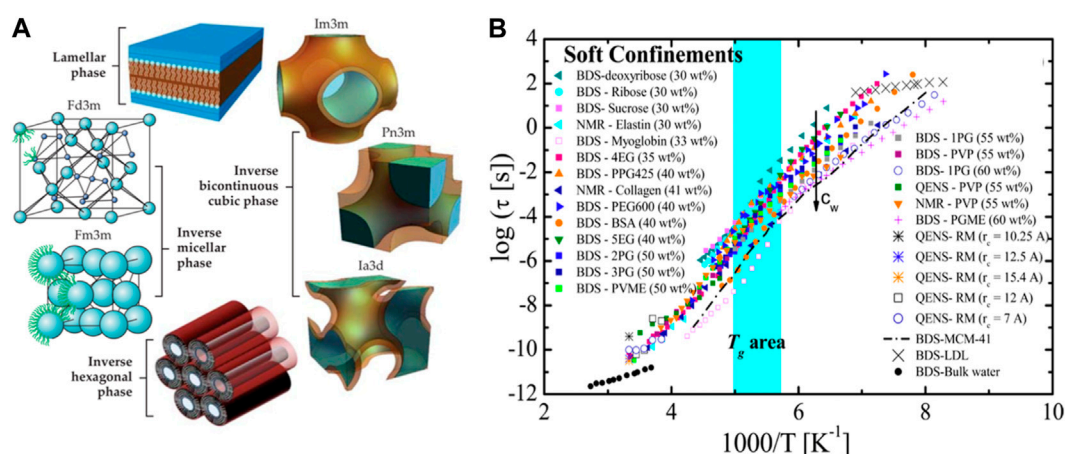


FIGURE 1

(A) A summary of main symmetries involved in lipid mesophases soft nanoconfinement. Reproduced with permission from Aleandri and Mezzenga (2020), AIP copyrights. (B) Relaxation time of water vs. inverse of temperature for most known soft nanoconfinement systems known. Reproduced with permission from Cervený et al. (2016), ACS copyrights.

opportunities which are yet to be fully appreciated within the wide body of literature, showcasing some less-known aspects of nanoconfined water.

Types of soft nanoconfinement

Possibly the most frequent soft nanoconfinement system studied is that formed by reverse micelles (RM) in which water is confined within a dispersed continuous hydrophobic phase, typically an oil, by the help of a surfactant. In this form of nanoconfinement water is most often organized within spherical micelles of a size typically ranging between 1 and 15 nm (Moilanen et al., 2009; Das et al., 2013; Yuan et al., 2017), although worm like micelles are also possible using typically ionic surfactants (Martiel et al., 2014). At larger hydration levels, where bulk water dominates, the range of nanoconfined water increases to 5–100 nm, and the RM are more frequently referred as microemulsions (Moulik and Paul, 1998). A second form of soft nanoconfinement is the one offered by inverse lipidic mesophases in which water is confined within 0D, 1D, 2D, and 3D symmetries depending on the lipid used, the amount of water and the temperature considered. A graphic summary of the main symmetries involved in lipidic mesophases is given in Figure 1A. Typical confinement in these systems forces water within domains ranging between 1 nm and 50 nm, but most typically within the 3–5 nm range (Mezzenga et al., 2019; Aleandri and Mezzenga, 2020). A third way to achieve soft nanoconfinement for water is via high concentration of solutes of molecular (e.g., glycerol) or macromolecular (polysaccharides, proteins, DNA, etc.) nature. This strategy may change the properties of water to the point that freezing can be completely suppressed or water nearly entirely immobilized at the solute/water interface. This specific form of soft nanoconfinement will not be considered in this short perspective mostly for reasons of space, but also because it differs substantially from the first two in such that a straightforward length-scale for the nanoconfinement cannot be easily defined. Interested readers are referred to more extensive

literature dealing with this topic (Hatakeyama et al., 2010; Yan et al., 2018; Das Mahanta et al., 2023).

Challenges

Depression of water freezing point

Certainly the most well understood feature of nanoconfined water is the depression of the freezing point, which is rationalized via the well-established Gibbs–Thompson equation, according to which the temperature depression ($T_{m,B} - T_{m,N}$), where $T_{m,B}$ and $T_{m,N}$ are the freezing temperature of bulk and nanoconfined water, respectively, scales with the diameter d of the confining pore as $(T_{m,B} - T_{m,N}) \sim 1/d$. The Gibbs–Thompson equation explains well the depression of the freezing point of water under medium and strong nanoconfinement, typically down to 4 nm (Corti et al., 2021), but as the equation diverges only for $d \rightarrow 0$, the complete suppression of freezing observed in several soft nanoconfined systems is not correctly explained. This has led to an empirical modification of the equation into $T_{m,B} - T_{m,N} \sim 1/(d-t)$ where t is the thickness of the un-freezable liquid bound to the pore wall. This allows for the possibility of full suppression of crystallization at a critical, yet finite size of t (Corti et al., 2021). For comparison water in (hard) confined silica hexagonal mesopores (MCM-41) of less than 4 nm, does not freeze at any temperature (Yoshida et al., 2008). The reason for such a behavior is that ice needs to overcome a critical nucleus size in order to growth, as in any systems undergoing nucleation and growth. Many systems have been shown to depress or suppress crystallization of ice due to soft nanoconfinement, although the level of temperature depression depends on the various system.

Glass transition

While the effects of nanoconfinement are relatively well understood in first order thermodynamic transitions of water

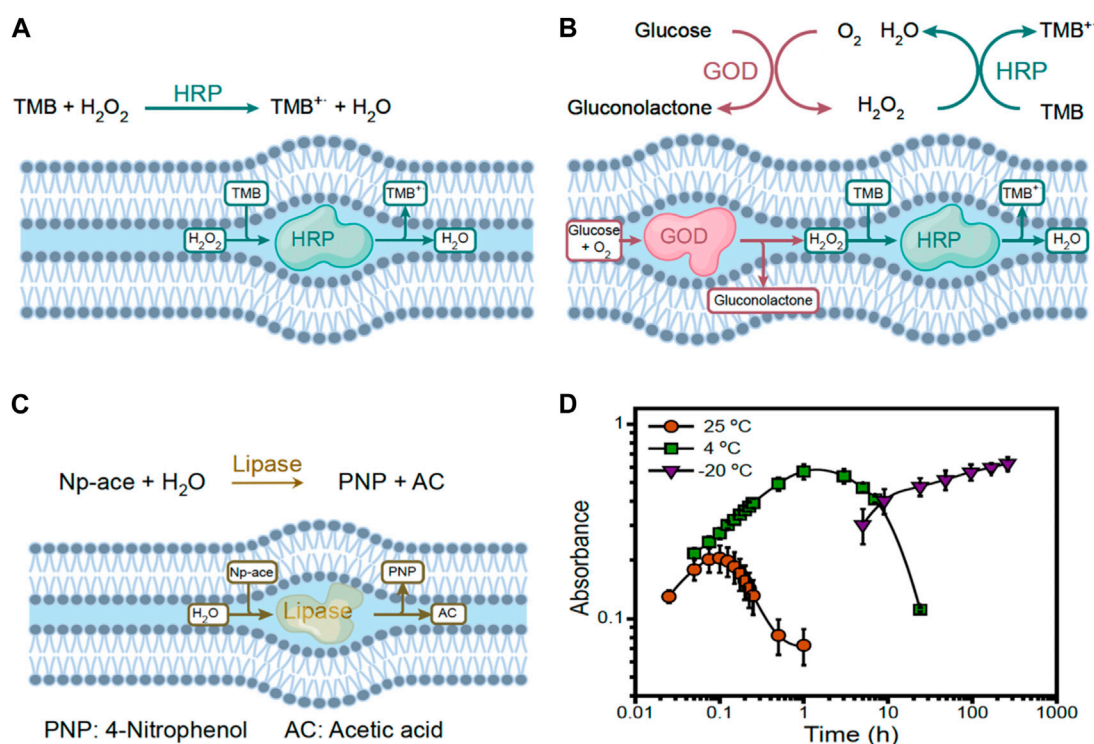


FIGURE 2

Typical enzymatic reactions explored at cryogenic conditions under lipidic mesophase soft nanoconfinement. (A) TMB oxidation by HRP; (B) TMB oxidation by GOD-HRP cascade reaction; (C) Hydrolysis of 4-Nitrophenyl acetate (Np-ace) by lipase; (D) Kinetic curves of GOD-HRP cascade reaction at 25, 4, and -20 °C, as sketched in panel (B). Reproduced with permission from Yao et al. (2021).

(freezing/melting), the situation with second (or higher order) transitions is far from being univocally established. Glass transition (T_g) of water under nanoconfinement is a clear example. The exact location of the glass transition temperature of bulk water is already debated and depending on how it is measured, different values have been obtained. It is generally agreed, however, that it locates between 136 K and 165 K (Johari et al., 1987; Velikov et al., 2001; Debenedetti and Stanley, 2003), although some recent reports even suggest a T_g of bulk water as high as (or even higher than) 190 K (Cerveny et al., 2016). The location of glass transition of water under confinement is obviously more uncertain. Basic considerations would suggest the T_g of confined water to be depressed over the corresponding T_g of the bulk water: for example, it is well established that nanoconfinement disrupts the h-bonding network and therefore speeds up relaxation of water: based on this argument alone one would expect that at the same cryogenic temperature nanoconfinement causes increased mobility and thus lower T_g of water (Cerveny et al., 2016). Similar conclusions can be reached by invoking the concept of water cluster, as originally introduced by Frank and Wen (1957), which is perturbed by neighboring molecules (Némethy and Scheega, 1962), or as in the present case, whose size is limited by the nanoconfinement, promoting liquid-like behavior over more viscous/glassy behavior, i.e., a depression on glass transition. A slightly more elaborated concept supporting the same idea of T_g depression with confinement is the idea proposed by Adam and Gibbs (1965), predicting cooperative re-arranging regions (CRR),

within which the molecules move cooperatively and beyond which motion of molecules becomes independent. A decrease in temperature would generally lead to an increase in the size of CRR, which a consequent shift towards more viscous/glassy behavior; as confinement sets a limit to the maximum CRR size, however, at a given temperature, glassy behaviour can no longer be enhanced by cooling. In other words, confinement sets a lower boundary to the possible T_g , promoting liquid like over glassy behavior (Spehr et al., 2011).

From an experimental point of view, however, resolving unambiguously the glass transition of water under nanoconfinement is not trivial. The main complications reside in resolving alpha relaxation from other possible relaxation and critical phenomena. A recent review provides three different scenarios to interpret the physical origins of low temperature relaxation of water under nanoconfinement (Cerveny et al., 2016). Yet, some universality traits can be captured when the relaxation time extracted by various methods, among which broadband dielectric spectroscopy (BDS), nuclear magnetic resonance (NMR) and quasi-elastic neutron scattering (QENS), is plotted against $1/T$ (See Figure 1B). Although different soft confining systems affect water relaxation in different ways, a crossover temperature is observed from an Arrhenius dependence at low temperature to a super-Arrhenius behavior at high temperature, often modelled via a Vogel-Fulcher-Tamman (VFT) relation (Gallo et al., 2010). Furthermore, increasing the water content leads in all cases to faster relaxation times, in some cases by four orders of

magnitude. The tentative glass region in Figure 1B extends from 172 to 200 K; yet comparison with bulk T_g of water is problematic both from an experimental and theoretical point of view (Cerveny et al., 2016). This transition of relaxation times (and hence viscosity) from an Arrhenius dependence at low temperature to a super-Arrhenius behavior upon heating is also called a strong-to-fragile transition, where strong is a synonym of Arrhenius-like behavior.

Dynamic of water

The peculiarities of water under soft nanoconfinement are apparent also when studying the dynamic and diffusion behavior. In general, different techniques probe different characteristic times. A large body of literature has been devoted to this topic and excellent reviews are available. Here we briefly summarize the salient features of the dynamic of nanoconfined water. To start, different techniques probe different timescales: molecular vibrations (10–100 fs) are typically probed by linear spectroscopies, as FT-IR and Raman, and non-linear ones as sum frequency generation spectroscopy (SFG); molecular rotation (1–100 ps) are accessible via IR pump-probe experiments and two-dimensional rotational spectroscopy, while timescales of 1 ns or more are typically probed by molecular fluorescence techniques (Perakis et al., 2016). A recent review by Levinger and Swafford provides a nice overview on some of the most widely used techniques such as Steady-State and Time-Resolved Infrared Spectroscopy, IR time-resolved anisotropy, vibrational echoes, and two-dimensional IR spectroscopy (Levinger and Swafford, 2009). The majority of experimental results available to date has been generated using ultrafast laser spectroscopy in reverse micelles using pump-probe techniques, that is a fluorescent probe which is excited first and whose fluorescence time behavior is studied during its solvation by the surrounding water molecules. Almost all studies converge towards a general picture in which, nanoconfined water exhibits a bimodal distribution of the relaxation times, with one relaxation time typical of bulk water (~ps) and a much slower time of the order of hundreds of ps (Bhattacharyya and Bagchi, 2000). By studying the fluorescence dynamics at various water content, the two components and their relative weight can be resolved, with the conclusion that the fast-relaxing water-like behavior component is reminiscent of bulk-like water, whereas the slow relaxation is the signature of the confined or interfacial water. This has led to a widely adopted core-shell model in which bulk-like properties of water vanish at a confinement of the order of $w_0 = 2$, i.e., when 2 water molecules for surfactant are present, pretty much independently from the molecular traits of the surfactant. The main challenge here is that, since the greatest majority of fluorescent probes are poorly water soluble, it becomes difficult to separate the effect of nanoconfinement from the effect of interfaces (Levinger and Swafford, 2009). Yet, similar conclusions are also reached by techniques not relying on fluorescence, such as in the case of quasi-elastic neutron scattering (QENS) (Spehr et al., 2011), further supporting the core-shell model.

Translational and rotational diffusion of nanoconfined water present features which may be seen as even more puzzling. In general, rotational diffusion of water in reverse micelles is found to exhibit a slow mode in near proximity of interfaces and a bulk-like behavior far (beyond ~0.8 nm) from the interfaces, provided the

water hydration is such to reach bulk-like properties, i.e., $w_0 = 7.5$ (Pieniazek et al., 2009). The translational diffusion coefficient is found to follow similar trends; yet, a distinction must be made among free self-diffusion of water in nanoconfined geometries and neat macroscopic flow (forced flow) under a pressure drop: in forced flow: the general view is that water flow in nanopores deviates significantly from the ideal no-slip conditions of the Hagen–Poiseuille model, with a positive effective slip length at the interface for hydrophobic interfaces and a negative effective slip length at hydrophilic interfaces. Here, hydrophilic and hydrophobic refer to contact angles lower/larger than 90° and to water-interface h-bonding stronger/weaker than water-water pairs, respectively (Lynch et al., 2020). Compared to the ideal Hagen–Poiseuille model this leads to a “super-diffusion” in hydrophobic nanopores, such as carbon nanotubes, and an under-diffusion in hydrophilic nanopores. Yet, recent contributions have highlighted the oversimplification of such a scheme and stressed the necessity to modify the effective slip length, as a linear sum of true slip, (a direct function of the contact angle), and an apparent slip, depending on the spatial features of nanoconfined water (Wu et al., 2017). In general, however, whether self-diffusion or effective diffusion are considered, deviations from the bulk-like behavior and the Hagen–Poiseuille ideal case become more pronounced with the level of nanoconfinement.

Opportunities

Water reactivity

The effect of nanoconfinement on water reactivity has been recently reviewed by Corti et al. (2021), who have discussed the correlation between confinement and increased reaction rates in several model reactions from microdroplets to nanodroplets. Although enhanced reactivity of organic reactions in reverse micelles has been known for decades, a quantitative breakthrough came with the work of Fallah-Araghi et al. (2014), who proposed a quantitative model based on the effect of interfaces, capable to preferentially adsorb the reactant over the product, and speeding up the reaction via a non-catalytic reaction-adsorption scheme. Notably, the model proposed by these authors was able to correctly describe the $\sim 1/d$ dependence of the effective reaction rate of bimolecular synthetic reactions over the confining geometry feature size, d . This was further supported by Wilson et al. (2020), who confirmed numerically the $\sim 1/d$ dependence of the equilibrium constant reactants/products by comparing stochastic simulations and experiments on imine synthesis. These studies address the effect of confinement in simple, model organic reactions, but set an important ground on which understanding more complex biochemical reactions, such as those involving enzymes and macromolecules.

Enzymatic reactions

Enzymatic reactions may highly benefit from confined geometries across different length scales. The general effect of

surface and volume confinement on enzymatic reactions have been recently reviewed by Küchler et al. (2016), who have discussed conditions of mild confinement. Here, given the brevity of this perspective, we focus on enzymatic reactions under strong soft nanoconfinement provided by lipidic mesophases, since in these systems the confinement, generally strong (<3 nm), can also be released by the help of co-surfactants.

A first distinction must be made on the type of enzyme considered: for example, Sun et al. (2016) demonstrated that while membrane-bound enzymes such as D-fructose dehydrogenase (FDH) preserve full activity within lipidic mesophases and follow the classic Michaelis–Menten kinetics, as a result of the “natural” reconstitution within lipid bilayers (although organized according to bicontinuous cubic phase symmetries), bulk enzymes such as horse radish peroxidase (HRP) do follow a different kinetics, which can better be rationalized by the Hill model, typical of bound enzymes. This immediately demonstrates that the very same nanoconfinement environment imparts different behavior to different types of enzymes (membrane-bound vs. soluble). Additionally, and more generally, soluble enzymes do not follow only different kinetics, but also lead to different fate of the converted substrate. Vallooran et al. (2016) were the first to show that various enzymes confined within lipidic cubic mesophases may lead to the crystallization of converted substrates due to the decreased solubility of the substrates after enzymatic reaction in nanoconfined water compared to bulk water. The crystals of enzymatically converted substrates were easily detectable via simple cross-polarized microscopy or even optical observation due to the transparent and isotropic background of the host bicontinuous mesophases. By connecting HRP to antibodies, Vallooran et al. (2016) extended this concept to detection of biomarkers (e.g., glucose, cholesterol), bacteria (*E. Coli*), viruses (HIV, Ebola) and even parasites (malaria), establishing a general platform for bio-detection via enzymatic reactions run under the strong soft nanoconfinement of lipidic mesophases. As Vallooran et al. (2019) further demonstrated, the molecular mechanism for this crystallization (and hence detection) is really based on the peculiar status of nanoconfined water, within which solubility of organic substances changes significantly: by releasing the nanoconfinement from a diameter of 2.6 nm–7.6 nm using co-surfactants capable to swell the lipidic mesophase channels, the same authors showed that the crystals change from microcrystals, to needle-like, to then fully dissolve upon further relaxation of nanoconfinement. Additionally, on top of this effect, different symmetries of the same mesophases do also affect the activity of the enzyme: Sun et al. (2015) showed that the connectivity of the topology may influence the activity of the enzyme at the same confinement level (water channel): four-fold connected bicontinuous cubic phases of Pn3m symmetry were found to impart higher activity to HRP than three-folded Ia3d bicontinuous cubic phases and 1-fold (columnar) hexagonal phases, respectively.

The strong lipidic nanoconfinement offered by lipidic mesophases opens new opportunities and enable expanding the scope of enzymatic reactions in general. Salvati Manni et al. (2019) realized that a modification of common lipid (monolinolein) tails preventing lipid from crystallizing at low temperature, gives access to undercooled water down to 6 K. Yao et al. (2021) expanded this concept to more common lipids (phytantriol) without needs of chemical modification and went on showing the possibility to run enzymatic reactions at cryogenic conditions at temperatures well

below those of freezing bulk water (See Figure 2 for details). In a first work they used both simple enzymatic reactions of HRP as well as cascading reactions of glucose oxidase and HRP to demonstrate not only the possibility to run these reactions below 0°C, but even to do so with increased turnover. The reason was found on stabilization of molecular intermediates of enzymatic reactions which are short-living at ordinary temperatures but that can be preserved at lower temperatures. In a second work, they expanded cryogenic enzymatic reactions in lipidic mesophases to Benzaldehyde lyase (Zhou et al., 2021). Interestingly, the unique soft nanoconfinement offered by lipidic mesophases has also been used to host enzymatic reactions with optimized stereochemistry synthesis. Zhou et al. (2018) showed that asymmetric synthesis of carbohydrates can be performed with increased turn-over by using aldolase nanoconfined in lipidic mesophases. In that specific case, the increased efficiency was understood to be a result of eased access of the substrate to the catalytic reaction center, located at the glycerol rich lipid–water interface, highlighting again the combined effects nanoconfined water with increased surface-volume ratios typical of strong nanoconfinement. Very recently Züblin et al. (2023) demonstrated that enzymatic polymerization of polysaccharides is highly enhanced in molecular weight and yield when performed under lipidic mesophase nanoconfinement compared to bulk, and even that it is possible to run the same enzymatic polymerization at cryogenic temperatures, further expanding the reach of enzymatic reactions *in-meso*.

- Cryogenic Properties

Before closing this brief perspective, we touch on two additional possible applications arising from the unique cryogenic properties of water within lipidic mesophases: low-temperature reconstitution of biological macromolecules and possible liquid storage of water for lunar manned applications.

The first application is motivated by the fact that lipid mesophases are ideal matrices to reconstitute and even crystallize membrane proteins via the so-called *in-meso* method (Landau et al., 1996). As a lamellar intermediate is presumed to be the structure assisting the reconstitution step prior to *in-meso* crystallization, it appears reasonable to expect reconstitution of membrane proteins and other biomacromolecules within the lamellar phase of those lipidic mesophases capable of escaping water and lipid crystallization (Yao et al., 2021).

The second application is motivated by a recent conceptual proposal suggesting phytantriol–water mesophases as a cyclic storage system for maintaining liquid water on the surface of the moon in anticipation of man-based lunar missions expected by the Global Exploration Roadmap before the end of this decade (Banica et al., 2023). The most fascinating aspect is that these two very diverse applications appear to be enabled by using the very same soft nanoconfinement system (water and phytantriol) and the very same mesophase symmetry (lamellar).

Outlook and conclusion

In this short perspective I have highlighted only a few of the many opportunities arising from the peculiar status of water under

soft nanoconfinement, some rudiments of the physical background needed to understand at least the basic features and how these could be serving in disparate fields ranging from chemical and enzymatic reactions in “soft nanoreactors,” to cryogenic reconstitution and preservation of biological macromolecules, to the most exotic application of liquid water storage on the surface of the moon. The overarching theme of this article is centered on the contrasting behavior between the ubiquity of liquid water and the diverse applications stemming out from its unique behavior under soft nanoconfinement. This contribution is meant to stimulate further our investigation of the many physical and chemical properties of nanoconfined water, which are still poorly understood, and to shed light on the plethora of applications possible for water under soft nanoconfinement.

Data availability statement

The original contributions presented in the study are included in the article/Supplementary material, further inquiries can be directed to the corresponding author.

Author contributions

RM: Conceptualization, Formal Analysis, Funding acquisition, Project administration, Resources, Validation, Visualization, Writing—original draft, Writing—review and editing.

References

- Adam, G., and Gibbs, J. H. (1965). On the temperature dependence of cooperative relaxation properties in glass-forming liquids. *J. Chem. Phys.* 43 (1), 139–146. doi:10.1063/1.1696442
- Alandri, S., and Mezzenga, R. (2020). The physics of lipidic mesophase delivery systems. *Phys. Today* 73 (7), 38–44. doi:10.1063/PT.3.4522
- Banica, M. C., Altorfer, T., Inauen, J., Wichser, D., Dudli, D., Sutter, M. W., et al. (2023). Conceptual assessment of a lipid-based liquid water storage system for lunar life support and exploration. *J. Aerosp. Eng.* 36 (6), 04023084. doi:10.1061/JAEEZ.ASENG-5187
- Bhattacharyya, K., and Bagchi, B. (2000). Slow dynamics of constrained water in complex geometries. *J. Phys. Chem. A* 104 (46), 10603–10613. doi:10.1021/JP001878F
- Cerveny, S., Mallamace, F., Swenson, J., Vogel, M., and Xu, L. (2016). Confined water as model of supercooled water. *Chem. Rev.* 116 (13), 7608–7625. doi:10.1021/ACS.CHEMREV.5B00609
- Corti, H. R., Appignanesi, G. A., Barbosa, M. C., Bordin, J. R., Calero, C., Camisasca, G., et al. (2021). Structure and dynamics of nanoconfined water and aqueous solutions. *Eur. Phys. J. E* 44 (11), 136–150. doi:10.1140/EPJE/S10189-021-00136-4
- Das, A., Patra, A., and Mitra, R. K. (2013). Do the physical properties of water in mixed reverse micelles follow a synergistic effect: a spectroscopic investigation. *J. Phys. Chem. B* 117 (13), 3593–3602. doi:10.1021/JP3102833
- Das Mahanta, D., Dennis, A., Brown, R., Pezzotti, S., Han, S., Schwaab, G., et al. (2023). Local solvation structures govern the mixing thermodynamics of glycerol–water solutions. *Chem. Sci.* 14 (26), 7381–7392. doi:10.1039/D3SC00517H
- Debenedetti, P. G., and Stanley, H. E. (2003). Supercooled and glassy water. *Phys. Today* 56 (6), 40–46. doi:10.1063/1.1595053
- Fallah-Araghi, A., Meguellati, K., Baret, J. C., El Harrak, A., Mangeat, T., Karplus, M., et al. (2014). Enhanced chemical synthesis at soft interfaces: a universal reaction-adsorption mechanism in microcompartments. *Phys. Rev. Lett.* 112 (2), 028301. doi:10.1103/PHYSREVLETT.112.028301
- Frank, H. S., and Wen, W. Y. (1957). Ion-solvent interaction. Structural aspects of ion-solvent interaction in aqueous solutions: a suggested picture of water structure. *Discuss. Faraday Soc.* 24 (0), 133–140. doi:10.1039/DF9572400133
- Gallo, P., Rovere, M., and Chen, S. H. (2010). Dynamic crossover in supercooled confined water: understanding bulk properties through confinement. *J. Phys. Chem. Lett.* 1 (4), 729–733. doi:10.1021/JZ9003125
- Hatakeyama, T., Tanaka, M., and Hatakeyama, H. (2010). Thermal properties of freezing bound water restrained by polysaccharides. *J. Biomaterials Sci. Polym. Ed.* 21 (14), 1865–1875. doi:10.1163/092050610X486946
- Huber, P. (2015). Soft matter in hard confinement: phase transition thermodynamics, structure, texture, diffusion and flow in nanoporous media. *J. Phys. Condens. Matter* 27 (10), 103102. doi:10.1088/0953-8984/27/10/103102
- Johari, G. P., Hallbrucker, A., and Mayer, E. (1987). The glass–liquid transition of hyperquenched water. *Nature* 330 (6148), 552–553. doi:10.1038/330552a0
- Knight, A. W., Kalugin, N. G., Coker, E., and Ilgen, A. G. (2019). Water properties under nano-scale confinement. *Sci. Rep.* 9 (1), 8246. doi:10.1038/s41598-019-44651-z
- Küchler, A., Yoshimoto, M., Luginbühl, S., Mavelli, F., and Walde, P. (2016). Enzymatic reactions in confined environments. *Nat. Nanotechnol.* 11 (5), 409–420. doi:10.1038/nnano.2016.54
- Landau, E. M., Ju^{rg}, J., Rosenbusch, P., and Kaback, H. R. (1996). Lipidic cubic phases: a novel concept for the crystallization of membrane proteins. *Proc. Natl. Acad. Sci.* 93 (25), 14532–14535. doi:10.1073/PNAS.93.25.14532
- Levinger, N. E., and Swafford, L. A. (2009). Ultrafast dynamics in reverse micelles. *Annu. Rev. Phys. Chem.* 60, 385–406. doi:10.1146/ANNUREV.PHYSCHEM.040808.090438
- Lynch, C. I., Rao, S., and Sansom, M. S. P. (2020). Water in nanopores and biological channels: a molecular simulation perspective. *Chem. Rev.* 120 (18), 10298–10335. doi:10.1021/ACS.CHEMREV.9B00830
- Martiel, I., Sagalowicz, L., and Mezzenga, R. (2014). Viscoelasticity and interface bending properties of lecithin reverse wormlike micelles studied by diffusive wave spectroscopy in hydrophobic environment. *Langmuir* 30 (35), 10751–10759. doi:10.1021/LA502748E
- Mezzenga, R., Seddon, J. M., Drummond, C. J., Boyd, B. J., Schröder-Turk, G. E., and Sagalowicz, L. (2019). Nature-inspired design and application of lipidic lyotropic liquid crystals. *Adv. Mater.* 31 (35), 1900818. doi:10.1002/ADMA.201900818

Funding

The author declares financial support was received for the research, authorship, and/or publication of this article. Open access funding by ETH Zurich.

Acknowledgments

I am most thankful to Dr. Yang Yao and Dr. Serena Alfarano for literature suggestions and insightful discussions.

Conflict of interest

The author declares that the research was conducted in the absence of any commercial or financial relationships that could be construed as a potential conflict of interest.

Publisher's note

All claims expressed in this article are solely those of the authors and do not necessarily represent those of their affiliated organizations, or those of the publisher, the editors and the reviewers. Any product that may be evaluated in this article, or claim that may be made by its manufacturer, is not guaranteed or endorsed by the publisher.

- Moilanen, D. E., Fenn, E. E., Wong, D., and Fayer, M. D. (2009). Geometry and nanolength scales versus interface interactions: water dynamics in AOT lamellar structures and reverse micelles. *J. Am. Chem. Soc.* 131 (23), 8318–8328. doi:10.1021/JA901950B
- Moilanen, D. E., Fenn, E. E., Wong, D., and Fayer, M. D. (2009). Water dynamics at the interface in AOT reverse micelles. *J. Phys. Chem. B* 113 (25), 8560–8568. doi:10.1021/JP902004R
- Moulik, S. P., and Paul, B. K. (1998). Structure, dynamics and transport properties of microemulsions. *Adv. Colloid Interface Sci.* 78 (2), 99–195. doi:10.1016/S0001-8686(98)00063-3
- Némethy, G., and Scheeaga, H. A. (1962). Structure of water and hydrophobic bonding in proteins. I. A model for the thermodynamic properties of liquid water. *J. Chem. Phys.* 36 (12), 3382–3400. doi:10.1063/1.1732472
- Ortiz-Young, D., Chiu, H. C., Kim, S., Voitchovsky, K., and Riedo, E. (2013). The interplay between apparent viscosity and wettability in nanoconfined water. *Nat. Commun.* 4 (1), 2482–2486. doi:10.1038/ncomms3482
- Perakis, F., Marco, L. De, Shalit, A., Tang, F., Kann, Z. R., Kühne, T. D., et al. (2016). Vibrational spectroscopy and dynamics of water. *Chem. Rev.* 116 (13), 7590–7607. doi:10.1021/ACS.CHEMREV.5B00640
- Pieniazek, P. A., Lin, Y. S., Chowdhary, J., Ladanyi, B. M., and Skinner, J. L. (2009). Vibrational spectroscopy and dynamics of water confined inside reverse micelles. *J. Phys. Chem. B* 113 (45), 15017–15028. doi:10.1021/JP906784T
- Salvati Manni, L., Assenza, S., Duss, M., Vallooran, J. J., Juranyi, F., Jurt, S., et al. (2019). Soft biomimetic nanoconfinement promotes amorphous water over ice. *Nat. Nanotechnol.* 14 (6), 609–615. doi:10.1038/s41565-019-0415-0
- Smart, A. G. (2017). Supercooled water survives in no-man's-land. *Phys. Today* 70 (2), 18–21. doi:10.1063/PT.3.3452
- Spehr, T. L., Frick, B., Zamponi, M., and Stühn, B. (2011). Dynamics of water confined to reverse AOT micelles. *Soft Matter* 7 (12), 5745–5755. doi:10.1039/C1SM05204G
- Sun, W., Vallooran, J. J., Fong, W. K., and Mezzenga, R. (2016). Lyotropic liquid crystalline cubic phases as versatile host matrices for membrane-bound enzymes. *J. Phys. Chem. Lett.* 7 (8), 1507–1512. doi:10.1021/ACS.JPCLETT.6B00416
- Sun, W., Vallooran, J. J., and Mezzenga, R. (2015). Enzyme kinetics in liquid crystalline mesophases: size matters, but also topology. *Langmuir* 31 (15), 4558–4565. doi:10.1021/ACS.LANGMUIR.5B00579
- Vallooran, J. J., Assenza, S., and Mezzenga, R. (2019). Spatiotemporal control of enzyme-induced crystallization under lyotropic liquid crystal nanoconfinement. *Angew. Chem.* 131 (22), 7367–7371. doi:10.1002/ANGE.201901078
- Vallooran, J. J., Handschin, S., Pillai, S. M., Vetter, B. N., Rusch, S., Beck, H. P., et al. (2016). Lipidic cubic phases as a versatile platform for the rapid detection of biomarkers, viruses, bacteria, and parasites. *Adv. Funct. Mater.* 26 (2), 181–190. doi:10.1002/ADFM.201503428
- Velikov, V., Borick, S., and Angell, C. A. (2001). The glass transition of water, based on hyperquenching experiments. *Science* 294 (5550), 2335–2338. doi:10.1126/SCIENCE.1061757
- Wilson, K. R., Prophet, A. M., Rovelli, G., Willis, M. D., Rapf, R. J., and Jacobs, M. I. (2020). A kinetic description of how interfaces accelerate reactions in micro-compartments. *Chem. Sci.* 11 (32), 8533–8545. doi:10.1039/D0SC03189E
- Wu, K., Chen, Z., Li, J., Li, X., Xu, J., and Dong, X. (2017). Wettability effect on nanoconfined water flow. *Proc. Natl. Acad. Sci. U. S. A.* 114 (13), 3358–3363. doi:10.1073/PNAS.1612608114
- Yan, C., Kramer, P. L., Yuan, R., and Fayer, M. D. (2018). Water dynamics in polyacrylamide hydrogels. *J. Am. Chem. Soc.* 140 (30), 9466–9477. doi:10.1021/JACS.8B03547
- Yao, Y., Zhou, T., Färber, R., Grossner, U., Floudas, G., and Mezzenga, R. (2021). Designing cryo-enzymatic reactions in subzero liquid water by lipidic mesophase nanoconfinement. *Nat. Nanotechnol.* 16 (7), 802–810. doi:10.1038/s41565-021-00893-5
- Yoshida, K., Yamaguchi, T., Kittaka, S., Bellissent-Funel, M. C., and Fouquet, P. (2008). Thermodynamic, structural, and dynamic properties of supercooled water confined in mesoporous MCM-41 studied with calorimetric, neutron diffraction, and neutron spin echo measurements. *J. Chem. Phys.* 129 (5), 054702. doi:10.1063/1.2961029
- Yuan, R., Yan, C., Nishida, J., and Fayer, M. D. (2017). Dynamics in a water interfacial boundary layer investigated with IR polarization-selective pump-probe experiments. *J. Phys. Chem. B* 121 (17), 4530–4537. doi:10.1021/ACS.JPCB.7B01028
- Zhou, T., Vallooran, J. J., Assenza, S., Szekrenyi, A., Clapés, P., and Mezzenga, R. (2018). Efficient asymmetric synthesis of carbohydrates by aldolase nano-confined in lipidic cubic mesophases. *ACS Catal.* 8 (7), 5810–5815. doi:10.1021/ACSCATAL.8B01716
- Zhou, T., Yao, Y., Zhang, Q., and Mezzenga, R. (2021). Cryogenic activity and stability of benzaldehyde lyase enzyme in lipidic mesophases-nanoconfined water. *Chem. Commun.* 57 (46), 5650–5653. doi:10.1039/D1CC01315G
- Züblin, P., Zeller, A., Moulis, C., Remaud-Simeon, M., Yao, Y., and Mezzenga, R. (2023). Expanding the enzymatic polymerization landscape by lipid mesophase soft nanoconfinement. *Angew. Chem. Int. Ed.* doi:10.1002/anie.202312880



OPEN ACCESS

EDITED BY

Ali Miserez,
Nanyang Technological University,
Singapore

REVIEWED BY

Erica Pensini,
University of Guelph, Canada
Erik Van Der Linden,
Wageningen University and Research,
Netherlands

*CORRESPONDENCE

Anne-Laure Fameau,
✉ Anne-laure.fameau@inrae.fr

RECEIVED 26 October 2023

ACCEPTED 17 November 2023

PUBLISHED 30 November 2023

CITATION

Dari C, Si Y, Douliez J-P, Tahon J-F,
Benezech T, Clegg PS and Fameau A-L
(2023), Mixture of fatty alcohols and alkyl
polyglucosides stabilizing water-in-
water emulsions.
Front. Soft Matter 3:1328195.
doi: 10.3389/frsfm.2023.1328195

COPYRIGHT

© 2023 Dari, Si, Douliez, Tahon,
Benezech, Clegg and Fameau. This is an
open-access article distributed under the
terms of the [Creative Commons
Attribution License \(CC BY\)](#). The use,
distribution or reproduction in other
forums is permitted, provided the original
author(s) and the copyright owner(s) are
credited and that the original publication
in this journal is cited, in accordance with
accepted academic practice. No use,
distribution or reproduction is permitted
which does not comply with these terms.

Mixture of fatty alcohols and alkyl polyglucosides stabilizing water-in-water emulsions

Carolina Dari¹, Yuchen Si², Jean-Paul Douliez³,
Jean-François Tahon⁴, Thierry Benezech¹, Paul S. Clegg² and
Anne-Laure Fameau^{1*}

¹CNRS, INRAE, Centrale Lille, UMET, University of Lille, UMR 8207, Lille, France, ²School of Physics and Astronomy, University of Edinburgh, Edinburgh, United Kingdom, ³Biologie du Fruit et Pathologie, UMR 1332, INRAE, Université De Bordeaux, Villenave d'Ornon, France, ⁴Unité Matériaux Et Transformations (UMET), UMR CNRS 8207, Université de Lille Nord de France, USTL-ENSCL, Villeneuve D'Ascq, France

The combination of surfactants and fatty alcohols leads to the formation of lamellar gel network (LGNs) which are widely used in cosmetic and pharmaceutical industries. Alkyl polyglucosides are known to stabilize oil-in-water emulsions and here, we report their use in combination with fatty alcohol for the stabilization of all-aqueous water-in-water (W/W) emulsions based on dextran-in-poly(ethylene glycol). Two different APGs were used: decyl glucoside and lauryl glucoside. We systematically studied the influence of the concentrations of APGs, and the molar ratio between the APGs and decanol as model fatty alcohol on the size and stability of the aqueous emulsion droplets with time. The self-assembled structure formed by decanol/APGs was characterized by using Small Angle X-ray Scattering and confocal microscopy, and shown to be lamellar in the bulk phase and probably also at the surface of dextran-rich droplets. We also demonstrated that the stabilization of W/W emulsions can be extended to other alkyl polyglucoside and to other fatty alcohols. In addition, we reported the production of a foam using such W/W emulsions as the continuous phase. Our results show that it is possible to stabilize W/W emulsions using LGNs based on different APGs and fatty alcohols, which will undoubtedly expand the use of W/W emulsions for various fields.

KEYWORDS

emulsion, lamellar phase, fatty alcohol, alkyl polyglucoside, foam

1 Introduction

Emulsions, which are commonly used in a wide range of applications, are made up of two thermodynamically incompatible solutions or solvents (Leal-Calderon et al., 2007). The most conventional ones are oil-in-water or water-in-oil emulsions. However, a more unusual emulsion system is based on an aqueous solution that forms droplets into another aqueous solution, the so-called 'water-in-water emulsions' (W/W emulsions) (Esquena, 2016; 2023; Dickinson, 2019). The formation of W/W emulsions occurs when a moderately concentrated solution of incompatible polymers exhibits thermodynamic phase separation (Dickinson, 2019). In contrast to oil-in-water emulsions, W/W emulsions are much more difficult to stabilize since the surface tension is very low (around 0.1–100 $\mu\text{N} \cdot \text{m}^{-1}$) and the interface thickness is large (at least, few tens of nanometers) (Antonov et al., 2004; Esquena, 2016). For these physical reasons, W/W emulsions cannot be stabilized by the common surfactants usually used for the stabilization of the oil-in-water or water-in-oil emulsions. Thus, when

formed upon mixing, droplets coalesce with time more or less quickly, depending on the system investigated and then, macroscopic phase separation occurs. The lack of stability of W/W emulsions is the main drawback that limits their use for practical applications (Esquena, 2016). Several applications of W/W emulsions have been reported in various fields: food, biomedical, drug delivery, etc. (Esquena, 2016; Esquena, 2023). For example, they can be used to encapsulate active components and labile molecules, and then be used as delivery systems. They can also be used as microreactors for the synthesis of high value-added products (Esquena, 2016; Esquena, 2023). The field of water-in-water emulsions is experiencing growth, driven by the discovery of new methods to improve their stability. Therefore, finding new methods to effectively stabilize W/W emulsions is a major challenge for scientists to expand their use.

Despite the difficulties in stabilizing them, W/W emulsions have been shown to be efficiently stabilized by using a wide variety of chemicals and particles as reviewed by several authors (Nicolai and Murray, 2017; Dickinson, 2019; Chao and Shum, 2020). For example, W/W emulsions can be stabilized by polymer particles (Poortinga, 2008; Douliez et al., 2018; Douliez et al., 2019), microgels (Merland et al., 2022; You et al., 2023), cellulose nanocrystals (Ben Ayed et al., 2018; Xie et al., 2023), protein particles (Nguyen et al., 2013), etc. Other stabilization methods based on the use of amphiphiles are also described in the literature such as: block copolymers, self-assembly of fatty acids and phospholipids, oligonucleotides, liposomes, etc., (Dewey et al., 2014; Chao and Shum, 2020). These chemicals or particles are positioned at the interface of the droplets, which prevents their coalescence and, subsequently, macroscopic phase separation. The mechanisms by which this occurs remain unclear in most cases and is probably due to an equal affinity of the particles or chemicals for the droplet-forming polymer and the continuous aqueous phase enriched in the other polymer.

Recently, stable W/W emulsions have been designed by using sodium oleate (surfactant) and decanol (fatty alcohol) with a simple addition process of the components to the two aqueous phase system (Coudon et al., 2022). The mixture of surfactant and fatty alcohols are widely used forming Lamellar gel Network (LGNs) that are of strong interest in the field of cosmetic and pharmaceutical industries (Eccleston, 1997). Lamellar gel networks (LGNs), which are also called “ α -gel” in the literature, are used to give creamy texture to the products (Eccleston, 1997; Iwata, 2017). LGNs are based on the mixture of long-chain fatty alcohols with surfactants in aqueous solution (Iwata, 2017; Colafemmina et al., 2020; de Oliveira et al., 2020). By using appropriate concentrations and molar ratio of these two components, the formation of LGNs occurs. It can be described as a multi-phase colloidal structure mainly composed of lamellar phase and bulk water. When oil droplets are present in the formulation, they are entrapped and stabilized by the LGNs both present in the bulk aqueous phase and surrounding them (Junginger, 1984; Eccleston, 1997; Nakarapanich et al., 2001). The study of Coudon et al. was the first one showing the use of LGNs to stabilize water-in-water (W/W) emulsions (Coudon et al., 2022).

In the current context of growing concern for the environment, natural-based surfactants became popular as an alternative to the synthetic ones to produce LGNs and are widely used for cosmetic and pharmaceutical applications (Savic et al., 2005; Terescenco et al., 2018a; Terescenco et al., 2018b). Alkyl polyglucoside (APG) is one of

the well-known families of natural surfactants, derived from natural glucose and a fatty alcohol. It is considered as non-toxic, mild and environmentally friendly emulsifier (Dari et al., 2023). Our aim here was to study the stabilization of W/W emulsions by using LGNs based on various APGs. Interestingly, these surfactants (APGs) are non-ionic surfactant whereas most of the chemical components and particles that have been used in the literature for stabilizing W/W emulsions are either charged or at least, zwitterionic (Esquena, 2023). This could be an advantage when the systems require changes in pH or ionic strength that may alter the stability of the emulsion, as is the case when W/W emulsions are used for bacterial culture (Xie et al., 2023; Zhang et al., 2024).

Here, we used two different APGs: decyl glucoside (DG) and lauryl glucoside (LG). DG and LG differ in their alkyl chain length composition. DG comprises a mixture of alkyl chains ranging from 8 to 16 carbon atoms, while LG consists of a mixture ranging from 12 to 16 carbon atoms (Keck et al., 2014; Wu et al., 2017). In addition, they differ in their degree of glycosidation: DG has a value of 1.5 and LG, 1.4. These APGs were combined with decanol as model fatty alcohol. The model W/W emulsions system was based on dextran-in-poly(ethylene glycol) (PEG) droplets. We systematically investigated the influence of the concentrations of APG, and the molar ratio between this surfactant and the fatty alcohol on the size and stability with time of the aqueous emulsion droplets. Then, we gained insight into the structure by combining confocal microscopy and Small Angle X-ray Scattering (SAXS). We also demonstrated the versatility of these surfactants mixtures by extending the approach to another APG (coco-glucoside, CG) and other fatty alcohols (dodecanol and myristyl alcohol). Furthermore, we show that a foamulsion could be produced from such stabilized W/W emulsion. Our results show that it is possible to use the combination of fatty alcohols and APGs for the formulation of different type of W/W emulsions, which will surely broaden the use of W/W emulsions for various fields such as cosmetics and pharmaceuticals.

2 Materials and methods

2.1 Materials

The following chemicals were purchased from Sigma-Aldrich (Saint Quentin Fallavier, France) and used as received: dextran 450–650 kg/mol, poly(ethylene glycol) 20 kg/mol (PEG), Nile red, fluorescein isothiocyanate-dextran 500 kg/mol (FITC-dextran), 1-decanol, 1-dodecanol, ethanol, and sodium dodecyl sulfate (SDS) with 98.5% purity. Lauryl glucoside (plantacare 1200 up) (LG) with 51.3 wt% of active matter, decyl glucoside (plantacare 2000 up) (DG) with 53.0 wt% of active matter, coco glucoside (plantacare 818 up) with 51.4 wt% of active matter and myristyl alcohol (lanette 14) were provided by BASF (Ludwigshafen, Germany) and used as received. Milli-Q water was used for all experiments.

2.2 Preparation of the stock solutions

To prepare the all-aqueous emulsion, both the polymers PEG and Dextran were weighed in a flask and Milli-Q water was added so that the PEG concentration was 7 wt% and the dextran

concentration was 3.25 wt%. Then, the mixture was stirred magnetically at 60°C until polymers were completely dissolved. It formed a slightly turbid dispersion formed by polydisperse droplets enriched in Dextran in the continuous PEG phase, which coalesced with time until macroscopic phase separation occurs as expected for such aqueous emulsion (not shown).

A solution of APG (DG, LG or CG) was prepared by weighing into a flask the APG and adding Milli-Q water so that the final concentration of the APG active matter was 5 wt%, followed by stirring magnetically at 60°C until the APG was completely dissolved. Nile red was dissolved in ethanol to obtain a final concentration of 5 mg mL⁻¹, then an aliquot of this solution was added to each of the APGs solutions to obtain a final concentration of 0.1 mg mL⁻¹. A solution of FITC-dextran was prepared by weighing the dye and adding Milli-Q water so that the concentration was 20 mg mL⁻¹. All these stock solutions were stored at around 4°C in a fridge.

2.3 Preparation of the stabilized W/W emulsions

Different protocols were used to prepare W/W emulsions depending on the fatty alcohols used and its melting point. To produce PEG-in-dextran W/W emulsion, 5 mL of the PEG-dextran mixture was taken and placed in a 15 mL tube (Falcon) while stirring the mixture. 50 µL of the FITC-dextran stock solution were added to the tube and all was mixed by vortexing; followed by the addition of a given volume of the stock solution of APG (DG, LG or CG) doped with Nile red. Then the emulsion was vortexed for another 30 s. The same protocol was used to prepare the inverse W/W emulsion (PEG-in-dextran emulsions) but starting with the preparation of PEG at 2 wt% and Dextran at 14 wt%.

To prepare the dextran-in-PEG emulsions in the presence of APG and dodecanol, 5 mL of the PEG-dextran mixture was taken and placed in a 15 mL tube (Falcon) while stirring the mixture at 40°C. Then, 50 µL of the FITC-dextran stock solution was added to the tube and all were mixed by vortexing. A given volume of 1-dodecanol at 40°C was added to the previous mixture and mixed thoroughly by vortexing, followed by the addition of a given volume of the stock solution of LG or DG doped with Nile red, then the emulsion was vortexed for another 30 s.

To prepare dextran-in-PEG emulsions in the presence of APG and myristyl alcohol, the myristyl alcohol was first heated to 90°C, until it was completely melted, and then the required amount was weighed in a beaker. 5 mL of the PEG-dextran mixture was taken and placed in the same beaker while stirring the mixture, 50 µL of the FITC-dextran stock solution was added, and all were mixed together under magnetic stirring at 60°C until the myristyl alcohol was completely dissolved. The resulting mixture was placed in a 15 mL tube (Falcon) and a given volume of LG or DG doped with Nile red was added while vortexing. Then, the emulsion was vortexed for another 30 s.

2.4 Preparation of the foamulsion

A dextran-in-PEG emulsion (10 wt% of dextran and 10 wt% of PEG) stabilized with LG and decanol was prepared as previously

described. A given volume of the emulsion was transferred to a beaker and a given volume of surfactant was added. The mixture was slowly mixed with magnetic stirring for 30 s. To prepare the foamulsion, the double-syringe foaming technique was used (Gaillard et al., 2017). Two 10-mL syringes were connected with a Luer-lock connector. One syringe was filled with 3.5 mL of the mixture and 6.5 mL of air. The second syringe was maintained with the piston in the fully closed position. The foam was then produced by pushing the plungers of the connected syringes 30 times by hand. The stability of the resulting foams was followed by measuring both the evolution of the foam and the volume of drained liquid over time with the naked eye.

2.5 Stability and partial phase diagram of the W/W emulsions

The bulk stability of the W/W emulsions with different molar ratio (R) of decanol:APG was followed with the naked eye (phase separation), and also by confocal fluorescence microscopy observations. Experiments were performed immediately after the production of W/W emulsions ($t = 0$) and after 24 h ($t = 24$ h) of conservation at room temperature. Pictures of the tubes containing the samples were taken with an iPhone mini 13 (Apple). Microscopy images were acquired using a fluorescence confocal microscope (LSM 700, Zeiss) with $\times 63$ oil immersion objective. Dyes were excited by using the following excitation (λ_{ex}): FITC-dextran, $\lambda_{ex} = 488$ nm; Nile Red, $\lambda_{ex} = 555$ nm. The microscopy images were processed using ImageJ software, following the method introduced by Gaillard et al. (2015) in order to obtain the area of 50 droplets for each sample. Long-term evolution of the W/W was also done through microscopy observations of the samples using an epifluorescence microscope (Zeiss Axioskop 2 Plus, Oberkochen, Germany) with $\times 40$ objective.

2.6 Structural characterization of W/W emulsions by small angle X-ray scattering (SAXS)

SAXS experiments were performed on a XEUS 2.0 device (XENOCOS, Grenoble, France) operating under vacuum with a GeniX3D microsource ($\lambda = 1.54$ Å) at 0.6 mA and 50 kV and a 2D Pilatus 3R 200 K detector. The sample was loaded in thin quartz capillaries (optical path 1.5 mm, WJM-Glas/Müller GmbH, Germany) and the signal collected for 3 h. The detector was placed perpendicularly to the direct beam at distance of 2.3 m, calibrated in both cases with a Silver Behenate standard. Peak fit[®] software was used for diffractogram deconvolution by using combination of Gaussian and Lorentzian functions.

2.7 Determination of the critical micellar concentration (CMC) via surface tension

The CMC values of the surfactants were obtained by using the automatized surface tension plate reader Kibron Delta-8 (Kibron, Finland). A volume of 50 µL of aqueous dispersion was placed on the

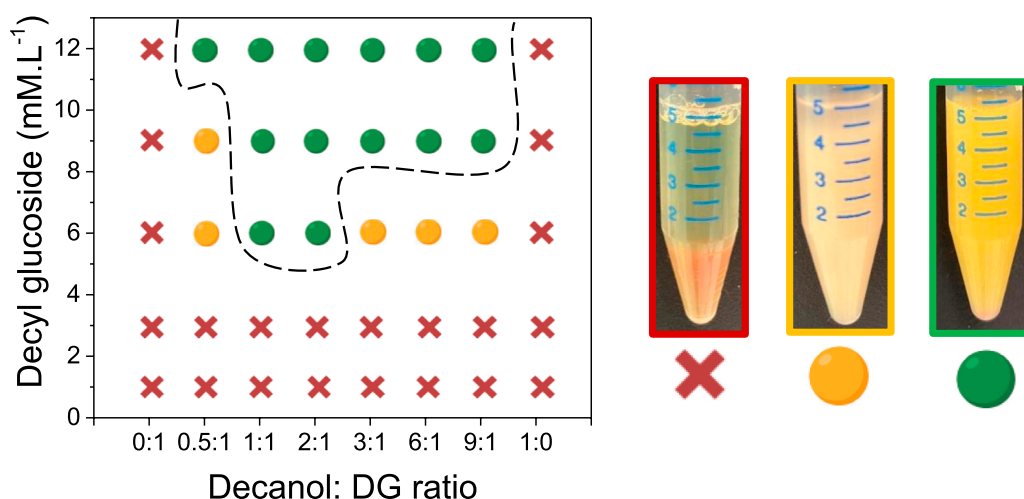


FIGURE 1

Partial phase diagram determined by visual observations by varying the decyl glucoside (DG) concentration as a function of the molar ratio between decanol and decyl glucoside showing the stable domain of W/W emulsion (dashed black line). Red crosses correspond to samples where macroscopic phase separation occurred after 24 h. Orange circles correspond to samples where a slight macroscopic phase separation occurred after 24 h. Green circles correspond to stable samples after 24 h. On the right side, pictures of samples illustrate the three regimes. The samples are from left to right: unstable W/W emulsion for DG = 9 mM and R = 0:1, medium stability W/W emulsion for DG = 6 mM and R = 3:1, and high stability W/W emulsion for DG = 9 mM and R = 2:1.

96-hole platform. Measurements were performed in duplicate at $28^{\circ}\text{C} \pm 1^{\circ}\text{C}$ after a waiting time of 10 min to ensure equilibrium at the air-water interface. A calibration was performed by using ultrapure water at $28^{\circ}\text{C} \pm 1^{\circ}\text{C}$.

2.8 Evaluation of the W/W stability by centrifugation

The samples were centrifuged in a centrifuge (Sigma 6K15, Thermo Fisher Scientific, Strasbourg, France) at $1500 \times g$ for 10 min. Microscopy images of the samples were taken before and after centrifugation using an epifluorescence microscope (Zeiss Axioskop 2 Plus, Oberkochen, Germany) with $\times 40$ objective.

2.9 Statistical analysis

The radius of 50 droplets was calculated for each sample and the average and standard deviation were determined. The results were compared by one-way analysis of variance and Tukey's test to analyze statistical differences ($p < 0.05$). The analysis was performed using SAS V8.0 software (SAS Institute, Gary, NC, United States).

3 Results and discussion

3.1 Phase diagram of the W/W emulsions

Dextran-in-PEG emulsions were prepared at 3.25 wt% (W/W) dextran (450–650 kg/mol) and at 7 wt% (W/W) PEG (20 kg/mol), since at this composition the polymers were fully phase-separated as

determined previously in the literature (Diamond and Hsu, 1989). In these experimental conditions, dextran enriched droplets formed in the continuous enriched PEG phase. Droplets of ca. 10–50 μm formed upon shaking when observed immediately after preparation but coalesced with time yielding macroscopic phase separation as already described in the literature (Coudon et al., 2022).

Then, we added different quantities of decyl glucoside (DG) and decanol varying from 1 to 12 mM as described in the Materials and Methods Section. The concentration of the APGs varied from 2 to 20 times the CMC (Supplementary Figures S1, S2). The molar ratio (R) corresponds to the moles number between decanol and DG, and it varied from 1:0 to 0:1. The stability of the W/W emulsions were determined after 24 h at room temperature with the naked eye to eventually determine the presence of a phase separation or a supernatant (Figure 1). When phase separation occurred, we defined this W/W emulsion as unstable. When a small supernatant was observed, we classified this emulsion as medium stability, and when no macroscopic change was observed, we defined these emulsions as stable (Figure 1).

The addition of the pure components, either DG or decanol, whatever the concentrations led to complete phase separation of the aqueous emulsion within 3 h. Then, the pure components did not have a significant effect on the behavior of the polymer's mixtures, and they could not stabilize dextran-rich droplets. However, the addition of the two components (DG and decanol) led to stabilization of emulsions for a relatively large domain of concentrations and molar ratios. A minimal concentration of DG (6 mM) and a minimal fraction of decanol ($R = 0.5:1$) were required to produce emulsions with medium stability. At the same DG concentration (6 mM), and with higher decanol fractions ($R = 1:1$ and $R = 2:1$) emulsions with high stability were observed. However, when the decanol fraction was further increased ($R \geq 3:1$), a supernatant was observed after 24 h leading to an emulsion with

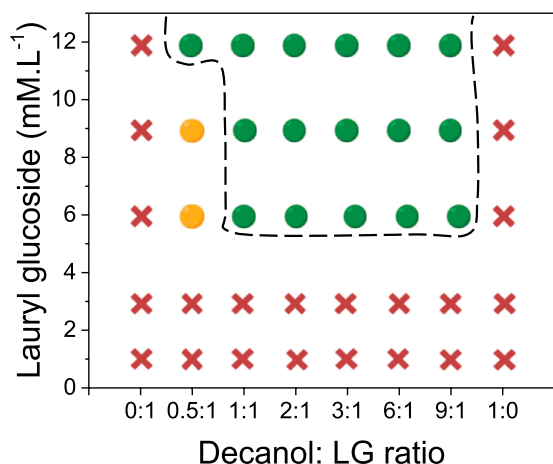


FIGURE 2

Partial phase diagram determined by visual observations by varying the lauryl glucoside (LG) concentration as a function of the molar ratio between decanol and Lauryl glucoside showing the stable domain of W/W emulsion (dashed black line). Red crosses correspond to samples where macroscopic phase separation occurred after 24 h. Orange circles correspond to samples where a slight macroscopic phase separation occurred after 24 h. Green circles correspond to stable samples after 24 h.

medium stability. When the concentration of DG was increased to 9 mM, an emulsion with medium stability was only observed for low R ($R = 0.5:1$). Then, emulsions with no supernatant were observed after 24 h for all the other R studied ($1:1 > R \geq 9:1$). At a DG concentration of 12 mM, emulsions with high stability were obtained both at low decanol fraction and at high decanol fractions (from $R = 0.5:1$ to $R = 9:1$).

We then decided to test the substitution of the DG by another APG with a longer alkyl chain: lauryl glucoside (LG). Dextran-in-PEG emulsions were then prepared with different concentrations of LG from 1 to 12 mM and with a molar ratio (R) between decanol and LG, R varying from 1:0 to 0:1. The stability of the W/W emulsions were determined in the same way as for the emulsions stabilized with DG described previously (Figure 2 and Supplementary Table S1B). The addition of pure LG whatever the concentration led to complete phase separation within 3 h, as previously described for pure DG or pure decanol. The addition of decanol in combination with LG was necessary to stabilize the emulsions. A minimal concentration of LG (6 mM) and a minimal fraction of decanol ($R \geq 0.5:1$) were required to produce emulsions with medium stability. This result was similar to the one obtained for DG. When the molar ratio was increased ($R \geq 1:1$), emulsions with high stability were obtained for all the concentrations (6, 9 and 12 mM). The increase of the concentration of LG to 12 mM led to emulsions with high stability even at a minimal fraction of decanol ($R = 0.5:1$). Stable emulsions with LG were produced for a wider range of R in comparison to DG (Figures 1, 2).

Then, we also determined the droplets size evolution between the initial size ($t = 0$, that stands for observations done immediately after mixing all components) and after 24 h with statistical analysis by confocal fluorescence microscopy of the samples doped with FITC-dextran and Nile red (Figure 3, Supplementary Figure S3 and Supplementary Tables S1A, B). First, we compared the initial

droplets size between DG and LG for all the R and concentrations to determine the main parameters leading to the smallest droplets size. For DG with $R = 0.5:1$, by varying the concentration from 6 to 12 mM, we observed a decrease of the average radius from 7.3 ± 3.6 to $2.1 \pm 1 \mu\text{m}$. The same trend was observed for all the concentrations and all the R showing that the initial droplet sizes decreased by increasing the DG concentration (Figure 3). For LG with $R = 0.5:1$, by varying the concentration from 6 to 12 mM, we observed a decrease of the average radius from 5.9 ± 3.1 to $3 \pm 1.1 \mu\text{m}$, respectively for 6 and 9 mM. However, there was no statistical differences from 9 to 12 mM, with an average radius of 3 ± 1.1 and of $2 \pm 0.5 \mu\text{m}$ for example, for $R = 0.5:1$. The concentration of the APG was a key parameter for controlling the initial droplet size. We hypothesize that by increasing APGs concentration leading also to a concomitant increase of decanol in the formulation, an increase of viscosity of the bulk phase could occur leading to a decrease of the droplets size. However, it is important to keep in mind that other parameters could also explain this phenomenon: quantity and structure of the self-assembly formed, interaction between APGs and polymers, etc.

Between the two APGs, we observed also statistical differences between the initial droplet sizes, with bigger droplets for DG than for LG when the concentration was set at 6 and 9 mM. However, the initial droplet size was the same at 12 mM for both APGs. The difference between DG and LG could be explained by the fact that APGs have different CMC values (Supplementary Figure S1), with LG having a lower CMC than DG. Here, all the samples were produced above the CMC. However, at the same concentration, LG with a longer alkyl chains and lower CMC than DG produce more easily rod-like micelles (Platz et al., 1995). Thus, it is easier to transit from rod-like micelles to lamellar phases by adding a small amount of fatty alcohol than from spherical micelles. Moreover, the presence of an excess of lauryl glucoside under rod-like micelles leading to a more viscous bulk continuous phase than for DG under spherical micelles could also explain the difference of stability at the lowest concentration (6 mM) (Stradner et al., 2000; Chu et al., 2013). We believe that the presence of rod-like micelles helps with the formation of the lamellar phases that stabilize the droplets. Then, we studied the effect of the molar ratio (R) between decanol and the APGs (DG or LG) on the initial droplets size (Supplementary Tables S1A, B). For DG at the three concentrations, we observed that for $R = 0.5:1$ the initial droplet size was always higher than for all the others R. The same trend was observed for LG. For $R = 0.5:1$, there was an excess of APGs in comparison to the decanol which could lead to the formation of a low quantity of lamellar structures in a mixture with APGs micelles and mixed micelles containing decanol (Möller et al., 1998). The quantity of lamellar structures could be not sufficient to stabilize small droplets during the production of the W/W emulsion. Then, we observed for both LG and DG that for R with high amount of decanol in comparison to the APG ($R = 6:1$ and $R = 9:1$), the droplet size was statistically lower than for $R = 0.5:1$ with an excess of APGs, but always higher than for intermediate R: $R = 3:1$, $R = 2:1$ and $R = 1:1$ (Figure 3 and Supplementary Figure S3). The best R to have high stability with small droplet size were $R = 3:1$, $R = 2:1$ and $R = 1:1$. These 3R lead to the smallest droplet size. Therefore, R is also a key parameter to take into account to reach small droplet size. A

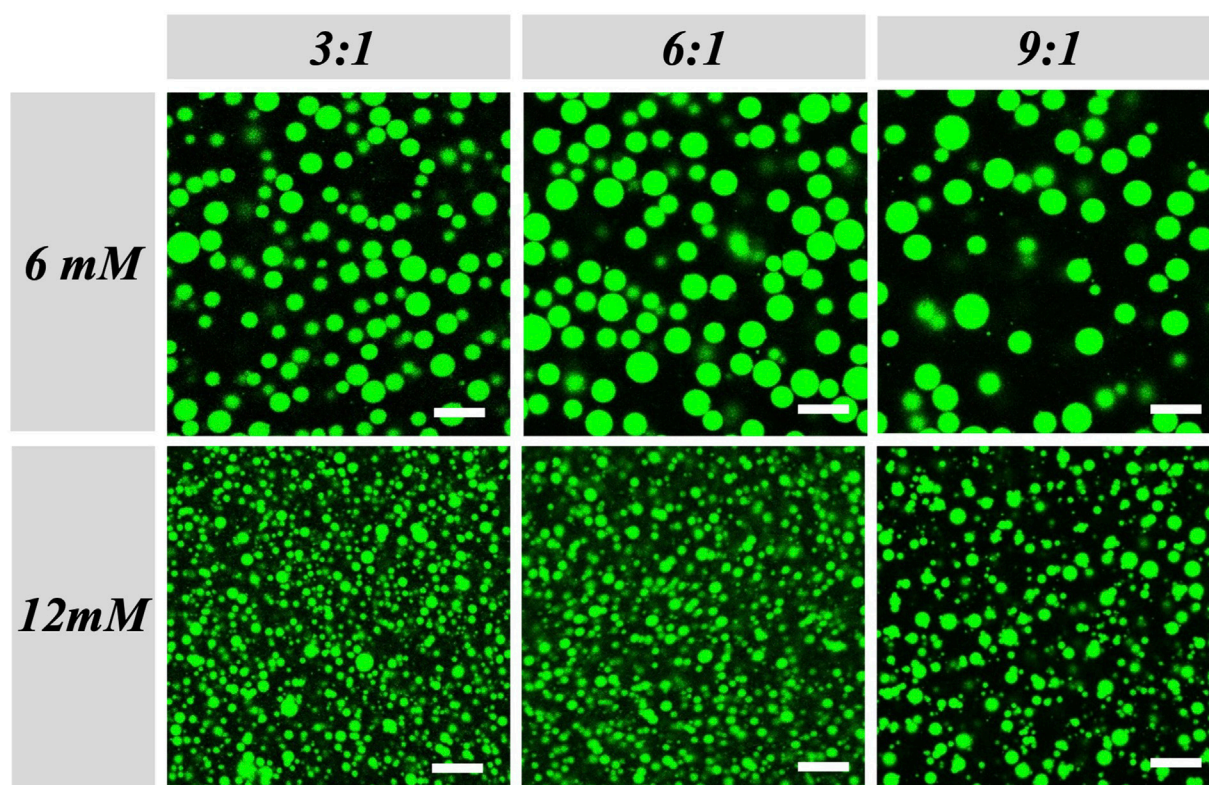


FIGURE 3

Effect of both DG concentration and decanol:DG ratio (R) on W/W emulsions droplets size. Confocal microscopy images of the W/W emulsions taken at $t = 0$ for two different DG concentrations: 6 mM (top) and 12 mM (bottom), and three different R : $R = 3:1$ (left), $R = 6:1$ (middle) and $R = 9:1$ (right). Droplets are labeled with FITC-dextran dye. The scale bar represents 15 μm .

large excess of APG ($R = 0.5:1$) or decanol ($R \geq 6:1$) is not appropriate for small droplet size. We compared also the droplet size evolution after 24 h for all the stable samples detected by visual observations (Figures 1, 2). No statistical difference was observed showing that in all cases the droplet size was stable after 24 h (Figure 3, Supplementary Figure S3 and Supplementary Tables S1A, B). Again, the composition (concentration and molar ratio) had been shown to influence the diameter of droplets in a similar system (Coudon et al., 2022).

Our results confirm that stabilization of the interface between hydrophilic polymers is not possible using amphiphilic molecules alone (Esquena, 2016). Instead, changing the self-assembly of these molecules by adding fatty alcohol proves to be an effective method to produce stable all-aqueous droplets (Coudon et al., 2022; Esquena, 2023). In addition, our results highlight that to obtain stable emulsions based on mixture of fatty alcohol and APGs, whatever the type of oil-in-water or water-in-water emulsion, a minimum molar ratio of 1:1 fatty alcohol:surfactant is required (Terescenco et al., 2018b). As described in the literature for LGNs formation based on mixture of fatty alcohols and surfactants, a minimum amount of fatty alcohol is required, and it is reported to be close to a weight ratio 1:1 as found in this study (Eccleston, 1997). Moreover, comparing our results to those obtained for LGNs based on sodium oleate and decanol, we observe that whatever the nature of the surfactants (anionic or non-ionic surfactants) with fatty alcohol,

stable W/W emulsions are only possible for a molar ratio higher than 1:1 (Coudon et al., 2022).

3.2 Long-term stability of W/W emulsions stabilized by LGNs

The long-term stability of the emulsions was studied by microscopy observations during 42 days. Fluorescence microscopy observations of the emulsions stabilized with DG at a concentration of 12 mM and with $R = 3:1$ showed the presence of uniform droplets that did not change significantly in size after 7 days compared to $t = 0$ (average radius = $1.4 \pm 0.4 \mu\text{m}$) (Supplementary Figure S4A). However, after 7 days a macroscopic phase separation was observed with the naked eye. Microscopy observations of the emulsions stabilized with LG at a concentration of 12 mM and with $R = 3:1$ showed the presence of uniform droplets that did not change significantly in size after 42 days compared to $t = 0$ (average radius = $1.6 \pm 0.6 \mu\text{m}$) (Supplementary Figure S4B). In addition, we tested the robustness of the emulsions with centrifugation. After centrifugation at $1500 \times g$ for 10 min, we observed neither phase separation nor supernatant showing that the self-assembled structure formed by decanol and APGs form a robust layer protecting the droplets against mechanical stress. We also checked the effect of the centrifugation directly on the droplets by measuring the droplets size before and after the centrifugation

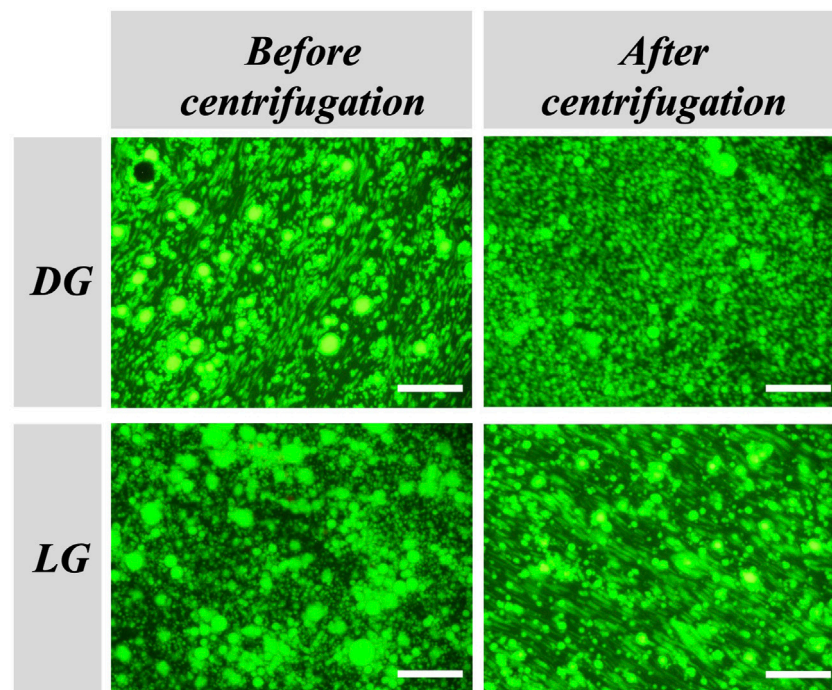


FIGURE 4

Effect of centrifugation on the stability of the W/W emulsions. Epifluorescence microscopy images of W/W emulsions stabilized with DG (top) or LG (bottom) at a concentration of 12 mM with a molar ratio of $R = 3:1$, taken before centrifugation (left) and after centrifugation (right). Droplets are labeled with FITC-dextran dye. The scale bar represents 60 μm .

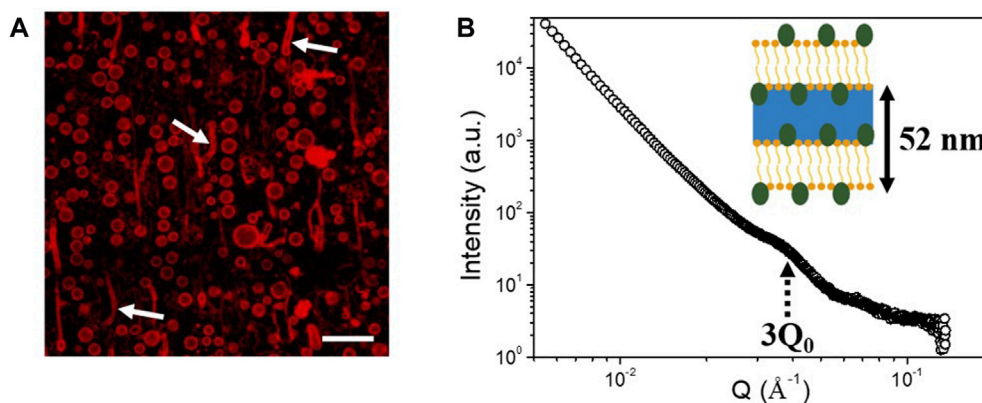


FIGURE 5

(A) Confocal microscopy image of dextran-in-PEG emulsion stabilized with LG at a concentration of 9 mM and with a molar ratio of decanol:LG at 1:1, showing the presence of lamellar phases (some of them identified with white arrows) in the continuous phase of the emulsion. Nile red was used to label the surfactant and fatty alcohol. The scale bar represents 15 μm . (B) 1D SAXS diffractogram of a water-in-water emulsion stabilized by a mixture of LG and decanol with a LG concentration of 12 mM and a molar ratio of decanol:LG at 3:1. Only the third order Bragg peak ($3Q_0$) is identified on the scattering pattern, labeled with a black arrow. Schematic showing the stabilization of the W/W emulsion by lamellar phase surrounding the dextran-rich droplets.

(Figure 4). The results show that both emulsions could be centrifuged without significant change in the droplet radius (average radius before centrifugation: 2.1 ± 0.7 and 1.7 ± 0.5 μm , respectively for DG and LG; average radius after centrifugation = 2.0 ± 0.6 μm for DG, and 1.8 ± 0.4 μm for LG) confirming that the self-assembled structures formed by APGs and decanol both in bulk and at the interface led to strong protection of the emulsion against destabilization.

3.3 Structural characterization of W/W emulsions

After establishing the phase diagrams of the W/W emulsions stabilized by the mixture of decanol and APGs, we tried to characterize the structure formed by the decanol:APGs in bulk and at the interface leading to the long-term stabilization of the

droplets for specific ratios. By using confocal fluorescence microscopy with Nile red staining, the fatty alcohol, it was possible to highlight the presence of surfactant assemblies in the bulk phase surrounding the droplets (Figure 5A). We observed the presence of lamellar structures in the bulk phase surrounding the droplets forming the so-called LGN.

However, with this microscopy technique it is impossible to study the interfacial structure and the eventual formation of LGNs around the droplets, since only a red layer is observed by confocal microscopy surrounding the droplets (Figure 5A). That is why we used SAXS to get information at the interface scale. The stable emulsion formulated with LG at 12 mM and with $R = 3:1$ was chosen for SAXS analysis due to the long-term stability and high concentration to optimize the SAXS signal. On the SAXS scattering pattern, only one main peak could be distinguished at $Q = 0.035 \text{ \AA}^{-1}$ (Figure 5B). By comparing with the literature and the SAXS results obtained by Coudon et al. (2022) on similar water-in-water emulsion system stabilized by a mixture of fatty alcohol and sodium oleate, we hypothesize that the peak at 0.035 \AA^{-1} is the third order peak of a lamellar phase surrounding the dextran-rich droplets. The lamellar phase would have a lamellar interspacing (d) of around 52 nm ($d = 2\pi/Q_0$). Indeed, in the study from Coudon et al., they determined a lamellar spacing of around 78 nm, corresponding to a third order peak around 0.024 \AA^{-1} close to the peak determined here (Coudon et al., 2022). In our system, the lamellar spacing was lower than in the case of the lamellar phase made of sodium oleate and decanol system, which can be explained by the fact that we are working with non-ionic surfactant and lamellar phases are stabilized by steric repulsion and not electrostatic repulsion such as in the case of sodium oleate/decanol system. It is known that steric repulsion produced in lamellar gel network based on fatty alcohol leads to lower interlamellar spacing than LGNs produced by anionic surfactants (Iwata, 2017). Therefore, the long-term stabilization and the resistance to centrifugation of the W/W emulsions could come from the LGNs formed by APGs and decanol both in bulk and at the interface leading to strong protection of the emulsion against destabilization. However, to confirm the interfacial structures, further investigations need to perform. For example, the use of freeze-Fracture transmission electron microscopy could help to better characterize the self-assembled structures formed at the interface as already demonstrated by Coudon et al. (2022). It is important also to notice that we do not know the quantity of each chemical components inside the self-assembled structures, and the concentration could be different from the initial weight ratios used to produce the W/W emulsion. Most probably lamellar phases are in coexistence with APGs micelles.

3.4 Versatility of the W/W emulsion stabilized by mixture of fatty alcohols and APGs

Here, we varied the experimental conditions, either the concentration of polymers or the nature of LGNs but investigated only few different concentrations of each to demonstrate the versatility of the systems. First, we studied the

effect of LGNs on the stabilization of the inverse W/W emulsion, that is, when polymer concentrations are adjusted so that PEG-rich droplets formed in a continuous dextran-rich phase (Supplementary Figure S5). Stable W/W emulsion were produced from both DG and LG at 12 mM with $R = 3:1$, since no change in the droplets size was observed after 24 h. This result shows a general mechanism based on APG and fatty alcohol for stabilizing PEG and dextran interfaces regardless the nature of the droplets, which is in accordance with the observations of Coudon et al. on the stabilization W/W emulsion with decanol and sodium oleate (Coudon et al., 2022).

In a second step, we extended the production of W/W emulsions to another well-known and widely used APG: coco-glucoside (CG), composed of a mixture of alkyl groups with carbon chain lengths ranging from 8 to 16 atoms and with a higher proportion of longer alkyl chains in comparison to DG and LG (Aguirre et al., 2014). Self-assembled structures (lamellar phases and/or micelles) produced with CG 12 mM at different decanol: CG molar ratios, from $R = 1:1$ to $R = 6:1$, effectively stabilized dextran-in-PEG emulsions, since microscopy images showed that no significant differences in the droplet size were observed after 24 h compared to the initial size (Supplementary Figure S6).

Finally, we extended our approach of stabilizing W/W emulsions produced from DG and LG to other fatty alcohols with longer alkyl chain length (dodecanol and myristyl alcohol) (Figure 6 and Supplementary Figure S7). Microscopy images showed that dextran-in-PEG emulsions with high stability can be produced with DG at a concentration of 12 mM in combination with dodecanol (dodecanol:DG molar ratio $R = 6:1$), since no significant differences in the droplet size were shown after 24 h compared to the initial size (average radius $4 \pm 1.2 \mu\text{m}$). The same observations were performed for emulsions stabilized with LG at a concentration of 12 mM (dodecanol:LG molar ratio $R = 6:1$) but the droplet size was slightly smaller (average radius $2.2 \pm 0.7 \mu\text{m}$ at $t = 0$). The stabilization of dextran-in-PEG emulsion with APG and myristyl alcohol was also possible. Emulsions stabilized with DG at a concentration of 12 mM and myristyl alcohol ($R = 6:1$), showed high stability without significant changes in droplet size after 24 h compared to the initial size (average radius $= 3.2 \pm 0.7 \mu\text{m}$). The same emulsion stabilized with LG at a concentration of 12 mM ($R = 6:1$) led to a decrease in droplet size (average radius $1.6 \pm 0.3 \mu\text{m}$ at $t = 0$), with no significant change in size after 24 h. These results show that it is possible to formulate W/W emulsions using APGs and different fatty alcohols. Thus, W/W emulsion stabilization is possible by using APGs and fatty alcohol when suitable concentration and ratios are used to obtain self-assembled structures such as lamellar phases.

For certain applications, bubbles are added into emulsions to change their mechanical properties and/or sensorial performances (Salonen, 2020). It is the case, for example, for ice creams, whipped creams and pharmaceutical or cosmetic applications (Parsa et al., 2019; Murray, 2020; Luengo et al., 2021). These three phase systems are called foamulsions or “foamed emulsions,” where the gas bubbles are surrounded by a continuous phase, traditionally composed of oil and water (Salonen, 2020; Zheng et al., 2022). The continuous phase is generally present in the form of oil-in-water emulsions, although it can also be in the form of water-in-oil emulsions (Salonen, 2020). However, to the best of our knowledge, a foamulsion where the

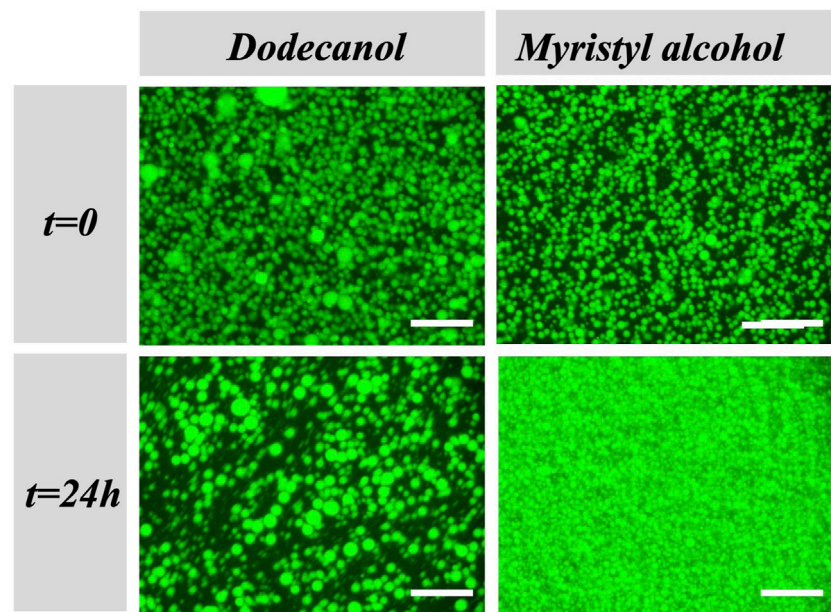


FIGURE 6

W/W emulsions stabilized with DG in combination with two different fatty alcohols: dodecanol and myristyl alcohol. Epifluorescence microscopy images of W/W emulsions stabilized with DG at 12 mM and Dodecanol: DG ratio equal to 6:1 (left) and DG at 12 mM and myristyl alcohol: DG ratio equal to 6:1 (right), taken at $t = 0$ (top) and at $t = 24$ h (bottom). Droplets are labeled with FITC-dextran dye. The scale bars represent 60 μm .

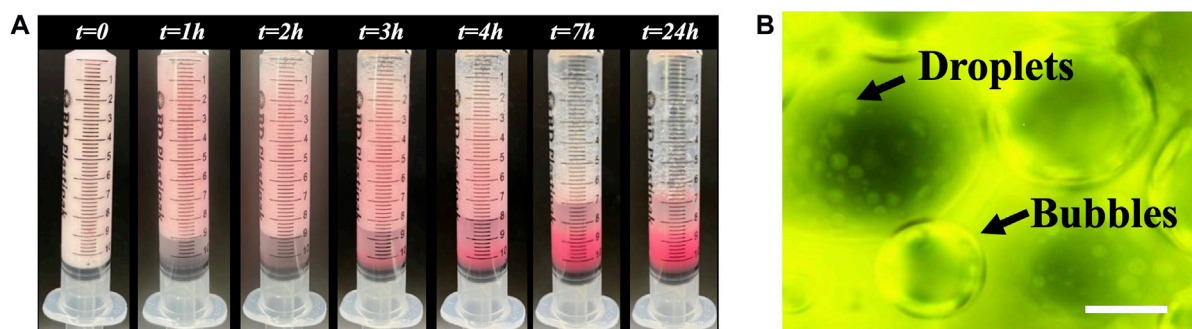


FIGURE 7

(A) Stability of the foamulsion. Pictures of the foam produced with the W/W emulsion (LG 12 mM, decanol: LG ratio 3:1) with the addition of SDS at 18 mM and its evolution over time. (B) Epifluorescence microscopy image of the foamulsion at $t = 0$. Droplets are labeled with FITC-dextran dye. The scale bar represents 30 μm .

continuous phase is composed of W/W emulsions has never been reported. We took the advantage of the high stability of the W/W emulsions developed here to study the possibility of producing a foamulsion by using dextran-in-PEG emulsion as the continuous phase of the foam. First, we prepared a dextran-in-PEG emulsion (10 wt% of dextran and 10 wt% of PEG) stabilized with LG at a concentration of 12 mM and with a molar ratio of decanol: LG equal to 3:1. Then, the double-syringe technique was used to produce the foams (Gaillard et al., 2017). First, we measured the foamability, that is to say the quantity of foam produced at the end of the foaming process. Then, the stability of the foams was followed by measuring both the evolution of the foam volume and the volume of drained liquid over time with the naked eye (Supplementary Figure S8).

Production of foam from the W/W emulsion stabilized by lamellar structures formed by APGs and fatty alcohols without the addition of additional surfactants was not possible (Supplementary Figure S8A). Then, we tested the addition of surfactant inside the W/W emulsion and we studied the resulting foaming properties. With the addition of DG at a concentration of 18 mM, no foam was produced (Supplementary Figure S8B). However, in the presence of SDS at a concentration of 18 mM, a high quantity of foam which was relatively stable with time was obtained (Figure 7A). By fluorescence microscopy, the presence of droplets surrounding the air bubbles were clearly distinguished similar to the ones observed for foamulsion based on oil-in-water emulsion (Figure 7B) (Salonen, 2020). The initial foam volume was around 10.5 mL showing the good foamability of the foamulsion. Then, the

foam volume decreased slightly in the first 4 h to reach a foam volume around 7 mL associated with drainage (liquid volume inside the foam around 1 mL after 4 h). After 24 h, no more foam was present only few bubbles remained (Figure 7A and Supplementary Figure S9). We performed control experiments by producing foams with only dextran and SDS or only PEG and SDS at the same concentration (18 mM). The foamulsion stabilized by mixture of fatty alcohols and APGs with 18 mM of SDS was observed to be much more stable than the foams produced with only dextran or only PEG since these controlled foams disappeared after 2–3 h (Supplementary Figures S10A, B). In the same way, no more foam was present after 3 h when foam was produced directly from the pure W/W emulsion not stabilized by fatty alcohols and APGs and with only SDS (Supplementary Figure S10C).

4 Conclusion

In this study, we demonstrated that W/W emulsions can be efficiently stabilized by mixtures of APGs and fatty alcohol. The stability of the W/W emulsions is linked to the APGs concentration and the molar ratio between the APG and the fatty alcohol. We demonstrated the robustness of this system by using various APGs: decyl glucoside, lauryl glucoside and coco-glucoside, and also by using fatty alcohols with different alkyl chain lengths (decanol, dodecanol and myristyl alcohol). An effect of the APGs alkyl chain length between DG and LG was observed, since the use of LG made it possible to produce emulsions with the same droplet size as with DG but at a lower concentration. In addition, emulsions prepared with LG were more stable in the long-term than emulsions prepared with DG. The molar ratio between the fatty alcohol and the APG is also a key parameter governing the stability. We hypothesized that the mixture of fatty alcohols and APGs led to the formation of LGNs stabilizing the W/W emulsions due to their presence both in the bulk phase and surrounding the droplets. The structure of the LGNs seems to depend on the molar ratio and APG concentration in the same way already described in aqueous solution (Terescenco et al., 2018a; Terescenco et al., 2018b).

Altogether, this confirms that stabilization of such aqueous droplets occurs when the chemicals (and eventually their assemblies) used for this task have an equivalent affinity for both the polymer within droplets and the polymer in the continuous phase. We believe that adjusting the concentrations and molar ratio control this affinity and affords chemicals to come and stay at the droplet interface, further preventing droplet coalescence. Further investigations using freeze-Fracture transmission electron microscopy and small angle neutron scattering are planned to better characterize the self-assembled structures formed both in the bulk and at the interface, and to confirm the formation of LGNs.

With preliminary results, we showed for the first time that the production of a foam based on W/W emulsion is possible; and that its stability is better than the foam produced with the polymers alone or with polymers in mixture without being stabilized by self-assembled structures formed by APGs and fatty alcohols. The inclusion of a third phase to emulsions could be a promising strategy to expand the use of W/W emulsions in various fields (Luengo et al., 2021; Zhili, 2022). Our

results offer the possibility to formulate W/W emulsions based on chemical components widely used at industrial scale and at low cost associated with an easy and simple formulation process. Our approach could be extended to more complicated systems such as multiple water-in-water emulsion systems, and they could be used for encapsulation, drug delivery, as micro reactors, etc. (Solans et al., 2003; Singh et al., 2018; Michaux et al., 2021).

Data availability statement

The original contributions presented in the study are included in the article/Supplementary Material, further inquiries can be directed to the corresponding author.

Author contributions

CD: Conceptualization, Formal Analysis, Investigation, Methodology, Validation, Writing—original draft, Writing—review and editing. YS: Investigation, Methodology, Writing—review and editing. J-PD: Conceptualization, Methodology, Writing—review and editing. J-FT: Investigation, Writing—review and editing. TB: Formal Analysis, Writing—review and editing. PSC: Conceptualization, Investigation, Resources, Supervision, Writing—review and editing. A-LF: Conceptualization, Funding acquisition, Investigation, Methodology, Project administration, Supervision, Writing—original draft, Writing—review and editing.

Funding

The authors declare financial support was received for the research, authorship, and/or publication of this article. This research was funded by the Region Hauts de France and the INRAe TRANSFORM department. This study was also supported by the French government through the Program “Investissements d’avenir” (I-SITE ULNE/ANR-16-IDEX-0004 ULNE) managed by the National Research Agency.

Acknowledgments

We acknowledge financial support from INRAe, TRANSFORM department, and region Hauts de France for the PhD grant of CD. CD would like to thank “l’École internationale de recherche d’Agreenium (EIR-A)” and the graduate program “Science for a Changing Planet” for the allocation of her travel grant to University of Edinburgh. Chevreul Institute (FR 2638), Ministère de l’Enseignement Supérieur, de la Recherche et de l’Innovation, Région Hauts de France and FEDER are acknowledged for SAXS facilities.

Conflict of interest

The authors declare that the research was conducted in the absence of any commercial or financial relationships that could be construed as a potential conflict of interest.

The authors declared that they were an editorial board member of Frontiers, at the time of submission. This had no impact on the peer review process and the final decision.

Publisher's note

All claims expressed in this article are solely those of the authors and do not necessarily represent those of their affiliated organizations, or those of the publisher, the editors and the

reviewers. Any product that may be evaluated in this article, or claim that may be made by its manufacturer, is not guaranteed or endorsed by the publisher.

Supplementary material

The Supplementary Material for this article can be found online at: <https://www.frontiersin.org/articles/10.3389/frsfm.2023.1328195/full#supplementary-material>

References

- Aguirre, T. A. S., Rosa, M., Guterres, S. S., Pohlmann, A. R., Coulter, I., and Brayden, D. J. (2014). Investigation of coco-glucoside as a novel intestinal permeation enhancer in rat models. *Eur. J. Pharm. Biopharm.* 88, 856–865. doi:10.1016/j.ejpb.2014.10.013
- Antonov, Y. A., Van Puyvelde, P., and Moldenaers, P. (2004). Interfacial tension of aqueous biopolymer mixtures close to the critical point. *Int. J. Biol. Macromol.* 34, 29–35. doi:10.1016/j.ijbiomac.2004.01.001
- Ben Ayed, E., Cochereau, R., Dechancé, C., Capron, I., Nicolai, T., and Benyahia, L. (2018). Water-in-water emulsion gels stabilized by cellulose nanocrystals. *Langmuir* 34, 6887–6893. doi:10.1021/acs.langmuir.8b01239
- Chao, Y., and Shum, H. C. (2020). Emerging aqueous two-phase systems: from fundamentals of interfaces to biomedical applications. *Chem. Soc. Rev.* 49, 114–142. doi:10.1039/C9CS00466A
- Chu, Z., Dreiss, C. A., and Feng, Y. (2013). Smart wormlike micelles. *Chem. Soc. Rev.* 42, 7174–7203. doi:10.1039/C3CS35490C
- Colafemmina, G., Palazzo, G., Mateos, H., Amin, S., Fameau, A.-L., Olsson, U., et al. (2020). The cooling process effect on the bilayer phase state of the CTAC/cetearyl alcohol/water surfactant gel. *Colloids Surfaces A Physicochem. Eng. Aspects* 597, 124821. doi:10.1016/j.colsurfa.2020.124821
- Coudon, N., Navailles, L., Nallet, F., Ly, L., Bentaleb, A., Chapel, J.-P., et al. (2022). Stabilization of all-aqueous droplets by interfacial self-assembly of fatty acids bilayers. *J. Colloid Interface Sci.* 617, 257–266. doi:10.1016/j.jcis.2022.02.138
- Dari, C., Dallagi, H., Faille, C., Dubois, T., Lemy, C., Deleplace, M., et al. (2023). Decantation of spores on model stainless-steel surface by using foams based on alkyl polyglucosides. *Molecules* 28, 936. doi:10.3390/molecules28030936
- de Oliveira, T. E., Leonforte, F., Nicolas-Morgantini, L., Fameau, A.-L., Querleux, B., Thalmann, F., et al. (2020). Fluid bilayer phase in aqueous mixtures of fatty alcohol and cationic surfactant. *Phys. Rev. Res.* 2, 013075. doi:10.1103/PhysRevResearch.2.013075
- Dewey, D. C., Strulson, C. A., Cacace, D. N., Bevilacqua, P. C., and Keating, C. D. (2014). Bioreactor droplets from liposome-stabilized all-aqueous emulsions. *Nat. Commun.* 5, 4670. doi:10.1038/ncomms5670
- Diamond, A. D., and Hsu, J. T. (1989). Phase diagrams for dextran-PEG aqueous two-phase systems at 22°C. *Biotechnol. Tech.* 3, 119–124. doi:10.1007/BF01875564
- Dickinson, E. (2019). Particle-based stabilization of water-in-water emulsions containing mixed biopolymers. *Trends Food Sci. Technol.* 83, 31–40. doi:10.1016/j.tifs.2018.11.004
- Douliez, J.-P., Martin, N., Beneyton, T., Eloi, J.-C., Chapel, J.-P., Navailles, L., et al. (2018). Preparation of swellable hydrogel-containing colloidosomes from aqueous two-phase pickering emulsion droplets. *Angew. Chem. Int. Ed. Engl.* 57, 7780–7784. doi:10.1002/anie.201802929
- Douliez, J.-P., Perro, A., and Béven, L. (2019). Stabilization of all-in-water emulsions to form capsules as artificial cells. *ChemBiochem* 20, 2546–2552. doi:10.1002/cbic.201900196
- Eccleston, G. M. (1997). Functions of mixed emulsifiers and emulsifying waxes in dermatological lotions and creams. *Colloids Surfaces A Physicochem. Eng. Aspects* 123 (124), 169–182. doi:10.1016/S0927-7757(96)03846-0
- Esquena, J. (2016). Water-in-water (W/W) emulsions. *Curr. Opin. Colloid & Interface Sci.* 25, 109–119. doi:10.1016/j.cocis.2016.09.010
- Esquena, J. (2023). Recent advances on water-in-water emulsions in segregative systems of two water-soluble polymers. *Curr. Opin. Food Sci.* 51, 101010. doi:10.1016/j.cofs.2023.101010
- Gaillard, T., Honorez, C., Jumeau, M., Elias, F., and Drenckhan, W. (2015). A simple technique for the automation of bubble size measurements. *Colloids Surfaces A Physicochem. Eng. Aspects* 473, 68–74. doi:10.1016/j.colsurfa.2015.01.089
- Gaillard, T., Roché, M., Honorez, C., Jumeau, M., Balan, A., Jedrzejczyk, C., et al. (2017). Controlled foam generation using cyclic diphasic flows through a constriction. *Int. J. Multiph. Flow* 96, 173–187. doi:10.1016/j.ijmultiphaseflow.2017.02.009
- Iwata, T. (2017). “Lamellar gel network,” in *Cosmetic science and technology* (Netherlands: Elsevier), 415–447. doi:10.1016/B978-0-12-802005-0.00025-2
- Junginger, H. E. (1984). Colloidal structures of O/W creams. *Pharm. Weekbl. Sci. Ed.* 6, 141–149. doi:10.1007/BF01954041
- Keck, C. M., Kovačević, A., Müller, R. H., Savić, S., Vuleta, G., and Milić, J. (2014). Formulation of solid lipid nanoparticles (SLN): the value of different alkyl polyglucoside surfactants. *Int. J. Pharm.* 474, 33–41. doi:10.1016/j.ijpharm.2014.08.008
- Leal-Calderon, F., Bibette, J., and Schmitt, V. (2007). *Emulsion science: basic principles*. New York, NY: Springer New York. doi:10.1007/978-0-387-39683-5
- Luengo, G. S., Fameau, A.-L., Léonforte, F., and Greaves, A. J. (2021). Surface science of cosmetic substrates, cleansing actives and formulations. *Adv. Colloid Interface Sci.* 290, 102383. doi:10.1016/j.cis.2021.102383
- Merland, T., Waldmann, L., Guignard, O., Tatry, M.-C., Wirotius, A.-L., Lapeyre, V., et al. (2022). Thermo-induced inversion of water-in-water emulsion stability by bis-hydrophilic microgels. *J. Colloid Interface Sci.* 608, 1191–1201. doi:10.1016/j.jcis.2021.10.074
- Michaux, M., Salinas, N., Miras, J., Vilchez, S., González-Azón, C., and Esquena, J. (2021). Encapsulation of BSA/alginate water-in-water emulsions by polyelectrolyte complexation. *Food Hydrocoll.* 113, 106406. doi:10.1016/j.foodhyd.2020.106406
- Möller, A., Lang, P., Findenegg, G. H., and Keiderling, U. (1998). Location of butanol in mixed micelles with alkyl glucosides studied by SANS. *J. Phys. Chem. B* 102, 8958–8964. doi:10.1021/jp981819q
- Murray, B. S. (2020). Recent developments in food foams. *Curr. Opin. Colloid & Interface Sci.* 50, 101394. doi:10.1016/j.cocis.2020.101394
- Nakarapanich, J., Barameesangpet, T., Suksamranchit, S., Sirivat, A., and Jamieson, A. M. (2001). Rheological properties and structures of cationic surfactants and fatty alcohol emulsions: effect of surfactant chain length and concentration. *Colloid Polym. Sci.* 279, 671–677. doi:10.1007/s003960000470
- Nguyen, B. T., Nicolai, T., and Benyahia, L. (2013). Stabilization of water-in-water emulsions by addition of protein particles. *Langmuir* 29, 10658–10664. doi:10.1021/la402131e
- Nicolai, T., and Murray, B. (2017). Particle stabilized water in water emulsions. *Food Hydrocoll.* 68, 157–163. doi:10.1016/j.foodhyd.2016.08.036
- Parsa, M., Trybala, A., Malik, D. J., and Starov, V. (2019). Foam in pharmaceutical and medical applications. *Curr. Opin. Colloid Interface Sci.* 44, 153–167. doi:10.1016/j.cocis.2019.10.007
- Platz, G., Poelike, J., Thunig, C., Hofmann, R., Nickel, D., and von Rybinski, W. (1995). Phase behavior, lyotropic phases, and flow properties of alkyl glycosides in aqueous solution. *Langmuir* 11, 4250–4255. doi:10.1021/la00011a015
- Poortinga, A. T. (2008). Microcapsules from self-assembled colloidal particles using aqueous phase-separated polymer solutions. *Langmuir* 24, 1644–1647. doi:10.1021/la703441e
- Salonen, A. (2020). Mixing bubbles and drops to make foamed emulsions. *Curr. Opin. Colloid & Interface Sci.* 50, 101381. doi:10.1016/j.cocis.2020.08.006
- Savic, S., Vuleta, G., Daniels, R., and Muller-Goymann, C. C. (2005). Colloidal microstructure of binary systems and model creams stabilized with an alkylpolyglucoside non-ionic emulsifier. *Colloid Polym. Sci.* 283, 439–451. doi:10.1007/s00396-004-1174-4
- Singh, P., Medronho, B., Miguel, M. G., and Esquena, J. (2018). On the encapsulation and viability of probiotic bacteria in edible carboxymethyl cellulose-gelatin water-in-water emulsions. *Food Hydrocoll.* 75, 41–50. doi:10.1016/j.foodhyd.2017.09.014
- Solans, C., Esquena, J., and Azemar, N. (2003). Highly concentrated (gel) emulsions, versatile reaction media. *Curr. Opin. Colloid & Interface Sci.* 8, 156–163. doi:10.1016/S1359-0294(03)00021-9
- Stradner, A., Glatzer, O., and Schurtenberger, P. (2000). A hexanol-induced sphere-to-flexible cylinder transition in aqueous alkyl polyglucoside solutions. *Langmuir* 16, 5354–5364. doi:10.1021/la991679r

- Terescenco, D., Picard, C., Clemenceau, F., Grisel, M., and Savary, G. (2018a). Influence of the emollient structure on the properties of cosmetic emulsion containing lamellar liquid crystals. *Colloids Surfaces A Physicochem. Eng. Aspects* 536, 10–19. doi:10.1016/j.colsurfa.2017.08.017
- Terescenco, D., Savary, G., Clemenceau, F., Merat, E., Duchemin, B., Grisel, M., et al. (2018b). The alkyl polyglucoside/fatty alcohol ratio effect on the formation of liquid crystal phases in binary systems. *J. Mol. Liq.* 253, 45–52. doi:10.1016/j.molliq.2017.12.149
- Wu, P.-S., Lin, C.-H., Kuo, Y.-C., and Lin, C.-C. (2017). Formulation and characterization of hydroquinone nanostructured lipid carriers by homogenization emulsification method. *J. Nanomater.* 2017, 1–7. doi:10.1155/2017/3282693
- Xie, Y., Ruan, M., Zhang, J., Kibitia, M., Li, Y., Li, B., et al. (2023). Water-in-water Pickering emulsion stabilized by cellulose nanocrystals as space-confined encapsulating systems: from establishment to stability. *Food Hydrocoll.* 141, 108719. doi:10.1016/j.foodhyd.2023.108719
- You, K.-M., Murray, B. S., and Sarkar, A. (2023). Tribology and rheology of water-in-water emulsions stabilized by whey protein microgels. *Food Hydrocoll.* 134, 108009. doi:10.1016/j.foodhyd.2022.108009
- Zhang, J., Xie, Y., Liu, C., Cao, H., Li, Y., Li, B., et al. (2024). Water-in-water Pickering emulsion: a fascinating microculture apparatus for embedding and cultivation of *Lactobacillus helveticus*. *Food Hydrocoll.* 147, 109398. doi:10.1016/j.foodhyd.2023.109398
- Zheng, R., Hu, X., Su, C., Jiang, J., Cui, Z., and Binks, B. P. (2022). Edible oil-water foamulsions stabilized by vesicle network of sucrose ester. *J. Mol. Liq.* 371, 121066. doi:10.1016/j.molliq.2022.121066
- Zhili, W. (2022). Editorial overview: moving towards designing new food colloids for healthy and sustainable foods. *Curr. Opin. Food Sci.* 46, 100844. doi:10.1016/j.cofs.2022.100844



OPEN ACCESS

EDITED BY

Mohd Sajid Ali,
King Saud University, Saudi Arabia

REVIEWED BY

Animesh Pan,
University of Rhode Island, United States
Ajaya Bhattarai,
Tribhuvan University, Nepal

*CORRESPONDENCE

Erica Pensini,
✉ epensini@uoguelph.ca

RECEIVED 27 October 2023

ACCEPTED 29 November 2023

PUBLISHED 18 December 2023

CITATION

Bartokova B, Marangoni AG, Laredo T and Pensini E (2023), Effect of sorbitan ester structure on the separation between tetrahydrofuran and water.
Front. Soft Matter 3:1329058.
doi: 10.3389/frsfm.2023.1329058

COPYRIGHT

© 2023 Bartokova, Marangoni, Laredo and Pensini. This is an open-access article distributed under the terms of the [Creative Commons Attribution License \(CC BY\)](https://creativecommons.org/licenses/by/4.0/). The use, distribution or reproduction in other forums is permitted, provided the original author(s) and the copyright owner(s) are credited and that the original publication in this journal is cited, in accordance with accepted academic practice. No use, distribution or reproduction is permitted which does not comply with these terms.

Effect of sorbitan ester structure on the separation between tetrahydrofuran and water

Bibiana Bartokova¹, Alejandro G. Marangoni^{2,3}, Thamara Laredo⁴ and Erica Pensini^{1,3*}

¹School of Engineering, University of Guelph, Guelph, ON, Canada, ²Food Science Department, University of Guelph, Guelph, ON, Canada, ³Biophysics Interdepartmental Group (BIG), University of Guelph, Guelph, ON, Canada, ⁴Chemistry Department, Lakehead University, Orillia, ON, Canada

This study separates tetrahydrofuran (THF)-water mixtures containing varying THF percentages, using sorbitan esters (Spans) with different tail characteristics. We probe the separation mechanisms using attenuated total reflectance-Fourier transform infrared spectroscopy and small angle X ray scattering (SAXS). THF and water are miscible and interact through hydrogen bonds. Water splits the COC absorbance band of THF into a peak at $\approx 1,070\text{ cm}^{-1}$ (crystalline THF) and a dominant peak at $\approx 1,050\text{ cm}^{-1}$ (glassy THF), indicating disorder. Depending on the Span, separation occurs for mixtures containing up to 70% THF (v/v, relative to water). Spans with unsaturated tails separate the lowest THF percentages. Tail length and number of Span tails enhances ordering of THF, and the crystalline THF peak at $\approx 1,070\text{ cm}^{-1}$ dominates. Spans interact with THF through hydrogen bonds, as reflected in the splitting of the COC band of THF. Furthermore, C-H...O hydrogen bonds cause a blueshift in the $\nu_{\text{as}}(\text{CH}_2)$ band of Spans with increasing THF. This effect is most significant in Span 40 and 60, indicating that they interact with THF more strongly than Span 20, Span 80 and Span 85. In contrast, they interact with water less strongly than Span 20, Span 80 and Span 85, as indicated by their flocculation at low THF percentages. Therefore, we propose that separation between THF and water occurs *primarily* through two mechanisms: 1) Span 20, Span 80 and Span 85 compete against THF for interactions with water through their hydrophilic head, and 2) Span 40 and Span 60 preferentially interact with THF through their tails. Nonetheless, water also interacts with the heads of Span 40 and Span 60, as indicated by SAXS. SAXS shows that in THF Spans self-assemble into micelles, which aggregate into either surface fractals or mass fractals. There are two persistence lengths because of the limited order in THF. Water orders self-assembled structures, likely by favoring the formation of micelles which host water in their interior. Therefore, we identify a single persistence length ($\approx 25\text{ Å}$), representative of the distance between the micelle centers.

KEYWORDS

mixing behaviour, separation, sorbitan esters, hydrogen bonding, solvent structure

1 Introduction

THF, acetonitrile, dimethylformamide or methanol are water miscible pollutants used in industrial processes (Sales et al., 2013; Yin et al., 2017; Earnden et al., 2022a; Earnden et al., 2022b; Earnden et al., 2022c; Marshall et al., 2022; Bartokova et al., 2023a). They are found in industrial wastewater as well as in groundwater, in the case of spills such as those caused by

the notable Ohio trail derailment accident (2023). Our study focuses on THF, which is used as a stabilizer for chlorinated solvents, as well as to produce pharmaceuticals and pesticides (Sales et al., 2013; Yin et al., 2017).

Beyond their intrinsic toxicity, spills of water miscible solvents are particularly problematic because they can rapidly migrate in impacted aquifers, harming downstream receptors (Bartokova et al., 2023a). Furthermore, their separation from water presents greater challenges compared to water-immiscible pollutants, such as hydrocarbons (Bartokova et al., 2023a). These can be removed from water through mechanical separation methods (e.g., coalescers (Kolehmainen and Turunen, 2007)) or chemical methods (such as oxidation (Wang et al., 2013; Malakahmad and Ho, 2017; Besha et al., 2018)). Also, when they are present in groundwater below levels at which they are toxic to the bacteria, they can biodegraded (Boonchan et al., 1998; Belhaj et al., 2002; Barman et al., 2017). Since biodegradation tends to be a fairly slow process, there are limitations to its use in the case of rapidly migrating pollutants. These consideration also apply to phytoremediation using plants (Hall et al., 2011; Sun et al., 2011). Moreover, phytoremediation is only effective for shallower contamination, which can be reached by the roots of the plants. In the case of miscible organic solvents, pervaporation is often used (Yoshikawa et al., 2002). Beyond its high energy cost, its implementation for the treatment of impacted aquifers is not feasible. This is because complex treatment units could be integrated in a chemical plant, but they cannot be built as part of a remediation plant on polluted sites. Therefore, it is necessary to identify cost-effective, facile methods to separate miscible solvents from either industrial wastewater or groundwater. These methods were scant until our most recent research.

Previous studies used CO₂ switchable species (Jessop and Cunningham) or increased the hydrophobicity of the organic solvent (Longeras et al., 2020) to increase their incompatibility with water, thereby leading to separation. Other studies used species that preferentially interact with water, at the expense of its interactions with the solvent. Examples of these species are sugars and their alcohols (Wang et al., 2008; Dhamole et al., 2010; de Brito Cardoso et al., 2014) as well as salts, such as sodium chloride and choline salts (Tabata et al., 1994; Souza et al., 2015).

In our recent research, we have used amphiphiles to separate miscible solvents from water. Examples include sodium lauroyl lactylate (Marshall et al., 2022), glycerol monooleate (Earnden et al., 2022c), fatty acids (Earnden et al., 2022a; Earnden et al., 2022b; Bartokova et al., 2023a) and a sorbitan ester (Span 80, (Bartokova et al., 2023b)). In these studies, we showed that separation involves preferential interactions either between water and the amphiphile [e.g., in the case of Span 80, (Bartokova et al., 2023b)] or preferential interactions between the solvent and the amphiphile [e.g., in the case of stearic acid, (Bartokova et al., 2023a)]. To investigate interactions between water and other components in the mixture (solvent and amphiphiles), we probed the OH stretch band of water using Attenuated Total Reflectance–Fourier Transform Infrared (ATR-FTIR) spectroscopy. We deconvolved the OH stretch peak into four peaks, representing water species with different coordination to other molecules in the mixtures. Specifically, we considered double (DD) and single (SD) hydrogen (H) bond

donors, and double (DA) and single (SA) H bond acceptors. Based on this analysis, we concluded that separation is promoted when amphiphiles interact with water the same way the solvent does, i.e., when amphiphiles compete with the solvent for interactions with the same water species. We also analyzed H bonding of solvent with hydrophobic amphiphiles, such as stearic acid (Bartokova et al., 2023a). We showed that the COC band of THF contains information about H bonding, by comparing changes of the OH stretch band of water and the COC band of THF, in THF-water mixtures (Bartokova et al., 2023a). By analyzing this band, we demonstrated that stearic acid separates water from THF because it competes for interactions with the same THF species, i.e., THF molecules that H bond and coordinate the same way with other molecules in solution (Bartokova et al., 2023a).

Furthermore, we highlighted that the tail plays an important role in separation. For example, separation between THF and water does not occur upon adding acetic acid, although the structure of acetic acid is the same as the head of stearic acid (Bartokova et al., 2023a). Given this similarity, both acetic acid and stearic acid H bond with THF the same way (Bartokova et al., 2023a). We proposed that the tail of stearic acid promotes H bonding between THF and the hydrophilic tail at the expense of THF-water interactions. In contrast, in the absence of the tail, acetic acid can H bond either water or THF, thereby enabling the existence of a ternary solution. Indeed, solubility plays a key role. Specifically, separation is favored when the amphiphile added has intermediate solubility in the mixture, and is soluble in either water or the solvent, but not both (Marshall et al., 2022). In ternary mixtures where all components are miscible two by two, there are instances where separation may still occur, but predictions of the mixing behaviour are notably more complex (Bartokova et al., 2023c). Solubility of the amphiphile in each component and in the mixture is clearly affected by the tail. While our previous studies started highlighting the role of the tail, we had not yet conducted a systematic analysis of the role of the tail on solvent separation. The current study aims to fill this research gap.

In particular, the objective of this study is to expand on our previous research, comparing the separation between THF and water using sorbitan esters with a different tail structure (e.g., tail length and hence hydrophobicity, and double vs. single bonds in the tail). Specifically, we investigate interactions (H bonding) between THF and different sorbitan esters, comparing them with interactions between THF and water. We also analyze the role of the tail on THF ordering and its separation from water.

This objective supports the overall goal of our research, which is to develop a robust approach to predict the separation of water from miscible solvents, and to identify the most effective amphiphiles for water purification. The toolbox we are building relies on calculated values for H bonds between solvent-water couples, amphiphile-water couples, as well as amphiphile-solvent couples. We are calculating these values in our research. Values estimated on representative amphiphile and solvents will be used to provide initial estimated for other similar compounds, predicting the mixing behaviour of ternary mixtures. Our toolbox also relies on building a systematic and quantitative understanding of the effect of the tail characteristics and amphiphile solubility. The current study will be followed by others, where broader groups of amphiphiles will

be used to consolidate the portion of our predictive toolbox focused on the tails. Our approach will be complementary to models such as COSMO, which we recently used to predict activity coefficients, because they are correlated to solvent separation (Bartokova et al., 2023a).

2 Materials and methods

2.1 Materials

Sorbitan esters (Span 20, Span 40, Span 60, Span 65, Span 80 and Span 85) were purchased from Sigma Aldrich (Canada). Their structure and hydrophilic lipophilic balance (HLB) number are given in Table 1 and Scheme 1. THF (reagent grade, Caledon laboratory chemicals) was purchased from Fisher Scientific (Canada). All experiments were conducted using deionised (DI) water.

2.2 Bottle tests

Samples were prepared using 40 g/L of sorbitan esters and mixtures containing varying percentages of DI water and THF (0%–100% THF, v/v relative to water). Samples were agitated by hand for 10 s after heating to 65°C for 2 min, using a hotplate. Samples were then cooled and observed at 20°C under quiescent conditions for 24 h, to qualitatively determine their phase behavior. These same samples were also imaged using optical microscopy (Section 2.3) and analyzed using ATR-FTIR (Section 2.4).

2.3 Optical microscopy

A VHX-5000 digital microscope (Keyence) was used to image THF-water emulsions stabilized with different sorbitan esters.

2.4 Attenuated total reflectance–Fourier transform infrared spectroscopy (ATR-FTIR)

Absorbance spectra were collected using an ATR-FTIR spectrometer (ThermoScientific Nicolet Summit FTIR spectrometer with an Everest ATR), with an accompanying IR solution software (Omnic 9, Thermo Fisher Scientific). Each spectrum was the average of 10 scans, with a resolution of 2 cm⁻¹. The wavenumbers ranged from 400 cm⁻¹ to 4,000 cm⁻¹. Measurements were conducted at least in duplicate.

Spectra were analyzed using Quasar 1.5.0 (Orange-Spectroscopy software), using a rubber band baseline correction. Additionally, the spectra were normalized using min-max normalization. To this end, each spectrum was divided by its Abs_{max}–Abs_{min} range.

2.5 Synchrotron based small angle X-ray scattering (SAXS)

SAXS experiments were carried out at the Canadian Light Source Synchrotron (CLS) on the Brockhouse Diffraction Sector

Undulator Beamline (BXDS-IVU) (Leontowich et al., 2021), to identify the self-assembly of sorbitan esters into either pure THF or THF-water mixtures containing 2% water (relative to THF). In this study, samples were introduced into quartz tubing (Polyamide 0.0575" ID x 0.0615" OD), which was sealed to avoid solvent evaporation during data collection. A clay compound was used for sealing. SAXS data was collected with a Rayonix MX300HE detector (8,192 × 8,192 pixels) with 2 × 2 binning (4,096 × 4,096 pixel) for an effective pixel size of 73.242 μm with background stability mode ON. SAXS patterns were collected with a photon energy of 12.18 keV and sample-to-detector distance of ~233 cm. SAXS patterns were collected in transmission geometry with a 120 s dwell time. Patterns were processed with GSASII (Argonne National Laboratory (C), 2010). This product includes software developed by the UChicago Argonne, LLC (Toby and Von Dreele, 2013; Von Dreele, 2014). SAXS data was calibrated with silver behenate (AgBeh) and instrument parameters such as sample-to-detector distances, detector tilt, beam centre, were refined as described elsewhere (Von Dreele, 2014). SAXS patterns were integrated from $q = 0.012$ to $q = 0.637 \text{ \AA}^{-1}$. Measurements were done in duplicate for each sample.

Absolute intensity with background removed as a function of the scattering vector, q , were fitted to a model recently developed by our group. It has the general form,

$$I(q) = Cq^{-s} + I_0 \exp^{-0.5\left(\frac{q}{q_0}\right)^2} + \sum_{i=1}^n I_i \exp^{-0.5\left(\frac{q-q_{pi}}{q_{pi}}\right)^2} \quad (1)$$

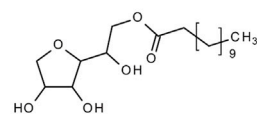
The scattering intensity is interpreted as arising from scale-independent fractal scattering in the low q -range, superimposed on top Guinier's form factor, namely a zero-mean Gaussian. Any periodicities arising from other correlations in the system are captured by non-zero mean Gaussians. In our case, we only required one zero mean Gaussian and one non-zero mean Gaussian.

The fractal dimension is captured in the modeling process by writing the scattering intensity, such as

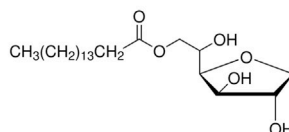
$$I(q) \sim q^{D_s-2(D_m+D_p)+2d} \quad (2)$$

This is a simple power-law decay on a double logarithmic scale within a given q -range limited by reciprocal fractal outer and inner cutoffs, q_{oc} and q_{ic} , respectively, i.e., when $q_{oc} < q < q_{ic}$. It is also known in the literature as the fractal region. Here, q is the module of the scattering vector, D_s , D_m and D_p are the surface, mass and respectively the pore fractal dimensions, and d is the Euclidean dimension of the space in which the fractal is embedded. In the case of surface fractals $d-1 < D_s < d$, $D_m = D_p = d$ and the scattering intensity reduces to $I(q) \sim q^{D_s-2d}$. For mass fractals $0 < D_m < d$, $D_m = D_s$ and $D_p = d$, and $I(q) \sim q^{D_m}$, while for pore fractals $D_p = D_s$ and $D_m = d$, and thus $I(q) \sim q^{-D_p}$. Therefore, one can obtain the fractal dimension from the slope (s) of the experimental scattering curve. Moreover, one can differentiate between mass and surface fractals, i.e., if the measured slope is $s < d$ then the sample is a mass fractal, while if $d < s < d + 1$, the sample is a surface fractal. For a surface fractal, D_s is equal to 2 for a perfectly smooth surface, and approaches 3 for a highly folded/convoluted surface.

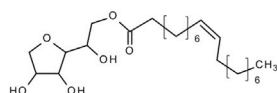
SPAN 20



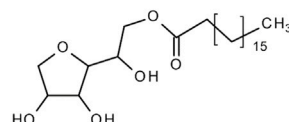
SPAN 40



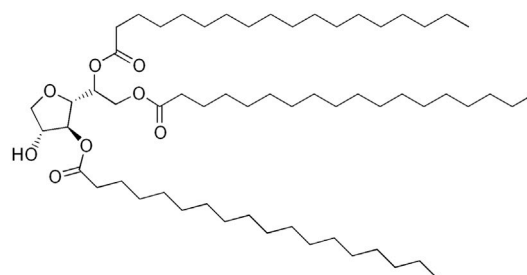
SPAN 80



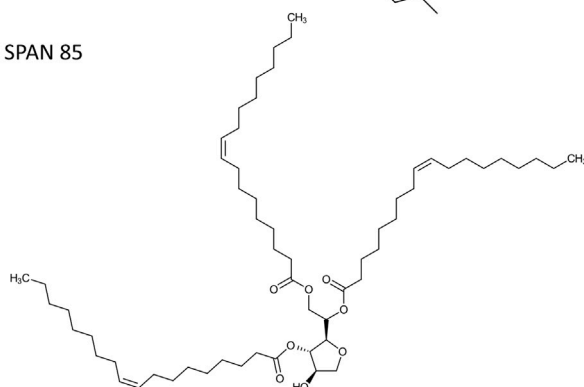
SPAN 60



SPAN 65



SPAN 85



SCHEME 1

Structures of the compounds used.

TABLE 1 HLB number and tail length of the Spans used in this study.

Surfactant name	HLB	Tail length
Span 20 (sorbitan monolaurate)	8.6	11
Span 40 (sorbitan monopalmitate)	6.7	15
Span 60 (sorbitan monostearate)	4.7	17
Span 80 (sorbitan monooleate)	4.3	17
Span 65 (sorbitan tristearate)	2.1	17 on each tail, 3 tails
Span 85 (sorbitan trioleate)	1.8	17 on each tail, 3 tails

TABLE 2 Summary of the different phases observed in THF-water mixtures, with different THF to water ratios, and with different sorbitan esters. This table reflects observations with the naked eye and with an optical microscope, over a 24 h period. The colors of the cells distinguish different phase behaviours, and are used as visual aid. 1L = one liquid phase, based on observations with the naked eye and under an optical microscope; 1L + F = one liquid phase, based on observations with the naked eye and under an optical microscope, mixed with flocculated surfactant; E = emulsion, as seen under an optical microscope; 2L = separation into bulk phases, as seen with the naked eye in bottle tests.

Span	HLB	Tail			THF % (v/v, relative to water)									
		Number of carbons	Number of tails	Bonds	10	20	30	40 (L)	50 (L)	60 (L)	70 (L)	80 (L)	90 (L)	
Span 20	8.6	11	1	Single	E	E	E	2	2	2	1	1	1	
Span 40	6.7	15	1	Single	1L + F	1L + F	1L + F	2	2	2	2	1	1	
Span 60	4.7	17	1	Single	1L + F	1L + F	1L + F	2	2	2	2	1	1	
Span 80	4.3	17	1	Double	E	E	E	2	2	2	2	1	1	
Span 65	2.1	17	3	Single	1L + F	E	E	2	2	2	2	2	1	
Span 85	1.8	17	3	Double	E	E	E	2	2	2	2	2	1	

The term q_p corresponds to the center of the Gaussian peak, while σ corresponds to the standard deviation of the Gaussian, which characterizes the width of the distribution.

The model was fitted to the data by non-linear regression using Prism 10.1 (GraphPad Software, San Diego, CA). We used a standard nonlinear regression routines (Levenberg, 1944; Marquardt, 1963), and data were weighted by $1/Y^2$. This was done to ensure that solutions were stable and in order to determine confidence intervals.

The center position of the Gaussian peaks in reciprocal space was converted to its corresponding value in direct space, d_p , by $d_p = 2\pi/q_p$. To determine the domain size, correlation length, coherence length, sometimes referred to the persistence length of the scattering event related to the Gaussian peaks we used an approximation based on the standard Scherrer model:

$$\xi = \left(\frac{K2\pi}{\Delta q} \right) \quad (3)$$

The term Δq refers to the full width half maximum of a peak. The conversion of a standard deviation to a full-width half maximum is $FWHM = 2\sqrt{2\ln 2}\sigma$, while the shape factor is usually assumed to be $K = K = 2\sqrt{\frac{\ln 2}{\pi}}$ for spherical domains of cubic symmetry. The correlation length can then be calculated from the standard deviation of the Gaussian using:

$$\xi = \left(\frac{\sqrt{2\pi}}{\sigma} \right) \quad (4)$$

2.6 FTIR spectromicroscopy

FTIR spectromicroscopy (in ATR mode) was used to analyze emulsions prepared using different sorbitan esters and varying percentages of THF and water.

Measurements were conducted at the Canadian Light Source (CLS) in Saskatoon (Canada) using an Agilent Cary 670 FTIR

Interferometer with Cary 620 Microscope, employing a 2D Focal Plane Array MCT-A detector. The hyperspectra were collected in transmission mode by placing 0.5 μ L in between two calcium fluoride windows separated by a 10 μ m Teflon spacer. This technique was used to map the samples, characterizing compositional differences between the interior and the exterior of emulsified droplets.

3 Results and discussion

THF and water are freely miscible in one another in binary solutions. Our previous study revealed that Span 80, a sorbitan ester, separates THF from water (Bartokova et al., 2023b). Here, we examine THF-water separation with different sorbitan esters (cf. Table 1), to assess the effect of their structure, and their tail in particular, on the mechanisms of solvent-water separation.

Note that in our study, separation was qualitatively assessed through bottle tests, optical microscopy and FTIR spectromicroscopy (Table 2). Our previous research conducted using Span 80 quantitatively showed that this sorbitan ester increases the water purity, but does not reduce THF to values compatible with legislative limits. These are for instance 50–1,300 μ g/L in different states in the United States (Isaacson et al., 2006). Span 80 is also one of the sorbitan esters analyzed in our current study. A modeling study reports that swing distillation could theoretically achieve up to 99.9% removal of THF from water (Lee et al., 2011). Swing distillation is, however, energy intensive. Another study conducted using electrooxidation reports that THF removal was higher than 90% with suitable electrodes (Urtiaga et al., 2014). However, electrokinetic methods also use energy and require the installation of electrodes in impacted aquifers, which can be challenging and costly. The goal of our study is to reduce the concentrations of THF in water using low energy approaches, to then allow for subsequent treatments to be effective. As an example, a study reported the successful removal of THF from water using anaerobic bacteria and membranes (Hu et al., 2018).

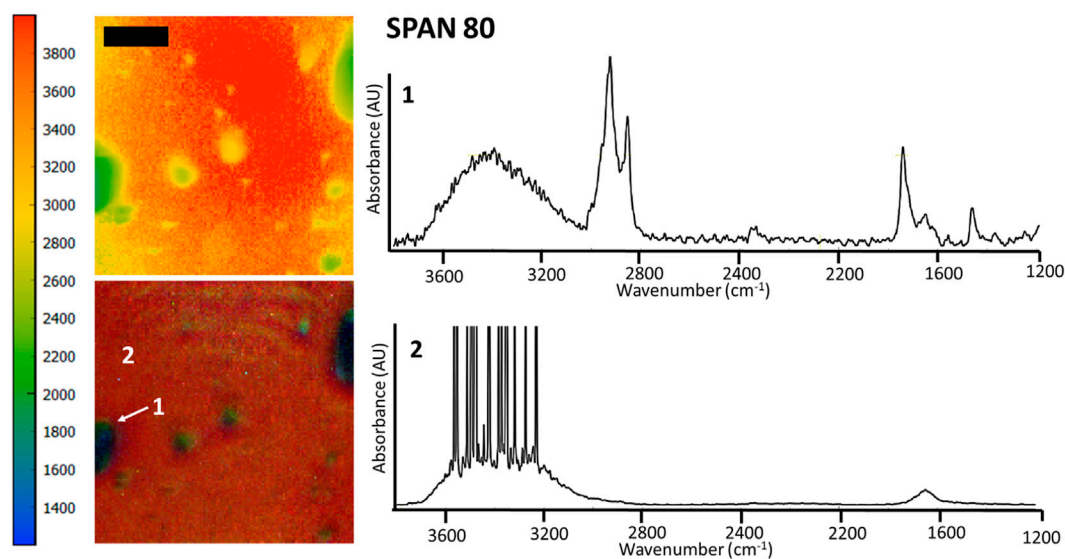


FIGURE 1

FTIR spectromicroscopy images of THF-rich droplets in water, stabilized by 40 g/L Span 80. Samples contained 30% THF (v/v, relative to water). The scale bar is 100 μm . The colored scale bar shows the wavenumbers, providing an indication of the different chemical composition of droplets and the bulk phase in the rainbow colored image (red/orange = water, labelled as 2, with a dominant OH stretch at 2,500–4,000 cm^{-1} ; green = THF and sorbitan esters, labelled as 1). Note that in these experiments samples were inserted in a compression cell, explaining the distortion in the droplet shape and their relatively large size. The compression cell was used to limit the thickness of the water layer. Nonetheless, the OH stretch band of water is saturated in the IR spectra of the water-rich phase (spectrum 2). FTIR spectromicroscopy images of THF-water mixtures separated by Span 60 and Span 85 are in the supporting information file (Supplementary Figure S1.2).

TABLE 3 D and fractal type of sorbitan ester self assembled structures, for different sorbitan esters.

	THF			
	D	Fractal type	Persistence length 1	Persistence length 2
Span 20	2.13	Surface	25.1	11.9
Span 40	2.78	Mass	25.5	13.7
Span 60	N/A			
Span 65	2.41	Mass	27.2	12.1
Span 80	2.38	Surface	26.6	15.9
Span 85	2.38	Surface	27.4	21.6
	THF +2% water			
	D	Fractal type	Persistence length 1	Persistence length 2
Span 20	2.75	Surface	27.4	19.3
Span 40	2.18	Surface	27.2	24.3
Span 40, replicate	2.21	Surface	27.3	23.9
Span 60	2.46	Surface	26.9	23.3
Span 65	2.27	Surface	23.9	23.2
Span 80	2.72	Surface	23.2	24.8
Span 85	2.15	Mass	24.5	31.6
Span 85, replicate	2.17	Mass	24.4	32.1

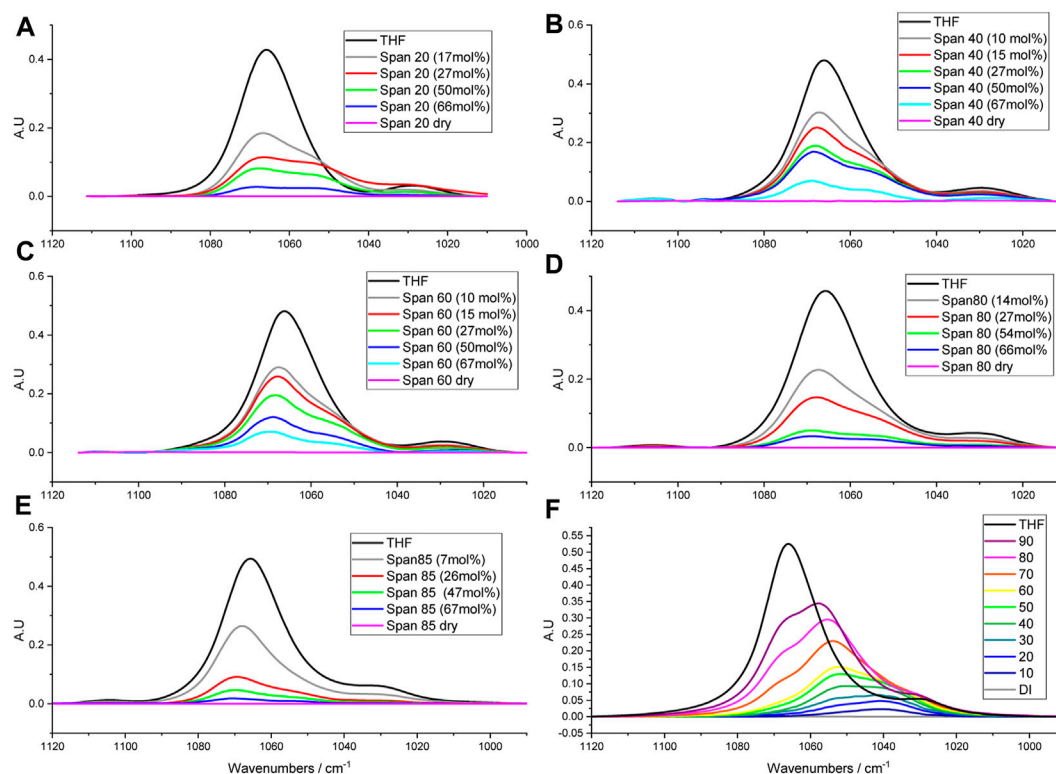


FIGURE 2

Absorbance spectra in the COC region for THF mixtures with different sorbitan esters. (F) was reprinted from Bartokova et al. (2023a) with permission. (A–E) show the spectra for THF mixtures with different Spans. (F) shows THF mixtures in water, containing different THF percentages. In (F), deionised water is abbreviated as DI.

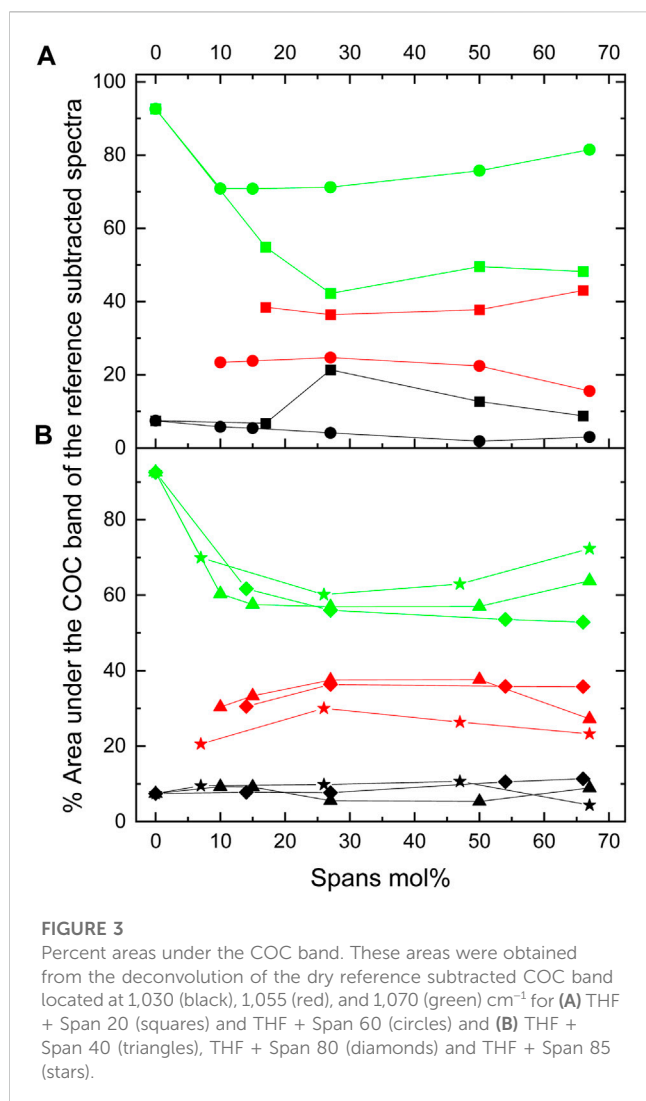
Bacterial remediation is energy effective, but bacteria can remediate pollutants only below concentrations at which they are toxic to them. Therefore, our approach can represent the first step in a treatment train for the removal of THF from water. Identifying the mechanism of separation and the surfactant characteristics that lead to effective separation will allow us to optimize this first step.

Bottle tests and optical microscopy show that separation occurs at THF to water ratios dependent on the type of sorbitan ester (cf. Table 2; Figure 1; Supplementary Figures S1.1–S1.3). Specifically, we observe that both the hydrophobic lipophilic balance (HLB) number and saturation of the tail affect the THF to water ratio at which separation occurs.

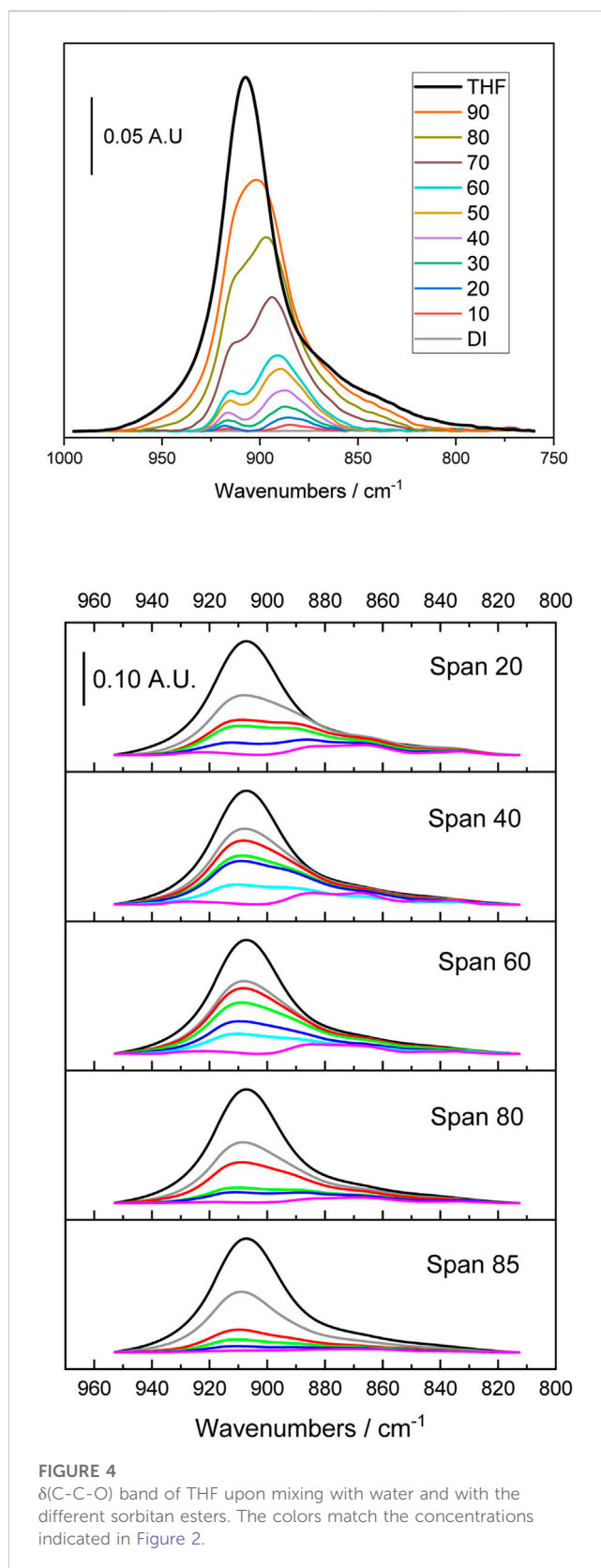
While all sorbitan esters are hydrophobic (soluble in THF, insoluble in water), Span 20 has the highest HLB number (HLB = 8.6). It yields emulsions with 10%–30% THF (v/v, relative to water), free layers with 40%–60% THF and one liquid phase with 70%–80% THF. Span 40 (HLB = 6.7), Span 60 (HLB = 4.7) and Span 80 (HLB = 4.3) have intermediate HLB numbers. They separate THF from water into free layers with THF percentages ranging from 40% to 70%, while yielding one liquid phase only at 80% THF. With Span 40 and Span 60, separation does not occur with 30% THF or less, where the observed turbidity is due to flocs (Supplementary Figure S1.2). With Span 80, emulsions are observed at 30% THF or below (Supplementary Figure S1.2). Although Span 80 and Span 60 have similar HLB and the same tail length, Span 80 differs from Span 60 in that it has a double bond in its tail (i.e., its

tail is unsaturated). Finally, Span 65 (HLB = 2.1) and Span 85 (HLB = 1.8) have the lowest HLB number, and they yield free phases with THF percentages from 40% to 80% THF. With 20%–30% THF, they yield emulsions. Finally, with 10% THF and Span 65, the observed turbidity is due to flocs (Supplementary Figure S1.2), while emulsions form with Span 85. Note that, similar to Span 80 and Span 60, Span 65 and 85 have similar HLB and the same tail length for each of their three tails. However, Span 85 has double bonds in its tails, while Span 65 does not. In both cases, double bonds in the tail (i.e., unsaturated tails) promote separation at the lowest THF percentages.

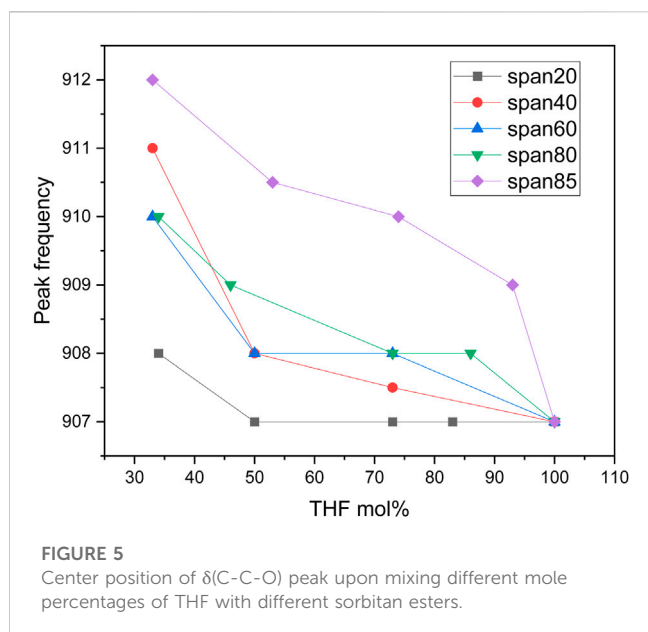
In our previous study, we explained water-THF separation by Span 80 based on the ability of Span 80 to compete against THF for hydrogen (H) bonding with water (Bartokova et al., 2023b). Here, we explore the alternative hypothesis that sorbitan esters interact with THF, competing against water. In our previous studies, we investigated H bonding between water and THF by probing the OH stretch band of water (Earmden et al., 2022b; Bartokova et al., 2023b). Water species coordinate differently with other molecules in solution. In particular, they can donate one (single donors, SD) or two (double donors, DD) hydrogens, and accept one (single acceptor, SA) or two (double acceptor, DA) hydrogens (Bartokova et al., 2023a; Bartokova et al., 2023b). Therefore, water species include the following: SD-DA (coordination = 3, at ~2,850–3,200 cm⁻¹), SD-SA (coordination = 2, at ~3,200–3,300 cm⁻¹), DD-SA (coordination = 3, at ~3,400–3,550 cm⁻¹) and DD-DA (coordination = 4, at



$\sim 3,300\text{--}3,400\text{ cm}^{-1}$). In some instances, water species are intermediate between these four main species, as indicated by their peak position. The relative abundance of each water species can be estimated from the area of each of the peaks representing them. In our previous research, we found that in pure water SD-SA and DD-DA are the most abundant species, and have similar abundance (Bartokova et al., 2023a; Bartokova et al., 2023b). THF alters the distribution of water species, because it H bonds and mainly accepts hydrogens (Patel et al., 2023). Therefore, DD-SA dominate at high THF percentages (above 70%) (Patel et al., 2023). Instead, DD-DA is dominant up to 40% THF. At intermediate THF percentages (50%–70% THF), the dominant water species is intermediate between DD-DA and SD-SA. The COC peak of THF at $\approx 1,065\text{ cm}^{-1}$ can also reveal H bonding between THF and water. Upon mixing with water, the COC peak of THF shifts and splits, as seen in Figure 2. Our recent study compared the OH stretch band of water and the COC band of THF, in THF-water mixtures (Bartokova et al., 2023a). This comparison showed that THF species that interact with DD-SA water species correspond to the $1,070\text{ cm}^{-1}$ peak in the COC band. The peak at $1,050\text{ cm}^{-1}$ dominates with $>30\%$ THF (v/v, relative to water), and it is related to THF species that mainly accept a single H. These water



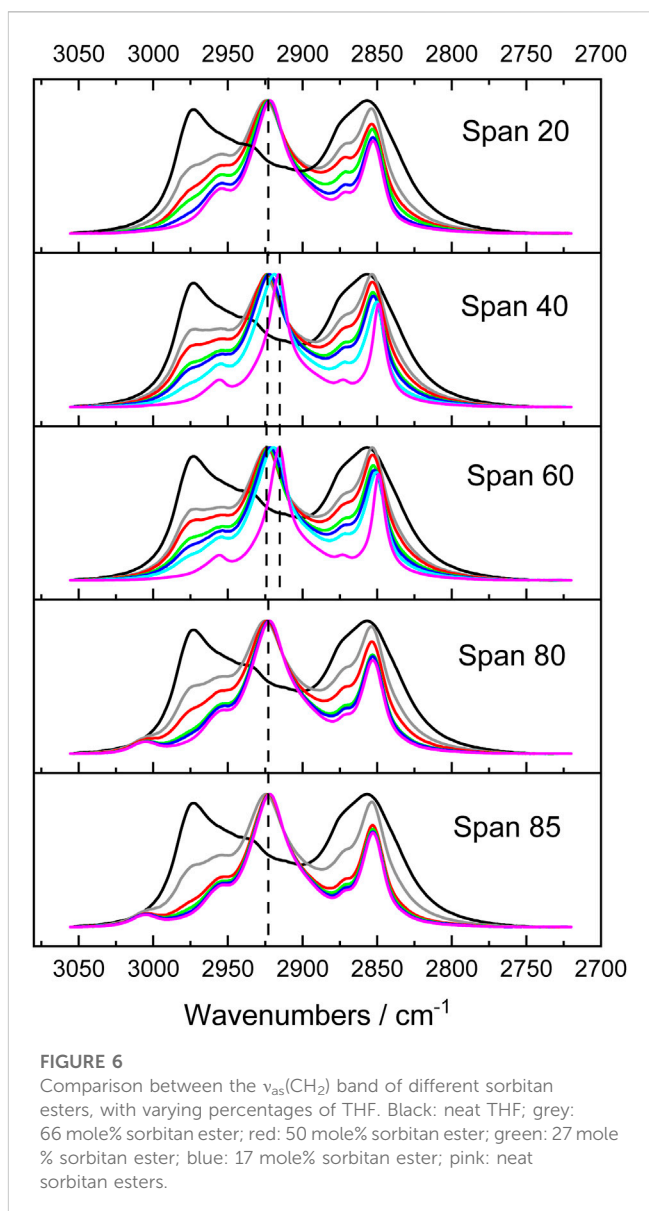
species correspond to SD-SA below 30% THF, and to species intermediate between SD-SA and DD-DA above 30% THF. Finally, the peak at $1,040\text{ cm}^{-1}$ corresponds to THF species that interact with SD-DA and DD-DA water species. In light



of our previous study, we now use the COC band to study H bonding between THF and water, and between THF and sorbitan esters.

In particular, we analyze the COC band of THF to probe the hypothesis that sorbitan esters H bond THF. We also compare how H bonding of THF with water and with sorbitan esters affects the COC band of THF. With pure THF, we observe a dominant COC stretch peak at $\approx 1,070 \text{ cm}^{-1}$ (Liu et al., 2022), and a significantly smaller peak at $1,027 \text{ cm}^{-1}$ (Sionkowska and Planecka, 2013) (Figure 1). As mentioned above, upon mixing with water, the peak at $\approx 1,070 \text{ cm}^{-1}$ splits into three peaks, at $\approx 1,070 \text{ cm}^{-1}$, $\approx 1,050 \text{ cm}^{-1}$ and $\approx 1,040 \text{ cm}^{-1}$. A previous study on THF hydrates reports that peaks associated with the CO stretch are affected by temperature, with a single CO stretch peak at 80 K (-193°C), a shoulder at 40 K (-233°C) and splitting at 13 K (-260°C) (Fleyfel and Devlin, 1991). Specifically, at 13 K the band at $1,070 \text{ cm}^{-1}$ splits into $1,071$ and $1,076 \text{ cm}^{-1}$. The authors attribute this band to crystalline THF and ascribe its split to the distribution of THF molecules over two unequal positions in the hexacaidecahedral water cages (Fleyfel and Devlin, 1991). In addition to the crystalline THF band at $1,070 \text{ cm}^{-1}$, the authors also identify a band at $1,052\text{--}1,054 \text{ cm}^{-1}$ and ascribe it to less ordered (or glassy) THF. In our study, a peak at $\approx 1,050 \text{ cm}^{-1}$ (glassy THF) appears upon mixing with water, while being absent for pure THF at ambient pressure and 20°C (Figure 2). Importantly, upon mixing with water, the peak at $\approx 1,050 \text{ cm}^{-1}$ (glassy THF) is more prominent than the peak at $1,070 \text{ cm}^{-1}$ (crystalline or ordered THF). This result is in agreement with a previous study, which also reports that mixing THF with water increases the proportion of amorphous (glassy) THF (Aliaga et al., 2011). Note that our results were obtained at ambient pressure. A split of the CO stretch band was also previously observed upon crystallizing methanol by super-pressing it to pressures of 101 kbar (Mammone et al., 1980).

Sorbitan esters also interact with THF through H bonds, as indicated by splitting of the COC band in THF-sorbitan ester mixtures. We propose that H bonding occurs between the oxygen on the ether ring of THF and the OH groups of the



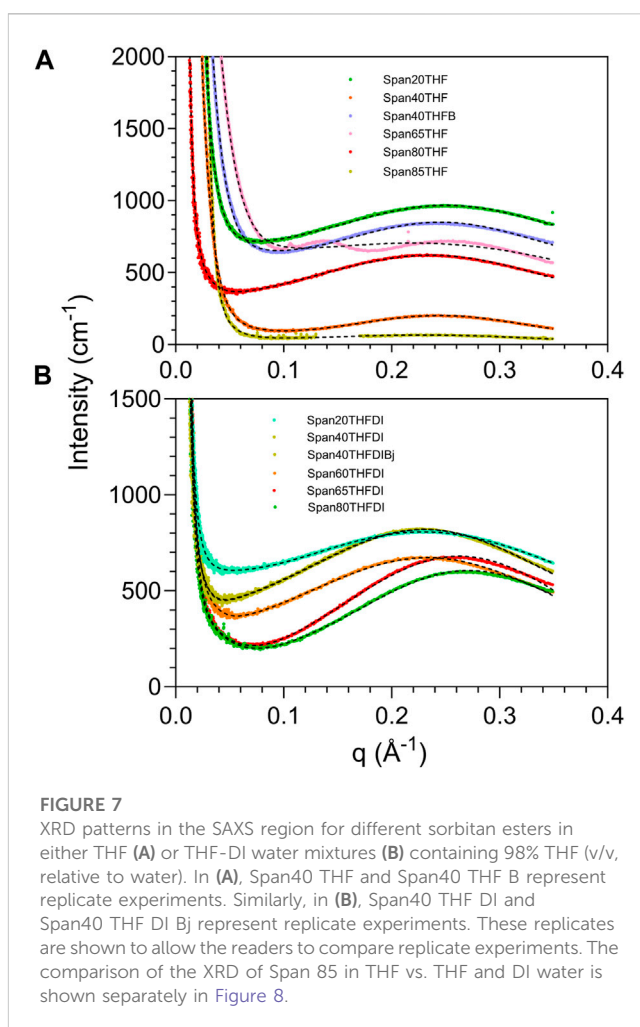
sorbitan esters. Qualitatively, we observe that this interaction results in a shift of the OH stretch band of sorbitan esters (Supplementary Figure S1.4). Figure 2 shows the COC band of THF, which can be deconvolved into three peaks at $\approx 1,050 \text{ cm}^{-1}$ (glassy THF), at $\approx 1,070 \text{ cm}^{-1}$ (crystalline THF) and at $\approx 1,030 \text{ cm}^{-1}$. Figure 3 shows the percent area under each peak, with the different sorbitan esters. These areas represent the relative abundance of the different THF types, e.g., crystalline vs. glassy. Dissimilar to observations with water, in mixtures of THF and sorbitan esters the peak at $\approx 1,050 \text{ cm}^{-1}$ (glassy THF) is less prominent than the peak at the peak at $1,070 \text{ cm}^{-1}$ (crystalline or ordered THF). This result suggests that THF is more ordered upon mixing with sorbitan esters compared to water, thereby leading to a more crystalline-like structure. THF ordering depends on the length and number of the sorbitan esters tails. THF is least ordered with Span 20, with the highest HLB number and the greatest $1,050\text{--}1,070 \text{ cm}^{-1}$ ratio. Ordering increases when increasing the length of a single saturated tail from eleven carbons (for Span 20) to seventeen

carbons (for Span 60), as seen in Figure 2A. Also, THF is less ordered with Span 80 (one unsaturated tail with 17 carbons) than with Span 85 (three unsaturated tails with 17 carbons), as seen in Figure 2B. While Span 65 was not analyzed in detail and is not shown in Figures 2, 3, its effect on the COC band is qualitatively similar to Span 85, as it also has a low HLB number (Supplementary Figure S1.5). Analyzing in detail the effect of Span 65 on the COC band of THF will be the objective of future research.

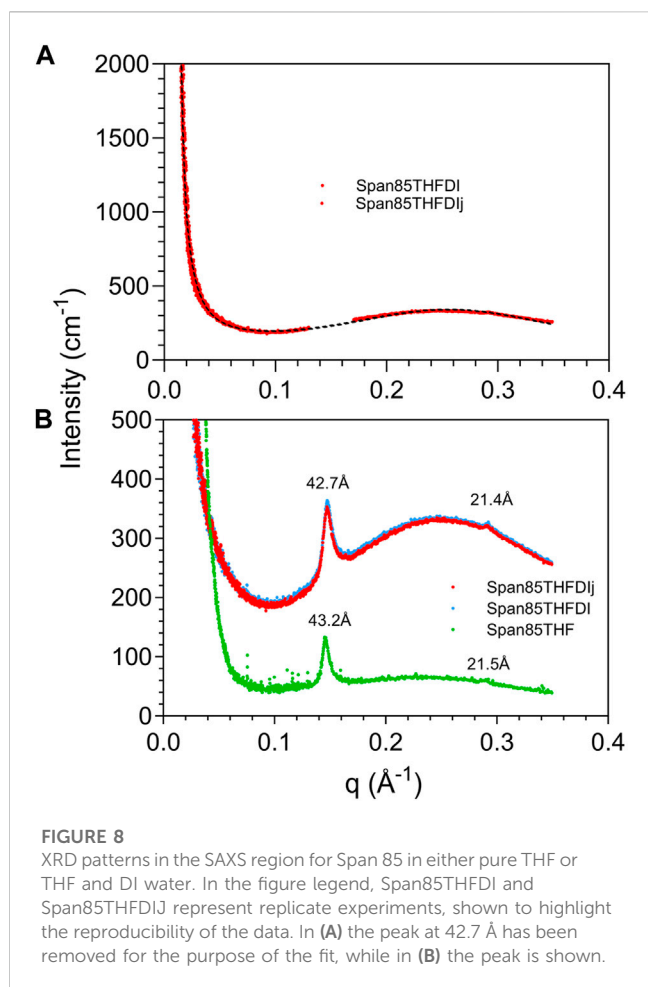
Moreover, in pure THF, we observe a peak at 905 cm^{-1} , which corresponds to $\delta(\text{C-C-O})$ (Harthcock, 1989) (Figure 4). Mixing THF with water causes splitting of this peak, in agreement with previous studies (Figure 4). For example, in a Raman study, the authors observed peaks at 914 cm^{-1} and $2,870\text{--}2,960\text{ cm}^{-1}$, which are assigned to a ring breathing mode (Li et al., 2016). The authors report that in a 19.1 wt % THF solution, the bands centered at 914 cm^{-1} for pure THF split into two peaks at 892 and 918 cm^{-1} , due to interactions between THF and water molecules (Li et al., 2016). Another Raman study also reports a split of the peak at 916 cm^{-1} into two peaks at 920 and 891 cm^{-1} in aqueous mixtures of THF (Prasad et al., 2007). Note that the position of the peaks in Raman is shifted compared to IR. By correlating the $\delta(\text{C-C-O})$ band to the COC stretch, we propose that the peak at approximately 890 cm^{-1} corresponds to glassy THF and the peak at 910 cm^{-1} corresponds to crystalline THF.

The $\delta(\text{C-C-O})$ band of THF is also affected by mixing THF with sorbitan esters (cf. Figure 4). In this case, the peak at 890 cm^{-1} (glassy THF) appears as a shoulder while the dominant peak is at 910 cm^{-1} (crystalline THF), in contrast with THF-water mixtures. This effect is most marked with the most hydrophobic sorbitan esters, Span 65 and Span 85, as qualitatively seen in Figure 4. We also quantitatively analyze the overall position of the $\delta(\text{C-C-O})$ peak, rather than the two peaks convolved under it (Figure 5). Figure 5 shows that the shift of the peak to higher wavenumbers is greatest with the most hydrophobic sorbitan ester (e.g., Span 85), in line with the greater ordering of THF, whereas the shift is smallest with the most hydrophilic sorbitan ester (Span 20). Note that while we have not analyzed Span 65 in detail, its effect on the $\delta(\text{C-C-O})$ is qualitatively similar to Span 85 (Figure 5), with a similar HLB number. In summary, the analysis of the $\delta(\text{C-C-O})$ confirms the hypothesis that THF interacts with sorbitan esters through H bonds. It also indicates that THF is more ordered upon mixing with sorbitan esters than with water, in agreement with the analysis of the COC stretch band of THF.

So far, we have discussed H bonding between sorbitan esters and THF. We also highlighted that THF ordering upon mixing with sorbitan esters is correlated to their HLB numbers. Now, we compare the interactions between the different sorbitan ester tails and THF. Recall that sorbitan esters with saturated tails flocculate at low THF percentages, whereas this does not occur when tails are unsaturated. This result suggests that the characteristics of the tails influence THF-sorbitan ester interactions. To probe this aspect, we examine the CH band in the spectrum of sorbitan esters (Figure 6). In our previous study, we analyzed the CH bands of THF, to study THF interactions with water (Bartokova et al., 2023b). We found that this band shifts to higher wavenumbers upon mixing THF with water (Bartokova et al., 2023b), in agreement with a study conducted by Mizuno et al. (2003). Mizuno et al. proposed that water formed a bifunctionally hydrogen-bonded hydration complex with



1,4 dioxane. In this complex, water acts both as a proton donor (in a conventional $\text{OH} \cdots \text{O}$ hydrogen bond with the ether oxygen) and as a proton acceptor (which accepts the H from the CH group, to form $\text{CH} \cdots \text{OH}_2$) (Mizuno et al., 2003). Here, we analyze the $\nu_{\text{as}}(\text{CH}_2)$ band of sorbitan esters, to examine their interactions with THF. The second derivative of spectra allows for the identification of convoluted peaks under a band envelope in the form of negative peaks. From the second derivative, we can be confident that the THF band does not interfere with the $\nu_{\text{as}}(\text{CH}_2)$ band of sorbitan esters (Supplementary Figure S1.6). This is different from the $\nu_{\text{s}}(\text{CH}_2)$, which is heavily overlapped with the THF band and less clear to interpret, justifying our focus on the $\nu_{\text{as}}(\text{CH}_2)$ band. Our data reveal that there is a blueshift in the $\nu_{\text{as}}(\text{CH}_2)$ band of sorbitan esters with increasing THF content (Figure 6). $\text{C-H} \cdots \text{O}$ hydrogen bonds are widely accepted, as discussed above. They manifest in IR as a shortening of the C-H bond (not lengthening like a regular H bond) and therefore a blue shift (Mizuno et al., 2003). Therefore, the data indicate that with increasing THF percentages in binary mixtures of THF and sorbitan esters, $\text{C-H} \cdots \text{O}$ bonding becomes stronger, as expected. Importantly, the effect of this interaction is most significant in Span 40 and 60. Recall that Span 40 and Span 60 form flocs at low THF percentages relative to water, whereas Span 20, Span 80 and Span 85 form emulsions (cf. Supplementary Figure S1.2). This observation, in conjunction with the analysis of the CH



band, indicates that Span 40 and Span 60 interact with THF more strongly than Span 20, Span 80 and Span 85. In contrast, Span 40 and Span 60 interact with water less strongly than Span 20, Span 80 and Span 85. Both the length and the saturation of the tail play a role. Span 40 and Span 60 have saturated tails, whereas Span 80 and Span 85 have unsaturated tails. Span 20 also has a saturated tail, but the tail is short. In light of these results, we propose that separation between THF and water occurs *primarily* (but not exclusively) because the hydrophilic head of Span 20, Span 80 and Span 85 competes for interactions with water against THF. This is in line with our previous study, where proposed that Span 80 competes against THF for interactions with water, based on the analysis of the OH stretch band (Bartokova et al., 2023b). In contrast, we propose that separation between THF and water occurs *primarily* (but not exclusively) due to preferential interactions between the tail of Span 40 and Span 60 and THF. Note that we are not excluding interactions between THF and the tails of Span 20, Span 80 and Span 85, or between water and the heads of Span 40 and Span 60. Indeed, SAXS data demonstrate interactions between the heads of all sorbitan esters and water, as discussed below.

In particular, we use SAXS to compare the self-assembly of sorbitan esters in pure THF and with low (2%) water percentages relative to THF. While higher water percentages lead to emulsification of larger droplets or bulk separation, at low water percentages we can observe the onset of THF-water separation. In

pure THF, we propose that sorbitan esters can interact with the solvent through either their heads or tails, leading to their self-assembly into micelles with their heads pointing outwards or inwards. This hypothesis is confirmed by SAXS data (Figures 7, 8). The SAXS patterns of all sorbitan esters in pure THF display broad peaks, which are characteristic of micelles with their heads pointing outwards or inwards (Bartokova et al., 2023a). In THF, either the heads or the tails of the sorbitan esters could be pointing outwards, because both have the ability to interact with THF. This is similar to observations of stearic acid in THF, as reported in our previous study (Bartokova et al., 2023a). Span 85 also displays a crystalline peak, which indicates that it is not fully solubilized in THF. In pure THF, the self-assembled structures formed by Span 40 and Span 65 are mass fractals, whereas surface fractals are observed for Span 20, Span 80 and Span 85, as summarized in Table 3 (results are less clear for Span 60). These results correlate to the liquid vs. solid state of neat sorbitan esters. Neat Span 40 and Span 65 are solids, whereas Span 20, Span 80 and Span 85 are liquids at 20°C, at which measurements were conducted. Optical microscopy observations show self-assembly into large flocs with Span 40, Span 60 and Span 65 in pure THF (Supplementary Figure S1.7). While the scales observed with optical microscopy and SAXS are clearly different, we are comparing these two techniques because fractals are scale invariant. In THF, the persistence length determined based on the peak center and from the standard deviation of the zero mean Gaussian peak are ≈ 25 Å for Span 20 and Span 40 and larger (≈ 27 Å) for Span 80, Span 65 and Span 85, consistent with their larger size. We interpret these values as the distance between the centers of micelles with their heads pointing outwards or inwards. Interestingly, in THF, we also identify a significantly smaller, second persistence length (≈ 16 Å for Span 20, Span 40, Span 80 and Span 65, and ≈ 21 Å for Span 85), based on the standard deviation of the non-zero mean Gaussian peak. We ascribe the difference between these two persistence lengths to the limited order in mixtures of sorbitan esters in THF. With 2% water in THF, self-assembled structures of sorbitan esters are surface fractals in all cases, except Span 85. Span 85 is a mass fractal and displays a crystalline peak in its SAXS pattern, similar to observations in pure THF. This result could be due to incomplete hydration of Span 85 during the time frame analyzed, with the small amounts of water added. We ascribe the transition from mass to surface fractals for all other sorbitan esters to the fact that water promotes the formation of micelles with their heads pointing inwards. These contain water in their interior, towards which the heads point. Note that while SAXS patterns could indicate either micelles with heads pointing outwards or inwards, samples contained 2% water and 98% THF. In such samples, THF should be the continuous phase because of its high percentage, while water should be inside the micelle. Since the hydrophobic Span tails cannot interact with water, the hydrophilic head would be pointing inwards. Dissimilar to observations with 2% water, in THF, either the heads or the tails of the sorbitan esters could be pointing outwards. This is because both have the ability to interact with THF, as mentioned above. As a result of the enhanced ordering induced by addition of 2% water, we find a single persistence length. Specifically, with 2% water, the average persistence length determined for the different sorbitan esters based on the peak center and from the standard deviation of

the zero mean Gaussian peak is ≈ 25 Å. This value is close to the persistence length determined based on the standard deviation of the nonzero mean Gaussian peak. Once again, this is in contrast with THF, where we have less ordered self-assembled structures and identified two persistence lengths. Note that we did not conduct SAXS experiments with high water percentages. In this case, we would expect that sorbitan esters would be forming micelles, which would contain THF in their interior and would have their hydrophilic heads pointing outwards towards the water.

In summary, IR data suggest that the longer, saturated tail of some sorbitan esters (e.g., Span 40 and Span 60) interact with THF more strongly than the shorter, saturated tail of Span 20, or the unsaturated tails of Span 80 and Span 85. SAXS data complement these findings. They show that interactions between all sorbitan esters and water play a role in THF-water separation, beyond differences in the way they interact with THF. Indeed, in all cases 2% water enhances ordering, since it favors the formation of micelles with water in their interior.

4 Conclusion

Bottle tests, optical microscopy and FTIR spectromicroscopy show that sorbitan esters (Span 20, Span 40, Span 60, Span 80, Span 65 and Span 85) separate THF and water, which would otherwise be miscible due to H bonding. Separation occurs with up to 70% THF (v/v, relative to water), at THF to water ratios dependent on the sorbitan ester structure. Span 80 and Span 85 have double bonds in their tails. Double bonds in the tail (i.e., unsaturated tails) promote separation at the lowest THF percentages. In contrast, Span 40 and Span 60 (with saturated tails) flocculate at the lowest THF percentages (10%–30% THF) and do not effectively separate these THF-water mixtures. This suggests weaker interactions with water, and hence lower solubility at high water percentages. Saturated, but shorter tails (e.g., Span 20) still allow separation at low THF percentages.

We use ATR-FTIR to study separation mechanisms between THF and water by sorbitan esters. ATR-FTIR reveals that mixing with water disorders THF, resulting in an increase of the percentage of glassy to crystalline THF.

Sorbitan esters impede THF-water interactions. Similar to water, they H bond with THF. However, dissimilar to water, they order THF. Ordering increases with tail length (e.g., from Span 20 to Span 60) and with increasing number of tails (e.g., from Span 80 to Span 85). This is reflected in the COC and $\delta(\text{C-C-O})$ band of THF.

Furthermore, we observe a blueshift in the $\nu_{\text{as}}(\text{CH}_2)$ band of sorbitan esters upon mixing with increasing THF percentages, because of the formation of C-H...O H bonds. The blueshift is most marked for Span 40 and 60. This result indicates that Span 40 and Span 60 interact with THF more strongly than Span 20, Span 80 and Span 85. In contrast, Span 40 and Span 60 interact with water less strongly than Span 20, Span 80 and Span 85, as indicated by their flocculation at the lowest THF percentages (10%–30% THF, v/v relative to water).

Based on these results, we propose that separation between THF and water occurs due to two primary mechanisms, depending on the sorbitan ester characteristics. Specifically, separation occurs *primarily* (but not exclusively) because the hydrophilic head of Span 20, Span 80 and Span 85 compete for

interactions with water against THF. In contrast, separation occurs *primarily* (but not exclusively) due to preferential interactions between the tail of Span 40 and Span 60 and THF. Note that we are not contending that these are the only mechanisms involved. Indeed, THF interacts with the tails of all sorbitan esters, and water interacts with their heads.

The role of water-sorbitan ester interactions on THF-water separation is highlighted by SAXS data. In THF, sorbitan esters self-assemble into micelles with their heads pointing outwards or inwards, because both the heads and the tails of sorbitan esters interact with THF. Both types of micelles further assemble to form either closed-packed clusters (surface fractals, in the case of Span 20, Span 80, and Span 85), or open-packed clusters (mass fractals, in the case of Span 40, Span 60 and Span 65). In THF, we identify two different persistence lengths, because of the limited order of sorbitan ester self-assembled structures. With 2% water, we observe a transition from mass to surface fractals in all cases except Span 85, possibly due to its incomplete hydration. Under these conditions, sorbitan esters self assemble into micelles with their heads pointing inwards, which host water in their interior. We identify a single persistence length (≈ 25 Å), which corresponds to the distance between the micelle centers. This shows enhanced ordering.

Our future research will focus on further elucidating how separation mechanisms are affected by the tail structure, for different amphiphiles, including ones the head of which does not interact with THF, as well as others with varying heads that H bond THF. This research is part of our overall goal of developing a predictive toolbox to optimize solvent separation from water.

Data availability statement

The original contributions presented in the study are included in the article/[Supplementary Material](#), further inquiries can be directed to the corresponding author.

Author contributions

BB: Data curation, Formal Analysis, Investigation, Validation, Visualization, Writing—original draft, Writing—review and editing. AM: Data curation, Formal Analysis, Investigation, Methodology, Software, Validation, Visualization, Writing—original draft, Writing—review and editing. TL: Data curation, Formal Analysis, Software, Visualization, Writing—review and editing. EP: Conceptualization, Data curation, Formal Analysis, Funding acquisition, Investigation, Project administration, Resources, Software, Supervision, Validation, Visualization, Writing—original draft, Writing—review and editing.

Funding

The author(s) declare financial support was received for the research, authorship, and/or publication of this article. Part of the research described in this paper was performed at the Canadian Light Source, a national research facility of the University of

Saskatchewan, which is supported by the Canada Foundation for Innovation (CFI), the Natural Sciences and Engineering Research Council (NSERC), the National Research Council (NRC), the Canadian Institutes of Health Research (CIHR), the Government of Saskatchewan, and the University of Saskatchewan. The authors acknowledge the support of the Natural Sciences and Engineering Research Council of Canada (provided through an NSERC Discovery grant, awarded to EP, PIN 537871).

Conflict of interest

The authors declare that the research was conducted in the absence of any commercial or financial relationships that could be construed as a potential conflict of interest.

References

- Aliaga, C., Tsung, C. K., Alayoglu, S., Komvopoulos, K., Yang, P., and Somorjai, G. A. (2011). Sum frequency generation vibrational spectroscopy and kinetic study of 2-methylfuran and 2, 5-dimethylfuran hydrogenation over 7 nm platinum cubic nanoparticles. *J. Phys. Chem. C* 115, 8104–8109. doi:10.1021/jp111343j
- Barman, S. R., Banerjee, P., Mukhopadhyay, A., and Das, P. (2017). Biodegradation of acenaphthene and naphthalene by *Pseudomonas mendocina*: process optimization, and toxicity evaluation. *J. Environ. Chem. Eng.* 5, 4803–4812. doi:10.1016/j.jece.2017.09.012
- Bartokova, B., Laredo, T., Marangoni, A. G., and Pensini, E. (2023a). Mechanism of tetrahydrofuran separation from water by stearic acid. *J. Mol. Liq.* 391, 123262. doi:10.1016/j.molliq.2023.123262
- Bartokova, B., Marangoni, A. G., Laredo, T., and Pensini, E. (2023b). Role of hydrogen bonding on solvent separation using amphiphilic sorbitan ester. *Colloids and Surfaces C* 1, 100004.
- Bartokova, B., Marangoni, A. G., Laredo, T., Stobbs, J., Meszaros, P., and Pensini, E. (2023c). Effect of hydrogen bonding on the mixing behaviour of ternary aqueous mixtures. *J. Mol. Liq.* 283, 122124. doi:10.1016/j.molliq.2023.122124
- Belhaj, A., Desnoues, N., and Elmerich, C. (2002). Alkane biodegradation in *Pseudomonas aeruginosa* strains isolated from a polluted zone: identification of alkB and alkB-related genes. *Res. Microbiol.* 153, 339–344. doi:10.1016/s0923-2508(02)01333-5
- Besha, A. T., Bekele, D. N., Naidu, R., and Chadalavada, S. (2018). Recent advances in surfactant-enhanced In-Situ Chemical Oxidation for the remediation of non-aqueous phase liquid contaminated soils and aquifers. *Environ. Technol. Innovation* 9, 303–322. doi:10.1016/j.eti.2017.08.004
- Boonchan, S., Britz, M. L., and Stanley, G. A. (1998). Surfactant-enhanced biodegradation of high molecular weight polycyclic aromatic hydrocarbons by *Stenotrophomonas maltophilia*. *Biotechnol. Bioeng.* 59, 482–494. doi:10.1002/(sici)1097-0290(19980820)59:4<482::aid-bit11>3.0.co;2-c
- de Brito Cardoso, G., Nascimento Souza, I., Mourão, T., Freire, M. G., Soares, C. M. F., and Silva Lima, A. (2014). Novel aqueous two-phase systems composed of acetonitrile and polyols: phase diagrams and extractive performance. *Sep. Purif. Technol.* 124, 54–60. doi:10.1016/j.seppur.2014.01.004
- Dhamole, P. B., Mahajan, P., and Feng, H. (2010). Phase separation conditions for sugaring-out in Acetonitrile–Water systems. *J. Chem. Eng. Data* 55 (9), 3803–3806. doi:10.1021/jc1003115
- Earnden, L., Marangoni, A. G., Laredo, T., Stobbs, J., Marshall, T., and Pensini, E. (2022a). Decontamination of water co-polluted by copper, toluene and tetrahydrofuran using lauric acid. *Sci. Rep.* 12, 15832–15920. doi:10.1038/s41598-022-20241-4
- Earnden, L., Marangoni, A. G., Laredo, T., Stobbs, J., and Pensini, E. (2022b). Mechanisms of separation between tetrahydrofuran and water using hydroxystearic acid. *Phys. Fluids* 34, 097119. doi:10.1063/5.0108008
- Earnden, L., Marangoni, A. G., Laredo, T., Stobbs, J., and Pensini, E. (2022c). Self-Assembled glycerol monooleate demixes miscible liquids through selective hydrogen bonding to water. *J. Mol. Liq.* 367, 120551. doi:10.1016/j.molliq.2022.120551
- Fleyfel, F., and Devlin, J. P. (1991). Carbon dioxide clathrate hydrate epitaxial growth: spectroscopic evidence for formation of the simple type-II carbon dioxide hydrate. *J. Phys. Chem.* 95, 3811–3815. doi:10.1021/j100162a068
- Hall, J., Soole, K., and Benthall, R. (2011). Hydrocarbon phytoremediation in the family Fabaceae—a review. *Int. J. Phytoremediation* 13, 317–332. doi:10.1080/15226514.2010.495143
- Harthcock, M. A. (1989). Probing the complex hydrogen bonding structure of urethane block copolymers and various acid containing copolymers using infra-red spectroscopy. *Polymer* 30, 1234–1242. doi:10.1016/0032-3861(89)90041-4
- Hu, D., Li, X., Chen, Z., Cui, Y., Gu, F., Jia, F., et al. (2018). Performance and extracellular polymers substance analysis of a pilot scale anaerobic membrane bioreactor for treating tetrahydrofuran pharmaceutical wastewater at different HRTs. *J. Hazard. Mater.* 342, 383–391. doi:10.1016/j.jhazmat.2017.08.028
- Isaacson, C., Mohr, T. K., and Field, J. A. (2006). Quantitative determination of 1, 4-dioxane and tetrahydrofuran in groundwater by solid phase extraction GC/MS/MS. *Environ. Sci. Technol.* 40, 7305–7311. doi:10.1021/es0615270
- Jessop, P., and Cunningham, M. (20206). *CO₂-switchable materials*. London, United Kingdom: Royal Society of Chemistry.
- Kolehmainen, E., and Turunen, I. (2007). Micro-scale liquid–liquid separation in a plate-type coalescer. *Chem. Eng. Process. Process Intensif.* 46, 834–839. doi:10.1016/j.cep.2007.05.027
- Lee, J., Cho, J., Kim, D. M., and Park, S. (2011). Separation of tetrahydrofuran and water using pressure swing distillation: modeling and optimization. *Korean J. Chem. Eng.* 28, 591–596. doi:10.1007/s11814-010-0467-1
- Leontowich, A. F., Gomez, A., Diaz Moreno, B., Muir, D., Spasyuk, D., King, G., et al. (2021). The lower energy diffraction and scattering side-bounce beamline for materials science at the Canadian Light Source. *J. Synchrotron Radiat.* 28, 961–969. doi:10.1107/s1600577521002496
- Levenberg, K. (1944). A method for the solution of certain non-linear problems in least squares. *Q. Appl. Math.* 2, 164–168. doi:10.1090/qam/10666
- Li, H., Stanwix, P., Aman, Z., Johns, M., May, E., and Wang, L. (2016). Raman spectroscopic studies of clathrate hydrate formation in the presence of hydrophobized particles. *J. Phys. Chem. A* 120, 417–424. doi:10.1021/acs.jpca.5b11247
- Liu, L., Xia, Y., Wang, L., Shi, R., Yan, S., Zhao, X., et al. (2022). Cyanate ester resin with high heat-resistance and degradable diacetal structure: synthesis, polymerization, and properties. *Macromol. Mater. Eng.* 307, 2200423. doi:10.1002/mame.202200423
- Longeras, O., Gautier, A., Ballerat-Busserolles, K., and Andanson, J. M. (2020). Deep eutectic solvent with thermo-switchable hydrophobicity. *ACS Sustain. Chem. Eng.* 8, 12516–12520. doi:10.1021/acssuschemeng.0c03478
- Malakahmad, A., and Ho, L. L. H. (2017). UV/H₂O₂ oxidation process optimization by response surface methodology for removal of polycyclic aromatic hydrocarbons (PAHs) from water. *Desalination Water Treat.* 65, 408–417. doi:10.5004/dwt.2017.20278
- Mammone, J. F., Sharma, S. K., and Nicol, M. (1980). Raman spectra of methanol and ethanol at pressures up to 100 kbar. *J. Phys. Chem.* 84, 3130–3134. doi:10.1021/j100460a032
- Marquardt, D. W. (1963). An algorithm for least-squares estimation of nonlinear parameters. *J. Soc. Industrial Appl. Math.* 11, 431–441. doi:10.1137/0111030
- Marshall, T., Earnden, L., Marangoni, A. G., Laredo, T., and Pensini, E. (2022). Cubic mesophases of self-assembled amphiphiles separate miscible solvents. *Colloids Surfaces A* 650, 129548. doi:10.1016/j.colsurfa.2022.129548
- Mizuno, K., Imafuji, S., Fujiwara, T., Ohta, T., and Tamiya, Y. (2003). Hydration of the CH groups in 1,4-dioxane probed by NMR and IR: contribution of blue-shifting CH...OH 2 hydrogen bonds. *J. Phys. Chem. B* 107, 3972–3978. doi:10.1021/jp021712+
- Patel, V., Marangoni, A. G., Mirzaee Ghazani, S., Laredo, T., Stobbs, J., and Pensini, P. (2023). Effect of bacterial surfactants on the phase behavior of miscible pollutants in water. *Colloids Surf. C* 1, 100013. doi:10.1016/j.colsuc.2023.100013

Publisher's note

All claims expressed in this article are solely those of the authors and do not necessarily represent those of their affiliated organizations, or those of the publisher, the editors and the reviewers. Any product that may be evaluated in this article, or claim that may be made by its manufacturer, is not guaranteed or endorsed by the publisher.

Supplementary material

The Supplementary Material for this article can be found online at: <https://www.frontiersin.org/articles/10.3389/frsrm.2023.1329058/full#supplementary-material>

- Prasad, P. S. R., Prasad, K. S., and Thakur, N. K. (2007). Laser Raman spectroscopy of THF clathrate hydrate in the temperature range 90–300 K. *Spectrochim. Acta Part A* 68, 1096–1100. doi:10.1016/j.saa.2007.06.049
- Sales, C. M., Grostern, A., Parales, J. V., Parales, R. E., and Alvarez-Cohen, L. (2013). Oxidation of the cyclic ethers 1, 4-dioxane and tetrahydrofuran by a monooxygenase in two *Pseudonocardia* species. *Appl. Environ. Microbiol.* 79, 7702–7708. doi:10.1128/aem.02418-13
- Sionkowska, A., and Planecka, A. (2013). Preparation and characterization of silk fibroin/chitosan composite sponges for tissue engineering. *J. Mol. Liq.* 178, 5–14. doi:10.1016/j.molliq.2012.10.042
- Souza, R. L., Lima, R. A., Coutinho, J. A., Soares, C. M., and Lima, Á. S. (2015). Aqueous two-phase systems based on cholinium salts and tetrahydrofuran and their use for lipase purification. *Sep. Purif. Technol.* 155, 118–126. doi:10.1016/j.seppur.2015.05.021
- Sun, Y., Zhou, Q., Xu, Y., Wang, L., and Liang, X. (2011). Phytoremediation for co-contaminated soils of benzo [a] pyrene (B [a] P) and heavy metals using ornamental plant *Tagetes patula*. *J. Hazard. Mater.* 186, 2075–2082. doi:10.1016/j.jhazmat.2010.12.116
- Tabata, M., Kumamoto, M., and Nishimoto, J. (1994). Chemical properties of water-miscible solvents separated by salting-out and their application to solvent extraction. *Anal. Sci.* 10, 383–388. doi:10.2116/analsci.10.383
- Toby, B. H., and Von Dreele, R. B. (2013). GSAS-II: the genesis of a modern open-source all purpose crystallography software package. *J. Appl. Crystallogr.* 46, 544–549. doi:10.1107/s0021889813003531
- Urriaga, A., Gómez, P., Arruti, A., and Ortiz, I. (2014). Electrochemical removal of tetrahydrofuran from industrial wastewaters: anode selection and process scale-up. *J. Chem. Technol. Biotechnol.* 89, 1243–1250. doi:10.1002/jctb.4384
- Von Dreele, R. B. (2014). Small-angle scattering data analysis in GSAS-II. *J. Appl. Crystallogr.* 47, 1784–1789. doi:10.1107/s1600576714018366
- Wang, B., Ezejias, T., Feng, H., and Blaschek, H. (2008). Sugaring-out: a novel phase separation and extraction system. *Chem. Eng. Sci.* 63, 2595–2600. doi:10.1016/j.ces.2008.02.004
- Wang, W. H., Hoag, G. E., Collins, J. B., and Naidu, R. (2013). Evaluation of surfactant-enhanced *in situ* chemical oxidation (S-isco) in contaminated soil. *Soil Pollut.* 224, 1713. doi:10.1007/s11270-013-1713-z
- Yin, Y., Yang, Y., de Lourdes Mendoza, M., Zhai, S., Feng, W., Wang, Y., et al. (2017). Progressive freezing and suspension crystallization methods for tetrahydrofuran recovery from Grignard reagent wastewater. *J. Clean. Prod.* 144, 180–186. doi:10.1016/j.jclepro.2017.01.012
- Yoshikawa, M., Masaki, K., and Ishikawa, M. (2002). Pervaporation separation of aqueous organic mixtures through agarose membranes. *J. Membr. Sci.* 205, 293–300. doi:10.1016/s0376-7388(02)00131-x



OPEN ACCESS

EDITED BY

Jay X. Tang,
Brown University, United States

REVIEWED BY

Anne-Laure Fameau,
Institut National de Recherche pour
l'Agriculture, l'Alimentation et l'Environnement
(INRAE), France
Oscar Domenech,
University of Barcelona, Spain

*CORRESPONDENCE

Marité Cárdenas,
✉ marite.cardenas@mau.se,
✉ marite.cardenas@ehu.eus
Ali Miserez,
✉ ali.miserez@ntu.edu.sg

RECEIVED 16 November 2023

ACCEPTED 31 December 2023

PUBLISHED 19 January 2024

CITATION

Gudlur S, Ferreira FV, Ting JSM, Domene C,
Maricar S, Le Brun AP, Yepuri N, Moir M,
Russell R, Darwish T, Miserez A and Cárdenas M
(2024), pH-dependent interactions of
coacervate-forming histidine-rich peptide with
model lipid membranes.
Front. Soft Matter 3:1339496.
doi: 10.3389/frsfm.2023.1339496

COPYRIGHT

© 2024 Gudlur, Ferreira, Ting, Domene, Maricar,
Le Brun, Yepuri, Moir, Russell, Darwish, Miserez
and Cárdenas. This is an open-access article
distributed under the terms of the [Creative
Commons Attribution License \(CC BY\)](#). The use,
distribution or reproduction in other forums is
permitted, provided the original author(s) and
the copyright owner(s) are credited and that the
original publication in this journal is cited, in
accordance with accepted academic practice.
No use, distribution or reproduction is
permitted which does not comply with these
terms.

pH-dependent interactions of coacervate-forming histidine-rich peptide with model lipid membranes

Sushanth Gudlur¹, Filipe Viana Ferreira¹, Javier Shu Ming Ting²,
Carmen Domene³, Syed Maricar¹, Anton P. Le Brun⁴,
Nageshwar Yepuri⁵, Michael Moir⁵, Robert Russell⁵,
Tamim Darwish⁵, Ali Miserez^{1,2*} and Marité Cárdenas^{2,6,7,8*}

¹Biological and Biomimetic Materials Laboratory (BBML), Center for Sustainable Materials (SusMat), School of Materials Science and Engineering, Nanyang Technological University (NTU), Singapore, Singapore, ²School of Biological Sciences, Nanyang Technological University (NTU), Singapore, Singapore, ³Department of Chemistry, University of Bath, Claverton Down, Bath, United Kingdom, ⁴Australian Centre for Neutron Scattering, Australian Nuclear Science and Technology Organisation (ANSTO), Lucas Heights, NSW, Australia, ⁵National Deuterium Facility (NDF), Australian Nuclear Science and Technology Organisation (ANSTO), Lucas Heights, NSW, Australia, ⁶Department of Biomedical Sciences, Biofilm Research Center for Biointerfaces, Malmö University, Malmö, Sweden, ⁷Instituto Biofisika (CSIC, UPV/EHU), Fundación Biofisika Bizkaia/Biofisika Bizkaia Fundazioa (FBB), Leioa, Spain, ⁸Ikerbasque, Basque Foundation for Science, Bilbao, Spain

Peptide-based liquid droplets (coacervates) produced by spontaneous liquid-liquid phase separation (LLPS), have emerged as a promising class of drug delivery systems due to their high entrapping efficiency and the simplicity of their formulation. However, the detailed mechanisms governing their interaction with cell membranes and cellular uptake remain poorly understood. In this study, we investigated the interactions of peptide coacervates composed of HBpep—peptide derived from the histidine-rich beak proteins (HBPs) of the Humboldt squid—with model cellular membranes in the form of supported lipid bilayers (SLBs). We employed quartz crystal microbalance with dissipation monitoring (QCM-D), neutron reflectometry (NR) and atomistic molecular dynamics (MD) simulations to reveal the nature of these interactions in the absence of fluorescent labels or tags. HBpep forms small oligomers at pH 6 whereas it forms μm -sized coacervates at physiological pH. Our findings reveal that both HBpep oligomers and HBpep-coacervates adsorb onto SLBs at pH 6 and 7.4, respectively. At pH 6, when the peptide carries a net positive charge, HBpep oligomers insert into the SLB, facilitated by the peptide's interactions with the charged lipids and cholesterol. Importantly, however, HBpep coacervate adsorption at physiological pH, when it is largely uncharged, is fully reversible, suggesting no significant lipid bilayer rearrangement. HBpep coacervates, previously identified as efficient drug delivery vehicles, do not interact with the lipid membrane in the same manner as traditional cationic drug delivery systems or cell-penetrating peptides. Based on our findings, HBpep coacervates at physiological pH cannot cross the cell membrane by a simple passive mechanism and are thus likely to adopt a non-canonical cell entry pathway.

KEYWORDS

LLPS, peptide coacervates, neutron reflectivity, membrane interaction, model membrane, molecular dynamic simulations, supported lipid bilayers

1 Introduction

Peptide-based liquid droplets, also known as coacervates, assembled by liquid-liquid phase separation (LLPS) have emerged as a new class of therapeutic delivery vehicles (Liu et al., 2023). Their attractiveness stems from their exceptionally high entrapping efficiency (Lim et al., 2018; Lim et al., 2020), their versatility in entrapping a broad variety of large macromolecular therapeutics (Sun et al., 2022), and their simple formulation methodology that avoids the use of organic solvents. Depending on the peptide design, the formation and disassembly of these liquid droplets can be controlled via various external triggers such as pH, temperature, ionic strength, etc. This versatility has led to the development of stimuli-responsive peptide coacervates whose delivery into various cell types *in vitro* have resulted in comparable or superior outcomes to those achieved with lipid- and polymer-based nanoparticles (Sun et al., 2022; Sun et al., 2023).

In contrast to well-studied drug delivery platforms, such as lipid- (e.g., liposomes, lipid nanoparticles, nanostructured lipid carriers, etc.) and nanoparticle-based vehicles (e.g., polymeric, cationic, metallic and carbon-based, etc.), mechanistic understanding related to coacervate/cell membrane interactions and their subsequent cellular uptake remains largely incomplete. Current understanding indicates that coacervates, characterized as dense, viscoelastic, μm -sized liquid droplets, exert sufficient compressive stresses to bend the plasma membrane inward (Yuan et al., 2021). Additional factors reported to be involved in coacervate interactions with the membrane surface, and possibly contributing to their cellular uptake, include membrane wetting (partial or complete) (Lu et al., 2022), capillary force generation (Gouveia et al., 2022) and free energy release through adhesion between viscoelastic media (Bergeron-Sandoval et al., 2021).

The specific route of cellular uptake of drug delivery vehicles depends on several factors, including its size, shape, composition, surface charge, hydrophobicity or hydrophilicity, and the specific cell type into which they are delivered (Behzadi et al. 2017). Endocytosis, an umbrella term covering multiple different pathways and mechanisms for cellular entry, is the principal route of entry for most delivery systems into cells (Jones et al., 2003; Kazmierczak et al., 2020). In this regard, charge-based interactions at the plasma membrane, while not the exclusive mode of interaction, often play a significant role in the initial stages of endocytosis, with either beneficial or detrimental implications for the cellular uptake of the delivery vehicle (Harush-Frenkel et al., 2008; Vedadghavami et al., 2020; Gyanani and Goswami, 2023; Spleis et al., 2023).

On one hand, the surface charge on the delivery vehicle can facilitate endocytosis by inducing local deformations in the membrane, causing the membrane to bend or wrap around it (Harush-Frenkel et al., 2008). Such deformations can promote the formation of membrane invaginations that are characteristic of endocytosis. In addition, these interactions could promote other types of chemical interactions, or assist in binding to specific receptors on the cell membrane. On the other hand, surface charge-bearing delivery vehicles and cell-penetrating peptides have the ability to destabilize cell membranes through electrostatic interactions (Thoren et al., 2005; Herce and Garcia, 2007; Rehman et al., 2013). Such interactions can induce changes in

lipid organization and fluidity, as well as the formation of transient nanoparticle-induced pores (Karal et al., 2015). Moreover, the disruptive effects of cationic nanoparticles on the cell membrane can trigger cellular responses, such as membrane repair mechanisms and changes in membrane protein activity (Stewart et al., 2018). These cellular responses could, in turn, impact cellular uptake processes and intracellular signaling pathways. Gaining insights into these interactions can guide the design and optimization of delivery systems for enhanced therapeutic efficacy.

In our most recent work, we discovered that HeLa and HepG2 cells internalized simple coacervates—comprised of a single peptide type—mainly through a cholesterol-dependent, non-canonical cell entry pathway involving cytoskeleton rearrangement and filipodia-like protrusions that capture the coacervates (Shebanova et al., 2022). However, to enable live cell imaging, the study employed enhanced green fluorescent protein (EGFP) as a client molecule, which is spatially distributed both in the interior and at the corona of peptide coacervates. In general, client molecules located near the outside surface of coacervates could potentially alter the overall surface charge (Welsh et al., 2022), form layered droplets (Boeynaems et al., 2019; Latham and Zhang, 2022) and affect interfacial tension (Wang et al., 2023) thereby influencing coacervate interaction with lipid membranes and cellular uptake in ways that we still do not understand. Whether these interfacial interactions mediated by client molecules significantly influence cellular uptake remained unexplored in our previous work.

In this study, we employ quartz crystal microbalance with dissipation monitoring (QCM-D), neutron reflectometry (NR) and atomistic molecular dynamic (MD) simulations to investigate peptide coacervate interactions with model membranes, in the absence of client molecules. The aforementioned techniques enable direct monitoring of coacervate-membrane interactions without the potential influence of fluorescently-labelled cargos or other types of client molecules. QCM-D and NR are complementary surface sensitive techniques, offering insights into both the overall adsorption processes occurring at the model membrane surface and detailed structural information about the membrane, including changes in composition of the lipid bilayer tail region, due to peptide incorporation or solvent penetration (Clifton et al., 2020). The nature of the interaction is verified by MD simulations, which provide a complementary picture to NR measurements.

2 Materials and methods

2.1 Materials

All peptides were purchased as lyophilized powder and certified >95% purity from GL Biochem (Shanghai) Ltd., China. Monobasic sodium phosphate (NaH_2PO_4), dibasic sodium phosphate (Na_2HPO_4), tribasic sodium phosphate (Na_3PO_4), sodium chloride (NaCl), Corning® black 384 transparent-bottom plates were purchased from Sigma-Aldrich (Singapore). Deuterated phospholipids and deuterated cholesterol were synthesized by ANSTO's National Deuteration Facility. Isopropyl alcohol, cholesterol and non-deuterated phospholipids used in QCM-D and SLB experiments were purchased from Sigma Aldrich (Singapore), QCM-D sensors were acquired from Biolin Scientific

AB (Gothenburg, Sweden). Silicon wafers for NR were purchased from El-Cat Inc. (NJ, United States).

2.2 Turbidity measurements for peptide concentration and pH profile

Stock solutions of HB*pep* peptide were prepared by solubilizing the lyophilized peptide directly in 10 mM acetic acid to achieve a final peptide concentration of 10 mg/mL. At this low pH (~3), the peptides remain largely monomeric and do not coacervate. Sodium phosphate buffer solutions (10 mM, 154 mM NaCl final concentration) with pH ranging between 2–11 were prepared by mixing appropriate volumes of NaH₂PO₄, Na₂HPO₄, and Na₃PO₄ stock solutions to achieve the desired pH, which were later confirmed using a pH meter (Mettler Toledo, Singapore) before and after the addition of peptide stock solutions. For determining the concentration range within which HB*pep* coacervate, 11 different samples were prepared in a 38-well transparent-bottom microtiter plate by diluting the peptide stock solution into sodium phosphate buffer (pH 7.4) such that the final peptide concentration varied between 0 and 1 mg/mL in 0.1 mg/mL increments and a final volume of 100 μ L. The volume of 10 mM acetic acid was kept constant in all the above samples. Immediately after the addition of the peptide, the absorbance of the samples were collected between 400 and 800 nm using a Tecan Spark (Männedorf, Switzerland) multimode plate reader. The mean of the absorbance values at 600 nm (A_{600}) for each sample, collected from three separate experiments, was plotted against the corresponding peptide concentration and fitted to a dose response curve using OriginPro 2021. Error bars indicate standard error of the mean. For characterizing the pH range within which HB*pep* coacervate, samples were prepared in a 38-well transparent-bottom microtiter plates by diluting the peptide stock solution into sodium phosphate buffer (10 mM, 154 mM NaCl) of varying pH such that the final pH of the sample varied between 2–11 in small increments and a final volume of 100 μ L. Absorbance of the samples was collected and the data plotted as described above.

2.3 Dynamic light scattering (DLS) measurements

All DLS measurements were carried out in a Malvern Zetasizer Nano ZS (Malvern Panalytical Ltd., Singapore). HB*pep* coacervates were prepared in a quartz cuvette (10 mm pathlength) by diluting the peptide stock solution that was previously dissolved in 10 mM acetic acid, into sodium phosphate buffer (pH 6, 7.4 or 8) such that the final peptide concentration was 0.1, 0.25, 0.5 or 1 mg/mL. DLS measurements were conducted at a 173° detection angle for 60 min at a fixed temperature of 25°C. Data was plotted using OriginPro 2021. Experiments were done in duplicates.

2.4 Differential interference contrast (DIC) microscopy

About 20 μ L of the peptide solution of various (0.1–1 mg/mL) concentrations prepared in sodium phosphate buffer (10 mM,

154 mM NaCl, pH 7.4) was pipetted on to the cover glass of a MatTek dish (cover glass No. 1.5) and the sample imaged using a Carl Zeiss Axio Observer Z1–Inverted Microscope fitted with a motorized stage and an EC Plan-Neofluar 63x/1.25 oil, FWD 0.1 mm, CG 0.17 mm (DIC) objective. All images were collected using an AxioCam MRm CCD camera, 1,388 \times 1,040 pixels, 6.45 μ m/pixel. All images were acquired using Zen 2 (blue) software and processed using ImageJ2 (version 2.3.0/1.53f). Experiments were done in duplicates.

2.5 Deuterated lipids

2.5.1 DOPG-d₆₆ (94 \pm 2% D)

We report here the production of sub-gram quantities of tail deuterated 1,2-dioleoyl-d₆₆-*sn*-glycero-3-phospho-(1'-*sn*-glycerol) (DOPG-d₆₆) and its structural characterization. Oleic acid-d₃₃, a precursor for the synthesis, was produced using our previously reported methods (Darwish et al., 2013). The primary and secondary hydroxyl groups of 3-benzoyloxy-*sn*-glycerol (at *sn*-1 and *sn*-2) were esterified using deuterated oleic acid-d₃₃ in the presence of dicyclohexylcarbodiimide (DCC) and a catalytic amount of 4-dimethylaminopyridine (DMAP). The benzyl group was removed using boron trichloride to afford 1,2-dioleoyl-d₆₆-*sn*-glycerol. The free alcohol was phosphorylated with phosphorus oxychloride, to give the corresponding 1,2-diacyl phosphatidic dichloride, which was used in the next step without further purification. Coupling of the phosphatidic dichloride with 1,2-isopropylidene-*sn*-glycerol in the presence of the anhydrous pyridine afforded acetonide protected DOPG-d₆₆. The protecting group was cleaved under mild acidic conditions to give DOPG-d₆₆ as colourless waxy solid.

2.5.2 POPC-d₆₄ (94 \pm 2% D)

1-Palmitoyl-d₃₁-2-oleoyl-d₃₃-glycero-3-phosphocholine (POPC-d₆₄) was produced using previously reported methods for the synthesis of mixed acyl glycerophospholipids (Moir et al., 2022) from palmitic acid-d₃₁ and oleic acid-d₃₃ (Darwish et al., 2013).

2.5.3 Cholesterol-d₄₅ (80 \pm 2% D)

Deuterated cholesterol (average 80% D as determined by mass spectrometry) was produced using previously reported methods (Sebastiani et al., 2021; Recsei et al., 2023) (ca. 90% D₂O in the growth medium).

2.6 Quartz crystal microbalance with dissipation monitoring (QCM-D)

Measurements were performed using a Q-SENSE E4 system (Q-Sense, Sweden) connected to an Ismatec peristaltic pump model ISM596D. The 50 nm SiO₂ coated Au sensors were cleaned in 2 v/v % Hellmanex under bath sonication for 10 min, followed by extensive rinsing with MilliQ water and ethanol. The sensors were dried under N₂ flow and subjected to oxygen plasma cleaning for 2 min in a Harrick plasma cleaner (Model No. PDC-002, Harrick Plasma Inc. United States) fitted with a gas flow mixer (PLASMAFLO PDC-FMG, Harrick Plasma Inc. United States) for

controlling oxygen flow rate. A lipid vesicle suspension was prepared at 0.2 mg/mL in MilliQ water (hydrodynamic diameter smaller than 50 nm as confirmed by DLS, prepared by tip sonication in H₂O). The composition of the lipid vesicles was 1-palmitoyl-2-oleoyl-sn-glycero-3-phosphocholine (POPC), 1-palmitoyl-2-oleoyl-sn-glycero-3-[phospho-rac-(1-glycerol)] (POPG) and cholesterol (POPC:POPG:Cholesterol) at a 7:1:2 molar ratio. This composition was chosen to represent the overall charge of mammalian cells (Virtanen et al., 1998). The lipid films were prepared by mixing appropriate amounts of lipids from chloroform stocks and gently evaporating the solvent under N₂ flow and rotation, and finally subjecting to vacuum for at least 1 h.

Prior to experiments, the fundamental frequency (5 MHz) and five overtones (3rd, 5th, 7th, 9th, and 11th) were found and recorded in MilliQ water. The flow rate was set to 0.1 mL/min, and the temperature was controlled as specified. A baseline was obtained in MilliQ water prior to injection of the vesicle solution (the lipid vesicle suspension was mixed in a 1:1 volume ratio with 4 mM CaCl₂ just prior injection into the solid-liquid cells). A constant flow of vesicles was maintained until stable signals were obtained before rinsing with excess MilliQ water. The supported lipid bilayers (SLBs) gave signals of typically -24–25 Hz and 0.2–0.4 ppm in dissipation, in line with previous results (Clifton et al., 2020). Rinsing with 10 mM phosphate buffer enriched with 154 mM NaCl at pH 7.4 or pH 6 was performed. HBpep coacervates (0.25 mg/mL) were formed and incubated for 5 min prior to addition to the SLBs. QCM-D measurements were performed in duplicates. For measurements in which coacervate sedimentation was avoided, the instrument was set upside down as previously done for other systems (Lind et al., 2019).

2.7 Supported lipid bilayers on glass

The supported lipid bilayers (SLBs) were prepared on a glass coverslip in a microfluidic chip by the solvent-assisted method reported by Ferhan et al. (2019) with slight modifications. To clean and hydrophilize the glass surface, the coverslip was soaked overnight in a 1 v/v% solution of Hellmanex, washed with MilliQ water and ethanol, dried in an oven then subjected to oxygen plasma cleaning for 2 min in a Harrick plasma cleaner (Model No. PDC-002, Harrick Plasma Inc. United States) fitted with a gas flow mixer (PLASMAFLO PDC-FMG, Harrick Plasma Inc. United States) for controlling oxygen flow rate. Immediately after this, the coverslip was attached to a multichannel microfluidic chip (Ibidi sticky-Slide VI0.4), and all microfluidic channels were filled with MilliQ water. The chip has six microfluidic channels, each with a length of 17 mm, a width of 3.8 mm and a height of 400 μ m.

To prepare the lipid solution, POPC, cholesterol and two fluorescent markers, namely, 18:1 Liss Rhod PE and 25-NBD cholesterol (that selectively mix with POPC and cholesterol, respectively), were solubilized in isopropanol, while POPG was solubilized in ethanol. Appropriate amounts of each of those five components were mixed and diluted in water:isopropanol with 1:1 volume ratio to create a 0.4 mg/mL POPC:POPG:Cholesterol solution with a 7:1:2 molar fraction. Liss Rhod PE and NBD cholesterol were used at a concentration of 3.4 μ g/mL and 1.8 μ g/mL, respectively.

To create a SLB, an Ismatec peristaltic pump model ISM596D was used. First, water:isopropanol with a 1:1 volume ratio was pumped for several minutes to ensure complete exchange of the MilliQ water that previously filled the channel. Then, the lipid solution was pumped for 10 min at 50 μ L/min, the flow was stopped for 5 min, and MilliQ water was pumped, also for 10 min at 50 μ L/min. The resulting SLB homogeneously and completely covered the glass substrate in the microfluidic channel.

The coacervate experiment was then carried out just as in the QCM-D, the only difference being the reduced flow rate of 50 μ L/min. Images were collected as the experiment was ongoing in a Carl Zeiss Axio Observer Z1 inverted fluorescence microscope fitted with a motorized stage and a Plan-Apochromat 63x/1.40 oil DIC, FWD 0.19 mm, CG 0.17 objective. All images were acquired using a Carl Zeiss AxioCam 503 Mono camera, 1,936 \times 1,460 pixels, 72 nm/pixel using Zen 2 (blue) software and processed using ImageJ2 (version 2.9.0/1.54f).

2.8 Neutron reflection (NR)

Experiments were performed on the reflectometer SPATZ at the Australian Nuclear Science and Technology Organisation (ANSTO) using a setup for solid/liquid interfaces (Le Brun et al., 2023). The momentum transfer range and momentum transfer (Q) resolution used was $0.011 \text{ \AA}^{-1} < Q < 0.273 \text{ \AA}^{-1}$ and $\Delta Q/Q = 5.8\%$, respectively. The instrument uses the time-of-flight principle and a disc chopper pairing of discs 1 and 2 set 480 mm apart running at 25 Hz was used ($2.5 \text{ \AA} < \lambda < 20 \text{ \AA}$). Collimation slits used were set to 2.66 mm and 0.75 mm for an angle of incidence of 0.85° and 10.94 mm and 3.09 mm for 3.5° , providing an illuminated footprint of 55 mm along the beam. Data was reduced with the *refnx* software package (Nelson and Prescott, 2019) where the time-of-flight is converted to wavelength which is used to calculate Q, accounts for detector efficiency, re-bins the data to instrument resolution, subtracts the background, stitches the data from the two angles of incidence together at the appropriate overlap region, and scales the data so that the reflectivity at the critical edge is equal to 1.

The silicon blocks (100) of 100 mm diameter and 10 mm thickness and O-rings (TEFLON of 100 μ m thickness) were cleaned in the following series of solvents: 2% Hellmanex for at least 1 h followed by extensive rinsing with MilliQ water. Before assembling the cells, the blocks were dried with a flow of nitrogen gas and exposed for 30 min to ozone to finally be assembled in dry conditions. During the assembling, the substrate was sealed with the polished surface in contact with the liquid using a thin Teflon O-ring, and the cells were connected to an HPLC pump to allow the exchange of solvent with D₂O, H₂O, and CMSi (38:62 v/v D₂O: H₂O).

The solid/liquid cells were pre-equilibrated to 25°C using a circulating water bath and the surfaces were characterized in H₂O and D₂O to determine the roughness and the thickness of the silicon oxide layer. Then, the SLBs were formed using vesicle fusion as described in Section 2.6, and characterized in three isotropic contrasts composed of H₂O based-, D₂O based, and CMSi-based (38:62 D₂O: H₂O (v/v)) buffer. The composition of the lipid vesicles was POPC-d₆₄:DOPG-d₆₆:Cholesterol-d₄₅ at a 7:1:2 molar ratio. Here, d₆₄:DOPG was used since synthesis of tail

deuterated POPG has not been reported or performed to the date of publication. The lipid films were prepared by mixing appropriate amounts of lipids from chloroform stocks and gently evaporating the solvent under N_2 flow and rotation, and finally subjecting to vacuum for at least 1 h.

The SLBs were fitted using a 4-layer model constituted by the oxide layer and three layers that correspond to the heads-tails-heads of the lipid membrane. During the data fitting, the lipid bilayer was constrained to be symmetric, that is, the coverage, the thickness, and the scattering length density (SLD) of the heads were the same for both leaflets. Additionally, the roughness was constrained to be the same across the whole bilayer. The HB pep peptide was slowly introduced via a syringe at concentrations of 0.25 mg/mL in the corresponding buffer, upon re-equilibration of ~ 5 min. After roughly 1 h 20 min of incubation, the samples were rinsed with H_2O based buffer and re-characterized in all three contrasts by using 1/10 of the final peptide concentration. Data was collected prior and after buffer exchange in H_2O based buffer and no changes in reflectivity were observed.

To fit the data in the three isotropic contrasts after protein incubation and rinsing, the head-group thickness and coverage was kept constant but the thickness and SLD of the tails were allowed to vary. A layer of protein was added on top of the SLB. The experiments were performed only once due to the restricted availability of beam time. Data fitting was performed using the MOTOFIT package (Nelson, 2006) and to determine the errors of the fits, a Monte Carlo error analysis was performed using genetic optimization.

2.9 Peptide modeling

The structure of the peptide was built using the PEP-FOLD4 server (Rey et al., 2023; Tufféry and Derreumaux, 2023), which has the advantage over other available servers that it embeds a Debye-Hückel formalism to treat pH conditions and salt concentration variations. Peptide conformations are pH- and salt concentration-dependent, and thus, two systems were considered to mimic neutral and acidic conditions. The main input was the sequence in FASTA format (GHGVY GHGVY GHGPY GHGPY GHGLYW). The forward-backtrack sampling algorithm was selected to sample the structural alphabet profile and the number of models generated was 100. Default parameters related to the Monte Carlo protocol (10,000 steps) and the pseudo-random generator seed were adopted to generate the 3D models. The Debye-Hückel contribution was switched on, and the pH was specified as well as an ionic strength of 154 mM NaCl to match the experimental conditions. The use of the zwitterionic forms of the peptides and the default pKa values of 6 for His residues were used.

2.10 Molecular dynamics simulations

A membrane containing POPC, POPG and cholesterol molecules in a proportion 70:10:20 (POPC:POPG:Cholesterol) was generated using CHARMM-GUI Membrane Builder (Jo et al., 2008; Jo et al., 2009; Wu et al., 2014). The membrane contained 210 POPC molecules, 30 POPG molecules and

60 cholesterol molecules in the mixed bilayer. Subsequently, the multicomponent assembler (Kern et al., 2023) of CHARMM-GUI facilitated to build two all-atom molecular models at neutral or acidic pH, using the first 15 peptides rendered by PEP-FOLD4 (the more favorable energetically), and the previously built complex membrane. The combined system (bilayer and peptides) was then solvated to produce a rectangular box of dimensions $(130 \times 130 \times 100) \text{ \AA}^3$. Ions were added resulting in a final concentration of 154 mM NaCl (Humphrey et al., 1996). The final system contained over 168,000 atoms. CHARMM22 (Li et al., 2005) parameters (with CMAP correction) were used for the peptides, CHARMM36 for lipids (Klauda et al., 2010), standard parameters for ions (Noskov et al., 2004) and the TIP3P (Jorgensen et al., 1983) model for water. NAMD 3.0alpha GPU (Phillips et al., 2005) and Gromacs 2023 (Berendsen et al., 1995) were employed to calculate the dynamics of the systems throughout (Phillips et al., 2005). Although we started using NAMD, due to performance, we switched to Gromacs. One simulation of the neutral system and one of the charged system were obtained with NAMD, and five replicas per pH were obtained with Gromacs. The total cumulative production time is $12 \times 0.2 \text{ \mu s}$ (2.4 \mu s).

Initially, 10,000 steps of minimization were performed to remove steric clashes, followed by the progressive removal of constraints at 500 ps intervals to allow for gradual equilibration of the system. Constraints were released in the following order: i) bulk water and lipid tails; ii) lipid head groups; iii) peptide side chains. Unrestrained dynamics was then undertaken in the NPT ensemble. The Particle Mesh Ewald method was used for the treatment of full-system periodic electrostatic interactions; interactions were evaluated every second timestep with a value of 1 \AA to determine grid spacing (Darden et al., 1993). Electrostatic and van der Waals forces were calculated every timestep and up to a cutoff distance of 12 \AA . A switching distance of 10 \AA was chosen to smoothly truncate the non-bonded interactions. Only atoms in a Verlet pair list within a cutoff distance of 13.5 \AA were considered, with the list reassigned of reassigned every 20 steps (Verlet, 1967). The SETTLE algorithm was used to constrain all bonds involving hydrogen atoms to allow the use of a 2 fs timestep (Miyamoto and Kollman, 1992). The Nose-Hoover-Langevin piston method was employed to control the pressure with a 200 fs period, 50 fs damping constant and a desired value of 1 atmosphere (Martyna et al., 1994; Feller et al., 1995). The system was coupled to a Nose-Hoover thermostat to sustain a temperature of 298 K throughout.

3 Results and discussion

3.1 Identifying optimal conditions for peptide-coacervate and model cell membrane interactions studies

HB pep is a 26-residue peptide inspired by the Histidine-rich beak proteins (HBPs) of the Humboldt squid (Tan et al., 2015). The peptide sequence (GHGVY GHGVY GHGPY GHGPY GHGLY W) consists of five GHGxY repeats, [where x is either valine (V), proline (P) or leucine (L)], and a C-terminal tryptophan residue, both of which are important drivers of phase separation (Figure 1A) (Wang et al., 2018; Gabryelczyk et al., 2019). HB pep phase separates under

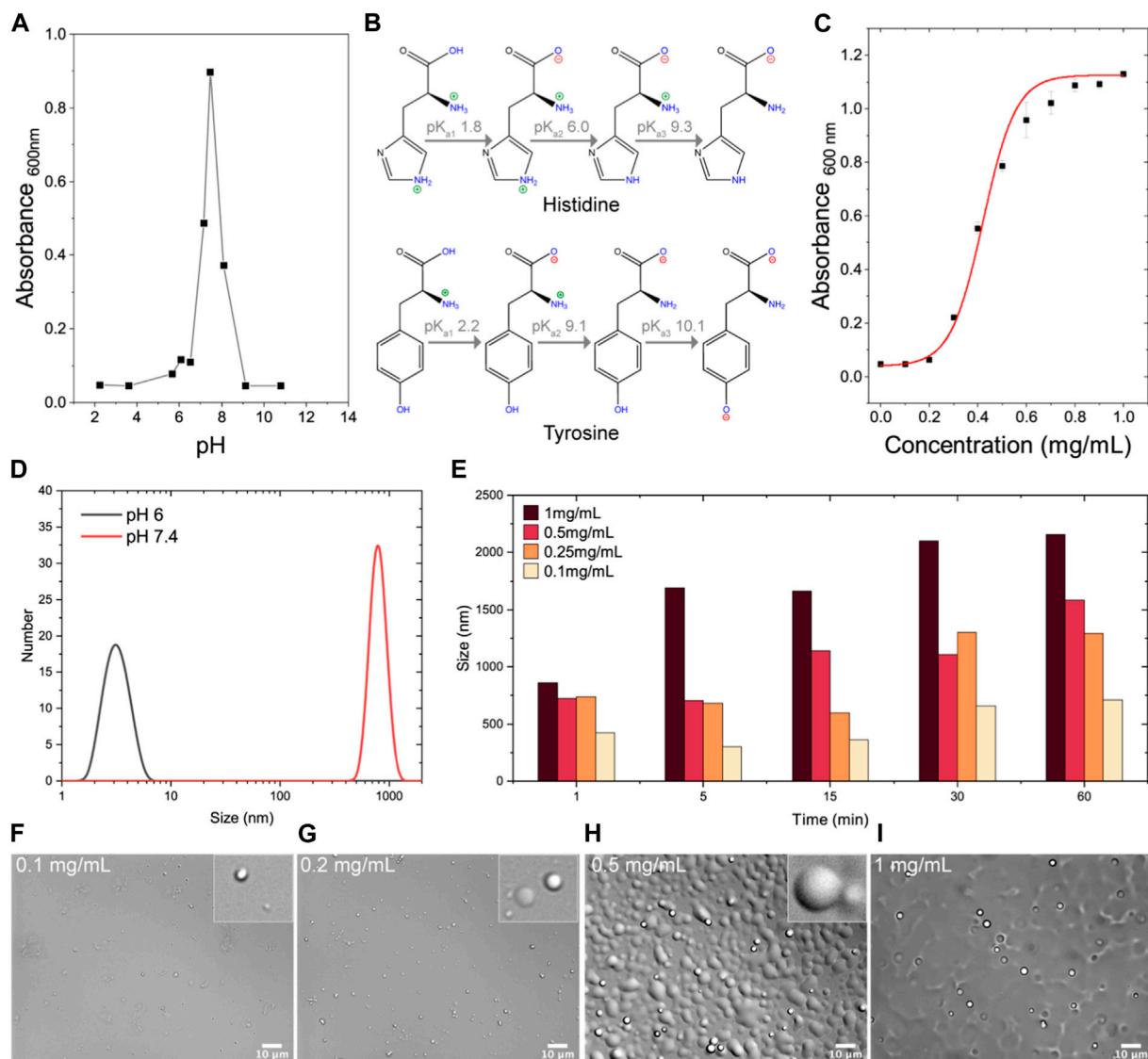


FIGURE 1

Characterization of HBpep to determine optimal experimental conditions for HBpep-membrane interactions studies. (A) Turbidity measurements of HBpep (Seq: GHGVY GHGVY GHGPY GHGPY GHGLYW) within a pH range of 2–11 indicate optimal coacervation at physiological pH. (B) Different pKa values of histidine (top) and tyrosine (bottom) are illustrated to highlight that when the pH is below 6 or above 9, HBpep is unable to coacervate due to the positive and negative charge contributions from the histidine and tyrosine side-chains, respectively, resulting in charge-charge repulsion at these pH ranges. (C) Turbidity measurements of HBpep samples within a concentration range of 0.1–1 mg/mL when prepared at pH 7.4 indicate a concentration-dependent increase in turbidity. (D) DLS measurements of HBpep samples at pH 6 and 7.4 suggest an oligomeric state at pH 6 and coacervates at pH 7.4. (E) DLS measurements of HBpep coacervates prepared at pH 7.4 and at four different concentrations when monitored up to 60 min indicate particle size of ~1 μm diameter whose size gradually increased with increasing concentration. (F–I) DIC imaging of the HBpep samples confirm coacervation and its size-correlation with increasing HBpep concentration. The illustration for histidine pKa in C has been recreated with minor modifications from Saurabh et al. (2022), licensed CC-BY-4.0.

physiological conditions into μm-sized coacervate microdroplets that exhibit an extremely high efficiency (>99%) to recruit a wide variety of therapeutics within their dense phase (Lim et al., 2018; Lim et al., 2020). Consequently, HBpep and its variant were developed into an intracellular delivery system capable of delivering a wide variety of therapeutics into different cell types *in vitro* with little to no cytotoxicity (Sun et al., 2022).

In order to identify the optimal experimental conditions for investigating HBpep-coacervate and model cell membrane interactions, turbidity measurements were carried out with

HBpep at different conditions of pH and concentrations (Figures 1A, C). In general, coacervation of phase-separating peptides and proteins can occur over a wide pH range and can be monitored by measuring sample turbidity (Supplementary Figure S1), coacervate size (Supplementary Figure S2), or both. However, turbidity measurements—the standard practice in the field—allow for the determination of “phase-separation (a.k.a coacervation) propensity” when the coacervate size remains more or less similar across a pH range. Turbidity measurements of HBpep prepared in sodium phosphate buffers spanning a pH range of 2–11, indicated that the

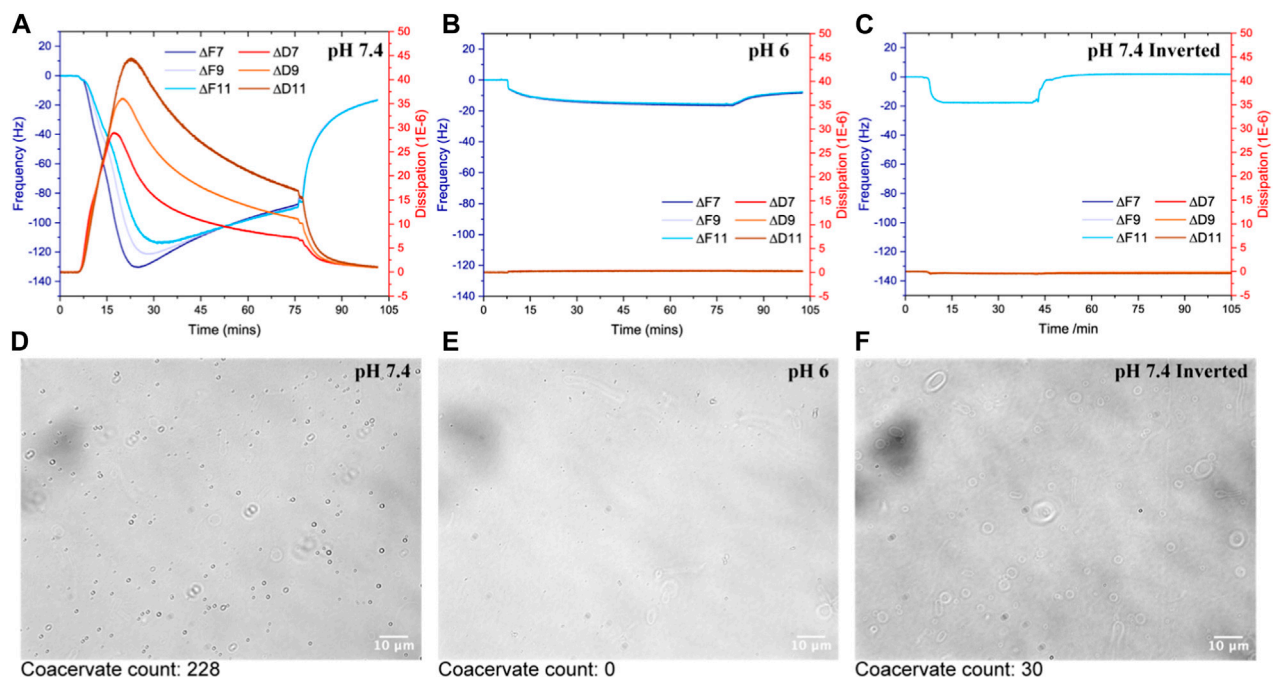


FIGURE 2

Interaction of HBpep on SLBs composed by POPC:POPG:Cholesterol at a 7:1:2 molar ratio in 10 mM phosphate buffer enriched with 154 mM NaCl at pH 6 (A) and pH 7.4 (B). The QCM-D signals (Frequency in Hz and dissipation in ppm) are given as a function of time. In panel (C), the E4 unit was flipped upside down to avoid sedimentation on the sensor surface. The flow was kept constant at 0.1 mL/min and all measurements were made at 25°C. (D–F) are DIC images of SLBs (POPC:POPG:Cholesterol at a 7:1:2 molar ratio) prepared using a solvent-assisted method on glass slides with experimental conditions kept consistent with those used in the QCM-D experiments depicted in (A–C).

highest turbidity was observed at pH 7.4 which is close to the peptide's theoretical pI of 7.96 (Figure 1A). In acidic conditions and at pH values above 9, HBpep displayed minimal turbidity indicating its inability to coacervate and likely remained monomeric or resulted in low-level oligomerization. This pH-dependent behavior is due to the positive charges arising from the five histidine side groups when the pH is below its pK_{a2} of 6 (Saurabh et al., 2022), and to the negative charges arising from the tyrosine side groups when the pH is above its pK_{a2} of ~10 (Figure 1B), which result in charge-charge repulsion at these pH ranges. Since HBpep is acetyl-capped at the N-terminus and amidated on the C-terminus, we do not expect any end terminal charge contribution.

Similarly, a concentration-dependent behavior was observed when HBpep stock solutions were diluted into a buffer maintained at pH 7.4 (Figure 1C). An increase in turbidity (OD_{600}) correlated with an increase in HBpep concentration, with a detection threshold at 0.2 mg/mL and a peak turbidity signal at 0.6 mg/mL, beyond which the signal plateaued. At pH 6, where the peptide carries a net positive charge, DLS measurements suggest an oligomeric state for the peptide at 1 mg/mL (the oligomeric formation was confirmed by SANS data, data not shown) (Figure 1D). At pH 7.4, HBpep coacervate droplet sizes varied from 400–800 nm (Figure 1D), with size being both time- and concentration-dependent (Figure 1E). Micrometer-sized droplets were observed within 5 min for peptides at a concentration of 1 mg/mL, whereas sub- μ m size particles were observed at a lower peptide concentration of 0.25 mg/mL (Figure 1D). Furthermore, μ m size droplets sedimented over time, and the coalescing property of the coacervates became more discernible at higher peptide concentrations

as seen from DIC microscopy images (Figures 1F–I). Based on the above results, a pH of 7.4 and 6 were chosen as the coacervating and non-coacervating pHs for the peptide, respectively. Since high peptide concentrations (>0.5 mg/mL) led to coacervate coalescence and a concomitant increase in droplet size, we determined 0.25 mg/mL as an appropriate peptide concentration to use for all further experiments as we expect the coacervate size to remain relatively stable under these conditions.

3.2 QCM-D

The interactions between HBpep coacervates and model cell membranes were followed via QCM-D on SLBs formed by vesicle fusion using vesicles composed by POPC:POPG:Cholesterol in a 7:1:2 molar ratio as a model of the charge in mammalian cell membranes (Virtanen et al., 1998). HBpep coacervates (0.25 mg/mL) were prepared and incubated for 5 min prior to addition to the SLBs. Analysis of the raw QCM-D data (Figures 2A, B) confirmed HBpep binding at pH 6, a condition where no significant coacervation occurs (Figures 1A, D). The observed QCM-D signal at acidic conditions closely resembles that of cell penetrating peptides such as penetratin (Hedegaard et al., 2018). Upon rinsing with buffer, partial desorption of HBpep occurred, which is also consistent with data observed for cell penetrating peptides (Hedegaard et al., 2018) (Figure 2B). In contrast, at pH 7.4, substantial adsorption of HBpep coacervates on the SLB coated SiO_2 sensor was observed (Figure 2A). The resulting QCM-D signal resembles the adsorption of lipid vesicles on SiO_2 and their

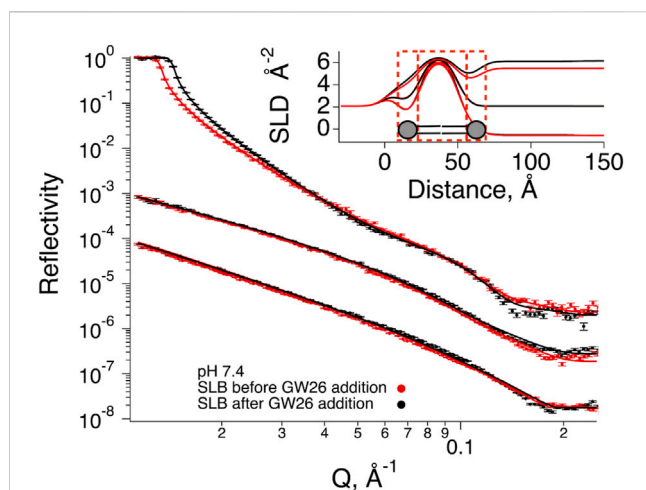


FIGURE 3
Neutron Reflection data for SLBs composed by POPC- d_{64} , DOPG- d_{66} , cholesterol- d_{45} (7:1:2 mol%) before (red) and after (black) exposure to HBpep at pH 7.4 buffer. The experimental data is given by symbols. Best fits (parameters in Table 1) are represented by solid lines. HBpep coacervates were prepared 5 min prior to the addition to the SLBs and incubated for 1 h 20 min. Rinsing with a peptide solution containing 1/10 of the original concentration at different contrasts was then performed to collect the three data sets shown in the figure. The cmSi and H₂O based data was offset for clarity. The inset gives SLD profiles for the best fit to the data.

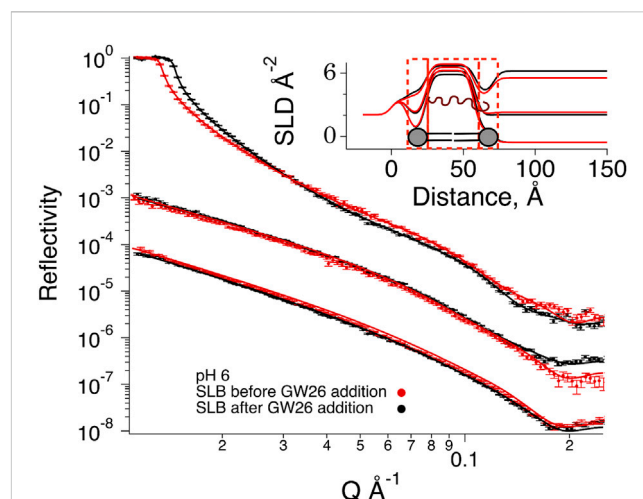


FIGURE 4
Neutron Reflection data for SLBs composed by POPC- d_{64} , DOPG- d_{66} , cholesterol- d_{45} (7:1:2 mol%) before (red) and after (black) exposure to HBpep at pH 6 buffer. The experimental data is given by symbols. Best fits (parameters in Table 1) are represented by solid lines. HBpep coacervates were prepared 5 min prior to the addition to the SLBs and incubated for 1 h 20 min. Rinsing with a peptide solution containing 1/10 of the original concentration at different contrasts was then performed to collect the three data sets shown in the figure. The cmSi and H₂O based data was offset for clarity. The inset gives SLD profiles for the best fit to the data.

eventual rupture, as evidenced by the sharp decrease in frequency and the increase in dissipation with time, followed by an inversion of the signals (increase in frequency and decrease in dissipation). Thus, it is likely that some of the μ m-sized coacervates spread out on the SLB-coated sensor, mirroring what was observed by microscopy on glass slides (Figures 1H, I). We note that most of the adsorbed coacervates could be removed upon rinsing with buffer at pH 7.4 suggesting that the adsorption was largely reversible and could be due to simple droplet sedimentation.

In order to decouple the effect of molecular adsorption on the SLB and sedimentation, the QCM-D E4 unit was flipped upside down and the experiment at pH 7.4 was repeated (Figure 2C). In this case, a signal mirroring that measured at pH 6 was detected with full reversibility upon rinsing with a solution containing 1/10 of the original coacervate solution (i.e., 0.025 mg/mL) followed by excess buffer. Taken together, both peptide and coacervate adsorption takes place regardless of pH, but the adsorption is fully reversible only at neutral pH. The latter suggests that no major rearrangement of the lipid bilayer structure takes place due to peptide adsorption at pH 7.4. This was independently verified with SLBs prepared using a solvent-assisted method on glass slides that were imaged using DIC microscopy (Figures 2D–F). The experimental conditions were kept consistent with those used in the QCM-D experiments depicted in Figures 2A–C.

The DIC images reveal that at pH 7.4 in the upward position of the chamber (Figure 2D), more μ m-sized coacervates adsorbed to the SLB compared to when the microfluidic chamber was set-up upside down (Figure 2F). At pH 6, no coacervates were observed (Figure 2E) as expected based on turbidity and DLS measurements (Figures 1A, D). A manual count (Supplementary Figures S3, S4) of the number of coacervates in each of the representative DIC images in Figures 2D–F revealed the count to be 228 for pH 7.4, 0 for pH 6 and

30 for upside down at pH 7.4. Since at pH 6 HBpep does not significantly coacervate into large droplets, the black dots observed in Figure 2E do not correspond to coacervates and are most likely pH dependent salt crystallization, or low-level oligomerization below the resolution limit of the microscope objective used.

3.3 Neutron reflectometry

Neutron reflection data were collected at three isotropic contrasts before and after exposure to 0.25 mg/mL HBpep at pH 6 (Figure 3) or pH 7.4 (Figure 4), and the data were fitted assuming a symmetric lipid bilayer structure (lipid heads–lipid tails–lipid heads). The thickness of the core lipid bilayer, the head groups and the roughness at pHs 6 and 7.4 are summarized in Table 1. The coverage was in both cases above 90%. The values in Table 1 compare well to those reported by Waldie et al. (Waldie et al., 2018; Waldie et al., 2019) for which 30.9–33.5 Å thick core was measured for 10–40 mol% cholesterol in various phosphatidylcholine SLBs including POPC. The head group region was found to be 7–8 Å thick for PC-cholesterol (Waldie et al., 2018; Waldie et al., 2019). The larger headgroups [12.9 and 13.3 (± 0.3) Å at pH 6 and pH 7.4, respectively] and headgroup hydration is thus expected from the presence of charged phosphatidylglycerol groups (Le Brun et al., 2014).

At pH 7.4 (where HBpep coacervation takes place), there were minimal changes in reflectivity (Figure 4). The small changes observed at low Q are simply due to small differences in the D₂O content in the buffer, typical when there is incomplete exchange upon flushing with buffer. There was though a very small increase in reflectivity mainly observable for the H₂O based

TABLE 1 Parameters for the best fits shown in Figures 3, 4.

	SLD (10^{-6} \AA^2)	Thickness (\AA)	Coverage (%)	Roughness (\AA)	Mean molecular area (\AA^2)
pH 7,4					
SiO ₂		10.2 ± 0.3		7.0 ± 0.5	
Head	1.95 ^a	13.0 ± 0.2	46 ± 1	6.8 ± 0.4	53 ± 2
Tail	6.4 ± 0.1	29.0 ± 0.2	93 ± 1	6.8 ± 0.4	63 ± 1
Head	1.95 ^a	13.0 ± 0.2	46 ± 1	6.8 ± 0.4	53 ± 2
After HB _{pep} addition					
Head	1.95 ^a	13 ^a	39 ± 2	6.8 ^a	63 ± 2
Tail	6.4 ^a	29 ^a	100 ± 1	6.8 ^a	59 ± 1
Head	1.95 ^a	13 ^a	39 ± 2	6.8 ^a	63 ± 2
Protein slab		69 ± 4	1.3 ± 0.2	6.8 ^a	
pH 6					
SiO ₂		11.2 ± 0.2		3.7 ± 0.4	
Head	1.95 ^a	12.5 ± 0.1	46 ± 1	5.4 ± 0.3	54 ± 2
Tail	7.02 ± 0.04	33.3 ± 0.2	90 ± 1	5.4 ± 0.3	58 ± 1
Head	1.95 ^a	12.5 ± 0.1	46 ± 1	5.4 ± 0.3	54 ± 2
After HB _{pep} addition					
Head	1.95 ^a	10.7 ± 0.1	46 ± 1	3.8	65 ± 2
Tail	6.78 ± 0.03	34.4 ± 0.3	96 ± 1	3.8	52 ± 1
Head	1.95 ^a	10.7 ± 0.1	46 ± 1	3.8	65 ± 2
Protein slab		58 ± 5	2.6 ± 0.5	3.8	

^aFixed parameters.
Heads were co-fitted as symmetric across contrasts, roughness was co-fitted across layers and contrasts, tail SLD, was co-fitted across contrasts. The SLD, for D₂O corresponds to 85%–89% and 0.2% to 0.9% D₂O before and after peptide addition as determined by the position of the critical scattering angle.

buffer. These changes can be interpreted as an increase in the coverage or scattering length density (SLD) of the SLB. Indeed, upon co-refinement of the data using a four-layer model (lipid heads–tails–lipid heads–HB_{pep}), a suitable fit was obtained assuming a constant layer thickness of the SLB but allowing for increase in the coverage of 7%. There was neither any significant peptide adsorption on top of the SLB, nor any significant drop in the SLD of the lipid bilayer region. During SLB formation by vesicle fusion, it is common that a small fraction of vesicles remain bound, these are hardly seen by NR (Lind et al., 2014). Together, these values suggest the rupture of a few vesicles that might have remained bound to the SLB after the rinsing step, and that there was neither significant peptide binding nor integration in the lipid bilayer, consistent with the QCM-D results (Figure 2C).

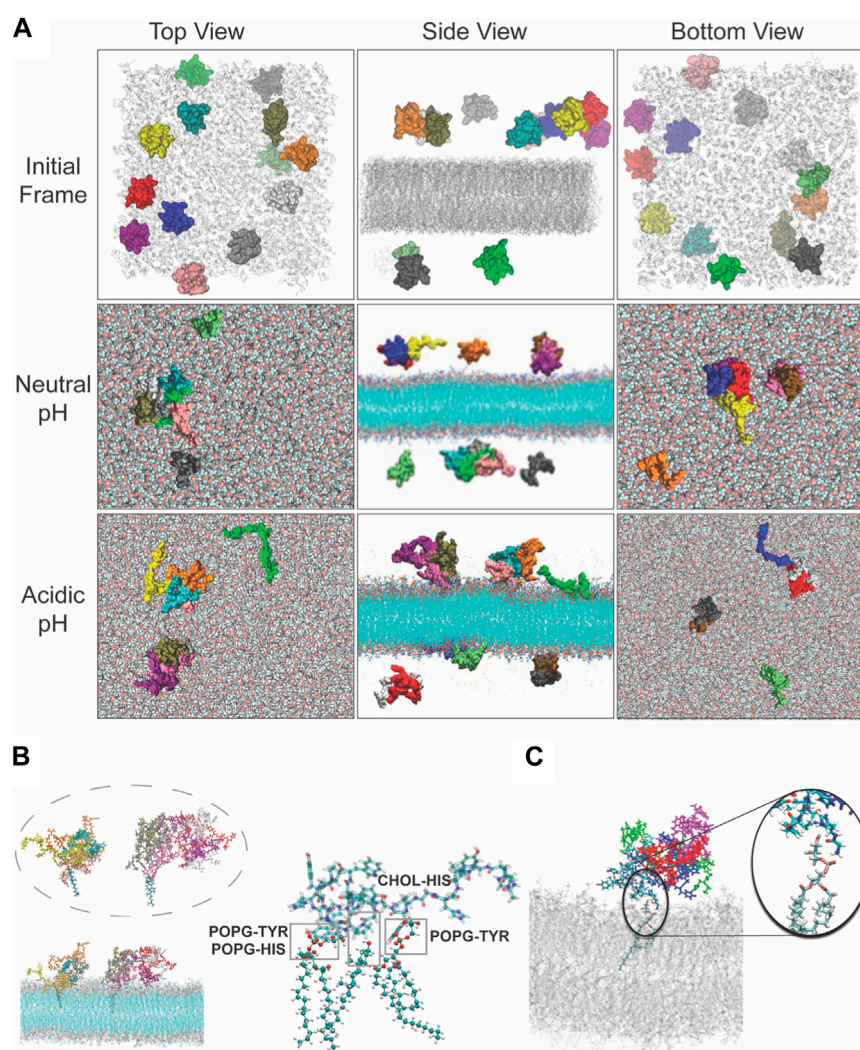
At pH 6, where HB_{pep} remains mostly in the monomeric or oligomeric state (Figure 1E), significant changes in reflectivity were noticed at all contrasts besides the small changes observed at low Q for D₂O-based buffer due to incomplete exchange upon flushing with buffer. In particular, the cross over in the D₂O based buffer contrast suggest a change in the SLB structure/composition (Lind T. K. et al., 2015). Indeed, upon co-refinement of the data using a four-layer model (lipid heads–tails–lipid heads–HB_{pep}), a suitable fit was obtained with a 1.4 Å increase in the lipid tail layer thicknesses, a

lowering of $0.24 \times 10^{-6} \text{ \AA}^{-2}$ in the lipid tail layer SLD, and a coverage increase by 6%. Together, these values point towards the integration of peptide in the layer. This corresponds to 5 % of the layer being composed of peptide and 95% of lipids. There was some peptide adsorption on top of the SLB, although minimal.

NR indicates that at conditions in which the peptide is cationic and does not form coacervates (i.e., at low pH), the peptide intercalates in the lipid bilayer, partially removing some lipids, a finding in agreement with observations for cationic peptides with antimicrobial capacity (Lind T. et al., 2015; Nielsen et al., 2019; Hedegaard et al., 2020). For neutral pH, where the peptide is largely uncharged and mainly present in the coacervate phase, minimal interaction was detected with the SLB. Instead, a slight increase in the coverage of the SLB was observed without affecting the lipid core SLD. This suggests that eventual non-fused lipid vesicles collapsed due to the presence of coacervates in the bulk phase.

3.4 MD simulations

Figures 5A–C presents comparative snapshots of the SLB before and after 200 ns of simulation at both neutral and acidic conditions. At neutral conditions, the HB_{peps} predominantly form aggregates

**FIGURE 5**

Interactions observed between the peptide and POPG or cholesterol during the molecular dynamics simulations under neutral and acidic conditions. **(A)** Top, side and bottom view of the model system at the beginning of the simulation where peptides were randomly placed at either side of the membrane in the solution. Peptides are shown in van der Waals representation and colored differently, and the lipid membrane is shown in grey. Top, middle and lower row give representative snapshot of the model under neutral or acidic conditions. Snapshot of the interactions observed between the peptide and POPG or cholesterol during the molecular dynamics simulations under **(B)** neutral and **(C)** acidic conditions (the middle structure highlights the interactions between residues and lipid headgroups under acidic conditions).

within the solution, consisting of clusters of 4–6 members, where they remain for the duration of the simulations. In acidic conditions, however, HBpeps display a distinct behavior: they land on the surface of the bilayer either as individual entities or as small aggregates comprised of 2, 3 or 4 peptides, subsequently penetrating into the membrane core. Note that oligomeric formation agrees well with the DLS data presented in Figure 1D at acidic pH. Even though larger aggregates are not observed at neutral pH, all peptides in the simulation box form aggregates while only a few do form oligomers at acidic pH. The primary interactions between the HBpeps and the bilayer is via His and the phosphate group of POPG or the aromatic ring of Tyr, Trp or His and the hydroxyl group of cholesterol, as depicted in Figure 5B. These observations indicate that charged lipids and cholesterol are crucial for facilitating the binding of HBpep to membranes, in agreement with findings from previous cell studies (Sun et al., 2023).

4 Conclusion

HBpep coacervates do not interact with the lipid membrane at neutral pH in the same manner as traditional cationic drug delivery systems or cell penetrating peptides. Our data indicate that at pH 6 HBpep does not coacervate but forms small oligomers with a positive net charge. In this case, the peptide is able to insert into the lipid bilayer of a model cell membrane as shown both by NR experiments and MD simulations. These interactions are both charge driven but also promoted by π -OH interactions with cholesterol. However, at physiological pH, where the peptide phase-separates into μ m or sub- μ m sized droplets, it does not strongly interact with the lipid membrane. This indicates that the cell entry mechanism of HBpep coacervates prior to cargo delivery in the cytoplasm differs from that of cell penetrating peptides or cationic drug delivery vehicles. On-going studies on the cellular

uptake mechanism of coacervates, investigated using electron microscopy and live cell imaging, suggest a non-canonical uptake pathway mediated by cholesterol and will be published in a separate article.

Data availability statement

The original contributions presented in the study are included in the article/[Supplementary Material](#), further inquiries can be directed to the corresponding authors.

Author contributions

SG: Data curation, Formal Analysis, Investigation, Supervision, Writing—original draft, Writing—review and editing. FF: Data curation, Formal Analysis, Investigation, Writing—review and editing. JSMT: Data curation, Formal Analysis, Writing—review and editing. CD: Data curation, Formal Analysis, Investigation, Writing—original draft, Writing—review and editing. SM: Data curation, Formal Analysis, Writing—review and editing. AL: Data curation, Formal Analysis, Resources, Writing—review and editing. NY: Methodology, Resources, Writing—review and editing. MM: Methodology, Resources, Writing—review and editing. RR: Methodology, Resources, Writing—review and editing. TD: Methodology, Resources, Writing—review and editing. AM: Conceptualization, Funding acquisition, Resources, Supervision, Writing—review and editing. MC: Conceptualization, Data curation, Formal Analysis, Investigation, Supervision, Writing—original draft, Writing—review and editing.

Funding

The author(s) declare financial support was received for the research, authorship, and/or publication of this article. This research was funded by the Ministry of Education (MOE), Singapore, through an Academic Research Fund (AcRF) Tier 3 grant (Grant No. MOE 2019-T3-1-012). The operations of the Spatz neutron beam instrument and the National Deuteration Facility are partly supported by the National Collaborative Research Infrastructure Strategy—an initiative of the Australian Government. This publication is part of project number PID2022-137440NB-I00, funded by MCIN/AEI/10.13039/501100011033/FEDER, UE. MC

References

- Behzadi, S., Serpooshan, V., Tao, W., Hamaly, M. A., Alkawareek, M. Y., Dreaden, E. C., et al. (2017). Cellular uptake of nanoparticles: journey inside the cell. *Chem. Soc. Rev.* 46 (14), 4218–4244. doi:10.1039/c6cs00636a
- Berendsen, H. J. C., Vanderspoel, D., and Vandrunen, R. (1995). Gromacs - a message-passing parallel molecular-dynamics implementation. *Comput. Phys. Commun.* 91 (1-3), 43–56. doi:10.1016/0010-4655(95)00042-e
- Bergeron-Sandoval, L. P., Kumar, S., Heris, H. K., Chang, C. L. A., Cornell, C. E., Keller, S. L., et al. (2021). Endocytic proteins with prion-like domains form viscoelastic condensates that enable membrane remodeling. *Proc. Natl. Acad. Sci. U. S. A.* 118 (50), e2113789118. doi:10.1073/pnas.2113789118
- Boeynaems, S., Holehouse, A. S., Weinhardt, V., Kovacs, D., Van Lindt, J., Larabell, C., et al. (2019). Spontaneous driving forces give rise to Protein–rna condensates with coexisting phases and complex material properties. *Proc. Natl. Acad. Sci.* 116 (16), 7889–7898. doi:10.1073/pnas.1821038116
- Clifton, L. A., Campbell, R. A., Sebastiani, F., Campos-Teran, J., Gonzalez-Martinez, J. F., Bjorklund, S., et al. (2020). Design and use of model membranes to study biomolecular interactions using complementary surface-sensitive techniques. *Adv. Colloid Interface Sci.* 277, 102118. doi:10.1016/j.cis.2020.102118
- Darden, T., York, D., and Pedersen, L. Particle Mesh Ewald: an N-Log(N) method for Ewald sums in large systems. *J. Chem. Phys.* 1993, 98 (12), 10089–10092. doi:10.1063/1.464397
- Darwish, T. A., Luks, E., Moraes, G., Yepuri, N. R., Holden, P. J., and James, M. (2013). Synthesis of deuterated [D32]oleic acid and its phospholipid derivative [D64]dioleoyl-

thanks the Swedish Research Council (2018-04833 and 2018-03990), Biofilm Research Center for Biointerfaces (Malmö University) and Wennergren foundation for financial support.

Acknowledgments

We thank the NTU Optical Bio-Imaging Centre (NOBIC) at the Singapore Centre for Environmental Life Sciences Engineering (SCELSE), NTU for the use of DIC microscopes and Dr. Yong Hwee Foo for his help and suggestions with imaging. This research was undertaken on the SPATZ beamline at the Australian Centre for Neutron Scattering, part of ANSTO. We are thankful to ANSTO for this opportunity and for allowing us to use their facilities. CD acknowledges use of computing resources on HPC platforms granted via the UK High-End Computing Consortium for Biomolecular Simulation, HECBioSim (<http://hecbiosim.ac.uk>), supported by EPSRC (Grant No. EP/R029407/1). MC thanks the Swedish Research Council, Biofilm—Research center for Biointerfaces, and Wennergren foundation for funding.

Conflict of interest

The authors declare that the research was conducted in the absence of any commercial or financial relationships that could be construed as a potential conflict of interest.

Publisher's note

All claims expressed in this article are solely those of the authors and do not necessarily represent those of their affiliated organizations, or those of the publisher, the editors and the reviewers. Any product that may be evaluated in this article, or claim that may be made by its manufacturer, is not guaranteed or endorsed by the publisher.

Supplementary material

The Supplementary Material for this article can be found online at: <https://www.frontiersin.org/articles/10.3389/frsrm.2023.1339496/full#supplementary-material>

- Sn-Glycero-3-Phosphocholine. *J. Label. Comp. Radiopharm.* 56 (9–10), 520–529. doi:10.1002/jlcr.3088
- Feller, S. E., Zhang, Y., Pastor, R. W., and Brooks, B. R. (1995). Constant pressure molecular dynamics simulation: the Langevin piston method. *J. Chem. Phys.* 103 (11), 4613–4621. doi:10.1063/1.470648
- Serhan, A. R., Yoon, B. K., Park, S., Sut, T. N., Chin, H., Park, J. H., et al. (2019). Solvent-assisted preparation of supported lipid bilayers. *Nat. Protoc.* 14 (7), 2091–2118. doi:10.1038/s41596-019-0174-2
- Gabryelczyk, B., Cai, H., Shi, X., Sun, Y., Swinkels, P. J. M., Salentini, S., et al. (2019). Hydrogen bond guidance and aromatic stacking drive liquid-liquid phase separation of intrinsically disordered histidine-rich peptides. *Nat. Commun.* 10 (1), 5465. doi:10.1038/s41467-019-13469-8
- Gouveia, B., Kim, Y., Shaevitz, J. W., Petry, S., Stone, H. A., and Brangwynne, C. P. (2022). Capillary forces generated by biomolecular condensates. *Nature* 609 (7926), 255–264. doi:10.1038/s41586-022-05138-6
- Gyanani, V., and Goswami, R. (2023). Key design features of lipid nanoparticles and electrostatic charge-based lipid nanoparticle targeting. *Pharmaceutics* 15 (4), 1184. doi:10.3390/pharmaceutics15041184
- Harush-Frenkel, O., Rozen, E., Benita, S., and Altschuler, Y. (2008). Surface charge of nanoparticles determines their endocytic and transcytotic pathway in polarized mdck cells. *Biomacromolecules* 9 (2), 435–443. doi:10.1021/bm700535p
- Hedegaard, S. F., Bruhn, D. S., Khandelia, H., Cárdenas, M., and Nielsen, H. M. (2020). Shuffled lipidation pattern and degree of lipidation determines the membrane interaction behavior of a linear cationic membrane-active peptide. *J. Colloid Interface Sci.* 578, 584–597. doi:10.1016/j.jcis.2020.05.121
- Hedegaard, S. F., Derbas, M. S., Lind, T. K., Kasimova, M. R., Christensen, M. V., Michaelsen, M. H., et al. (2018). Fluorophore labeling of a cell-penetrating peptide significantly alters the mode and degree of biomembrane interaction. *Sci. Rep.* 8 (1), 6327. doi:10.1038/s41598-018-24154-z
- Herce, H. D., and Garcia, A. E. (2007). Cell penetrating peptides: how do they do it? *J. Biol. Phys.* 33 (5–6), 345–356. doi:10.1007/s10867-008-9074-3
- Humphrey, W., Dalke, A., and Schulten, K. (1996). Vmd: visual molecular dynamics. *J. Mol. Graph.* 14 (1), 33–38. doi:10.1016/0263-7855(96)00018-5
- Jo, S., Kim, T., Iyer, V. G., and Im, W. (2008). Charmm-gui: a web-based graphical user interface for charmm. *J. Comput. Chem.* 29 (11), 1859–1865. doi:10.1002/jcc.20945
- Jo, S., Lim, J. B., Klauda, J. B., and Im, W. (2009). Charmm-gui membrane builder for mixed bilayers and its application to yeast membranes. *Biophysical J.* 97 (1), 50–58. doi:10.1016/j.bpj.2009.04.013
- Jones, A. T., Gumbleton, M., and Duncan, R. (2003). Understanding endocytic pathways and intracellular trafficking: a prerequisite for effective design of advanced drug delivery systems. *Adv. Drug Deliv. Rev.* 55 (11), 1353–1357. doi:10.1016/j.addr.2003.07.002
- Jorgensen, W. L., Chandrasekhar, J., Madura, J. D., Impey, R. W., and Klein, M. L. (1983). Comparison of simple potential functions for simulating liquid water. *J. Chem. Phys.* 79 (2), 926–935. doi:10.1063/1.445869
- Karal, M. A., Levandny, V., Tsuboi, T. A., Belaya, M., and Yamazaki, M. (2015). Electrostatic interaction effects on tension-induced pore formation in lipid membranes. *Phys. Rev. E Stat. Nonlin Soft Matter Phys.* 92 (1), 012708. doi:10.1103/PhysRevE.92.012708
- Kazmierczak, Z., Szostak-Paluch, K., Przybylo, M., Langner, M., Witkiewicz, W., Jedruchiewicz, N., et al. (2020). Endocytosis in cellular uptake of drug delivery vectors: molecular aspects in drug development. *Bioorg Med. Chem.* 28 (18), 115556. doi:10.1016/j.bmc.2020.115556
- Kern, N. R., Lee, J., Choi, Y. K., and Im, W. (2023). Charmm-gui multicomponent assembler for modeling and simulation of complex multicomponent systems. *bioRxiv*, 2023.08.30.555590. doi:10.1101/2023.08.30.555590
- Klauda, J. B., Venable, R. M., Freites, J. A., O'Connor, J. W., Tobias, D. J., Mondragon-Ramirez, C., et al. (2010). Update of the charmm all-atom additive force field for lipids: validation on six lipid types. *J. Phys. Chem. B* 114 (23), 7830–7843. doi:10.1021/jp101759q
- Latham, A. P., and Zhang, B. (2022). Molecular determinants for the layering and coarsening of biological condensates. *Aggreg. Hob.* 3 (6), e306. doi:10.1002/agt2.306
- Le Brun, A. P., Haigh, C. L., Drew, S. C., James, M., Boland, M. P., and Collins, S. J. (2014). Neutron reflectometry studies define prion protein N-terminal peptide membrane binding. *Biophysical J.* 107 (10), 2313–2324. doi:10.1016/j.bpj.2014.09.027
- Le Brun, A. P., Huang, T.-Y., Pullen, S., Nelson, A. R., Spedding, J., and Holt, S. A. (2023). Spatz: the time-of-flight neutron reflectometer with vertical sample geometry at the opal research reactor. *J. Appl. Crystallogr.* 56 (1), 18–25. doi:10.1107/s160057672201086x
- Li, H., Robertson, A. D., and Jensen, J. H. (2005). Very fast empirical prediction and rationalization of protein pKa values. *Proteins* 61 (4), 704–721. doi:10.1002/prot.20660
- Lim, Z. W., Ping, Y., and Miserez, A. (2018). Glucose-responsive peptide coacervates with high encapsulation efficiency for controlled release of insulin. *Bioconjug Chem.* 29 (7), 2176–2180. doi:10.1021/acs.bioconjchem.8b00369
- Lim, Z. W., Varma, V. B., Ramanujan, R. V., and Miserez, A. (2020). Magnetically responsive peptide coacervates for dual hyperthermia and chemotherapy treatments of liver cancer. *Acta Biomater.* 110, 221–230. doi:10.1016/j.actbio.2020.04.024
- Lind, T., Darré, L., Domene, C., Urbanczyk-Lipkowska, Z., Cárdenas, M., and Wacklin, H. (2015). Antimicrobial peptide dendrimer interacts with phosphocholine membranes in a fluidity dependent manner: a neutron reflection study combined with molecular dynamics simulations. *Biochimica Biophysica Acta (BBA)-Biomembranes* 1848 (10), 2075–2084. doi:10.1016/j.bbamem.2015.05.015
- Lind, T. K., Darre, L., Domene, C., Urbanczyk-Lipkowska, Z., Cardenas, M., and Wacklin, H. P. (2015). Antimicrobial peptide dendrimer interacts with phosphocholine membranes in a fluidity dependent manner: a neutron reflection study combined with molecular dynamics simulations. *Biochim. Biophys. Acta* 1848 (10), 2075–2084. doi:10.1016/j.bbamem.2015.05.015
- Lind, T. K., Cárdenas, M., and Wacklin, H. P. (2014). Formation of supported lipid bilayers by vesicle fusion: effect of deposition temperature. *Langmuir* 30 (25), 7259–7263. doi:10.1021/la500897x
- Lind, T. K., Skoda, M. W. A., and Cardenas, M. (2019). Formation and characterization of supported lipid bilayers composed of phosphatidylethanolamine and phosphatidylglycerol by vesicle fusion, a simple but relevant model for bacterial membranes. *ACS Omega* 4 (6), 10687–10694. doi:10.1021/acsomega.9b01075
- Liu, J., Spruijt, E., Miserez, A., and Langer, R. (2023). Peptide-based liquid droplets as emerging delivery vehicles. *Nat. Rev. Mater.* 8 (3), 139–141. doi:10.1038/s41578-022-00528-8
- Lu, T., Liese, S., Schoenmakers, L., Weber, C. A., Suzuki, H., Huck, W. T., et al. (2022). Endocytosis of coacervates into liposomes. *J. Am. Chem. Soc.* 144 (30), 13451–13455. doi:10.1021/jacs.2c04096
- Martyna, G. J., Tobias, D. J., and Klein, M. L. (1994). Constant pressure molecular dynamics algorithms. *J. Chem. Phys.* 101 (5), 4177–4189. doi:10.1063/1.467468
- Miyamoto, S., and Kollman, P. A. (1992). Settle: an analytical version of the shake and rattle algorithm for rigid water models. *J. Comput. Chem.* 13 (8), 952–962. doi:10.1002/jcc.540130805
- Moir, M., Yepuri, N. R., Marshall, D. L., Blanksby, S. J., and Darwish, T. A. (2022). Synthesis of perdeuterated linoleic acid-D31 and chain deuterated 1-palmitoyl-2-linoleoyl-Sn-Glycero-3-Phosphocholine-D62. *Adv. Synthesis Catal.* 364 (21), 3670–3681. doi:10.1002/adsc.202200616
- Nelson, A. (2006). Co-refinement of multiple-contrast neutron/X-ray reflectivity data using motifit. *J. Appl. Crystallogr.* 39 (2), 273–276. doi:10.1107/s0021889806005073
- Nelson, A. R. J., and Prescott, S. W. (2019). Refnx: neutron and X-ray reflectometry analysis in Python. *J. Appl. Crystallogr.* 52 (1), 193–200. doi:10.1107/S1600576718017296
- Nielsen, J. E., Lind, T. K., Lone, A., Gerelli, Y., Hansen, P. R., Jenssen, H., et al. (2019). A biophysical study of the interactions between the antimicrobial peptide indolicidin and lipid model systems. *Biochimica Biophysica Acta (BBA)-Biomembranes* 1861 (7), 1355–1364. doi:10.1016/j.bbamem.2019.04.003
- Noskov, S. Y., Berneche, S., and Roux, B. (2004). Control of ion selectivity in potassium channels by electrostatic and dynamic properties of carbonyl ligands. *Nature* 431 (7010), 830–834. doi:10.1038/nature02943
- Phillips, J. C., Braun, R., Wang, W., Gumbart, J., Tajkhorshid, E., Villa, E., et al. (2005). Scalable molecular dynamics with namd. *J. Comput. Chem.* 26 (16), 1781–1802. Research Support, N.I.H., Extramural Research Support, Non-U.S. Gov't Research Support, U.S. Gov't, P.H.S. doi:10.1002/jcc.20289
- Recsei, C., Russell, R. A., Cagnes, M., and Darwish, T. (2023). Deuterated squalene and sterols from modified *Saccharomyces cerevisiae*. *Org. Biomol. Chem.* 21 (32), 6537–6548. doi:10.1039/d3ob00754e
- Rehman, Z. u., Zuhorn, I. S., and Hoekstra, D. (2013). How cationic lipids transfer nucleic acids into cells and across cellular membranes: recent advances. *J. Control. Release* 166 (1), 46–56. doi:10.1016/j.jconrel.2012.12.014
- Rey, J., Murail, S., de Vries, S., Derreumaux, P., and Tuffery, P. (2023). Pep-Fold4: a ph-dependent force field for peptide structure prediction in aqueous solution. *Nucleic Acids Res.* 51 (W1), W432–W437. doi:10.1093/nar/gkad376
- Saurabh, S., Kalonia, C., Li, Z., Hollowell, P., Waigh, T., Li, P., et al. (2022). Understanding the stabilizing effect of histidine on mab aggregation: a molecular dynamics study. *Mol. Pharm.* 19 (9), 3288–3303. doi:10.1021/acs.molpharmaceut.2c00453
- Sebastiani, F., Yanez Arteta, M., Lerche, M., Porcar, L., Lang, C., Bragg, R. A., et al. (2021). Apolipoprotein E binding drives structural and compositional rearrangement of mrna-containing lipid nanoparticles. *ACS Nano* 15 (4), 6709–6722. doi:10.1021/acsnano.0c10064
- Shebanova, A., Perrin, Q., Gudlur, S., Sun, Y., Lim, Z. W., Sun, R., et al. (2022). Cellular uptake of his-rich peptide coacervates occurs by a macropinocytosis-like mechanism. *BioRxiv*, 502757. 2022.2008.2004. doi:10.1101/2022.08.04.502757
- Spleis, H., Sandmeier, M., Claus, V., and Bernkop-Schnurch, A. (2023). Surface design of nanocarriers: key to more efficient oral drug delivery systems. *Adv. Colloid Interface Sci.* 313, 102848. doi:10.1016/j.cis.2023.102848

- Stewart, M. P., Langer, R., and Jensen, K. F. (2018). Intracellular delivery by membrane disruption: mechanisms, strategies, and concepts. *Chem. Rev.* 118 (16), 7409–7531. doi:10.1021/acs.chemrev.7b00678
- Sun, Y., Lau, S. Y., Lim, Z. W., Chang, S. C., Ghadessy, F., Partridge, A., et al. (2022). Phase-separating peptides for direct cytosolic delivery and redox-activated release of macromolecular therapeutics. *Nat. Chem.* 14 (3), 274–283. doi:10.1038/s41557-021-00854-4
- Sun, Y., Xu, X., Chen, L., Chew, W. L., Ping, Y., and Miserez, A. (2023). Redox-responsive phase-separating peptide as a universal delivery vehicle for crispr/cas9 genome editing machinery. *ACS Nano* 17 (17), 16597–16606. doi:10.1021/acsnano.3c02669
- Tan, Y., Hoon, S., Guerette, P. A., Wei, W., Ghadban, A., Hao, C., et al. (2015). Infiltration of chitin by protein coacervates defines the squid beak mechanical gradient. *Nat. Chem. Biol.* 11 (7), 488–495. doi:10.1038/nchembio.1833
- Thoren, P. E., Persson, D., Lincoln, P., and Norden, B. (2005). Membrane destabilizing properties of cell-penetrating peptides. *Biophys. Chem.* 114 (2-3), 169–179. doi:10.1016/j.bpc.2004.11.016
- Tufféry, P., and Derreumaux, P. (2023). A refined ph-dependent coarse-grained model for peptide structure prediction in aqueous solution. *Front. Bioinform.* 3, 1113928. doi:10.3389/fbinf.2023.1113928
- Vedadghavami, A., Zhang, C., and Bajpayee, A. G. (2020). Overcoming negatively charged tissue barriers: drug delivery using cationic peptides and proteins. *Nano Today* 34, 100898. doi:10.1016/j.nantod.2020.100898
- Verlet, L. (1967). Computer "experiments" on classical fluids. I. Thermodynamical properties of Lennard-Jones molecules. *Phys. Rev.* 159 (1), 98–103. doi:10.1103/physrev.159.98
- Virtanen, J. A., Cheng, K. H., and Somerharju, P. (1998). Phospholipid composition of the mammalian red cell membrane can be rationalized by a superlattice model. *Proc. Natl. Acad. Sci.* 95 (9), 4964–4969. doi:10.1073/pnas.95.9.4964
- Waldie, S., Lind, T. K., Browning, K., Moulin, M., Haertlein, M., Forsyth, V. T., et al. (2018). Localization of cholesterol within supported lipid bilayers made of a natural extract of tailor-deuterated phosphatidylcholine. *Langmuir* 34 (1), 472–479. doi:10.1021/acs.langmuir.7b02716
- Waldie, S., Moulin, M., Porcar, L., Pichler, H., Strohmeier, G. A., Skoda, M., et al. (2019). The production of matchout-deuterated cholesterol and the study of bilayer-cholesterol interactions. *Sci. Rep.* 9 (1), 5118. doi:10.1038/s41598-019-41439-z
- Wang, J., Choi, J. M., Holehouse, A. S., Lee, H. O., Zhang, X., Jahnel, M., et al. (2018). A molecular grammar governing the driving forces for phase separation of prion-like rna binding proteins. *Cell* 174 (3), 688–699.e16. doi:10.1016/j.cell.2018.06.006
- Wang, Z., Yang, C., Guan, D., Li, J., and Zhang, H. (2023). Cellular proteins act as surfactants to control the interfacial behavior and function of biological condensates. *Dev. cell* 58 (11), 919–932.e5. doi:10.1016/j.devcel.2023.04.004
- Welsh, T. J., Krainer, G., Espinosa, J. R., Joseph, J. A., Sridhar, A., Jahnel, M., et al. (2022). Surface electrostatics govern the emulsion stability of biomolecular condensates. *Nano Lett.* 22 (2), 612–621. doi:10.1021/acs.nanolett.1c03138
- Wu, E. L., Cheng, X., Jo, S., Rui, H., Song, K. C., Dávila-Contreras, E. M., et al. (2014). Charmm-gui membrane builder toward realistic biological membrane simulations. *J. Comput. Chem.* 35 (27), 1997–2004. doi:10.1002/jcc.23702
- Yuan, F., Alimohamadi, H., Bakka, B., Trementozzi, A. N., Day, K. J., Fawzi, N. L., et al. (2021). Membrane bending by protein phase separation. *Proc. Natl. Acad. Sci. U. S. A.* 118 (11), e2017435118. doi:10.1073/pnas.2017435118



OPEN ACCESS

EDITED BY

Raffaele Mezzenga,
ETH Zürich, Switzerland

REVIEWED BY

Alejandro D. Rey,
McGill University, Canada
Konstantin Kornev,
Clemson University, United States

*CORRESPONDENCE

Erik van der Linden,
✉ erik.vanderlinden@wur.nl

RECEIVED 26 October 2023

ACCEPTED 11 December 2023

PUBLISHED 23 January 2024


CITATION

Sturtewagen L, Dewi BPC, Bot A,
Venema P and van der Linden E (2024),
Phase behavior in
multicomponent mixtures.
Front. Soft Matter 3:1328180.
doi: 10.3389/frsfm.2023.1328180

COPYRIGHT

© 2024 Sturtewagen, Dewi, Bot, Venema
and van der Linden. This is an open-
access article distributed under the terms
of the [Creative Commons Attribution
License \(CC BY\)](#). The use, distribution or
reproduction in other forums is
permitted, provided the original author(s)
and the copyright owner(s) are credited
and that the original publication in this
journal is cited, in accordance with
accepted academic practice. No use,
distribution or reproduction is permitted
which does not comply with these terms.

Phase behavior in multicomponent mixtures

Luka Sturtewagen¹, Belinda P. C. Dewi¹, Arjen Bot ^{1,2},
Paul Venema¹ and Erik van der Linden^{1*}

¹Laboratory of Physics and Physical Chemistry of Foods, Wageningen University and Research, Wageningen, Netherlands, ²Unilever Foods Innovation Centre, Wageningen, Netherlands

In this article, we study the phase behavior of two polydisperse hydrocolloids: dextran and polyethylene oxide. We combine the data on the experimental osmometric virial coefficients of the pure components with the experimental critical point of their aqueous mixture and the size distribution of each component from a previously published study in order to predict the phase boundary, spinodal, and fractionation upon demixing of the polydisperse mixture. We compare the results of our calculation to the experimental phase diagram. Our method reveals a better correspondence with the experimental binary phase behavior than modeling each component as monodisperse. The polydispersity of the hydrocolloids causes the phase separation boundary to shift to lower concentrations and the miscibility region to decrease and change its shape from a rotated U-shape to a W-shape.

KEYWORDS

assembly, gelation, non-equilibrium, configurational entropy, phase behavior, complexity, multicomponent, random matrix theory

1 Introduction

A solution may gel when assemblies of molecules in that solution span the solution. The properties of the assemblies and their mutual interactions determine the concentration range above which the gel forms and the properties of the gel. For example, in the case of fibrillar assemblies from protein-derived peptides, gelation occurs already at low concentrations of the building blocks of the fibril (van der Linden, 2012). Notably, such fibrils exhibit interesting collective properties at higher concentrations, such as their arrangement in an anisotropic manner like that of (nematic) liquid crystals (Bagnani et al., 2019).

The molecular assembly may reflect an equilibrium state, but, for most practically relevant systems, in particular for gelling systems, it more often reflects a non-equilibrium state. The structure of such a state depends on the specific spatial-temporal path through equilibrium and unstable regions in the phase diagram that are followed during the preparation of the system and on the rate of change of the thermodynamic conditions. As such, the equilibrium phase diagram plays an important role in predicting the characteristics of the structures within and the concomitant properties of the gel systems. This importance of phase diagrams holds for systems of any number of components. We will discuss a few examples of the above in simple systems in this Introduction section to set the scene, before addressing phase behavior in multicomponent mixtures in more detail in the next section.

As a first example, we choose a system composed of one component in water. We choose gelatin, which forms random coils at high temperatures and is a liquid, while below a critical temperature, its molecules form triple helices and its system shows gelation at sufficiently large concentrations. The work of Chatellier et al. (1985) demonstrates that a critical

concentration of helices exists, below which no gel forms. Joly-Duhamel et al. (2002a, 2002b), in addition, have clearly shown that the liquid–gel transition is, in fact, a percolation transition, with the concentration of triple helices being the control parameter. We have shown that the critical concentration of helices, below which the system gels, can be deduced from the structural characteristics of the triple helices, i.e., their persistence length and thickness (van der Linden and Parker, 2005). The helices can, in fact, be viewed as fibrils. Furthermore, the value of gel elasticity at low concentrations of helices can be solely deduced from entropy arguments (van der Linden, 2012), and this also holds for the elasticity value at higher concentrations (apart from the fact that one requires one adjustable fitting parameter which is predicted to be of order 1, as confirmed by fitting) (van der Linden, 2012). The elasticity over time is determined by the final temperature of the system and the rate at which this occurs (Normand et al., 2000; Normand and Parker, 2003). We clearly have a non-equilibrium gel state. Despite this non-equilibrium state, one can always predict elasticity solely on the basis of the helix concentration, which is a separately accessible observation of Joly-Duhamel et al. (2002a, 2002b).

For another case of fibrillar assembly under non-equilibrium conditions, Nguyen and Vaikuntanathan (2016) simulated the fibrilization of two components A and B for a given initial excess chemical potential of each type of monomer. This situation can be experimentally realized, for example, in a supersaturated solution of both types of monomers. The excess chemical potentials were assumed to be equal for both types. The interactions between the likewise species are also assumed to be equal. The fibrils were found to consist of blocks composed of A, connected to blocks composed of B. The less favorable the unlike particle interaction becomes, the longer the blocks become. If one now increases the initial excess chemical potential of the two types of monomers, the length of the blocks becomes smaller. As such, the structural diversity within a fibril increases upon increasing the initial excess chemical potential of the monomers, i.e., upon increasing the distance to the transition point. This in turn will affect the interactions and flexibility of the fibril and thus the properties of the gel it forms.

Another example of a “one-component” system, for which the equilibrium phase behavior is important in understanding the non-equilibrium gel state, consists of oil droplets in water, for which the interaction can be tuned by the temperature (Poulin et al., 1999). Above a sufficiently large enough attraction between the droplets, the authors find a transition, known as spinodal decomposition. This occurs in the region of the phase diagram that is referred to as the instability region. One finds a bi-continuous structure, with one of its parts being mostly droplets that are packed with a fractal dimension, d_f . This d_f can get as low as 1.7 at sufficiently high attraction, forming a gel state, while for lower attractions, one finds a d_f of approximately 3, indicating a fluid state, resulting in the end in a two-phase (de-mixed) system.

In order to better understand gelled systems made from multicomponent mixtures, the above urges us to investigate the phase diagrams of multicomponent mixtures. Hereto, we currently report on the recent theoretical and experimental results obtained to explain the experimental phase diagram for a multicomponent system in water containing differently sized coil-like polymers of dextran (D) and polyethylene oxide (PEO). Mixtures of such polydisperse bio-polymeric ingredients are

ubiquitous and therefore bear relevance to many practical situations. An important example is the understanding of functionality in food formulations of a variety of multicomponent mixtures that consist of minimally refined plant-based ingredients. This understanding facilitates the adaptation to use different ingredient sources, thereby supporting the development of a more sustainable food supply.

Aqueous mixtures of polymers such as polyethylene oxide and dextran form liquid–liquid two-phase systems at certain concentrations. These systems are often used as a model system for the phase behavior of macromolecules in solution because they show a clear macroscopic phase separation (Kang and Sandler, 1988; Edelman et al., 2003; Dewi et al., 2020). They also have practical applications, as they are often used to aid in the partitioning of biological materials such as proteins and cell materials (Johansson et al., 1998; Johansson and Walter, 1999).

For the prediction of their phase behavior, the polymers are often considered monodisperse. Experimental work by Edelman et al. (2003), however, has shown that upon demixing, considerable fractionation in the molecular weight occurs for both PEO and dextran. Not only is there an effect of the polydispersity of each component on fractionation but also the concentration in the parent phase plays a role. At lower total polymer concentrations in the parent phase, the depleted colloids have a broader distribution, i.e., there is less pronounced fractionation. The changes in the distribution are mainly prevalent in the depleted phase. The average molar mass in the enriched phase does not change considerably. The changes in the amount of fractionation, depending on the concentration along a dilution line, were also reported by Zhao et al. (2016). Furthermore, Gaube et al. (1993) showed that polydispersity plays a role in phase behavior and phase composition. They compared mixtures of PEO and dextran with various molecular sizes and found that for each polymer, the short-chain molecules preferentially partition to the phase enriched in the other polymer.

There has been some effort in incorporating the polydispersity of these polymers in the prediction of their phase behavior. Using a universal quasi-chemical (UNQUAC) model, Kang and Sandler (1988) incorporated polydispersity in their prediction and found that polydispersity of the polymers enlarged the two-phase region considerably near the critical point and resulted in smaller miscibility regions far from the critical point. They also found significant fractionation, and the difference in the average molecular weight of the components in each phase increased with larger polydispersity.

Most often, when the phase behavior of a binary mixture is studied experimentally, one or more dilution lines are used to obtain the concentration of each component in each phase. These concentrations are then used to construct the binodal (Albertsson, 1970). However, this approach does not shed light on polydispersity nor does it give an insight into the demixing in the metastable region, where a system de-mixes into multiple phases, but that is outside of the unstable (spinodal) region. It is also difficult to quantify the impact of polydispersity and its corresponding distribution on phase behavior (Dos Santos et al., 2004). In order to get more insights into the transition between one and two phases, Larsson and Mattiasson (1988) determined the experimental phase

boundary for polydisperse PEO and dextran. They found a significant broadening of the phase boundary compared to the approach of Albertsson (1970). The broadening increased with increasing polydispersity at the depleted side of the said polydisperse component (Larsson and Mattiasson, 1992).

In a previous numerical work, we predicted the phase behavior of a polydisperse binary mixture of hard spheres in solution using the virial coefficient approach (Sturtewagen and van der Linden, 2021; Sturtewagen and van der Linden, 2022), based on the theory of McMillan and Mayer (1945). Polydispersity was incorporated into the system by means of sub-components. The spheres had an asymmetric size ratio to aid in demixing (Dijkstra et al., 1999). Polydispersity of the largest component caused significant changes to the phase diagram. With an increase in polydispersity, the critical point shifted to higher concentrations, while also at the same time, the miscible region decreased. Not only polydispersity plays a role but also the type of distribution has an influence. We found that the largest components of the distribution impacted the phase diagram the most. De-mixed mixtures also showed significant fractionation. The smallest sub-components of the large polydisperse components favored the top phase that was enriched in the small monodisperse component.

In recent works, the experimental phase diagram for the macromolecules of PEO and dextran was theoretically reconstructed using osmotic virial coefficients as obtained from the fitting experimental data from an earlier published work (Dewi et al., 2020) and the experimentally obtained critical point of the binary mixture (Dewi et al., 2020). However, some aspects of the experimental phase diagram remained unexplained by the theoretically constructed one. Mainly, at low concentrations of dextran, the experimental system showed thermodynamic incompatibility and demixing into two phases, while the theory predicted a homogeneous mixture for these concentrations. We hypothesize that this discrepancy is due to the polydispersity of the macromolecules.

In this article, we take the polydispersity of both these components into account (by subdividing each polymer into sub-components of different sizes) when predicting the phase diagram based on the experimental data from Dewi et al. (2020). We study the position of the spinodal and binodal. We model the interactions between the different polydisperse sub-components using the second virial coefficient, where we assume that the polydisperse sub-components act as non-additive hard spheres. We start with describing the underlying theoretical background in Section 2. In Section 3, we describe the materials and methods. In Section 4, we discuss the results and compare it with that of other works in the area of multicomponent mixtures.

2 Theoretical background

To describe phase separation in a system containing particles of different diameters and of different types, we choose a framework that accounts for terms up to quadratic terms in concentration, i.e., including up to the second-order virial coefficients that are experimentally or theoretically accessible. We start from the

Helmholtz free energy F for an N -component mixture in a common solvent:

$$\frac{F}{RTV} = \sum_{i=1}^N c_i \ln(c_i) + \sum_{i,j=1}^N B_{ij} c_i c_j, \quad (1)$$

where $B_{ij} \equiv B_{ji}$, R represents the molar gas constant, T represents the temperature, and c_i represents the molar concentration of component i , with $c_i = n_i/V$, where n_i denotes the number of moles of component i in volume V , and B_{ij} represents the second virial coefficients, reflecting the interactions between components i and j . The osmotic pressure Π of a mixture can be written as

$$\frac{\Pi}{RT} = -\frac{1}{RT} \left(\frac{\partial F}{\partial V} \right)_{T, n_i} = \sum_{i=1}^N c_i + \sum_{i,j=1}^N B_{ij} c_i c_j. \quad (2)$$

In our case, the interactions between the particles are assumed to follow the non-additive hard sphere model (Sturtewagen and van der Linden, 2022), where the non-additivity refers to either an attractive or repulsive extra interaction on top of the excluded volume interaction. For such non-additive hard spheres, the virial coefficients for a system of two compounds, i and j , consisting of spheres of two different diameters, are given by

$$B_{ij} = \frac{2}{3} \pi \cdot \left[\frac{\sigma_i + \sigma_j}{2} \cdot (1 + \Delta_{ij}) \right]^3, \quad (3)$$

where σ_i refers to the diameter of the sphere of the compound i , and Δ_{ij} reflects the interaction contribution that is different from the excluded volume interaction. The term Δ_{ij} can be negative or positive in the non-additive regime, whereas it is zero while referring to a pure excluded volume interaction, with the latter referring to the so-called additive hard sphere model. The chemical potential μ_i for component i can be obtained from

$$\frac{\mu_i}{RT} = \frac{1}{RT} \left(\frac{\partial F}{\partial n_i} \right)_{T, V, n_{i \neq j}} = \frac{\mu_i^0}{RT} + \ln c_i + 2 \sum_{j=1}^N B_{ij} c_j, \quad (4)$$

where μ_i^0 is the standard chemical potential of compound i . Suppose we search for conditions for one or two macroscopic phases, there are three important aspects: the occurrence of instability, the critical point, and the coexistence region.

The first aspect is the occurrence of instability. In a two-component mixture, one refers to the boundary of this instability as the spinodal, which is a curve. To analyze the local stability of the mixture against phase separation, it is convenient to introduce the so-called Hessian matrix \mathbf{M}_1 . The Hessian matrix characterizes the local curvature of the Helmholtz free energy surface. The limit of stability is reached when the matrix has one zero eigenvalue and is otherwise a positive definite (Heidemann and Khalil, 1980). For a mixture with N distinguishable components, the Hessian matrix can be represented by an $N \times N$ matrix, referred to as \mathbf{M}_1 according to

$$\mathbf{M}_1 = \begin{bmatrix} 2B_{11} + \frac{1}{c_1} & \cdots & 2B_{1N} \\ \vdots & \ddots & \vdots \\ 2B_{1N} & \cdots & 2B_{NN} + \frac{1}{c_N} \end{bmatrix}. \quad (5)$$

The second aspect to consider is the critical point. In a binary mixture, the critical point is a stable point which lies on the stability limit (spinodal) (Heidemann and Khalil, 1980) and where the phase boundary and spinodal coincide. In mixtures with more than two components, these critical points are also called plait points.

Critical points and plait points are, in general, concentrations at which two or more phases are in equilibrium and become indistinguishable (Heidemann, 1994).

There are two criteria that have to be fulfilled to find the plait points. The first one is $\det(M_1) = 0$, which is the equation for the spinodal. The other criterion is based on the fact that at the critical point, the third derivative of free energy should also be zero. For a multicomponent system, this criterion can be reformulated using Legendre transforms as $\det(M_2) = 0$ (Beegle et al., 1974; Reid and Beegle, 1977), where

$$M_2 = \begin{bmatrix} \frac{\partial \mu_1}{\partial n_1} & \dots & \frac{\partial \mu_n}{\partial n_n} \\ \vdots & \ddots & \vdots \\ \frac{\partial M_1}{\partial n_1} & \dots & \frac{\partial M_1}{\partial n_N} \end{bmatrix}, \quad (6)$$

and matrix M_2 is matrix M_1 with one of the rows (in this case the lowest row) being replaced by the partial derivatives of the determinant of matrix M_1 . Note that it does not matter which row of the matrix is replaced.

The third aspect is the coexistence region. This is characterized by the equilibrium composition of the phases for N components, which is in turn characterized by a manifold (for two components, this becomes the binodal or coexistence curve). For a system that separates into two different phases, this manifold is found by simultaneously solving Eqs 7, 8:

$$\Pi^I = \Pi^{II}, \quad (7)$$

$$\mu_i^I = \mu_i^{II} \text{ with } i = 1, 2, \dots, N. \quad (8)$$

For a mixture containing N distinguishable components, which de-mixes into two phases, this yields $(N + 1)$ equations with $2 \times N$ unknowns. In order to solve not only for coexistence concentrations but also for phase volumes, we require extra equations. For the extra set of equations, we build on the fact that no particles are lost and no new particles are created during phase separation and the fact that we assume the total volume does not change. For a system that separates into two separate phases, indicated by I and II , we obtain an extra set of equations (Sturtewagen, 2020):

$$\begin{aligned} c_1 &= \alpha^I c_1^I + (1 - \alpha^I) c_1^{II}, \\ &\vdots \\ c_N &= \alpha^I c_N^I + (1 - \alpha^I) c_N^{II}, \end{aligned} \quad (9)$$

where $\alpha^I = \frac{V^I}{V^I + V^{II}}$, in which V^I represents the volume of phase I .

The solutions for the two-component mixtures are discussed elsewhere (Ersch et al., 2016; Dewi et al., 2020; Dewi et al., 2021; Bot et al., 2021a; Bot et al., 2021b). Eqs. 7–(9) allow for the determination of the concentration of each component in each of the phases along with the phase volume of each phase for any given parent concentration, given that the mixture will separate into two phases.

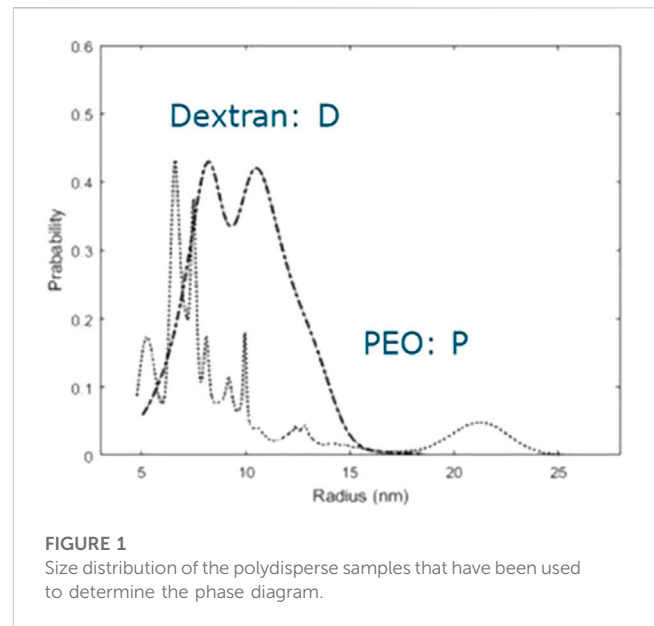


FIGURE 1
Size distribution of the polydisperse samples that have been used to determine the phase diagram.

3 Materials and methods

Size exclusion chromatography with multi-angle laser light scattering (SEC-MALLS) for both polyethylene oxide (PEO35) and dextran (D100) was performed by NIZO food research to obtain the molar mass and size distribution (size distributions are shown in Figure 1). The SEC-MALLS molar mass plots can be found in the Supplementary Materials. The experimental critical point and osmotic virial coefficients for the pure components PEO35 and D100 were taken from Dewi et al. (2020) (see Table I). The cross-virial coefficients used in the calculations are the result of a fitting that includes polydispersity as follows.

Both components exhibited polydispersity (see Figure 1). The size distributions for both components were binned [the number of bins ($N = N_{PEO} + N_D$) was $N_{PEO} = 1, 2$, and 5 for PEO and $N_D = 1, 2$, and 10 for dextran]. The obtained radii and fractions were taken as the starting point for the fit of the theoretical polydisperse virial coefficients to the experimentally obtained ones. The cross-interactions between the sub-components of PEO and the sub-components of dextran were also considered the same for all sizes (Δ_{PD}). For each bin size, one can calculate a virial coefficient and the corresponding cross-virial coefficients with the other “components”. Each virial coefficient resulted from a non-additive hard sphere interaction according to Eq. 3 for B_{ij} , where i can refer to D100 and PEO35 and j can refer to D100 and PEO35. In addition, we assume that for the “components,” the values for Δ_{D100} , Δ_{PEO35} , and Δ_{PD} are independent of the respective radii.

Subsequently, one calculates a number-averaged virial coefficient for dextran and PEO, B_{D100} and B_{PEO35} , respectively, and the cross-virial coefficient, B_{PD} , for the size distribution. These calculated expressions still contain the unknown values for the respective parameters, Δ_{D100} , Δ_{PEO35} , and Δ_{PD} . One then determines the values for the non-additivity parameters D_{D100} , D_{PEO35} , and D_{PD} , from fitting the calculated number-averaged expressions to the experimental values of B_{D100} , B_{PEO35} , and B_{PD} . Once the non-additivity parameters are known, we then determine

TABLE 1 Virial coefficients of polyethylene oxide (PEO35) and dextran (D100) and the critical point for their mixture obtained from experiments by Dewi et al. (2020), which were used in the fitting for the polydisperse virial-coefficient matrix.

B_{PEO35} (m^3/mol)	B_{D100} (m^3/mol)	Critical point (PEO35; D100) (mol/m^3)
4.74	1.31	(0.40; 1.06)

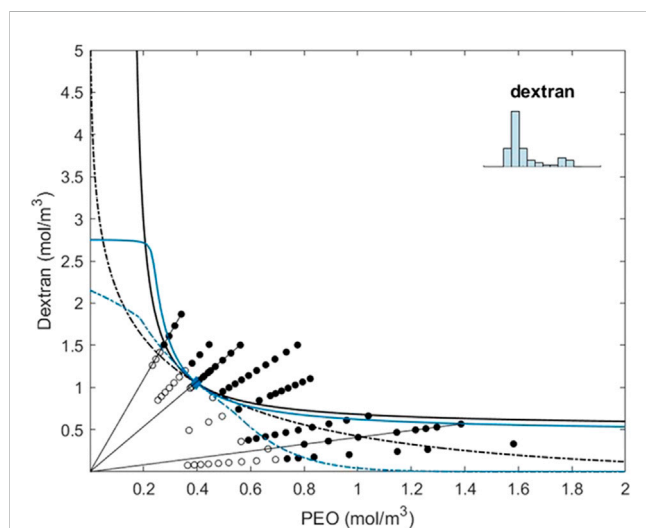


FIGURE 2

Coexistence line (black dotted) and instability line (black) for the two-component system of PEO and dextran obtained from solving Eqs 7–9 while substituting the three experimentally determined virial coefficients, as determined by osmometry (see also Dewi et al., 2020). The blue dotted line and the blue line represent the solutions of Eqs.(7)–(9) while using the binning strategy for PEO and dextran, as indicated in the inset of the figure and further described in the text. In fact, PEO is used as monodisperse in the specific strategy depicted here. The circular open symbols represent the experimentally determined one-phase systems and the circular closed symbols represent the two-phase systems.

the coexistence relationships and the instability line, and the critical point, and compare these with the ones obtained experimentally by conducting phase diagram studies. One can explore this procedure for the different binning strategies. While using the fitting procedure mentioned above, the sub-component fractions are obtained from the binned-size distribution, while adjusting the sizes of the sub-components within a small range and the non-additivity parameters (Δ_{PEO35} , Δ_{D100} , and Δ_{PD}). The values for the virial coefficients and critical points that were used in the fitting are given in Table 1. The obtained matrix of virial coefficients was used to calculate the phase boundary and fractionation of the polydisperse mixture. The resulting phase diagram was compared to the experimental phase diagram from Dewi et al. (2020). A fitting was considered good when the critical point of the polydisperse mixture was on the two-phase boundary and the dilution line through the critical point reached an equal volume at the critical point.

4 Results and discussion

From Figure 1, we conclude that both PEO and dextran show significant polydispersity. The distribution for PEO is relatively

narrow, is slightly bimodal, and has a small tail, while the distribution for dextran has more peaks and a considerably fat tail. Based on the research we did on the effect of polydispersity on the phase behavior of a binary mixture of non-additive hard spheres (Sturtewagen and van der Linden, 2022), we hypothesize that especially the larger components of dextran modify the phase behavior. The osmometric number-averaged virial coefficient of PEO is considerably larger than the number-averaged virial coefficient of dextran (Table 1), even though the radius of the PEO molecules is not larger. This indicates that the repulsive depletion interaction between PEO molecules is larger than the repulsive interaction between dextran molecules.

To determine which effect has the largest influence on the phase behavior (the large size difference between dextran molecules or the higher repulsive interaction between PEO molecules), we have stepwise introduced more polydispersity into our theoretical calculations of the phase diagram. We have compared the calculations to the experimental phase diagram from Dewi et al. (2020). We performed analyses for three cases. First, we introduced polydispersity only for PEO (Supplementary Materials), subsequently we introduced polydispersity only for dextran (Supplementary Materials), and third, we introduced polydispersity for both PEO and dextran (Supplementary Materials). We have compared the different binning strategies as shown in Figure 2; in the main text, we show the result that best fits all the three cases of the experimental coexistence and instability lines. This best fit was obtained using polydispersity of dextran as modeled by the means of 10 bins of equal width, and polyethylene oxide being modeled as monodisperse.

From Figure 2, we can conclude that the incorporation of polydispersity draws the (apparent) spinodal more toward the horizontal axis and a typical W-form emerges. We note that the term (apparent) spinodal stems from the fact that we plot the concentrations as determined experimentally, effectively hiding the polydispersity of the two polymers, which, if polydispersity would have been included, would, in fact, lead to a multi-dimensional phase diagram instead of a two-dimensional phase diagram.

When subdividing dextran into 10 bins of equal bin width, we capture the details of polydispersity in our fitting. This causes the spinodal to bend toward the vertical axis at higher dextran concentrations, indicating that at higher concentrations of dextran, the mixture can de-mix into two phases of dextran. The binodal of the mixture with this fitting also changes quite drastically. At the dextran-enriched side, the phase boundary first shifts toward higher PEO concentrations and then bends toward the axis with increasing dextran concentrations. The curve has a noticeable nod. This indicates a regime change in demixing. At the PEO-depleted side of the curve, two-phase demixing is with a phase enriched in PEO and a phase enriched in dextran, but it has a phase enriched in the smaller components of dextran and a phase enriched in the

larger components of dextran, similar to that described for PEO above. At the PEO-enriched side of the curve, the binodal shifts toward lower concentrations of dextran while asymptotically approaching the horizontal axis. Furthermore, the components with this pairwise interaction can de-mix into more than two phases; however, just as in the previous cases, the concentrations required for multi-phase demixing are unattainable with this particle distribution. The fitting captures more of the experimentally phase-separated samples with low dextran concentrations (filled circles in the plot) compared to the previous fittings. This indicates that our hypothesis that the polydispersity of dextran would be a driving factor in the demixing of these samples is valid.

Döbert et al. (1995) constructed a consistent osmotic virial equation to predict the phase behavior of a different type of polydisperse dextran and monodisperse PEO. They obtained an average molecular weight osmotic virial coefficient for the different polymer chains and compared their results to the predictions, assuming a binary monodisperse system. They report a better fit when polydispersity is taken into account. When predicting phase separation for mixtures close to the phase boundary, they also report that the binodal shifts closer to the axis in the dextran-depleted side of the binodal. They report a strong influence of the volume fraction of the phase enriched in dextran on the shape of the phase boundary and the fractionation of polydisperse dextran.

Regarding the validity of the virial approach up to the second order, we like to remark that we determine the second virial coefficients from the slope of the reduced osmotic pressure, (Π/RTc) as a function of c , in the limit of c approaching zero. The contributions of the higher order virial coefficients can be ignored for our system since the slope was found to be constant in the concentration range that was used. We note that the osmotic pressures were determined in the concentration range of 0.02–0.2 mol/m³, which is well below the critical concentrations: (PEO35; D100) = (0.4; 1.06) (Dewi et al., 2020). Interpreting the osmotic pressure experiments in terms of the polymers being modeled by non-additive hard spheres is justified as follows. The (estimated) overlap concentration of the polymers, c^* , for this system, lies in the order of 0.5 mol/m³ when assuming a radius of gyration of 10 nm. This radius of gyration is taken from the size distribution in Figure 1. The measurements for the virial coefficients are conducted well below this overlap concentration. The critical concentration is in the same range as the overlap concentration, but it is noted in support of the second-order approximation that the results for the critical point, as deduced from substituting the experimental values for the virial coefficients in the theoretical second-order model, yield a consistent picture with the experimental critical point. We, therefore, expect that the second-order virial approach gives reasonable predictions and refers to a more elaborate discussion on this topic in Sturtewagen and van der Linden (2023).

Predicting the phase behavior of multiple components has been of interest in the literature for some time. One approach that has been put forward recently builds on a convenient parameterization that leads to a set of equations that are much more easily analyzed than applying numerical methods to solve all equations (Bot et al., 2023). We briefly summarize this work in the following paragraph.

First, consider for simplicity the binodal of a two-component system. Two coexisting phases, named *I* and *II*, are represented by

two molar concentration coordinates $(c_1^I \text{ and } c_2^I)$ and $(c_1^{II} \text{ and } c_2^{II})$ on the binodal, which are connected by a so-called tie-line. Introducing the parameter $S_{m,21} = -(c_2^{II} - c_2^I)/(c_1^{II} - c_1^I)$, corresponding to (minus) the tie-line slope, allows for rewriting the coexistence equations. Introducing the parameter $S_{m,21}$ may seem like a step back, since it adds a fourth equation to the coexistence equations. However, two of these equations have analytical solutions in terms of the Lambert *W* function (Corless et al., 1996), and as a result, the original four-variable problem is reduced to a more succinct problem in the two concentration coordinates and the parameter $S_{m,21}$. From a physical perspective, the choice of (minus) the tie-line slope as a parameter seems to be a defensible choice, as the tie-line contains important information on the physics of the problem. For real arguments, the Lambert *W* function has zero, one, or two solutions, corresponding to, respectively, the isotropic mixing, location of the critical points, and binary phase separation. In case of two solutions, the solution for each component in phase *I* and *II* is located either on the W_{-1} -branch or W_0 branch of the Lambert *W* function. Surprisingly, this approach can be generalized to many components, i.e., for higher values than $N = 2$. There are N^2 parameters $S_{m,ij} = -(c_j^{II} - c_j^I)/(c_i^{II} - c_i^I)$, of which $(N - 1)$ are free variables and $S_{m,ii} = -1$ is fixed (for components *i* and *j*). This reduces the number of variables in the problem from $2N$ concentration variables to N concentration variables plus $(N - 1)$ variables $S_{m,ij}$. For more details, we refer to a recent publication of Bot et al. (2023). The results in Table 2 present a scheme to calculate the phase diagram using the abovementioned parametrization. Previously, results have been published for $N = 2$ (Bot et al., 2021a; Bot et al., 2021b) and $N = 3$ (Bot and Venema, 2023). A comparison between the calculations in terms of the parameters $S_{m,ij}$ (Table 2) and the numerical results for polydisperse two-component mixtures of PEO and dextran, which are presented in Section 4.2, remains to be evaluated. The calculation of the binodal manifolds in particular pose numerical challenges because of the large number of coupled non-linear algebraic equations. The calculation of the critical and spinodal manifolds presents fewer complications. For an arbitrary, large number of components *N*, it can be considered complementary to another interesting method, referred to in the literature as the random matrix theory (RMT) (Sear and Cuesta, 2003; Thewes et al., 2023).

This random matrix theory has been put forward in the context of phase behavior two decades ago by Sear and Cuesta (2003) as an alternative approach to handle the complexity of mixtures with many components, as a utilization of the general work by Wigner (1967). Setting details aside, this method allows for calculating the spinodal curve of complex mixtures using only averages and standard deviations of the second virial coefficients of the molecules in the mixture. This simplifies the calculations considerably. The RMT uses essentially the same expression for free energy as shown in Eq. 1. Additionally, it makes use of the large number of components and accordingly the large number of second virial coefficients. Instead of finding solutions for the spinodal manifold (with the result shown in the left column of Table 2), Sear and Cuesta (2003) calculated a point on the spinodal along the line $c_1 = c_2 = \dots = c_N$, where c_i is the molar concentration of component *i*, for a system of many components *N*. Note that because the number of components *N* is large, the individual concentrations of the components are very small. This approach was recently extended to the arbitrary concentrations of the components

TABLE 2 Expressions for the spinodal, critical, and binodal manifolds for an arbitrary number of components $N \geq 2$ in a common solvent, in terms of the parameters $S_{m,ij}$ and the Lambert W function, where $i = 1, \dots, N$, and z can be represented as “sp”, “c”, or “m” (adapted from Bot et al., 2023).

Spinodal point	Critical points	Coexistence equation	Common rules for parameters
$c_{i,sp} = \frac{1}{2(\sum_{j=1}^N B_{ij}S_{p,j})}$	$c_{i,c} = \frac{1}{2(\sum_{j=1}^N B_{ij}S_{c,j})}$	$c_{i,s} = \frac{1}{2(\sum_{j=1}^N B_{ij}S_{m,j})}$	$S_{m,ij} \equiv -\frac{c_j^{II}-c_j^I}{c_j^{II}-c_j^I}$
	$\sum_{j=1}^N \frac{S_{c,ji}^3}{c_{j,c}^3} = 0$	$\sum_{j=1}^N S_{m,ji} ((\frac{c_j^I}{c_{j,s}} - 1) + (\frac{c_j^{II}}{c_{j,s}} - 1)) = 0$	$S_{z,ji} = -1$
		$W(-\frac{c_j^I}{c_{j,s}} e^{-\frac{c_j^I}{c_{j,s}}}) = W(-\frac{c_j^{II}}{c_{j,s}} e^{-\frac{c_j^{II}}{c_{j,s}}})$	$S_{z,ij} = -\frac{1}{S_{z,ji}S_{z,ji}} = \frac{1}{S_{z,ji}}$

by Thewes et al. (2023). The second virial coefficients B_{ij} are assumed to form a (symmetric) matrix, composed of diagonal elements that can be randomly chosen due to the large number of components present, allowing randomization in this choice, with an average value b' and a standard deviation σ and off-diagonal elements with an average value b and also a standard deviation σ . The virial coefficients satisfy the criterion of statistical independence, and their absolute value is smaller than a finite value. These assumptions ensure that the virial coefficients, i.e., the matrix components, can be randomly chosen according to a predefined distribution. This considerably simplifies many aspects of the calculations of the spinodal manifold of such mixtures. The premise of the RMT is that if the random matrix is large enough, the actual values of B_{ij} typically do not matter anymore and only their average and standard deviations are of importance, and for some aspects, even the details of the distribution itself do not play a role anymore. It is not completely clear, however, which simplifications in the calculations are driven by mathematical convenience and which ones are driven by physical relevance, thus yielding some words of caution while applying the RMT approach, as was also mentioned by Jacobs (2023). The exact analytical expressions given in Table 2 allow us to separate the mathematical aspects of the RMT approach from the physical aspects in the calculation. In particular, the results in Table 2 encompass the critical point, the coexistence manifold, and the spinodal manifold, whereas the RMT only yields the spinodal manifold, often with more severe assumptions regarding the concentrations of the different components being all equal. For the present article, a direct comparison between the predictions of the RMT and Table 2 is out of scope.

5 Conclusion

The equilibrium phase behavior of multicomponent systems is relevant for understanding gelation of such mixtures. Controlling the gel properties can be attained via controlling the structures being formed during the non-equilibrium processes taking place during gel formation, while crossing equilibrium phase boundaries.

We have described the theoretical (numerical) work on predicting the equilibrium phase behavior of a multicomponent system consisting of polydisperse polymers and compared this to the experimental data on the phase diagram. Taking into account the polydispersity helps to more accurately predict the particular form of the spinodal and binodal.

Polydispersity plays an important role in the phase behavior of the polydisperse polymers PEO and dextran. The components with a larger-than-average molecular weight govern the transition between

one and two phases close to the phase boundary in their respective depleted concentration ranges. This causes a decrease in miscibility and a shift of the phase boundary to lower concentrations. This causes drastic changes to the shape of the phase boundary. When both components are polydisperse, the phase boundary drastically changes shape, and changes from a U-shape to a W-shape. It is not only the phase boundary that changes shape, but the spinodal curve also has different boundaries depending on the polydispersity. Even though multi-phase separations for mixtures with the fitted interactions are possible, the existing particle size distributions of PEO and dextran make concentrations resulting in multi-phase systems unattainable.

Upon demixing, the distribution of polydisperse components changes in each phase (Supplementary Materials). This fractionation is dependent on the parent distribution, the pair-wise interaction between the components of the same type, the pair-wise interaction of the components of a different type, and the concentration of both components in the parent mixture.

Our method of incorporating polydispersity allows for a more precise prediction of the phase boundary compared to assuming monodispersity, especially in the metastable region. Next to that, our method allows for prediction of the concentration and fractionation of each component in each phase depending on the parent concentration and the volume fraction of the said phases.

The best fit with the available data to the experimental data was when dextran was polydisperse and PEO was monodisperse.

Data availability statement

The raw data supporting the conclusion of this article will be made available by the authors, without undue reservation.

Author contributions

LS: conceptualization, investigation, methodology, manuscript writing—review and editing, data curation, software, and visualization. BPCD: investigation, methodology, visualization, manuscript writing—review and editing, and funding acquisition. AB: conceptualization, formal analysis, investigation, methodology, and manuscript writing—review and editing. PV: conceptualization, formal analysis, investigation, methodology, software, supervision, and manuscript writing—review and editing. EvL: conceptualization, funding acquisition, investigation, methodology, project administration, supervision, manuscript writing—original draft, review, and editing.

Funding

The author(s) declare financial support was received for the research, authorship, and/or publication of this article. BPCD acknowledges funding from the Indonesia Endowment Fund for Education (LPDP—Lembaga Pengelola Dana Pendidikan) scholarship, Ministry of Finance, The Republic of Indonesia.

Conflict of interest

Author AB was employed by Unilever.

The remaining authors declare that the research was conducted in the absence of any commercial or financial relationships that could be construed as a potential conflict of interest.

References

- Albertsson, P.-Å. (1970). Partition of cell particles and macromolecules in polymer two-phase systems. *Adv. Protein Chem.* 24, 309–341. doi:10.1016/s0065-3233(08)60244-2
- Bagnani, M., Nyström, G., De Michele, C., and Mezzenga, R. (2019). Amyloid fibrils length controls shape and structure of nematic and cholesteric tactoids. *ACS Nano* 13 (1), 591–600. doi:10.1021/acsnano.8b07557
- Beegle, B. L., Modell, M., and Reid, R. C. (1974). Thermodynamic stability criterion for pure substances and mixtures. *AIChE J.* 20 (6), 1200–1206. doi:10.1002/aic.690200621
- Bot, A., Dewi, B. P. C., and Venema, P. (2021a). Addition to “phase-separating binary polymer mixtures: the degeneracy of the virial coefficients and their extraction from phase diagrams”. *ACS Omega* 6 (30), 20086–20087. doi:10.1021/acsomega.1c03331
- Bot, A., Dewi, B. P. C., and Venema, P. (2021b). Phase-separating binary polymer mixtures: the degeneracy of the virial coefficients and their extraction from phase diagrams. *ACS Omega* 6 (11), 7862–7878. doi:10.1021/acsomega.1c00450
- Bot, A., van der Linden, E., and Venema, P. (2023). *Phase separation in complex mixtures with many components: analytical expressions for spinodal manifolds*. Arxiv 2306.17600. Available at: <https://doi.org/10.48550/arXiv.2306.17600>.
- Bot, A., and Venema, P. (2023). Phase behavior of ternary polymer mixtures in a common solvent. *ACS Omega* 8 (31), 28387–28408. doi:10.1021/acsomega.3c02604
- Chatellier, J. Y., Durand, D., and Emery, J. R. (1985). Critical helix content in gelatin gels. *Int. J. Biol. Macromol.* 7 (5), 311–314. doi:10.1016/0141-8130(85)90030-3
- Corless, R. M., Gonnet, G. H., Hare, D. E. G., Jeffrey, D. J., and Knuth, D. E. (1996). On the LambertW function. *Adv. Comput. Math.* 5 (1), 329–359. doi:10.1007/bf02124750
- Dewi, B. P. C., van der Linden, E., Bot, A., and Venema, P. (2020). Second order virial coefficients from phase diagrams. *Food Hydrocoll.* 101, 105546. doi:10.1016/j.foodhyd.2019.105546
- Dewi, B. P. C., van der Linden, E., Bot, A., and Venema, P. (2021). Corrigendum to “second order virial coefficients from phase diagrams.” [Food Hydrocolloids 101 (2020) 105546]. *Food Hydrocoll.* 112, 106324. doi:10.1016/j.foodhyd.2020.106324
- Dijkstra, M., Brader, J. M., and Evans, R. (1999). Phase behaviour and structure of model colloid-polymer mixtures. *J. Phys. Condens. Matter* 11, 10079–10106. doi:10.1088/0953-8984/11/50/304
- Döbert, F., Pfennig, A., and Stumpf, M. (1995). Derivation of the consistent osmotic virial equation and its application to aqueous poly(ethylene glycol)–dextran two-phase systems. *Macromolecules* 28 (23), 7860–7868. doi:10.1021/ma00127a037
- Dos Santos, T. E., Loh, W., and Pessôa-Filho, P. D. A. (2004). Phase equilibrium in aqueous two-phase systems containing ethylene oxide-propylene oxide block copolymers and dextran. *Fluid Phase Equilibria* 218 (2), 221–228. doi:10.1016/j.fluid.2004.01.001
- Edelman, M. W., Tromp, R. H., and van der Linden, E. (2003). Phase-separation-induced fractionation in molar mass in aqueous mixtures of gelatin and dextran. *Phys. Rev. E* 67 (2), 021404. doi:10.1103/physreve.67.021404
- Ersch, C., Meijvogel, L. L. C., van der Linden, E., Martin, A., and Venema, P. (2016). Interactions in protein mixtures. Part I: second virial coefficients from osmometry. *Food Hydrocoll.* 52, 982–990. doi:10.1016/j.foodhyd.2015.07.020
- Gaube, J., Höchemer, R., Keil, B., and Pfennig, A. (1993). Polydispersity effects in the system poly(ethylene glycol) + dextran + water. *J. Chem. Eng. Data* 38 (2), 207–210. doi:10.1021/je00010a005
- Heidemann, R. A. (1994). *The classical theory of critical points*. Dordrecht: Springer, 39–64.
- Heidemann, R. A., and Khalil, A. M. (1980). The calculation of critical points. *AIChE J.* 26 (5), 769–779. doi:10.1002/aic.690260510
- Jacobs, W. M. (2023). Theory and simulation of multiphase coexistence in biomolecular mixtures. *J. Chem. Theory Comput.* 19, 3429–3445. doi:10.1021/acs.jctc.3c00198
- Johansson, G., and Walter, H. (1999). Partitioning and concentrating biomaterials in aqueous phase systems. *Int. Rev. Cytol.* 192 (1896), 33–60. doi:10.1016/s0074-7696(08)60521-5
- Johansson, H. O., Karlström, G., Tjerneld, F., and Haynes, C. A. (1998). Driving forces for phase separation and partitioning in aqueous two-phase systems. *J. Chromatogr. B Biomed. Appl.* 711 (1–2), 3–17. doi:10.1016/s0378-4347(97)00585-9
- Joly-Duhamel, C., Hellio, D., Ajdari, A., and Djabourov, M. (2002a). All gelatin networks: 2. The master curve for elasticity. *Langmuir* 18 (19), 7158–7166. doi:10.1021/la020190m
- Joly-Duhamel, C., Hellio, D., and Djabourov, M. (2002b). All gelatin networks: 1. Biodiversity and physical chemistry. *Langmuir* 18 (19), 7208–7217. doi:10.1021/la020189n
- Kang, C. H., and Sandler, S. I. (1988). Effects of polydispersity on the phase behavior of the aqueous two-phase polymer systems. *Macromolecules* 21 (10), 3088–3095. doi:10.1021/ma00188a029
- Larsson, M., and Mattiasson, B. (1988). Characterization of aqueous two-phase systems based on polydisperse phase forming polymers: enzymatic hydrolysis of starch in a PEG–starch aqueous two-phase system. *Biotechnol. Bioeng.* 31 (9), 979–983. doi:10.1002/bit.260310910
- Larsson, M., and Mattiasson, B. (1992). Molecular weight distribution analysis of water-soluble polymers using aqueous two-phase systems. *Ann. N. Y. Acad. Sci.* 672 (1), 649–656. doi:10.1111/j.1749-6632.1992.tb32741.x
- McMillan, W. G., and Mayer, J. E. (1945). The statistical thermodynamics of multicomponent systems. *J. Chem. Phys.* 13 (7), 276–305. doi:10.1063/1.1724036
- Nguyen, M., and Vaikuntanathan, S. (2016). Design principles for nonequilibrium self-assembly. *Proc. Natl. Acad. Sci. U. S. A.* 113 (50), 14231–14236. doi:10.1073/pnas.1609983113
- Normand, V., Muller, S., Ravey, J.-C., and Parker, A. (2000). Gelation kinetics of gelatin: A master curve and network modeling. *Macromolecules* 33 (3), 1063–1071. doi:10.1021/ma9909455
- Normand, V., and Parker, A. (2003). “Scaling in the dynamics of gelatin gels,” in Proceedings of the third International Symposium on Food Rheology and Structure Lappersdorf, Germany, 2003 (Kerschensteiner Verlag).
- Poulin, P., Bibette, J., and Weitz, D. A. (1999). From colloidal aggregation to spinodal decomposition in sticky emulsions. *Eur. Phys. J. B. Condensed. Matter. Complex. Systems.* 7 (2), 277–281. doi:10.1007/s100510050614
- Reid, R. C., and Beegle, B. L. (1977). Critical point criteria in legendre transform notation. *AIChE J.* 23 (5), 726–732. doi:10.1002/aic.690230515
- Sear, R. P., and Cuesta, J. A. (2003). Instabilities in complex mixtures with a large number of components. *Phys. Rev. Lett.* 91 (24), 245701. doi:10.1103/physrevlett.91.245701
- Sturtewagen, L. (2020). *Predicting phase behavior of multi-component and polydisperse aqueous mixtures using a virial approach*. PhD Thesis. Wageningen: Wageningen University.

Publisher’s note

All claims expressed in this article are solely those of the authors and do not necessarily represent those of their affiliated organizations, or those of the publisher, editors, and reviewers. Any product that may be evaluated in this article, or claim that may be made by its manufacturer, is not guaranteed or endorsed by the publisher.

Supplementary material

The Supplementary Material for this article can be found online at: <https://www.frontiersin.org/articles/10.3389/frsfm.2023.1328180/full#supplementary-material>

- Sturtewagen, L., and van der Linden, E. (2021). Effects of polydispersity on the phase behavior of additive hard spheres in solution. *Molecules* 26 (6), 1543. doi:10.3390/molecules26061543
- Sturtewagen, L., and van der Linden, E. (2022). Towards predicting partitioning of Enzymes between macromolecular phases: effects of polydispersity on the phase behavior of nonadditive hard spheres in solution. *Molecules* 27 (19), 6354. doi:10.3390/molecules27196354
- Sturtewagen, L., and van der Linden, E. (2023). Ternary mixtures of hard spheres and their multiple separated phases. *Molecules* 28 (23), 7817. doi:10.3390/molecules28237817
- Thewes, F. C., Krüger, M., and Sollich, P. (2023). Composition dependent instabilities in mixtures with many components. *Phys. Rev. Lett.* 131 (5), 058401. doi:10.1103/physrevlett.131.058401
- van der Linden, E. (2012). From peptides and proteins to micro-structure mechanics and rheological properties of fibril systems. *Food Hydrocoll.* 26 (2), 421–426. doi:10.1016/j.foodhyd.2010.11.019
- van der Linden, E., and Parker, A. (2005). Elasticity due to semiflexible protein assemblies near the critical gel concentration and beyond. *Langmuir*. 21 (21), 9792–9794. doi:10.1021/la051312o
- Wigner, E. P. (1967). Random matrices in physics. *SIAM Rev.* 9 (1), 1–23. doi:10.1137/1009001
- Zhao, Z., Li, Q., Ji, X., Dimova, R., Lipowsky, R., and Liu, Y. (2016). Molar mass fractionation in aqueous two-phase polymer solutions of dextran and poly(ethylene glycol). *J. Chromatogr. A* 1452, 107–115. doi:10.1016/j.chroma.2016.04.075



OPEN ACCESS

EDITED BY

Raffaele Mezzenga,
ETH Zürich, Switzerland

REVIEWED BY

Mike Boland,
Massey University, New Zealand
Lilia Ahrné,
University of Copenhagen, Denmark

*CORRESPONDENCE

Daniel Dikovsky,
✉ daniel.dikovsky@redefinemeat.com

RECEIVED 24 November 2023

ACCEPTED 22 January 2024

PUBLISHED 06 February 2024

CITATION

Dikovsky D (2024), Addressing the structural sophistication of meat via plant-based tissue engineering.
Front. Soft Matter 4:1343906.
doi: 10.3389/frsfm.2024.1343906

COPYRIGHT

© 2024 Dikovsky. This is an open-access article distributed under the terms of the [Creative Commons Attribution License \(CC BY\)](#). The use, distribution or reproduction in other forums is permitted, provided the original author(s) and the copyright owner(s) are credited and that the original publication in this journal is cited, in accordance with accepted academic practice. No use, distribution or reproduction is permitted which does not comply with these terms.

Addressing the structural sophistication of meat via plant-based tissue engineering

Daniel Dikovsky*

Redefine Meat Ltd., Rehovot, Israel

The escalating environmental impact of traditional livestock farming, particularly beef production, has spurred the search for sustainable meat alternatives. This study introduces a novel Plant-Based Tissue Engineering (PBTE) approach, to replicate the complex structure and sensory experience of whole-muscle cuts of meat using plant-based ingredients. Leveraging principles of tissue engineering and advanced food manufacturing technologies, PBTE deconstructs meat into its fundamental components: muscle, fat, and connective tissue, and reconstructs them using a combination of plant proteins, fats and polysaccharide materials. The muscle component is reassembled to mimic the anisotropic fibrous structure of beef, while the fat component is engineered through lipid encapsulation within a hydrocolloid matrix. Advanced manufacturing techniques, including additive manufacturing and robotics, are utilized for precise spatial configuration and assembly of these components. Our findings demonstrate that PBTE can effectively replicate the mechanical integrity, texture, and sensory attributes of traditional meat, presenting a promising alternative that could significantly reduce the environmental footprint of meat production. This approach aligns with the principles of Soft Matter in the manipulation of artificial structures and materials for mimicking naturally occurring designs, such as whole cut meat foods. It also holds substantial potential for revolutionizing the alternative protein industry by catering to a broader consumer base, including flexitarians and meat-eaters.

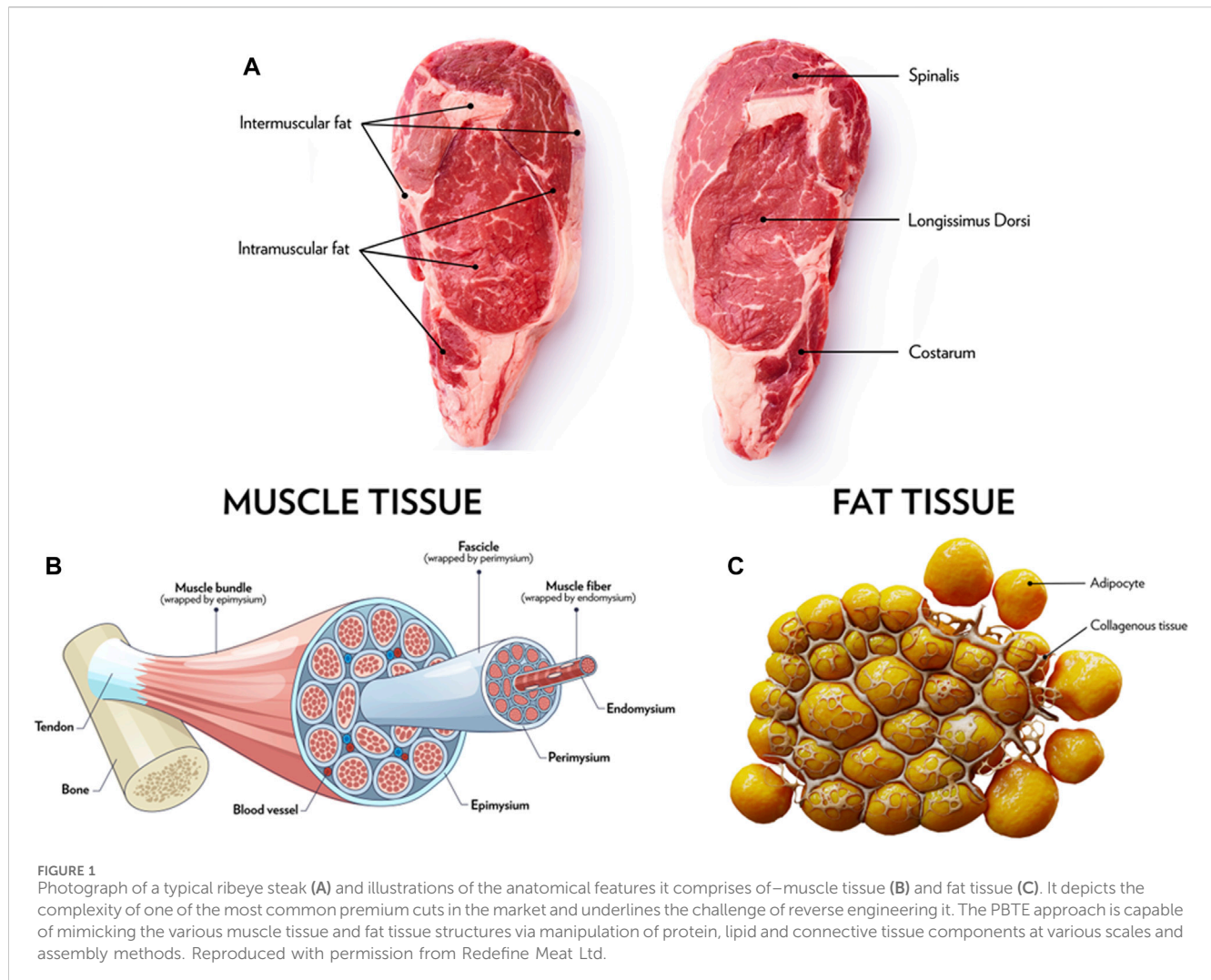
KEYWORDS

meat analog, beef, connective tissue, additive manufacturing, tissue engineering, plant-based meat

1 Introduction

Beef production is an especially resource-intensive industry. There is mounting evidence linking livestock farming to high greenhouse gas (GHG) emissions and to climate change (Steinfeld, 2006; Garnett, 2009; Heng et al., 2022). The beef industry's high ecological footprint underscores the urgent need for environmentally sound alternatives to traditional beef products, including whole-muscle cuts, which comprise a substantial portion of market sales (Close, 2014). As a result, the technological and scientific communities are those working on creative solutions to make meat production more sustainable (Kumar et al., 2022).

Meat substitutes have been an active part of the modern food industry, beginning with Kellogg's Protose (Protose, 1900). But despite advancements in the past century, alternative meat products have often been marketed mainly to vegetarian and vegan consumers, excluding broader segments of the population such as flexitarians. One reason for this is the apparent dissatisfaction of the market with the flavor and texture of meat alternatives



(Appiani et al., 2023). Another challenge is the limited structural sophistication, which has prioritized the development of high volume, low value products such as minced meat and chicken nuggets and excluded the complex nuances of premium products such as whole-muscle cuts of meat (Schreuders et al., 2021; Bushnell et al., 2022).

New approaches, such as better protein texturization methods (Dekkers et al., 2018), are improving the sensory appeal of plant-based meat. Still, the market is missing a systemic approach that addresses the multifaceted traits of meat. This article proposes a pioneering methodology that draws from the principles of tissue engineering and repurposes them using plant-based components, supported by advanced manufacturing technologies. The Plant-Based Tissue Engineering (PBTE) approach originated by Redefine Meat (Ben-Shitrit et al., 2020; redefinemeat) not only addresses the structural and sensory challenges of legacy plant-based products, but has the potential to mimic the full spectrum of animal meat products. We claim that PBTE has could significantly alter the landscape of meat consumption by addressing the expectations of quality, range and versatility of the broader base of consumers that, unlike the captive market segments of vegans and vegetarians, consume animal meat today (Broad, 2020).

2 Meat through the perspective of tissue engineering

2.1 Introduction to tissue engineering and meat structure

Tissue engineering, a discipline established in the 1960s, depicts living organisms as assemblages of various tissues, each characterized by complex architectures that involves diverse cell types and extracellular matrices that serve distinct biological and biomechanical functions (Ikada, 2006; Vacanti, 2006). Although they focus mainly on biomedical applications for repairing living tissues, these principles can also offer a new lens through which to study and replicate the structure of livestock meat, a “product” comprising muscle tissue, connective tissue, adipose tissue, and bone (Ben-Arye and Levenberg, 2019) (Figure 1).

2.2 Understanding the complexity of meat

In its processed form, the elements of meat are intricately organized to form familiar elements or “products” such as steaks,

which offer a unique culinary and organoleptic experience. Animal meat, with its inherent heterogeneous structure (such as the varied distribution of fat and muscle) and anisotropic characteristics (owing to muscle fibers and the orientation of connective tissue), presents a sophisticated challenge in food technology. The complex thermal transition during cooking, which is driven by the reactions of proteins and other biomolecules to heat, significantly influences its perceived quality and consumer experience (Tornberg, 2005; Yu et al., 2017). Previous attempts to replicate whole-muscle cuts with plant-based ingredients (Dekkers et al., 2018) often fell short of expectations, resulting in products with limited appeal to omnivores and minimal penetration beyond the vegetarian market (Szenderák et al., 2022).

2.3 The PBTE approach to meat replication

The Plant-Based Tissue Engineering (PBTE) approach addresses these complexities by deconstructing meat into simpler elements, and then mimicking them using accessible food manufacturing technologies, before reassembling them using innovative fabrication methods inspired by Additive Manufacturing (Hertafeld et al., 2019) and robotics. This section describes each of the main tissue elements and its relevant characteristics, highlighting the aspects that are crucial to replicating the meat-eating experience. It outlines the sufficient structural elements and behaviors that are required for successful imitation of the organoleptic qualities of meat, but at the same time strives to limit the complexity of the reverse-engineered tissue components and their spatial resolution accuracy to avoid unnecessary development and production costs (GFI, 2022).

2.3.1 Muscle tissue

The skeletal muscle tissue (Figure 1B) relevant to meat is composed of approximately 65%–75% water and 18%–23% protein, forming a hierarchical structure of muscle fibers interconnected by a network of connective tissue (Purslow, 2023). These fibers, organized into sarcomeres, myofibrils, fascicles, and complete muscles, are further interlinked by connective tissue elements such as endomysium, perimysium, and epimysium (Nishimura, 2010a; Purslow, 2020). Typically, whole muscle cuts are butchered to orient muscle fibers consistently, contributing to the meat's anisotropic characteristics, such as varying tensile, compression, and shear behaviors (Lepetit and Culioli, 1994), resulting in substantially different values when measured along vs. across fiber direction. The fibrous morphology and orientation are evident during manual or oral breakdown of meat (LILLFORD, 2001), impacting the organoleptic experience of its consumption. The physical properties of these fibers also influence the behavior of meat in raw and cooked form. Upon thermal processing, for example, muscle fibers contract (Purslow et al., 2016), expelling meat exudate rich in peptides and metabolites that are crucial for the Maillard reaction and flavor development (Mottram, 1998), altering simultaneously the aroma, juiciness, and appearance of meat (Flores, 2023).

2.3.2 Adipose tissue (fat)

Beef cuts typically contain between 10% and 25% of fat, which varies with the type of cut and the breed. This tissue is composed of about 90% lipids, 8% water and 2% proteins and is distributed as large intermuscular and subcutaneous inclusions or thinner intramuscular layers (Figure 1A), significantly influencing meat quality and culinary experience (Wood et al., 2008). Fat tissue consists of lipid-rich adipose cells encapsulated in a collagenous connective tissue matrix (Figure 1C), with cells about 0.1 mm in diameter and its surrounding collagenous tissue less than 0.01 mm thick (Tordjman, 2012). The lipid component of beef fat, known as tallow, has a melting point around 40°C–45°C (Grompone, 1989). During cooking lipids melt, altering the appearance and texture of the fat, but leaving the overall structure intact due to the thermally stable connective tissue matrix, which releases most lipids during chewing rather than cooking and contributes to the characteristic mouthfeel of fat (Frank et al., 2016).

2.3.3 Connective tissue

In muscle tissue, connective tissue (CT) structures such as endomysium, perimysium, and epimysium (Figure 1B) play vital roles in texture and integrity (Purslow, 2002; Nishimura, 2010a; Purslow, 2018). The perimysium, particularly significant due to its encasement of fascicle structures, is a thin and strong crossed-ply structure composed of partially cross-linked collagen fibers, constituting about 10% of muscle's dry mass (Bendall, 1967). Its properties, including significant strength and flexibility, are major contributors to meat toughness, with higher CT fractions typically leading to lower tenderness (Roy and Bruce, 2023). When cooked, collagen partially melts, but the cross-linked fraction remains, maintaining interconnectivity of muscle fibers. Extended cooking can degrade CT, affecting the meat's textural properties (Weston et al., 2002).

2.3.4 The organization of whole-muscle cuts

The diversity of whole muscle cuts in beef reflects varied arrangements of muscles and fat (Figure 1A), contributing to the unique characteristics of different steak types. These variations are influenced by multiple factors, including the animal's breed, growth conditions, feed, age, and butchery techniques, such as the specific area of the cut, meat aging, and processing conditions (Chriki et al., 2013). Each steak can be analyzed in terms of protein and fat composition, the amount of connective tissue, fat distribution, and the presence of bones—all of which contribute to the culinary classification, perceived quality, and market value (Dransfield, 1977).

The gastronomic qualities of meat are not solely determined by intrinsic properties but are also significantly influenced by the culinary process. Cooking methods, temperatures, and durations can drastically alter the texture, flavor, and nutritional value of the meat. For example, the Maillard reaction, which occurs during certain types of cooking, greatly enhances flavor and aroma, contributing to the overall appeal of the dish (Bailey, 1994; Mottram and Elmore, 2005).

This intricate balance of biological structure and culinary science underscores the challenge in replicating these characteristics in plant-based alternatives. It is crucial to consider these parameters when attempting to recreate the complex

architecture of whole-muscle cuts. The PBTE approach aims to address these challenges by meticulously analyzing and mimicking these properties using plant-based ingredients, assembling them in a manner that replicates the nuanced structure and sensory experience of traditional meat cuts. The subsequent sections will detail how each tissue type is analyzed, its key structural and physical parameters identified, and the methods used to reconstruct these elements with plant-based materials before assembling them into a cohesive, steak-like structure.

3 Reconstructing whole-muscle cuts of meat using the PBTE approach

3.1 Muscle component: Generating fascicles

One of the guiding principles of our development process was that it would need to address a set of key characteristics to successfully imitate muscle components:

- High protein content: This is essential if we aim to match the nutritional profile of meat.
- Anisotropic fibrous structure: Visible muscle strands (1–5 mm thick) that are densely packed and separable, mirroring the jagged-shaped interface morphology of natural meat. Resistance to shear should be higher across the fibers than along the fibers, aligning with values observed in livestock meat.
- Texture and Hardness: Defined by typical Texture Profile Analysis (TPA) tests, 20 mm cubic specimens at 70% strain should meet the load resistance values of raw (about 20–40N) and cooked (about 50–80N) livestock meat.
- Manufacturing ability: Allowing to form into steak-relevant form factor, say having dimensions of at least 150 × 80 × 15 mm.
- Liquids: Containing at least 60% water and usually some lipids as well. These liquid components are responsible for the experience of juiciness and for the development and delivery of taste and aroma during cooking and consumption.
- Color: Purple-red when raw, transitioning to grey-brown after cooking.

It is important to mention, that this is a minimal set of characteristics providing the entry-point to steak-relevant texture. Further analysis of tensile behavior, shear behavior and sensory analysis is crucial for generating a product that will be accepted by consumers.

Current alternative meat production methods, such as protein extrusion (Areas, 1992; Dekkers et al., 2018), are inadequate to meet all the above requirements. TVP (Textured Vegetable Protein) (Emin and Schuchmann, 2017) and HME (High Moisture Extrusion) (Lin et al., 2000) techniques fall short in mimicking all the above requirements to replicate the specific texture and structural integrity of meat. TVP is too porous and HME is too dense and impermeable, and neither can be formed into a steak form factor (e.g., at least 150 × 80 × 15 mm), while providing relevant orientation of fibers.

Methods like shear cell (Krintiras et al., 2016) address the dimensional requirements yet fall short in providing beef-relevant texture. Other techniques, such as spinning (Mattis and Marangoni, 2020), fail to provide sufficient throughput at an acceptable cost. Bioengineering approaches, such as mycelium (Kyoungju et al., 2011) or animal tissue culture (Post, 2012) still lack the required texture demands - and require supplementing them with plant-based texture elements (Ben-Arye et al., 2020), but even then, they fail to deliver the relevant meat performance operating in industrial environments (Post et al., 2020).

To meet the requirements of the muscle component, our research proposes disintegrating the tough and chewy TVP material into separate fibers (0.2–2 mm in diameter, about 2–20 mm in length), blending them with a proteinous dough made from soy or pea isolates (Ben-Shitrit et al., 2021). A typical TVP product suiting the toughness criteria typically comprises about 50% wheat protein and soy protein and has relatively low (<250% w/w) water holding ability, such as DuPont Danisco SUPRO® MAX 5050. This dough, when extruded using a progressive cavity pump (PCP, PCM Ecomoineau™ C) through a 3 mm nozzle, delivers strands that imitate the hierarchical structure of fibrous livestock meat, namely, stacked fascicles (Ben-Shitrit et al., 2021). To form a macroscopic muscle section, the deposition is made according to typical 3D-printing protocols, in a self-supporting manner, as the dough viscosity is sufficiently high (>300 P) to prevent gravitational flow or sagging at the fabrication temperature that is set to about 4°C to meet food safety requirements. Unidirectional deposition of such strands results in structure having prominent anisotropic behavior and its resistance to shear being comparable to that of animal meat. This approach allows the projection of the meat-like texture of TVP, but in a flexible manner, and in a scalable manner. At the same time, this muscle-like structure alone is insufficient in meeting livestock meat's tensile behavior values and fully mimic its inter-fascicle failure mechanisms. This deficiency required the development and introduction of a component that would act as connective tissue and reinforce the composite structure of the meat alternative and upgrade its toughness and behavior during cooking and eating (such as the disintegration of fibers) in a way that matches the behavior of animal meat.

3.2 From fascicles to muscle tissue

Developing a connective tissue (CT) component posed a few significant challenges:

- Obtaining Food-Grade Ingredients and Processes: Using ingredients and formulations that are safe and compliant for consumption, while meeting the structural requirements listed below. Most plant-based edible materials lack the strength that is characteristic of animal tissues.
- Formation into thin laminates less than 0.05 mm thick, to mimic naturally occurring connective tissue. Conventional food technologies do not require high spatial accuracy and are limited in providing such level of structural fidelity.

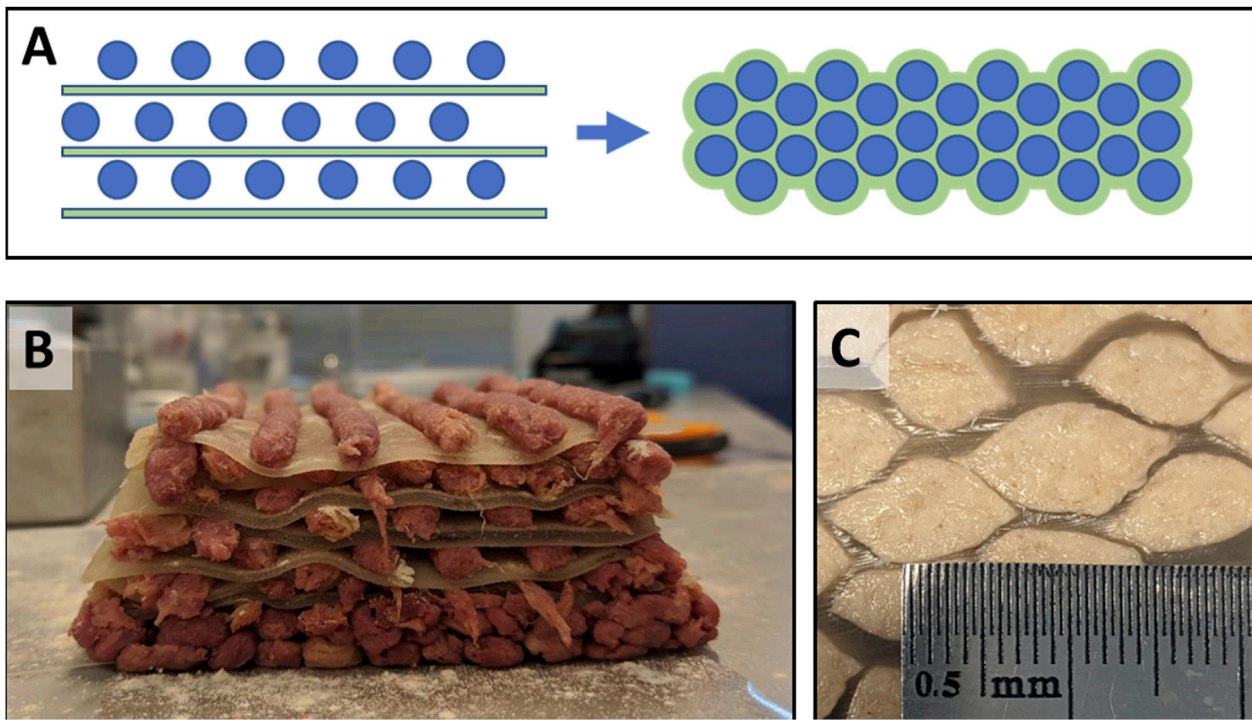


FIGURE 2 Demonstrating the importance of connective tissue for mimicking the complex mechanical behavior of livestock meat. Schematic illustration of muscle tissue fabrication process presented in cross-sectional view, where the circles represent extruded PB muscle strands and the lines represent sheets of edible material that laid in between to imitate CT component. The deposition sequence (A) and the resulting muscle tissue structure after compactization and thermal post-processing cycle that fuses the CT layers together into a continuous comb-shaped matrix. Photographs showing the composite structure of PB muscle tissue before compactization (B) and after (C). Reproduced with permission from Redefine Meat Ltd.

TABLE 1 Tensile behavior of meat with and without Connective Tissue Component.

Tensile strength (MPa)	Along fibers	St. Dev	Across fibers	St. Dev
Livestock Psoas Major References	0.062	0.006	0.026	0.006
Plant-based muscle without Connective Tissue component	0.032	0.002	0.011	0.005
Plant-based muscle with Connective Tissue component	0.056	0.003	0.022	0.014

c. **Strength and Durability:** Minimum tensile strength of 1 MPa in a 70% water environment when raw and retaining at least 0.2 MPa strength after heating to 75°C. This humidity level corresponds to hydrogels that are typically weak and brittle and require obtaining formulation with exceptional molecular bonding for delivering such strength.

We found that carrageenan-based materials with melting temperatures around 90°C fulfil these requirements and could be cast into films, which are then introduced in-between the fascicles during layer-wise fabrication (Figures 2A,B), while setting one step interlace between the strands (Dikovsky and Hausner, 2022). Post-hydration and thermal processing result in fusion of the carrageenan films and formation of continuous comb-shaped network (Figure 2C), with tensile strengths mimicking that of animal meat. Table 1 compares the tensile strength of meat measured along and across the direction of the fibers. It shows that the addition of the CT component

substantially improves the performance of PB meat, matching its strength to that of a tenderloin (Psoas Major) at 90% at longitudinal direction and 85% at transverse direction. Moreover, the plant-based muscle with CT demonstrates a different failure mode upon stretching (Figure 3A), that is comparable to livestock meat (Figure 3B) and substantially different from plant-based muscle without CT (Figure 3C). Internal sensory panel tests (n = 30) indicated 82% preference for alternative meat samples that contained CT compared to those without CT, with specific feedback from participants noting improvements in texture and appearance. The characteristic fibrous texture of such meat is shown after dissection in Figure 2G.

The muscle component and connective tissue component are integrated into a system that employs additive manufacturing methods accompanied by robotic film deposition, altogether digitally controlled, to deliver about a variety of alternative meat muscle tissue structures. The following parameters can easily be adapted to control the toughness, fibrousness, chewiness and cooking behavior of the alternative meat:

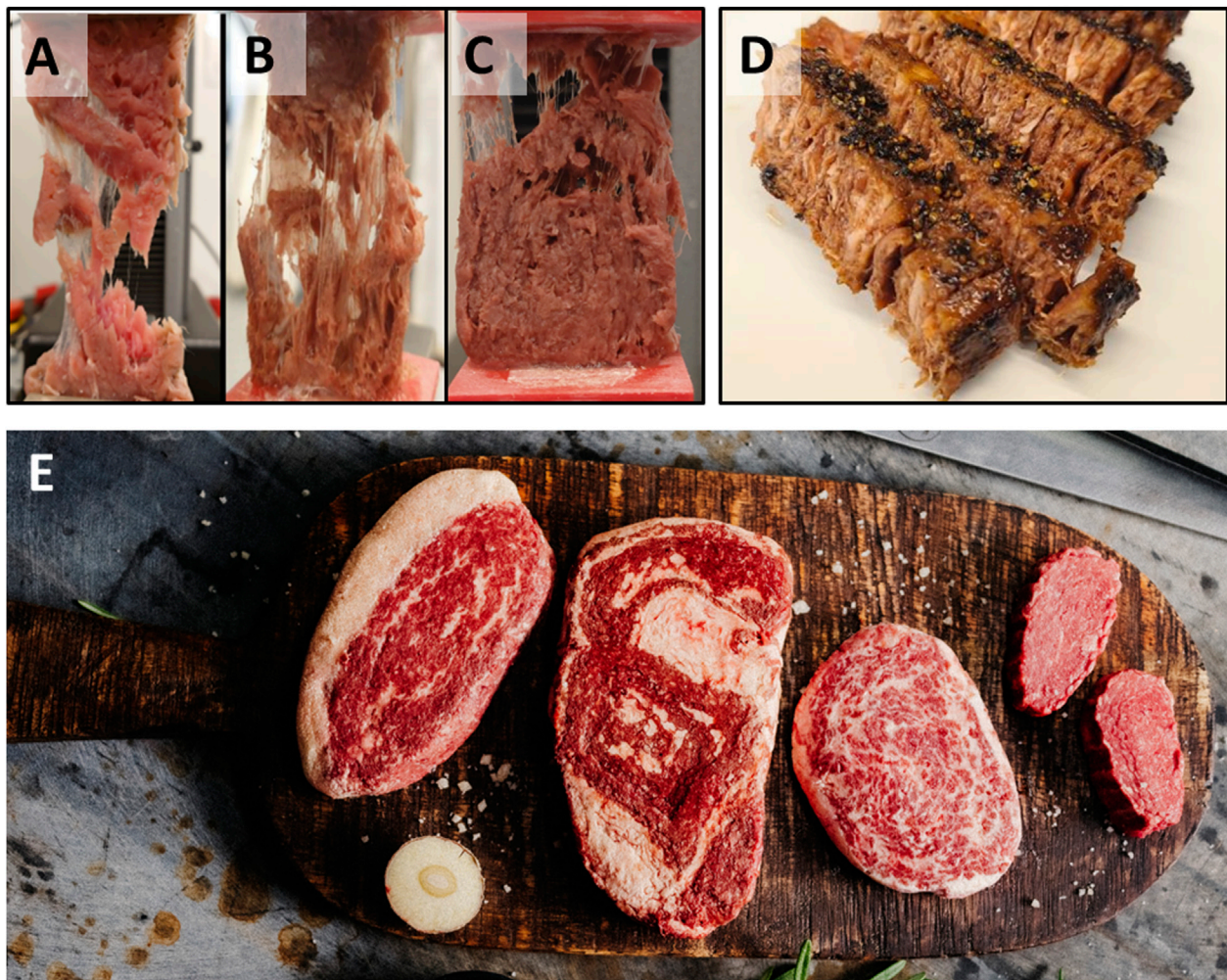


FIGURE 3
Demonstrating the structure and behavior of complete alt-meat whole-muscle cuts made via PBTE approach. Photographs of 3 types of raw meat subjected to tensile extension: livestock Psoas Major muscle (A), PB muscle with CT (B) and PB muscle without CT (C). Photograph of sliced cooked steak made via the PBTE approach (D). Photograph of raw PB steaks, each of which was created using advanced manufacturing that used the same set of muscle, fat and connective tissue components, but different fabrication protocols (E). Reproduced with permission from Redefine Meat Ltd.

- Type of TVP
- Fraction of TVP in the muscle component
- The composition of the Proteinous dough as well as its water percentage
- Thickness of muscle strands
- CT film composition, e.g., carrageenan ratio
- CT film thickness
- Additional adhesive layers between CT and muscle strands

The final last component in the list of components is fat, and fat distribution and marbling.

3.3 Fat

The fat component, crucial to achieve the desired texture and mouthfeel, involves encapsulating a lipid formulation (melting point $>35^{\circ}\text{C}$, using primarily cacao fat) in a hydrocolloid matrix.

This matrix, composed of methylcellulose, stabilizes the fat tissue during cooking and prevents it from melting out. The high lipid content ($\geq 75\%$ w/w) ensures a substantial liquid oily phase at serving temperature (50°C), contributing to a fatty mouthfeel. The different types of fat, such as intermuscular fat and intramuscular fat, can be recreated, for example, via the variation of overall lipid content and the concentration methylcellulose in the matrix. This fat component is compatible with the additive manufacturing process, allowing precise deposition to recreate specific marbling patterns. Here too, the viscosity of the fat component paste is maintained high enough to allow self-supporting deposition using typical PCP pumps. Due to the nature of marbling in beef steaks, the fat deposition resolution may require thinner nozzles, down to 1 mm. The interconnection between the muscle component and the fat component is facilitated by the presence of the CT component that holds together the unidirectional elements that form the muscle and fat tissue regions.

3.4 Advanced food manufacturing

Breaking meat down into components and addressing each component separately allows more accurate mimicking using plant-based ingredients. However, the assembly of these components into a complete meat product requires new approaches to food manufacturing. Inspired by Additive Manufacturing (AM) and robotics, we developed a process that uses high-pressure extrusion devices and a static multi-nozzle array, delivering high-viscosity component pastes onto a digitally controlled XYZ platform (Ben-Shitrit et al., 2020). Other elements of the plant-based meat, such as the CT laminates, are dispensed via dedicated robotic modules. The use of this advanced manufacturing method enables the creation of any spatial configuration of muscle and fat, supporting the production of relevant whole-muscle cut analogs.

The Additive Manufacturing (AM) process facilitates:

- Spatial configuration control of muscle and fat and realistic marbling.
- Mass customization of steaks and cuts.
- Inducing orientation of TVP fibers in plant-based muscle strands.
- The fabrication of composite structures, such as muscle with integrated CT.
- Unidirectional deposition of muscle strands, resulting in a culinary-relevant grain when the steaks are cut (Figure 1).

While successfully exploiting the benefits of AM, it was important to address its major weakness points, namely, cost and throughput, that frequently limit its implementation in industrial applications and could impact the market potential of the current solution. This was achieved through a design-for-function approach, where the fabrication system was optimized solely for beef whole muscle cuts application, while maximizing throughput. In practice this resulted in a system operating at relatively coarse spatial resolution, depositing about 3 mm strands, with no need for support material or curing, with all strands being laid in the same orientation forming long slabs, approximately 1-m in length. Altogether, this resulted in minimal tray idle time, maximized travel velocity and low waste. Once combined with a 12-nozzle plate simultaneously depositing material, the system generated a throughput of more than 10 kg/h, an equivalent of about cow a day of alt-meat products (Mandelik et al., 2021).

Figure 3E shows a set of animal-free whole muscle cuts made using the PBTE concept and matching some of the common premium cuts, such as tenderloin, sirloin, ribeye and wagyu. All of these were cut from slabs made with the same set of muscle, fat and connective tissue components and digitally manipulated to form the desired form factor and marbling patterns.

4 Discussion and conclusion

This paper presents a novel Plant-Based Tissue Engineering (PBTE) approach, leveraging principles of tissue engineering and advanced food manufacturing to recreate the complex structure of

whole-muscle meat cuts. Our findings demonstrate that the PBTE method effectively addresses the multifaceted challenges inherent in replicating the texture, structure, and sensory attributes of traditional meat products.

4.1 Significance in the field of Soft Matter

The PBTE approach represents a significant contribution to the field of Soft Matter, particularly in food science. It showcases how the manipulation of plant-based materials at the microstructural level can lead to the development of complex, multi-component food systems. By mimicking the hierarchical structure of muscle, adipose, and connective tissues in meat, we can bridge a crucial gap in the alternative protein industry, aligning with the Soft Matter principles of understanding and engineering complex structures and materials.

4.2 Key findings

- **Muscle Tissue Replication:** Through disintegration of TVP into fibers blended with proteinous dough, we successfully mimicked the anisotropic and fibrous structure of muscle tissue. The introduction of a connective tissue component further enhanced the mechanical integrity and sensory attributes of the muscle analog, closely resembling those of animal meat.
- **Fat Tissue Engineering:** The encapsulation of lipid formulation within a hydrocolloid matrix effectively recreated the mouthfeel and texture of intramuscular fat, a key element in the sensory profile of meat.
- **Advanced Manufacturing Techniques:** Our adoption of additive manufacturing and robotic systems enabled precise spatial configuration of muscle and fat components, offering a versatile platform for producing a wide range of meat analogs. This aspect is particularly groundbreaking, showcasing the potential of multi-material 3D-printing and robotics in revolutionizing food manufacturing.

4.3 Implications and future directions

- **Environmental Impact:** Given the resource-intensive nature of traditional meat production, the PBTE method offers a more sustainable alternative to meat, potentially reducing greenhouse gas emissions and the use of resources like water, land, and energy.
- **Market Potential:** The consumption of meat around the world continues to climb, despite a growing awareness of the negative impact of animal agriculture. This is also despite the introduction of plant-based meat analogues to the market, which have so far mostly focused on imitating burgers, chicken nuggets or other meat products on the low-end of the value chain. We believe that this technology opens new avenues for the alternative meat industry to cater to a broader consumer base, including flexitarians and meat-eaters, by offering products that closely replicate the sensory experience of animal meat, including whole-muscle cuts.

- **Relevance to other meats:** The PBTE approach can be extended to mimic other types of meat, besides beef. The reconstruction of naturally-occurring sophisticated structures through their breakdown into a set of simpler components and their independent reconstruction with a different set of materials, followed by a digital assembly for resembling the complex architecture of the original object can be applied to other foods. Naturally, this requires dedicated analysis of the target meat to determine the characteristics of its tissues and their organization. Then the plant-based components analogs need to be fine-tuned to match these characteristics. However, we are confident that the set of the plant-based ingredients, formulation methods and advanced manufacturing methods described here, can address a wide range of meat products.
- **Future Research:** We believe that the versatility of our approach together with its market potential and its expected environmental impact can attract further interest and research potential within both industrial and academical domains, and help accelerate its expansion to additional markets and product types. We emphasize the importance of further progress in developing plant-based components that have tougher textures, good processability, low levels of off-flavors, good nutritional profiles, competitive cost and availability at scale, while having low environmental footprint. In parallel, we expect further acceleration of this domain through the development and adaptation of advanced manufacturing techniques to food production environments.

In conclusion, the PBTE approach marks a pivotal step in the evolution of meat alternatives. By intricately replicating the structure and texture of animal meat using plant-based ingredients, we not only address environmental and ethical concerns but also cater to the growing demand for sustainable and diverse protein sources that meet consumer expectations for taste, texture and other parameters of meat. The principles and methodologies developed in this study hold significant potential for future innovations in the Soft Matter field, particularly in helping to develop sustainable food systems.

Author's note

This perspective manuscript was prepared by the sole author, based on a presentation at the 1st Soft Matter Conference in 2023 and it summarizes major work done by Redefine Meat Ltd. research groups between 2019 and 2023, with specific contribution by: Daniel Mandelik, Sagee Schechter, Or Sabbah, Alexey Tomsov, Nissim David, Inbar Haimovich, Hay Shaino, Yael Prigat Goldfinger, Moran Cohen, Jon

Hausner, Nina Bochner, Tal Shimony-Cohen, Eshchar Ben Shitrit and Adam Lahav. The photography presented in [Figure 3E](#) was made by Roscoe Raz and May Siri and reproduced with permission from Redefine Meat Ltd.

Data availability statement

The original contributions presented in the study are included in the article/Supplementary material, further inquiries can be directed to the corresponding author.

Author contributions

DD: Writing—original draft, Writing—review and editing.

Funding

The author declares financial support was received for the research, authorship, and/or publication of this article. The work was funded by Redefine Meat Ltd. and partially by Israeli Innovation Authority (IIA). The grant number for IIA is #71520. Redefine Meat Ltd. was not involved in the study design, collection, analysis, interpretation of data, the writing of this article, or the decision to submit it for publication.

Acknowledgments

The author would like to thank prof. Peter Purslow for his advisory on this project and the organizers of the first Soft Matter Conference: prof. Alejandro Marangoni, prof. Raffaele Mezzenga, prof. Ali Miserez and prof. Frank Alexis.

Conflict of interest

Author DD was employed by Redefine Meat Ltd.

Publisher's note

All claims expressed in this article are solely those of the authors and do not necessarily represent those of their affiliated organizations, or those of the publisher, the editors and the reviewers. Any product that may be evaluated in this article, or claim that may be made by its manufacturer, is not guaranteed or endorsed by the publisher.

References

- Appiani, M., Cattaneo, C., and Laureati, M. (2023). Sensory properties and consumer acceptance of plant-based meat, dairy, fish and eggs analogs: a systematic review. *Front. Sustain. Food Syst.* 7, 1–23. doi:10.3389/fsufs.2023.1268068
- Areas, J. (1992). Extrusion of food proteins. *Crit. Rev. Food Sci. Nutr.* 32 (4), 365–392. doi:10.1080/10408399209527604
- Bailey, M. E. (1994). "Maillard reactions and meat flavour development," in *Flavor of meat and meat products* (Boston, MA: Springer US), 153–173.
- Ben-Arye, T., and Levenberg, S. (2019). Tissue engineering for clean meat production. *Front. Sustain. Food Syst.* 3, 46. doi:10.3389/fsufs.2019.00046
- Ben-Arye, T., Shandalov, Y., Ben-Shaul, S., Landau, S., Zagury, Y., Ianovici, I., et al. (2020). Textured soy protein scaffolds enable the generation of three-dimensional bovine skeletal muscle tissue for cell-based meat. *Nat. Food* 1, 210–220. doi:10.1038/s43016-020-0046-5
- Bendall, J. R. (1967). The elastin content of various muscles of beef animals. *J. Sci. Food Agric.* 18 (12), 553–558. doi:10.1002/jsfa.2740181201

- Ben-Shitrit, E., Tomsov, A., Mandelik, D., Dikovsky, D., and Silberstein, S. (2020). *Meat analogues and methods of producing the same*. WO2020109503A1.
- Ben-Shitrit, E., Tomsov, A., Mandelik, D., Hazan, N., Bochner, N., Dikovsky, D., et al. (2021). *Whole muscle meat substitute and methods of obtaining the same*. WO2021095034A1.
- Broad, G. M. (2020). Making meat, better: the metaphors of plant-based and cell-based meat innovation. *Environ. Commun.* 14 (7), 919–932. doi:10.1080/17524032.2020.1725085
- Bushnell, C., Specht, L., and Almy, J. (2022). *State of the Industry Report | Plant-based meat, seafood, eggs, and dairy*.
- Chriki, S., Renand, G., Picard, B., Micol, D., Journaux, L., and Hocquette, J. F. (2013). Meta-analysis of the relationships between beef tenderness and muscle characteristics. *Livest. Sci.* 155 (2–3), 424–434. doi:10.1016/j.livsci.2013.04.009
- Close, D. (2014). *Ground Beef Nation: the effect of changing consumer tastes and preferences on the US cattle industry*.
- Dekkers, B. L., Boom, R. M., and van der Goot, A. J. (2018). Structuring processes for meat analogues. *Trends Food Sci. Technol.* 81, 25–36. doi:10.1016/j.tifs.2018.08.011
- Dikovsky, D., and Hausner, J. (2022). *Meat analogue and method of producing the same*. WO2022089717.
- Dransfield, E. (1977). Intramuscular composition and texture of beef muscles. *J. Sci. Food Agric.* 28 (9), 833–842. doi:10.1002/jsfa.2740280910
- Emin, M. A., and Schuchmann, H. P. (2017). A mechanistic approach to analyze extrusion processing of biopolymers by numerical, rheological, and optical methods. *Trends Food Sci. Technol.* 60, 88–95. doi:10.1016/j.tifs.2016.10.003
- Flores, M. (2023). The eating quality of meat: III—flavor. *Lawrie's Meat Sci.*, 421–455. doi:10.1016/b978-0-323-85408-5.00014-5
- Frank, D., Joo, S. T., and Warner, R. (2016). Consumer acceptability of intramuscular fat. *Korean J. food Sci. animal Resour.* 36 (6), 699–708. doi:10.5851/kosfa.2016.36.6.699
- Garnett, T. (2009). Livestock-related greenhouse gas emissions: impacts and options for policy makers. *Environ. Sci. policy* 12 (4), 491–503. doi:10.1016/j.envsci.2009.01.006
- GFI (2022). *Reducing the price of alternative proteins*.
- Grompone, M. A. (1989). Physicochemical properties of fractionated beef tallows. *J. Am. Oil Chem. Soc.* 66 (2), 253–255. doi:10.1007/bf02546070
- Heng, M., McCarl, B., and Fei, C. (2022). Climate change and livestock production: a literature review. *Atmosphere* 13 (1), 140. doi:10.3390/atmos13010140
- Hertafeld, E., Zhang, C., Jin, Z., Jakub, A., Russell, K., Lakehal, Y., et al. (2019). Multi-material three-dimensional food printing with simultaneous infrared cooking. *3D Print. Addit. Manuf.* 6 (1), 13–19. doi:10.1089/3dp.2018.0042
- Ikada, Y. (2006). Challenges in tissue engineering. *J. R. Soc. Interface* 3 (10), 589–601. doi:10.1098/rsif.2006.0124
- Krintiras, G. A., Gadea Diaz, J., van der Goot, A. J., Stankiewicz, A. I., and Stefanidis, G. D. (2016). On the use of the Couette Cell technology for large scale production of textured soy-based meat replacers. *J. Food Eng.* 169, 205–213. doi:10.1016/j.jfoodeng.2015.08.021
- Kumar, P., Abubakar, A. A., Verma, A. K., Umaraw, P., Adewale Ahmed, M., Mehta, N., et al. (2022). New insights in improving sustainability in meat production: opportunities and challenges. *Crit. Rev. Food Sci. Nutr.* 63, 11830–11858. doi:10.1080/10408398.2022.2096562
- Kyoungju, K., Byungsun, C., Inhee, L., Hyeyoung, L., Soonhyang, K., Kyoungyoung, O., et al. (2011). Bioproduction of mushroom mycelium of *Agaricus bisporus* by commercial submerged fermentation for the production of meat analogue. *J. Sci. Food Agric.* 91 (9), 1561–1568. doi:10.1002/jsfa.4348
- Lepetit, J., and Culioli, J. (1994). Mechanical properties of meat. *Mech. Prop. meat* 36 (1–2), 203–237. doi:10.1016/0309-1740(94)90042-6
- Lillford, P. J. (2001). Mechanisms of fracture in foods. *J. Texture Stud.* 32 (5–6), 397–417. doi:10.1111/j.1745-4603.2001.tb01244.x
- Lin, S., Huff, H. E., and Hsieh, F. (2000). Texture and chemical characteristics of soy protein meat analog extruded at high moisture. *J. Food Sci.* 65 (2), 264–269. doi:10.1111/j.1365-2621.2000.tb15991.x
- Mandelik, D., Comforti, E., Schachter, S., Shapira, G., and Dikovsky, D. (2021). *System and method for fabrication of a three-dimensional edible product*. WO2022079718.
- Mattis, K. D., and Marangoni, A. G. (2020). Comparing methods to produce fibrous material from zein. *Food Res. Int.* 128, 108804. doi:10.1016/j.foodres.2019.108804
- Mottram, D. S. (1998). Flavour formation in meat and meat products: a review. *Food Chem.* 62 (4), 415–424. doi:10.1016/s0308-8146(98)00076-4
- Mottram, D. S., and Elmore, J. S. (2005). “The interaction of lipid-derived aldehydes with the Maillard reaction in meat systems,” in *The maillard reaction in foods and medicine* (USA: Woodhead Publishing), 198–203.
- Nishimura, T. (2010a). The role of intramuscular connective tissue in meat texture. *Animal Sci. J.* 81 (1), 21–27. doi:10.1111/j.1740-0929.2009.00696.x
- Post, M. J. (2012). Cultured meat from stem cells: challenges and prospects. *Meat Sci.* 92 (3), 297–301. doi:10.1016/j.meatsci.2012.04.008
- Post, M. J., Levenberg, S., Kaplan, D. L., Genovese, N., Fu, J., Bryant, C. J., et al. (2020). Scientific, sustainability and regulatory challenges of cultured meat. *Nat. Food* 1, 403–415. doi:10.1038/s43016-020-0112-z
- Protose (1900). The new food that is all food. *Mod. Med.* 6, 144.
- Purslow, P. P. (2002). The structure and functional significance of variations in the connective tissue within muscle. *Comp. Biochem. Physiology Part A Mol. Integr. Physiology* 133 (4), 947–966. doi:10.1016/s1095-6433(02)00141-1
- Purslow, P. P. (2018). Contribution of collagen and connective tissue to cooked meat toughness: some paradigms reviewed. *Meat Sci.* 144, 127–134. doi:10.1016/j.meatsci.2018.03.026
- Purslow, P. P. (2020). The structure and role of intramuscular connective tissue in muscle function. *Front. Physiology* 11, 495. doi:10.3389/fphys.2020.00495
- Purslow, P. P. (2023). “The structure and growth of muscle,” in *Lawrie's meat science* (China: Woodhead Publishing), 51–103.
- Purslow, P. P., Oiseth, S., Hughes, J., and Warner, R. D. (2016). The structural basis of cooking loss in beef: variations with temperature and ageing. *Food Res. Int.* 89, 739–748. doi:10.1016/j.foodres.2016.09.010
- redefinemeat. Available at: <https://www.redefinemeat.com/technology>.
- Roy, B. C., and Bruce, H. L. (2023). Contribution of intramuscular connective tissue and its structural components on meat tenderness-revisited: a review. *Crit. Rev. Food Sci. Nutr.*, 1–31. doi:10.1080/10408398.2023.2211671
- Schreuders, F., Schlangen, M., Kyriakopoulou, K., Boom, R., and van der Goot, A. J. (2021). Texture methods for evaluating meat and meat analogue structures: a review. *Food control.* 127, 108103. doi:10.1016/j.foodcont.2021.108103
- Steinfeld, H. (2006). Livestock's long shadow: environmental issues and options. *Food and Agric. Org.*
- Szenderák, J., Fróna, D., and Rákó, M. (2022). Consumer acceptance of plant-based meat substitutes: a narrative review. *Foods* 11 (9), 1274. doi:10.3390/foods11091274
- Tordjman, J. (2012). “Histology of adipose tissue,” in *Physiology and physiopathology of adipose tissue* (Paris: Springer Paris), 67–75.
- Tornberg, E. V. A. (2005). Effects of heat on meat proteins—Implications on structure and quality of meat products. *Meat Sci.* 70 (3), 493–508. doi:10.1016/j.meatsci.2004.11.021
- Vacanti, C. A. (2006). The history of tissue engineering. *J. Cell. Mol. Med.* 10 (3), 569–576. doi:10.2755/jcmm010.003.20
- Weston, A. R., Rogers, R. W., and Althen, T. G. (2002). Review: the role of collagen in meat tenderness. *Prof. Animal Sci.* 18 (2), 107–111. doi:10.15232/s1080-7446(15)31497-2
- Wood, J. D., Enser, M., Fisher, A. V., Nute, G. R., Sheard, P. R., Richardson, R. I., et al. (2008). Fat deposition, fatty acid composition and meat quality: a review. *Meat Sci.* 78 (4), 343–358. doi:10.1016/j.meatsci.2007.07.019
- Yu, T. Y., Morton, J. D., Clerens, S., and Dyer, J. M. (2017). Cooking-induced protein modifications in meat. *Compr. Rev. Food Sci. Food Saf.* 16 (1), 141–159. doi:10.1111/1541-4337.12243



OPEN ACCESS

EDITED BY

Hui Jie Zhang,
Shaanxi University of Science and Technology,
China

REVIEWED BY

Anne-laure Fameau,
Institut National de recherche pour l'agriculture,
l'alimentation et l'environnement (INRAE), France
Marcel Krzan,
Jerzy Haber Institute of Catalysis and Surface
Chemistry, Poland

*CORRESPONDENCE

Antônio Machado,
✉ amachado@usfq.edu.ec
Frank Alexis,
✉ falexis@usfq.edu.ec

RECEIVED 28 December 2023

ACCEPTED 01 February 2024

PUBLISHED 23 February 2024

CITATION

Miño K, Pérez A, Iza-García TX, Cabascango DG,
Gordillo C, Gordillo A, Vispo N, Machado A,
Zamora-Ledezma C and Alexis F (2024),
Antimicrobial cellulose hydrogels against gram-
positive and gram-negative bacteria.
Front. Soft Matter 4:1362677.
doi: 10.3389/frsrm.2024.1362677

COPYRIGHT

© 2024 Miño, Pérez, Iza-García, Cabascango,
Gordillo, Gordillo, Vispo, Machado, Zamora-
Ledezma and Alexis. This is an open-access
article distributed under the terms of the
[Creative Commons Attribution License \(CC BY\)](https://creativecommons.org/licenses/by/4.0/).
The use, distribution or reproduction in other
forums is permitted, provided the original
author(s) and the copyright owner(s) are
credited and that the original publication in this
journal is cited, in accordance with accepted
academic practice. No use, distribution or
reproduction is permitted which does not
comply with these terms.

Antimicrobial cellulose hydrogels against gram-positive and gram-negative bacteria

Karla Miño¹, Antonela Pérez², Tamia Xaymara Iza-García³,
Dayanna Gabriela Cabascango³, Catalina Gordillo¹,
Andrea Gordillo¹, Nelson Vispo¹, Antônio Machado^{3*},
Camilo Zamora-Ledezma⁴ and Frank Alexis^{2*}

¹School of Biological Sciences and Engineering, Yachay Tech University, Imbabura, Ecuador,

²Departamento de Ingeniería Química, Universidad de San Francisco de Quito, Instituto de Microbiología, Instituto de Energía y Materiales, Quito, Ecuador, ³Colegio de Ciencias Biológicas y Ambientales COCIBA, Universidad San Francisco de Quito (USFQ), Instituto de Microbiología, Laboratorio de Bacteriología, Quito, Ecuador, ⁴Green and Innovative Technologies for Food, Environment and Bioengineering Research Group, Faculty of Pharmacy and Nutrition, UCAM-Universidad Católica San Antonio de Murcia, Murcia, Spain

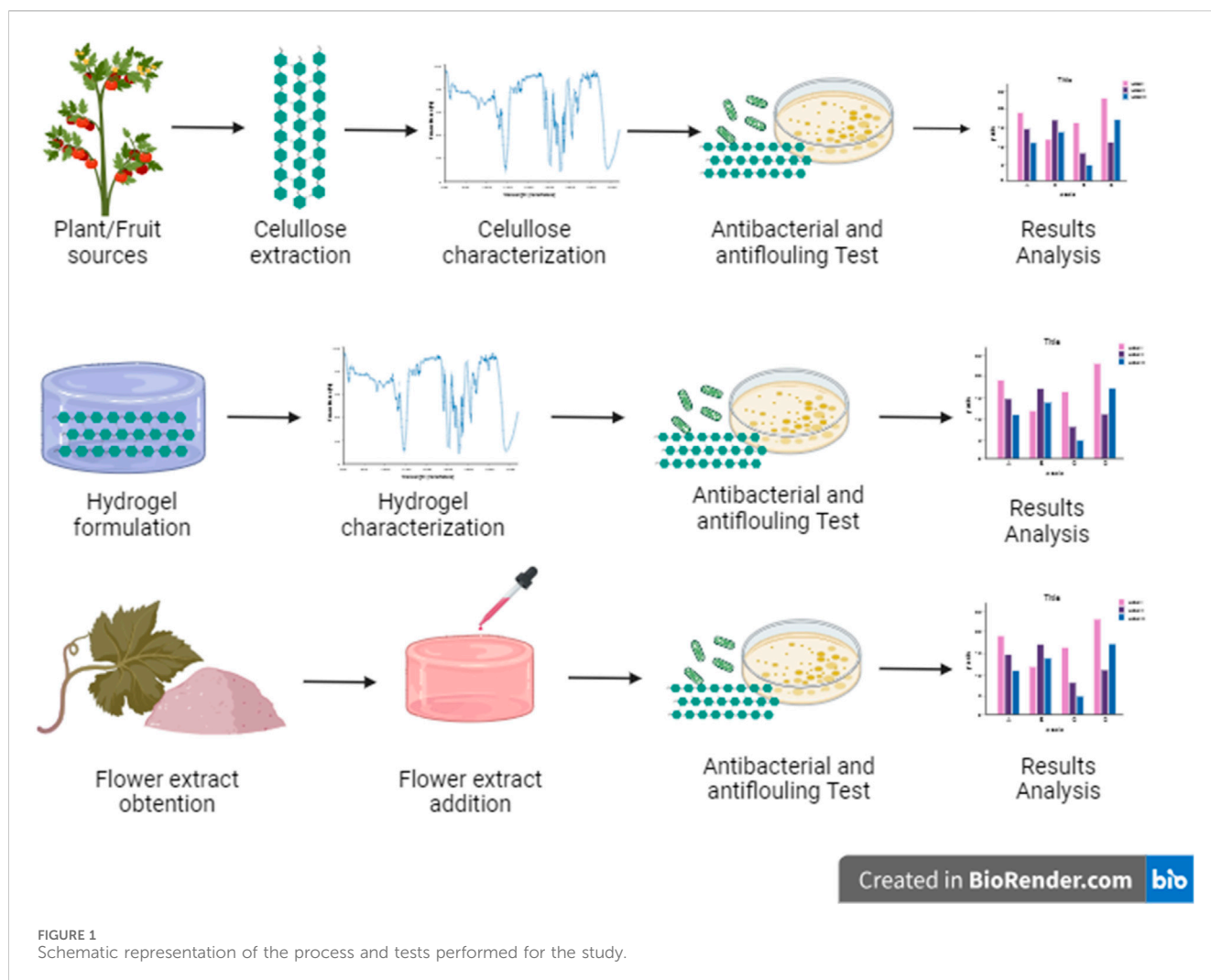
The development of hydrogels has a significant impact in fields such as tissue engineering and biomedical devices. The present study tests different cellulose particles extracted from plants to produce hydrogels and identify if these particles and hydrogels have antimicrobial properties. Nine cellulose particles from Ecuadorian biodiversity were obtained using an established chemical extraction protocol, characterized using known techniques, and evaluated for bacterial growth *in-vitro*. In addition, two particles of nine were selected to perform bacterial growth rates and bacterial adhesion assays. The bacterial growth rates with cellulose F1 and F53 were similar to the positive control (with antibiotic) with both *Escherichia coli* ATCC 25922 and TG1 strains. However, the results showed that the bacterial growth rate with seven of the nine cellulose particles was lower than the negative control (without antibiotics) suggesting antifouling properties. Based on the results using cellulose particles and hydrogels with antifouling properties, we prepared a plant extract to test the bactericide properties against Gram-positive (*Staphylococcus aureus* ATCC 25923) and Gram-negative (*E. coli* ATCC 25922) bacteria, evidencing the highest inhibitory effect at 40 and 60 mg/mL against *S. aureus* and *E. coli*, respectively. Lastly, we encapsulated the bactericide plant extract into the anti-fouling hydrogel. The results demonstrated that the combination of antifouling and bactericide properties could be an alternative approach for surface-modified cellulosic materials applications in the future.

KEYWORDS

cellulose, antibacterial, fiber, plant, biodiversity, antifouling

1 Introduction

Bacterial and other microorganism infections caused by implants are of great concern in the biomedical field because they cause many deaths each year worldwide (Alarfaj et al., 2016). The ability of these microbes to colonize surfaces rapidly and migrate allows these microcolonies to produce biofilms. Both Gram-positive and Gram-negative bacteria can cause biofilm formation in biomedical devices (Cangui et al., 2022). The most common



bacteria are *Enterococcus faecalis*, *Staphylococcus aureus*, *Staphylococcus epidermidis*, *Streptococcus viridans*, *Escherichia coli*, *Klebsiella pneumoniae*, *Proteus mirabilis*, and *Pseudomonas aeruginosa* (Cangui et al., 2023; Khatoon et al., 2018). Simultaneously, the formation of biofilms on medical implants allows bacteria to acquire antimicrobial resistance (Arciola et al., 2018). Due to the rise of antimicrobial resistance worldwide, alternative therapies and preventive measures are extremely needed nowadays (Zamora et al., 2022; Machado et al., 2023).

Antibiotics are typically employed as a general strategy to overcome bacterial infectious diseases; however, they can also generate resistance if they are not used correctly (Muñoz et al., 2021). According to the European Antimicrobial Resistance Surveillance System (EARSS), the prevalence of methicillin-resistant *S. aureus* (MRSA) in at least 10% of all *S. aureus*-associated infections has increased by as much as 40%–50% (Alarfaj et al., 2016).

The need to eliminate or reduce the formation of biofilms on surfaces of biomedical devices has focused on the fabrication of new antimicrobial coatings capable of preventing the colonization and proliferation by microorganisms on surfaces or the modification of the architecture of existing antibacterial surfaces to improve their yield (Hasan et al., 2013; Zamora-Mendoza et al., 2023) Antifouling

and bactericidal surfaces have been developed as two types of antimicrobial coatings. Antifouling surfaces can resist the adherence of bacteria to the implant due to the presence of structures that reduce the binding for microorganisms. Bactericidal surfaces cause cell death when bacteria come into contact with the implants; the coating can have either repellent or destructive molecules (Zamora et al., 2022; Machado et al., 2023).

Antimicrobial polymers present a great alternative to combat this issue since their action mechanisms differ from those of antibiotics. Polymers can also show antimicrobial properties and be applied for functionalization with other materials to avoid antibiotic resistance problems. Natural antimicrobial biopolymers are a promising area where further research is needed (Zamora et al., 2022). For this reason, this research aims to analyze the antimicrobial properties of a natural biopolymer, such as cellulose and its hydrogels. In the present study, we hypothesized that natural particles from plants could be an alternative material with the potential to prevent bacterial adhesion in future applications in biomaterials (Figure 1). Nine types of cellulose were characterized and tested against *Escherichia coli* ATCC 25922 and TG1 to find bactericidal or bacteriostatic effects based on the physical, chemical, and morphological characteristics. Then, two particles were selected to test antibacterial activity by

TABLE 1 List of plants and fruits used in the present study.

Label	Scientific name	Part of the plant
T1	<i>Passiflora tripartita</i>	Fruit exocarp
T3	<i>Psidium guajava</i>	Fruit exocarp
F20	<i>Chuquiraga jussieui</i>	Leaves
F1	<i>Pyrus communis</i>	Fruit exocarp
CC	<i>Cocos nucifera</i>	Fruit exocarp
CB	<i>Agave sisalana</i>	Fruit exocarp
F12	<i>Solanum betaceum</i>	Fruit exocarp
F53	<i>Hylocereus megalanthus</i>	Fruit exocarp
F55	<i>Alibertia patinoides</i>	Fruit mesocarp

determining colony-forming units per milliliter (CFU/mL). Next, we produced cellulose-based hydrogels and encapsulated a plant extract to test the antimicrobial properties against *E. coli* ATCC 25922 (Gram-negative) and *S. aureus* ATCC 25923 (Gram-positive) bacteria. To achieve this purpose, the main analyses made for the anti-fouling capacity of each hydrogel were developed by initial bacteria adhesion and bacterial growth inhibition over time assays. The results demonstrated that the combination of antifouling and bactericide properties could have been an approach for surface-modified cellulosic materials applications in the near future.

2 Materials and methods

2.1 Materials

The raw material of the cellulose was obtained from different Ecuadorian natural sources acquired in Ecuadorian popular markets. Control samples of commercial cellulose (Sigmacell cellulose, type 20, 20 µm) were supplied by Sigma-Aldrich with purity of 95%–99%.

2.2 Fiber preparations

Cellulose extraction was carried out according to a predetermined chemical extraction technique, which included numerous water washes to eliminate any remaining chemicals. After the extraction process, the pure cellulose was dried for 1 day in a lyophilizer (Labconco model 7670520). We obtained seven powdered celluloses and two fiber-type celluloses (Table 1).

2.3 Fiber characterization

2.2.1 Fourier Transform Infrared Spectroscopy (FTIR)

FTIR analysis was performed on a spectrometer model Cary 630. First, the spectrum of the gold-plated sample holder was acquired as background, and then the spectra of the samples were recorded. The

wavelength range for the analysis was between 500 and 4,000 cm⁻¹ in transmittance mode at a resolution of 4 cm⁻¹.

2.2.2 Scanning electron microscope (SEM)

SEM was used in this investigation to obtain images of the surface structure, porosity, and morphology of cellulose samples. The morphologies of the different cellulose samples were characterized using a Phenom Pro X scanning electron microscope operated at 10 kV. A pin with a carbon film was used to prepare the samples.

2.2.3 X-ray diffraction (XRD)

The X-ray generator was operated to 40 kV and 15 mA in a sealed tube CuKα radiation source. Additionally, for collecting data was employed a θ/2θ configuration in the scan-axis, 0.02° step, and 20.0°/min scan velocity in a range of 5°–90° in 2θ, and the D/tex Ultra2 detector in 1D scan mode. Finally, it used a Soler slit 1.25° receive and incident scattering and high-length receiving and incident slit 10.0 mm, 8.0 mm, and 13.0 mm, respectively.

The degree of crystallinity of each cellulose sample was analyzed using a powder diffractometer Rigaku, Miniflex-600, equipped with a D/tex Ultra2 detector. The crystallinity index can be calculated using the following equation:

$$I_c = \frac{I_{(002)} - I_{(am)}}{I_{(002)}} \times 100 \quad (1)$$

Where $I_{(002)}$ is the counter reading at peak intensity at a 2θ angle close to 22° representing crystalline material and $I_{(am)}$ is the counter reading at peak intensity at a 2θ angle close to 18° representing amorphous material.

2.4 Antibacterial test of the cellulose particle surface

The antibacterial activity of the cellulose surface was tested against two strains of *E. coli* ATCC 25922 and TG1 by two different methods, more exactly, qualitative evaluation with an agar diffusion assay and quantitative evaluation in a culture broth medium.

For the qualitative evaluation, overnight cultures of *E. coli* TG1 (1E+08 colony-forming units (CFU)/mL) were placed in a Petri dish filled with Luria Bertani (LB) agar. Different amounts of cellulose particles were placed in the spaces from 1 to 4 labeled on each plate at 1, 5, and 10 mg. Besides, as a control, 3 µL of ampicillin were used and placed over the colonies, and then the cultures were incubated at 37°C for 24 h. After the required time, a definite zone of bacterial inhibition around the samples was measured to evaluate antibacterial activity.

The antibacterial activity was also quantitatively determined in terms of growth inhibition by measuring the optical density of bacteria treated with cellulose particles. This test included a positive control (medium + bacteria + antibiotic), a negative control (medium + bacteria), and a cellulose control (medium + cellulose). The ampicillin was prepared at a concentration of 1 µL/mL. Overnight cultures were prepared by inoculating 100 µL of *E. coli* ATCC 25922 and TG1 in 3 mL of LB broth medium and

then incubated at 37°C and 180 rpm. Theoretical bacterial density (OD) at 600 nm was measured by immersing a 100 mg sample of each cellulose in 10 mL of LB medium with an initial optical density (OD) of 0.05 (approximately $1\text{E}+05$ CFU/mL) in all test tubes. The corresponding negative controls were added to the assays, as well as positive controls were prepared by adding 10 μL of ampicillin to 10 mL of LB medium. The cellulose's optical density affects the absorbance measurements because it begins to degrade over time. For this reason, optical density readings of controls were taken with each cellulose sample (100 mg) diluted in an LB medium. Then, this influence was analyzed in each case to obtain the actual absorbance. All the suspensions were incubated on a rotary shaker at 180 rpm at 37°C for 24 h. Each tube's absorbance was measured periodically at 600 nm using a UV-visible spectrophotometer (ZUZI model 4,211/50) at 3, 6, and 24 h.

2.5 Statistical analyses

For the statistical analysis, the Malthusian growth equation was used to understand bacteria's growth kinetics and extract information about their behavior with the cellulose particles under study. For this, the specific growth rates were calculated for each case with the following equation:

$$P_t = P_o e^{kt} \quad (2)$$

Where P_t is the population in a time, P_o is the initial population, k is the specific growth rate, and t is the time in hours.

Subsequently, a one-way analysis of variance (ANOVA) was performed with the growth rates obtained to determine if there were significant differences between the samples. After this, a Duncan Test was performed to classify the samples. Statistical software R was used for all analyses (<https://www.rstudio.com/>).

2.6 Hydrogel formulation

According to Guamba et al. (Guamba et al., 2023), the hydrogel formulation was prepared utilizing a 1:10 concentration of cellulose and a basic solvent. The solvent comprises 4% urea and 6% sodium hydroxide (NaOH). Following the formation of the hydrogel matrix, it underwent washing with distilled water until the basic pH transitioned to neutral. This procedural step was executed for both F1 fiber cellulose and the commercial cellulose by Sigma-Aldrich, serving the purpose of establishing a control reference.

2.7 Jamaica flower extract

To prevent any interference with the hydrogel formulation structure, the flower extract was prepared in a solvent-based manner. This involved employing a standardized ratio of 2:10 parts of previously dehydrated Jamaica calyx to distilled water and allowing for a 24-h extraction period. After the designated incubation time, the heterogeneous mixture was subjected to filtration and lyophilization processes.

2.8 Addition of Jamaica flower extract into the hydrogel

Despite the absence of any alcohol remnants in the obtained extract, the addition of Jamaica flower extract directly to the hydrogel solution was precluded due to its pH. Consequently, the hydrogel was introduced into a dilution of 50 mg/mL with the Jamaica extract for 5 h. This approach was employed considering the maximum swelling properties of the hydrogels while ensuring precautionary measures against degradation prompted by the pH of the extract.

2.9 Minimum inhibitory concentration of Jamaica flower extract

The minimum inhibitory concentration (MIC) value was determined following the protocol outlined by Wiegand et al. (Wiegand et al., 2008), employing a bacteria concentration of $1.5\text{E}+08$ CFU/mL in a Mueller-Hilton (MH) medium, *E. coli* ATCC 25922 and *S. aureus* ATCC 25923. These pathogens were selected based on their prevalence in cutaneous wound bacterial infections. The pathogen solution was added to a 96-well plate template, with the medium serving as a negative control, considering eight escalating extract concentrations (10, 20, 40, 60, 80, 100, 150, and 200 mg/mL) included, along with positive gentamicin control concentrations of 0.12, 0.5, and 1 $\mu\text{g/mL}$ for *S. aureus*. Gentamicin concentrations of 0.25, 0.5, and 1 $\mu\text{g/mL}$, as per the established manual of the Clinical and Laboratory Standards Institute (CLSI) (Weinstein and Clinical and Laboratory Standards Institute, 2021), were considered for MIC determination using the specified strains and gentamicin as the antibiotic reference. The absorbance analysis was conducted after 20 h of incubation at 37°C, utilizing the OD at 570 nm of the ELx8081IU spectrophotometer by Biotek Instruments. To validate the results obtained through absorbance measurements, 30 μL of resazurin were added to each well of the 96-well plate to identify the minimum bactericidal concentration (MBC) value. This was determined by observing the initial purple color change of the resazurin after 15 min of the chemical reaction (Wiegand et al., 2008; Elshikh et al., 2016).

2.10 Evaluation of the bacterial initial adhesion of the hydrogel surfaces

To assess the anti-fouling properties of each hydrogel, a bacteria adhesion methodology was developed in collaboration with the Institute of Microbiology at Universidad San Francisco de Quito (IM-USFQ), as previously described (Rodríguez et al., 2022). Briefly, the protocol commenced with a 24-h incubation of a bacterial culture at 37°C in MH agar medium, aiming to optimize bacterial initial adhesion of *E. coli* ATCC 25922 and *S. aureus* ATCC 25923. Subsequently, a bacteria dilution was prepared using 30 mL of the medium, incorporating bacterial colonies until reaching a concentration of $1\text{E}+09$ CFU/mL for bacterial inoculum (Rodríguez et al., 2022). In 6-well plate

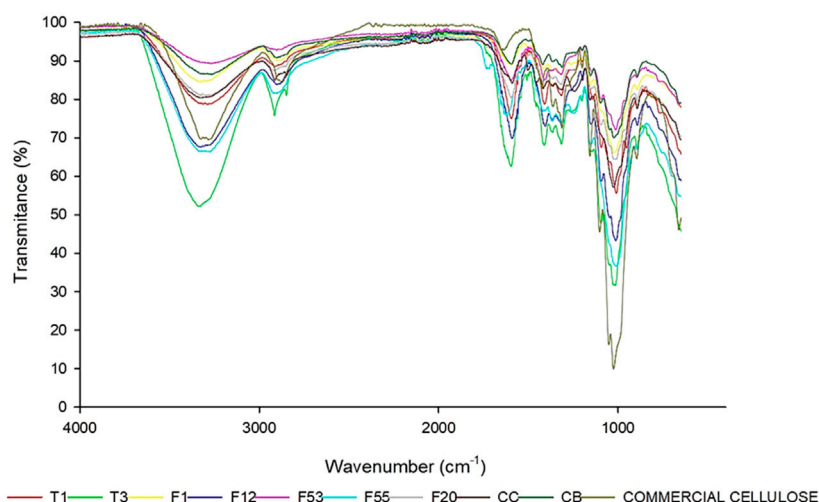


FIGURE 2
Fourier Transform Infrared Spectroscopy spectra of nine cellulose particles compared with commercial cellulose. T1, T3, F1, F12, F20, F53, F55, F20, CB, CC, and commercial cellulose.

templates, 3 mL of the bacteria solution was added to each well, along with coverslips, encompassing reference materials such as commercial cellulose hydrogel, F1, and F1+J.ext. hydrogels. To simulate the initial contamination of a wound, the templates were incubated at 37 °C for 30 min. Subsequently, the surfaces were washed once with 3 mL of PBS and transferred to a Falcon tube containing 15 mL of PBS, which was mixed for 5 min at maximum velocity using a vortex dispersing the initial adhered bacteria from the surface samples. After the dispersion step, a 100 μ L aliquot was extracted from the Falcon tube and placed on a coverslip, following the procedure outlined in the work of Rodríguez et al. (Rodríguez et al., 2022), to determine the cells/cm² adhesion on each surface, the coverslips were stained with crystal violet (0.01 M) for 1 min and observed under a microscope, considering 15 central fields.

2.11 Time-kill kinetics of hydrogels with plant extract

The antimicrobial activity of hydrogels containing Jamaica extract was assessed in terms of bacterial growth inhibition over time with optical density measurements taken during 24 h (Zamora-Mendoza et al., 2023; Guamba et al., 2023). *S. aureus* ATCC 25923 and *E. coli* ATCC 25922 bacteria, sourced from the collection of the IM-USFQ, were employed for the study. Two hydrogel treatments were evaluated: one without the extract (F1) and another with Jamaica extract (F1+J. ext.). included a positive control, consisting of the medium and the pathogen. These treatments were placed in 96-well plates, and 100 μ L of an initial bacterial concentration of 1E+05 CFU/mL was added to the MH broth medium. Subsequently, absorbance was measured at 0, 3, 6, and 24 h at 570 nm, following the methodology outlined in prior studies (Atencia et al., 2022; Cabezas et al., 2023).

3 Results, interpretation, and discussion

3.1 Characterization of fibers

The Fourier transform infrared (FTIR) was carried out to verify the successful separation of other residual components, such as lignin and hemicellulose, from the extracted cellulose.

FTIR spectra of all-natural cellulose particles are shown in Figure 2. All samples showed two central absorbance regions. The first one with large wavenumbers in a range of 2,700 cm⁻¹ to 3,500 cm⁻¹, and the second with lower wavenumbers in a range of 500 cm⁻¹ to 1800 cm⁻¹. The spectra exhibited characteristic peaks and absorption bands similar to commercial cellulose, which have individual and specific functionalities. One is the strong absorption band in the 1,635 cm⁻¹ region, corresponding to the stretching vibration O-H of the water molecules absorbed in the cellulose structure (Khan et al., 2020). Other absorbance bands at 896 cm⁻¹ correspond to the glycosidic bonds between monosaccharide units in cellulose molecules. Also, the bands located at 1,056 cm⁻¹ and 3,437 cm⁻¹ are attributed to the C-O-C stretching of the pyranose ring and the stretching O-H of the hydroxyl groups in the cellulose structure. Additionally, essential peaks are evident at ~1,300 cm⁻¹, ~2,900 cm⁻¹, and ~3,300 cm⁻¹, which correspond to rocking vibrations at C6, OH bending, and sp³ C-H stretching, respectively.

The commercial cellulose was used as a control to compare the FTIR bands of extracted cellulose. All samples showed a similar pattern to the commercial cellulose control, except for the low-intensity transmittance band at 1742 cm⁻¹ in sample F55 which is associated with C = O stretching vibration due to the presence of the small amount of residual lignin and acetyl or uronic ester groups of hemicellulose as shown in Figure 2.

X-ray powder diffraction (XRD) is an analytical technique used mainly for the phase identification of a crystalline material and its physical and chemical properties. X-ray diffraction (XRD) tests on the nine cellulose samples depicted distinct graphs and different

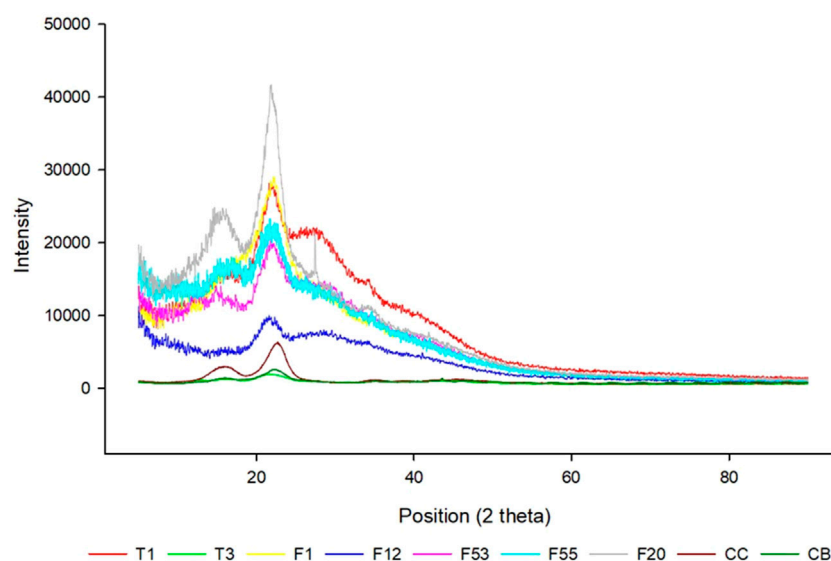


FIGURE 3
X-Ray diffraction analysis patterns of nine cellulose fibers: T1, T3, F1, F12, F20, F53, F55, F12, CB, and CC.

TABLE 2 The crystallinity index of cellulose samples.

Label	Crystallinity index
T1	46.6
T3	46.0
F20	54.9
F1	39.0
CC	51.5
CB	69.6
F12	43.7
F53	45.6
F55	28.44

degrees of crystallinity (Figure 3). All the XRD patterns indicated the presence of two major peaks. The first prominent peak around $2\theta = 22^\circ$ represents the crystalline structure of cellulose, and the peaks around $2\theta = 18^\circ$ represent the amorphous structure of the samples (Rambo and Ferreira, 2015).

The difference between the X-ray diffraction patterns can occur due to the nature of the samples and how they are prepared, which will influence the crystallinity index (Park et al., 2010). However, the extraction and process of cellulose used the same protocol, and the method to prepare the sample for XRD was also the same procedure. Therefore, it is expected that the differential crystallinity index is due to the different origins of cellulose. The results showed a variation of the index of crystallinity from 28% to 69% demonstrating that some of the cellulose particles are more amorphous than others (Table 2).

The morphology and topography of the nine cellulose particles were analyzed by scanning electron micrographs displayed in Figure 4. Each cellulose sample has a distinct shape determined by the plant source. The external structure of the samples T1, T3,

F53, F55, F12, CC, and CB demonstrated an irregular surface that exhibits roughness. In particular, some of these appeared to be irregular fiber fragments and also showed a network structure. There is also a more evident degree of porosity in some of this cellulose. The morphology of the particles F1 and F20 have a more elongated and compact structure.

3.2 Bactericide evaluation of cellulose particles

A qualitative assay was performed with *E. coli* TG1. For this test, three amounts of each cellulose sample were placed on the agar plate: 1, 5, and 10 mg. Each plate was divided into four parts: 1 mg of the sample was placed in space number one. In space number two, the antibiotic was placed as a positive control; in space three, 5 mg of the sample was placed; finally, 10 mg of the cellulose sample was placed in space four. The process was repeated twice for each cellulose sample, and then all plates were incubated at 37°C for 24 h. As shown in Figure 5, a negative response was obtained for the test; there was no inhibition against *E. coli* TG1. The results demonstrated that cellulose particles do not have bactericide properties.

Moreover, a quantitative assay was performed to determine the antibacterial activity of the cellulose against both *E. coli* ATCC 25922 and TG1 strains to measure the bacterial growth rate in solution. All the bacterial suspensions started with the same concentration of bacteria (1×10^5 CFU/mL), and then optical density measurements were made at 600 nm at 0, 3, 6, and 24 h for each cellulose sample. Two independent experiments were performed for each cellulose; the reported values correspond to the two experiments' mean. The bacterial growth of *E. coli* with each cellulose sample was compared with the *E. coli* cultures with ampicillin (positive control) and without ampicillin (negative control).

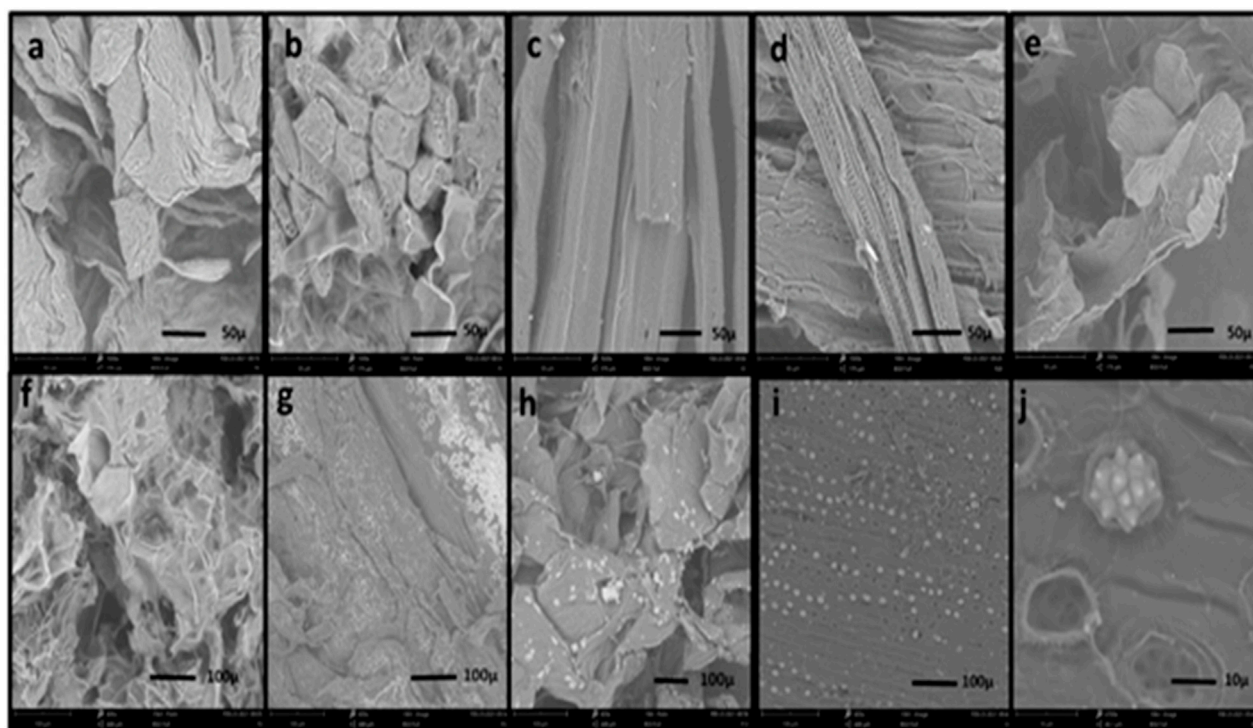


FIGURE 4
Scanning electron microscope (SEM) analysis of cellulose particles: (A) T1, (B) T3, (C) F1, (D) F20, (E) F53, (F) F55, (G) F12, (H) CB, (I) CC, and (J) special structure in CC.

At different times, the mean absorbance values of the cultures with the cellulose particles against the *E. coli* ATCC 25922 were recorded. The results in Figure 6 show that cellulose particles F1, F12, CC, T3, T1, F53, F55, F20, and CB had a similar tendency and decreased bacterial growth compared to the negative control. It is important to note that 3 h after the initial time, this cellulose had a remarkable decrease in absorbance values, unlike the negative control, and although as the culture time increased, the absorbance increased, after 24 h, the particles had a bacterial growth minor than the negative control so demonstrating the bacterial growth inhibition. The cellulose CC had a different tendency since the growth was similar to the negative control. According to the absorbance values obtained against *E. coli* ATCC 25922, there is a decrease in the bacterial suspension with most celluloses in each time interval compared to the negative control, which did not contain any antimicrobial agent. However, the absorbance values of antibiotic control were always lower.

The mean absorbance values of the cultures with the cellulose particles against *E. coli* TG1 are shown in Figure 7. In this case, the particles that had significantly decreased growth at 24 h when compared to the negative control were F12, F53, T3, F55, T1 and CB. The rest of the particles had a similar tendency to the negative control, while F20 presented an increase in its growth rate.

The specific growth rate (k) from the two experiments with both bacteria strains with the different cellulose samples was calculated using the Malthusian growth equation (Supplementary Appendix SA). This parameter k is essential since it represents microorganisms' dynamic growth and allows determining which treatment with cellulose particles grows with more or less intensity.

It was verified that the data followed a normal distribution with the Shapiro-Wilks and the Kolmogorov-Smirnov test (Supplementary Appendix SB). The ANOVA test results allowed us to compare the means of the specific growth rates of each cellulose sample to establish if there was a difference. Accept or reject the null hypothesis that states no differences between the means of the different groups. Considering the p -value (<0.05) obtained from the ANOVA test for the *E. coli* ATCC25922 and TG1 strains (Supplementary Appendix SC), it can be concluded that there is a significant difference between all cellulose samples.

Duncan's test is a multiple comparison test that compares the means obtained after rejecting the null hypothesis of equality of means using the ANOVA technique. The results obtained for this test classified all the samples. Duncan's distribution for the cellulose samples against both bacterial strains showed a highly significant difference between the cellulose particles being consistent with the experiment results (Supplementary Appendix SD).

Based on the absorbance data presented in Figure 8, the initial concentration added to the bacterial culture (10 mg/mL) demonstrated no inhibition for both bacterial growth. However, the inhibitory effect of the Jamaica flower extract becomes apparent from 20 mg/mL, with the highest inhibitory capacity observed at 40 mg/mL for *S. aureus* and 60 mg/mL for *E. coli*, reaching its maximum efficacy at 100 mg/mL. Furthermore, employing the resazurin indicator, the obtained MBC values against each studied bacterium were 40 and 60 mg/mL for *S. aureus* and *E. coli*, respectively.

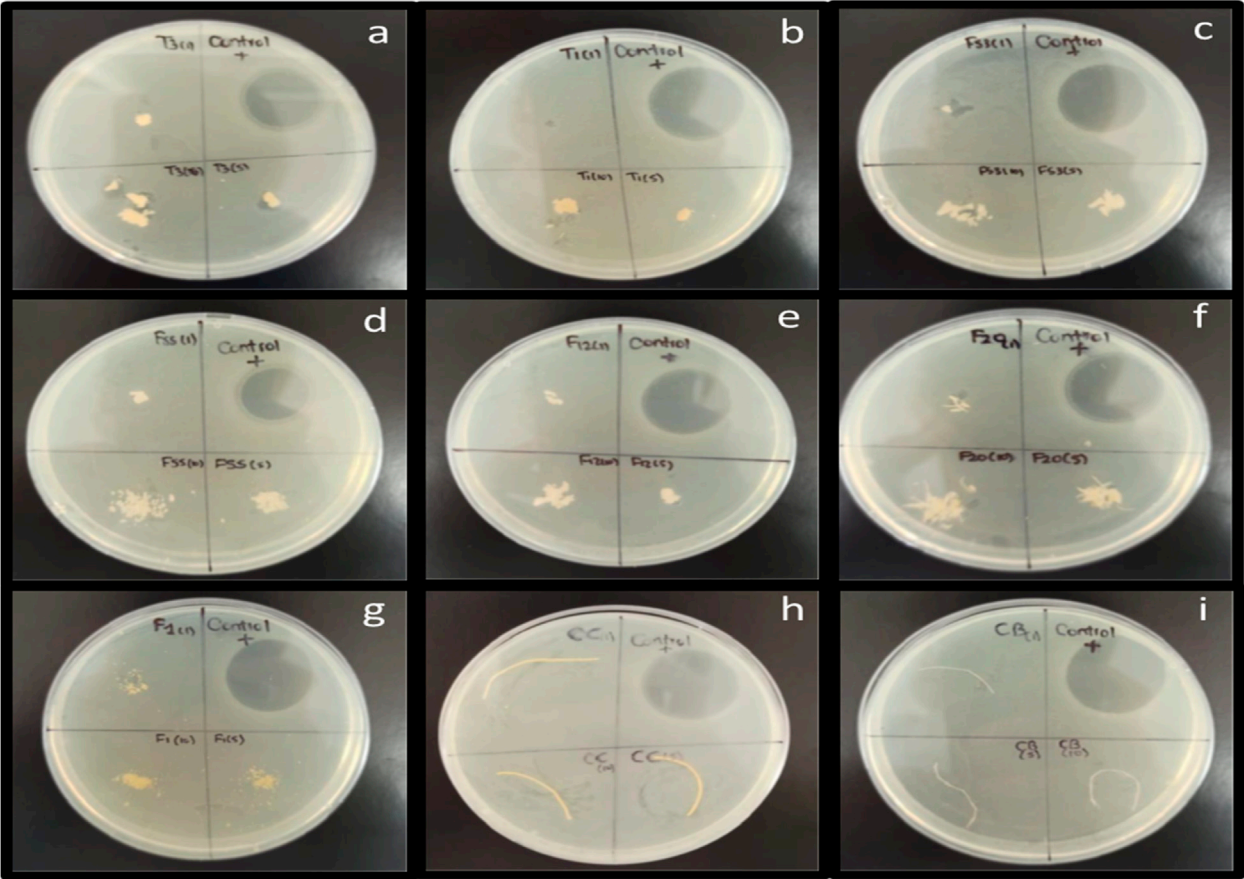


FIGURE 5
Antibacterial test against *E.coli* TG1 strain with the seven powdered cellulose: (A) T3, (B) T1, (C) F53, (D) F55, (E) F12, (F) F20, (G) F1, and two cellulose particles (H) CC and (I) CB.

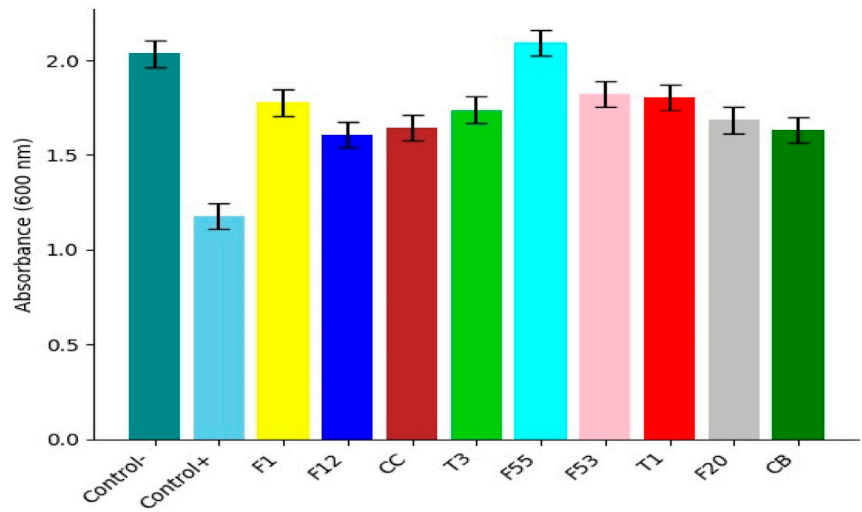


FIGURE 6
Bacterial growth with cellulose particles against *E. coli* ATCC 25922. In the graph, the growth of the bacteria with almost all celluloses is lower than the negative control. The growth rate with cellulose CC was similar to the negative control.

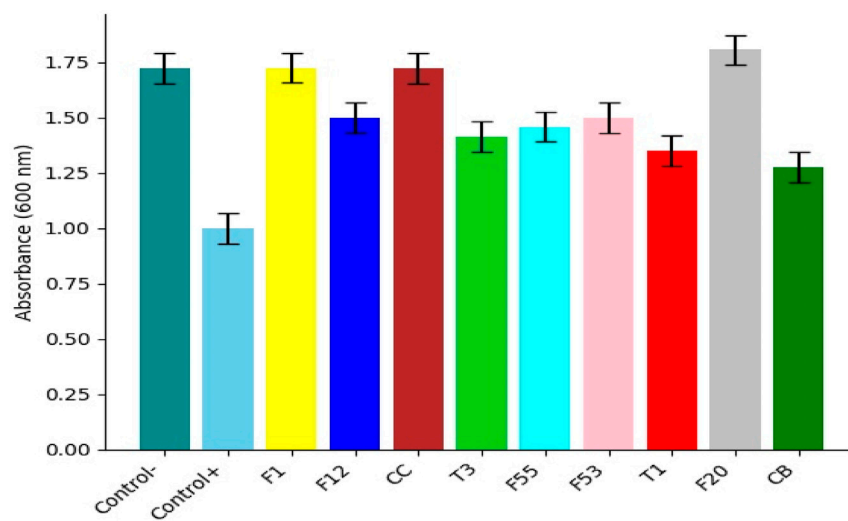


FIGURE 7

Bacterial growth with cellulose particles against *E. coli* TG1. In observing the graph, the bacterial growth with cellulose F12 and F53 was the most different from the negative control without the antibiotic.

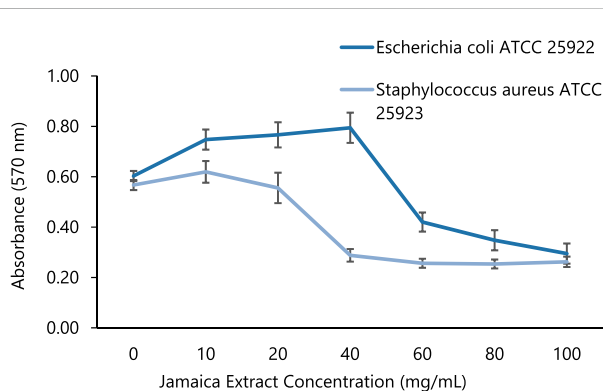


FIGURE 8

Bacterial growth inhibition analysis of Jamaica flower extract in different concentrations.

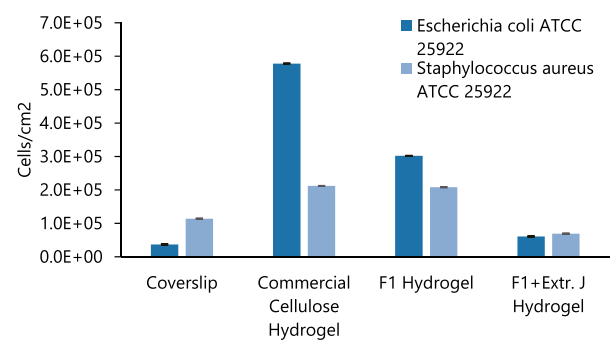


FIGURE 9

Initial bacteria adhesion of different materials (glass and hydrogel surfaces).

Based on Guamba et al. (Guamba et al., 2023), commercial cellulose fibers and hydrogels were fully characterized and do not exhibit antimicrobial and antifouling properties against *E. coli*. Nevertheless, commercial cellulose hydrogels demonstrate some antifouling properties against both gram-positive. In this context, the commercial cellulose hydrogel was employed as a control in the adhesion test. Further evaluation was realized by different materials on the bacterial initial adhesion into the hydrogel surfaces when compared to glass, as shown in Figure 9. According to the reference materials, the glass coverslip exhibited minimal bacterial adhesion for each bacterium. In contrast, the hydrogel formulated with commercial cellulose demonstrated the highest adhesion for *E. coli*, while showing a similar bacterial initial adhesion for *S. aureus* when compared to the natural cellulose hydrogel F1 with values of 2.12 and 2.08 E+05 (cells/cm²), respectively. On the other hand, the incorporation of Jamaica flower extract

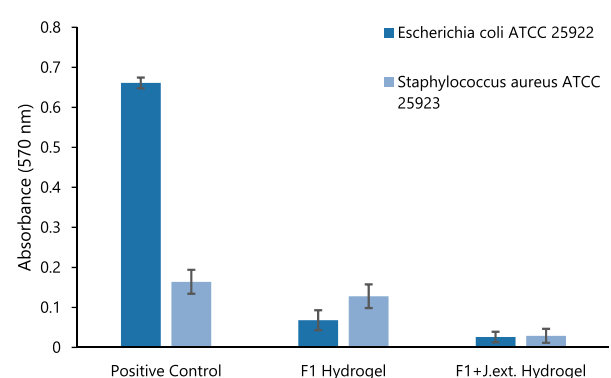


FIGURE 10

Bacterial growth with hydrogel against *E. coli* ATCC 25922 and *Staphylococcus aureus* ATCC 25923. Positive control, hydrogel F1 treatment, and hydrogel F1 treatment with Jamaica extract (F1+J.ext.).

into the hydrogel matrix significantly reduced the bacterial initial adhesion for both Gram-negative (*E. coli*) and positive (*S. aureus*) bacteria with adhesion levels comparable to the reference glass surface and surpassing the microbial adhesion inhibition recently reported by Rodríguez-Arias and colleagues (Rodríguez et al., 2022).

Finally, when evaluating the bacterial growth inhibition by F1 and F1 with Jamaica flower extract (F1+J.ext.) hydrogels, both hydrogels successfully inhibited *E. coli* and *S. aureus* growth at 24 h in comparison to the positive control (Figure 10). The positive control exhibited an average absorption of 0.661 and 0.164 nm for *E. coli* ATCC 25922 and *S. aureus* ATCC 25923, respectively. However, the average absorption of *S. aureus* ATCC 25923 for the F1 fiber hydrogel was similar to the positive control (0.128 vs. 0.164, respectively). Therefore, the overall results demonstrated an effective antibacterial property of the natural cellulose hydrogel against the Gram-negative pathogen but a lack of efficacy for the Gram-positive bacteria. On the other hand, the measured absorption reported for the F1+J.ext. hydrogel was close to the initial absorption for each bacterium (0.025 nm), more exactly a final absorption of 0.026 nm for *E. coli* ATCC 25922 and 0.029 nm for *S. aureus* ATCC 25923. This indicates a successful antibacterial activity of the natural cellulose hydrogel and the Jamaica flower extract in conjunction, even when the extract concentration was minimal against each pathogen based on the MIC analysis. These results revealed a high antimicrobial activity and applicability on future biomedical applications, as previously observed in the recent study of Zamora et al. (Zamora-Mendoza et al., 2023)

4 Conclusion

In this work, nine particles were successfully extracted from Ecuadorian plants with an established chemical protocol. The nine cellulose particles were characterized by FTIR, XRD, and SEM analyses. FTIR confirmed the effective removal of non-cellulosic material and cellulose extraction with a good purity level. XRD analysis verified a high degree of crystallinity in the samples, up to 69.6%. X-ray diffractograms showed that some samples, like CC and CB, were more crystalline than other samples, like F55, due to the natural source of each cellulose. SEM microscopy displayed unique characteristics of nine particles, like morphology, porosity, and size depending on the native origin, giving them distinctive features.

Antibacterial tests were performed with two strains, *E. coli* ATCC25922 and TG1, for 24 h to measure the bacterial growth rate in the presence of nine different cellulose fibers. Bacterial growth with cellulose F1, F12, F53, T1, T3, and CC was lower than that of the negative control with both strains of *E. coli*. Furthermore, cellulose F1 and F53 presented an inhibition similar to the antibiotic control, while F55 and F20 showed higher growth than the negative control. The bacterial growth rate of F1 at pH 7 exhibited the greatest inhibition.

The results were validated using the Malthusian growth equation and the growth rates of each cellulose particle. The highest growth rate was 0.1543, and the lowest was 0.1314, with *E. coli* ATCC 25922. The ANOVA and Duncan tests showed

differences between the samples, obtaining that cellulose F1 and F53 had the best performance. Therefore, the F1 and F53 cellulose have great potential as a biomaterial. Further antimicrobial evaluation demonstrated that Jamaica flower extract possesses MIC and MBC values of 40 mg/mL for *S. aureus* and 60 mg/mL for *E. coli*. When combined with F1 hydrogel, hydrogel F1 treatment with Jamaica flower extract evidenced the lowest bacterial initial adhesion levels and the highest bacterial growth inhibition. Overall results showed the most optimal and appropriate choice of F1 and Jamaica flower extract for further evaluation and a deeper investigation in biomedical applications. (Chauviere et al., 1992; Schierholz and Beuth, 2001; Tokiwa et al., 2009; Weerasekera M. M. et al., 2016; Weerasekera M. et al., 2016; Arciola et al., 2018; Han et al., 2018; Boukir et al., 2019; Sahar et al., 2020; Castro et al., 2022; Senthilrajan et al., 2022).

Data availability statement

The original contributions presented in the study are included in the article/Supplementary Material, further inquiries can be directed to the corresponding authors.

Ethics statement

Ethical approval was not required for the studies on humans in accordance with the local legislation and institutional requirements because only commercially available established cell lines were used.

Author contributions

KM: Data curation, Investigation, Methodology, Writing—original draft, Writing—review and editing. AP: Conceptualization, Data curation, Methodology, Writing—original draft, Writing—review and editing, Investigation. TI-G: Data curation, Investigation, Methodology, Writing—review and editing. DC: Data curation, Investigation, Methodology, Writing—review and editing. CG: Data curation, Investigation, Methodology, Writing—review and editing. AG: Data curation, Investigation, Methodology, Writing—review and editing. NV: Data curation, Investigation, Methodology, Writing—original draft. AM: Data curation, Investigation, Methodology, Writing—original draft, Supervision, Validation, Writing—review and editing. CL: Investigation, Methodology, Writing—review and editing. FA: Methodology, Writing—review and editing, Conceptualization, Data curation, Project administration, Supervision, Writing—original draft.

Funding

The author(s) declare that no financial support was received for the research, authorship, and/or publication of this article.

Conflict of interest

The authors declare that the research was conducted in the absence of any commercial or financial relationships that could be construed as a potential conflict of interest.

Publisher's note

All claims expressed in this article are solely those of the authors and do not necessarily represent those of their affiliated

organizations, or those of the publisher, the editors and the reviewers. Any product that may be evaluated in this article, or claim that may be made by its manufacturer, is not guaranteed or endorsed by the publisher.

Supplementary material

The Supplementary Material for this article can be found online at: <https://www.frontiersin.org/articles/10.3389/frsfm.2024.1362677/full#supplementary-material>

References

- Alarfaj, A., Lee, H. H. C., Munusamy, M. A., Ling, Q. D., Kumar, S., Chang, Y., et al. (2016). Development of biomaterial surfaces with and without microbial nano segments. *J. Polym. Eng.* 36, 1–12. doi:10.1515/polyeng-2015-0046
- Arciola, C., Campoccia, D., and Montanaro, L. (2018). Implant infections: adhesion, biofilm formation and immune evasion. *Nat. Rev. Microbiol.* 16 (7), 397–409. doi:10.1038/s41579-018-0019-y
- Atiencia, M., Cabezas, F., Vizuete, K., Debut, A., Tejera, E., and Machado, A. (2022). Evaluation of the biofilm life cycle between *Candida albicans* and *Candida tropicalis*. *Front. Cell Infect. Microbiol.* 12, 1155. doi:10.3389/fcimb.2022.953168
- Boukir, A., Fellak, S., and Doumenq, P. (2019). Structural characterization of *Argania spinosa* Moroccan wooden artifacts during natural degradation progress using infrared spectroscopy (ATR-FTIR) and X-Ray diffraction (XRD). *Heliyon* 5 (9), e02477. doi:10.1016/j.heliyon.2019.e02477
- Cabezas, F., Atiencia-Carrera, M. B., Villacrés-Granda, I., Proaño, A. A., Debut, A., Vizuete, K., et al. (2023). Evaluation of the polyphenolic profile of native Ecuadorian stingless bee honeys (Tribe: meliponini) and their antibiofilm activity on susceptible and multidrug-resistant pathogens: an exploratory analysis. *Curr. Res. Food Sci.* 7, 100543. doi:10.1016/j.crf.2023.100543
- Cangui, S., Nacato-Toapanta, A. L., Enríquez-Martínez, L. J., Salinas-Delgado, G. A., Reyes, J., et al. (2023). Battle royale: immune response on biofilms – host-pathogen interactions. *Curr. Res. Immunol.* 4, 100057. doi:10.1016/j.crimmu.2023.100057
- Cangui, S., Nacato, A., Enríquez, L., Reyes, J., Garzon, D., and Machado, A. (2022). Biofilm-forming microorganisms causing hospital-acquired infections from intravenous catheter: a systematic review. *Curr. Res. Microb. Sci.* 3 (Jan), 100175. doi:10.1016/j.crmicr.2022.100175
- Castro, J., Lima, Á., Sousa, L. G. V., Rosca, A. S., Muzny, C. A., and Cerca, N. (2022). Crystal violet staining alone is not adequate to assess synergism or antagonism in multi-species biofilms of bacteria associated with bacterial vaginosis. *Front. Cell Infect. Microbiol.* 11, 795797. doi:10.3389/fcimb.2021.795797
- Chauviere, G., Coconnier, M. H., Kerneis, S., Fourniat, J., and Servin, A. L. (1992). Adhesion of human lactobacillus acidophilus strain LB to human enterocyte-like Caco-2 cells. *J. Gen. Microbiol.* 138 (8), 1689–1696. doi:10.1099/00221287-138-8-1689
- Elshikh, M., Ahmed, S., Funston, S., Dunlop, P., McGaw, M., Marchant, R., et al. (2016). Resazurin-based 96-well plate microdilution method for the determination of minimum inhibitory concentration of biosurfactants. *Biotechnol. Lett.* 38 (6), 1015–1019. doi:10.1007/s10529-016-2079-2
- Guamba, E., Vispo, N. S., Whitehead, D. C., Singh, A. K., Santos-Oliveira, R., Niebieskikwiat, D., et al. (2023). Cellulose-based hydrogels towards an antibacterial wound dressing. *Biomaterial Science*, 11, 3461. doi:10.1039/D2BM01369J
- Han, W., Jiao, H., and Fox, D. (2018). "Scanning electron microscopy," in *Springer tracts in modern physics* Amsterdam, Netherlands (Elsevier Inc).
- Hasan, J., Crawford, R., and Ivanova, E. (2013). Antibacterial surfaces: the quest for a new generation of biomaterials. *Trends Biotechnol.* 31 (5), 295–304. doi:10.1016/j.tibtech.2013.01.017
- Khan, M., Rehman, N., Sharif, A., Ahmed, E., Farooqi, Z., and Din, M. (2020). Environmentally benign extraction of cellulose from dunchi fiber for nanocellulose fabrication. *Int. J. Biol. Macromol.* 153, 72–78. doi:10.1016/j.ijbiomac.2020.02.333
- Khatoun, Z., McTiernan, C., Suuronen, E., Mah, T., and Alarcon, E. (2018). Bacterial biofilm formation on implantable devices and approaches to its treatment and prevention. *Heliyon* 4 (12), e01067. doi:10.1016/j.heliyon.2018.e01067
- Machado, A., Zamora, L., Alexis, F., and Álvarez, J. M. (2023). Use of plant extracts, bee-derived products, and probiotic-related applications to fight multidrug-resistant pathogens in the post-antibiotic era. *Future Pharmacol.* 3 (3), 535–567. doi:10.3390/futurepharmacol3030034
- Muñoz, A., Cabezas, F., Tejera, E., and Machado, A. (2021). Comparative effectiveness of treatments for bacterial vaginosis: a network meta-analysis. *Antibiotics* 10 (8), 978. doi:10.3390/antibiotics10080978
- Park, S., Baker, J., Himmel, M., Parilla, P., and Johnson, D. (2010). Cellulose crystallinity index: measurement techniques and their impact on interpreting cellulase performance. *Biotechnol. Biofuels* 3, 10. doi:10.1186/1754-6834-3-10
- Rambo, M., and Ferreira, M. (2015). Determination of cellulose crystallinity of banana residues using near-infrared spectroscopy and multivariate analysis. *J. Braz. Chem. Soc.* 26, 1491. doi:10.5935/0103-5053.20150118
- Rodríguez, R., Guachi, B., Montalvo, D., and Machado, A. (2022). Lactobacilli displacement and *Candida albicans* inhibition on initial adhesion assays: a probiotic analysis. *BMC Res. Notes* 15 (1), 239. doi:10.1186/s13104-022-06114-z
- Sahar, D., Hoorieh, D., Farzaneh, N., and Malak, H. (2020). Characterization and the evaluation of antimicrobial activities of silver nanoparticles biosynthesized from *Carya illinoensis* leaf extract. *Heliyon* 6 (3), e03624. doi:10.1016/j.heliyon.2020.e03624
- Schierholz, J., and Beuth, J. (2001). Implant infections: a haven for opportunistic bacteria. *J. Hosp. Infect.* 49 (2), 87–93. doi:10.1053/jhin.2001.1052
- Senthilrajan, S., Venkateshwaran, N., Nareesh, K., Velmurugan, R., and Gupta, N. K. (2022). Effects of jute fiber length and weight percentage on quasi-static flexural and dynamic mechanical properties of jute/polyester composites for thin-walled structure applications. *Thin-Walled Struct.* 179, 109719. doi:10.1016/j.tws.2022.109719
- Tokiwa, Y., Calabia, B., Ugwu, C., and Aiba, S. (2009). Biodegradability of plastics. *Int. J. Mol. Sci.* 10 (9), 3722–3742. doi:10.3390/ijms10093722
- Weerasekera, M., Wijesinghe, G. K., Jayarathna, T. A., Gunasekara, C. P., Fernando, N., Kottegoda, N., et al. (2016). Culture media profoundly affect *Candida albicans* and *Candida tropicalis* growth, adhesion and biofilm development. *Mem. Inst. Oswaldo Cruz* 111 (11), 697–702. doi:10.1590/0074-02760160294
- Weinstein, M. P., and Clinical and Laboratory Standards Institute. (2021). *Performance standards for antimicrobial susceptibility testing*. Clinical and Laboratory Standards Institute, Wayne, PS, USA
- Wiegand, I., Hilpert, K., and Hancock, R. E. W. (2008). Agar and broth dilution methods to determine the minimal inhibitory concentration (MIC) of antimicrobial substances. *Nat. Protoc.* 3 (2), 163–175. doi:10.1038/nprot.2007.521
- Zamora, L., Guamba, E., Miño, K., Romero, M. P., Levoyer, A., Alvarez-Barreto, J. F., et al. (2022). Antimicrobial properties of plant fibers. *Molecules*, 27, 999. doi:10.3390/molecules2722999
- Zamora-Mendoza, L., Vispo, S. N., De Lima, L., Mora, J. R., Machado, A., and Alexis, F. (2023). Hydrogel for the controlled delivery of bioactive components from extracts of *eupatorium glutinosum* lam. Leaves. *Molecules* 28 (4), 1591. doi:10.3390/molecules28041591



OPEN ACCESS

EDITED BY

Ali Miserez,
Nanyang Technological University, Singapore

REVIEWED BY

Daniel Dikovsky,
Technion Israel Institute of Technology, Israel

*CORRESPONDENCE

Shai Barbut,
✉ sbarbut@uoguelph.ca

RECEIVED 15 December 2023

ACCEPTED 31 January 2024

PUBLISHED 15 March 2024

CITATION

Barbut S (2024), Advancement in automation of co-extrusion collagen casings.
Front. Soft Matter 4:1356641.
doi: 10.3389/frsfm.2024.1356641

COPYRIGHT

© 2024 Barbut. This is an open-access article distributed under the terms of the [Creative Commons Attribution License \(CC BY\)](#). The use, distribution or reproduction in other forums is permitted, provided the original author(s) and the copyright owner(s) are credited and that the original publication in this journal is cited, in accordance with accepted academic practice. No use, distribution or reproduction is permitted which does not comply with these terms.

Advancement in automation of co-extrusion collagen casings

Shai Barbut*

Department of Food Science, University of Guelph, Guelph, ON, Canada

Co extrusion sausage technology has been a game changer in the industry as it has transformed the traditional way of filling meat betters into premade casings (e.g., synthetic materials such as cellulose or natural casings) to producing the casings on top of the meat batter as it comes out of the stuffer. This allows full automation of the process (working 24/7) with lower waste, while also increasing food safety standards. The main material used is collagen which today is extracted from a limited type of beef hides. It is then treated with a strong alkaline solution, to breakdown some of the original structures, and later with a strong acid to allow swelling of the resulting suspension. The application of the collagen gel requires special equipment to line up the collagen fibers in such a way that they provide the strength and elasticity during the cooking operation (meat expands during cooking) and later provide the consumer with the characteristics bit/"snap" similar to natural casings. Understanding the interactions between the chemical and physical properties of collagen is essential in obtaining good results. During production it is important that the collagen is quickly dried and crosslinked so the shape of the product will not be modified. This requires special large horizontal dryers and a unit to apply liquid smoke (source of aldehydes for crosslinking). Currently most systems are built for large capacity production, and therefore require large investment, however the industry is working on developing smaller and more flexible units for future use.

KEYWORDS

automation, sausage casings, collagen, meat industry, co-extrusion technology

1 Introduction

The meat industry produces many types of meat products but is also known to be a fairly conservative industry. The products can be divided into three main categories: whole muscle, ground, and finely chopped meat products. The last two groups are the ones usually stuffed into casings. However, it should be mentioned that in the ground meat category we also find quite a few products that are not stuffed into casings (e.g., hamburgers, nuggets). Casings are used to hold a portion of the meat, give it a certain shape during cooking (until proteins denature and solidify) and later can stay on the product or be peeled off (i.e., edible and nonedible casings such as cellulose). If they stay on the product, they can also influence the textural properties of the sausage (e.g., natural and some fabricated collagen casings produce the typical "snap"). The oldest method of producing sausages has been with natural casings which has been used for thousands of years (Anonymous, 1990; Savic and Savic, 2016). This technology is still very popular today. It is interesting to note that only over the past 120 years new casing types have been introduced, including the ones manmade with cellulose, cotton fibers, prefabricated collagen, and plastic polymers. The development of those materials took place because they can be mass-produced, easier to apply, more economical, and easier to use at high-speed production lines/automated equipment. This is

mainly because they are much more uniform and possess consistent strength compared to natural casings. Co-extrusion collagen technology has been introduced only in the late 1970s (Burke, 1980; Kobussen et al., 2000). This technology has been a game-changing factor to the meat industry as co-extrusion involves forming the casings on top of the meat batter as it comes out of the stuffer, while the traditional casings (e.g., natural, cellulose, plastic) are brought to the plant and then filled/stuffed with meat. One of the big differences from the traditional premade casings is a need for a mechanism to quickly crosslink the collagen paste and form a rigid “envelope” around the product (the exact technology is discussed later). One of the major advantages of this technology is allowing more automation which is critical today when we face labor issues in the food industry. Another important advantage is related to food safety where we can remove people from the production line and also use cook-in-the-bag technology. This means that the product is not touched by people and later heat processed inside the bag, thus avoiding the need to later peel off the casings (e.g., cellulose casings commonly used in many high-volume hot dog production lines today). The removal of the casings from the fully cooked products at the processing plant provides an opportunity for post-cooking contamination. Overall, we have experienced a few major *Listeria* outbreaks in fully cooked meat products over the past few years (Howell and Miller, 2010; Kurpas et al., 2018). As will be discussed below, the co-extrusion technology also presents some big challenges to meat processors as cooking meat products in a closed package while they are touching each other can result in adhesion of adjacent products, etc. It should also be mentioned that from a sensory point of view, natural casings (sheep, hog, and bovine) still represent the gold standard for casings as they provide the unique and familiar “snap”/bite to sausages. This occurs because of the unique structure of the connective tissue in the GI tract which is composed of aligned collagen and some elastin fibers which together allow some stretching of the casings. The latter is important to the meat processor as the casings can expand during stuffing and heating, and later creating the “snap” effect. The concept of this new co-extrusion casings mainly relies today on collagen; however, this collagen has to first be extracted (mostly from selected beef hides), then limed (exposed to high pH) to break down some of the structures, followed by acidification to allow swelling of the collagen gel. Performing the extraction process in the right way is essential to obtain high quality collagen gel, as will be discussed below.

The advantage of using a collagen gel is the fact that the equipment can produce a very uniform casing with controlled thickness and strength as compared to using natural casings which can have weak spots, variation in diameter, and sometimes even holes/tears. The latter defect is usually caused by the cleaning process of natural casings while the formers are due to natural variation in biological specimens (Bakker et al., 1999). The occurrence of those things usually requires stopping the whole stuffing process and starting a new batch of casings (i.e., not ideal for automation, and results also in wasting some of the meat).

It should also be noted that today there are co-extrusion systems utilizing alginate which employ hydrocolloid gum (obtained from seaweed) and dispense it on the surface of the product and later crosslink it with calcium ions (Harper et al., 2015; Hilbig et al., 2020). However, on a worldwide basis, those systems represent a small market segment, although in certain regions can have a noticeable

presence. They will not be discussed here in great detail because of their low representation in the market and because their technology is not as complicated as the collagen co-extrusion. The latter refers to dealing with collagen fibers that need to be aligned around the product to provide strength as well as the unique “snap” (not achieved by alginate) and therefore require special equipment (Figure 1).

2 Advantages and limitations of using the technology

When introducing a new technology, the industry usually wants to be presented with three to four good reasons to embrace the technology and three to four limitations/disadvantages. A summary of those major points is provided, and those points are further discussed later in this Perspective.

2.1 Advantages

2.1.1 Fully automating the process

The co-extrusion process represents a game-changer as the meat batter, exiting the stuffer, is continuously coated with a collagen gel (commonly contains 4%–6% protein) that is later crosslinked, and heat processed. The traditional sausage stuffing process is a batch operation because it involves finite segments of casings that require stopping/changing the nozzle at the end of each casing's portion/sleeve. Eliminating this step allows us to fully automate the process, save on labor, and work 24/7.

2.1.2 Improving food safety

Removing people from the line, and then cooking the product in edible casing placed in a hermetically sealed bag that is only opened by the consumer, represents a big improvement. This eliminates the possible post-cooking contamination by pathogens such as *Listeria* and *Salmonella* of fully cooked products which can happen during casing removal and packaging the individual cooked sausages (Kurpas et al., 2018). It also reduces the risk of spoilage bacteria contamination and hence significantly improves shelf life, reduces waste, and enhances sustainability.

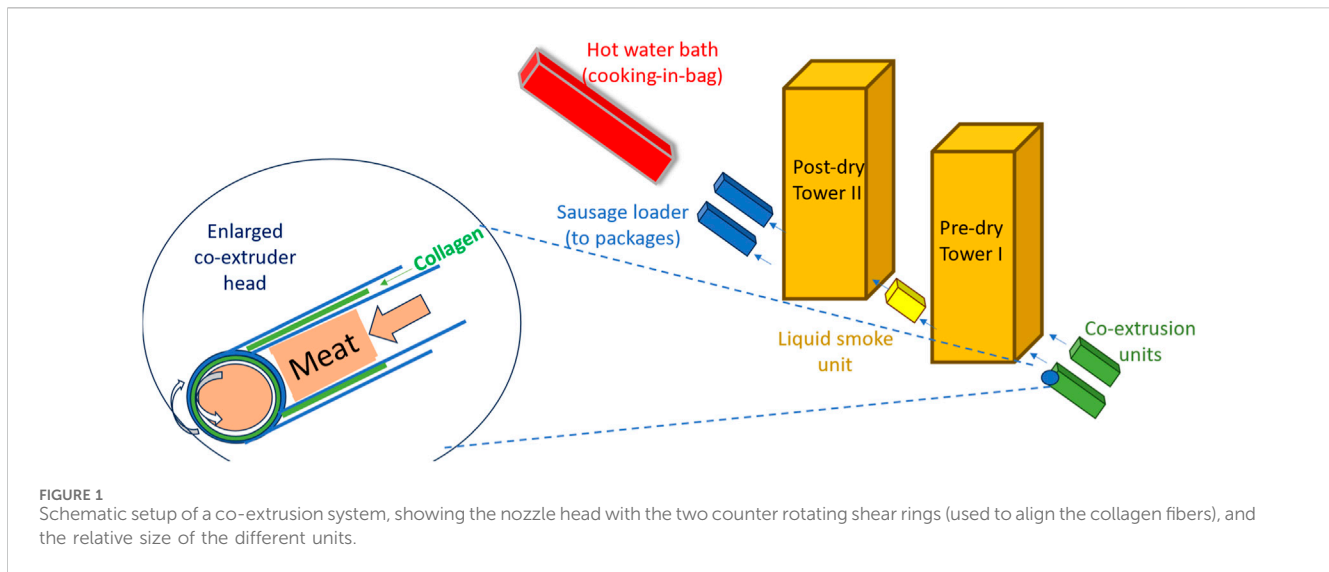
2.1.3 Producing uniform products

Since the product is continuously coated with collagen gel, very accurate weight control can be implemented and continuously adjusted during the production day when small deviations are detected. Some of the systems have the capacity to check the weight of each individual link and automatically adjust the weight of the product so expensive give-away is minimal. Uniformity also helps in implementing automation as dealing with similar size and shape sausage links is much easier than dealing with products stuffed into natural casings.

2.2 Limitations

2.2.1 Investment cost

The current systems are very big and require a large investment in equipment and floor space. Figure 1 illustrates the equipment



used, where a significant space/investment is required mainly for the drying towers. The first tower is used to pre-dry the casings, just after their application and submersion in a saturated salt solution (used to start dewatering). This is an important step as one needs to harden the casing quickly so the meat will not flow out. Actually, the drying is done when the casing is still unstable and therefore products are positioned horizontally and placed in baskets. This is followed by a liquid smoke bath/spray which is used to crosslink the collagen (via the aldehydes in the smoke) and further increase the casing's strength (Hoogenkamp et al., 2015; Suurs and Barbut, 2020). The next stage is referred to as post-drying (at $\sim 60^{\circ}\text{C}$) and is used to continue drying and hardening the casings. The products coming out have a surface temperature of about 50°C – 60°C and are not sticky anymore so they can be packaged in the so-called cook-in-the-bag plastic material. Bags are later submerged in hot water and fully cooked (heat conductivity of water is faster than air and thus more efficient than a regular smoke house; also, no evaporation losses encountered) which are other advantages of this technology. Due to the large investment, a company usually needs to already have a big market share of a certain product. This is currently the case for big companies that sell a large quantity of hot dogs, cocktail sausages, etc., where their traditional systems are working 24/7 and require quite a lot of manual labor. Depending on the production volume, the return on investment of a new co-extrusion system in such a case can be as low as 5 years.

2.2.2 Operation complexity

Operating the system requires substantial knowledge and understanding of material science, meat science, chemistry, and engineering. Integrating all those disciplines is important for the successful operation of the system. Paying attention to the different possible interactions (e.g., meat and casings while being formed together) is also crucial to optimizing such a high volume operation.

It is interesting to note that 40%–50% of the small diameter sausages produced in the United States are produced by co-extrusion (personal communication) and of that, over 50% of this amount is produced at one location. This location specializes only in co-extrusion and also provides co-packing services for the

industry. There are a few large operations in Europe but not any significant one in South America, for example.

However, as will be described below, equipment manufacturers are currently working on designing smaller systems that will make it easier to change the product line. The current big system can produce 5 tons of product per hour with a three to four nozzle head, while the smaller systems will be designed for a few hundred kg per hour. Another factor that contributes to the complexity is the lack of enough technical literature and specifications of the gels (Suurs et al., 2022). Currently, most gel suppliers only post basic technical information of the products. This information includes items such as total protein content, pH, number of microorganisms (per g), but not engineering parameters such as viscosity at different temperatures, shear thinning behavior, etc.

2.2.3 Limited flexibility

The large systems are designed to produce a certain diameter product while all the production parameters (e.g., pre-drying, post-drying, cooking time) are preprogrammed and therefore usually can be very time-consuming to change/modify. However, it should be noted that similar diameter products made from chicken, beef, or pork can be produced without any special modifications. Overall, one should realize those systems are very cost effective when calculating the production of each sausage unit.

3 Discussion

3.1 The mechanical process of extrusion

Figure 1 shows the way the collagen is introduced onto the meat batter coming out of the stuffer. It is important to realize that a unique delivery system had to be developed for the deposition of collagen as it is crucial to line up the fibers in a certain way. This is to provide the strength needed for the casings to first go through the cooking process (expansion of the meat batter during heating) and later to provide a good bite (the “snap” effect) when consumers are eating the product. The system that has been developed has two

TABLE 1 Analysis of endothermic peaks from differential scanning calorimetry (DSC) thermograms of five commercial co-extrusion collagen samples (C1 to 5) tested as collagen dispersions coming out of the box, and as partially dehydrated/brined films. From [Barbut et al. \(2020\)](#).

Collagen	Treatment	Onset temperature (°C)	Temperature of denaturation (°C)	Enthalpy ΔH (J/g)
C1	Dispersion	33.54 \pm 0.21	36.71 \pm 0.51	5.33 \pm 0.61
C2	Dispersion	34.59 \pm 0.15	38.44 \pm 0.06	3.05 \pm 0.06
C3	Dispersion	34.26 \pm 0.01	38.09 \pm 0.08	4.12 \pm 0.10
C4	Dispersion	35.41 \pm 0.11	38.94 \pm 0.02	3.93 \pm 0.26
C5	Dispersion	33.45 \pm 0.10	37.30 \pm 0.21	4.45 \pm 0.03
C1	Film	59.90 \pm 0.23	64.87 \pm 0.12	3.07 \pm 0.55
C2	Film	58.40 \pm 0.21	63.88 \pm 0.57	1.76 \pm 0.38
C3	Film	60.32 \pm 1.61	65.00 \pm 0.68	3.05 \pm 0.21
C4	Film	58.22 \pm 0.24	63.94 \pm 0.61	3.06 \pm 0.82
C5	Film	58.30 \pm 0.40	65.34 \pm 0.37	4.19 \pm 0.37

counter rotating cones with a space, tapering off to a size of a few mm at the exit point. The collagen is pumped into that space and the counter rotating cones (commonly 100–300 rpm) force the lining up of fibers around the meat batter in such a way that the outer collagen layer has fibers going around the circumference of the product, the fibers in the middle are randomly distributed, and the inner fibers are again lined up around the circumference of the product. [Hoogenkamp et al. \(2015\)](#) reported on how the differential speed of the two counter rotating cones affect the arrangement of the fibers (using second harmonic single imaging and quantifying the fiber orientation) and later the shear force values of the resulting casings.

3.2 Sources and preparation of the collagen gels

These are very important aspects as collagen quality has a major effect on the strength and sensory characteristics of the meat product. Currently, the main source of collagen is the corium layer obtained from certain beef hides. The layer is found on the inside part of the ventral beef skin and usually appears as a white layer of connective tissue. It is removed prior to processing the beef hide into leather (i.e., a byproduct of the meat industry). The challenge is that collagen quality is affected by factors such as breed, age, nutrition, and climate conditions. Right now, the industry is getting the collagen from a very specific breed of beef animals raised at a few geographical locations where the industry knows it can provide the quality required. However, in the past few years, researchers and industry have been examining other sources such as corium and skin from other beef breeds ([Suurs et al., 2023](#)), and broiler skins ([Oechsle et al., 2016](#)), as those collagen sources also represent byproducts of the meat industry and are found in large quantities, but currently go into low value pet food/fertilizer use.

The preparation of the collagen is critical to achieve the optimal casing characteristics. It basically involves liming the corium layer (exposing it to high concentration of NaOH at pH 12–13) for a few days to break down some of the collagen structures (note: need to be

careful not to overdo this as then the casings cannot be produced). This is followed by washing off the alkaline compounds, physically chopping the collagen (using a device similar to a home food processor) and then acidification with either HCl or organic acids to allow swelling of the collagen paste. [Oechsle et al. \(2016\)](#) describe precisely how different acids and the salts of the Hofmeister series affect the swelling of a collagen paste. [Hood \(1987\)](#) nicely described the effects of different pH values on collagen swelling, where swelling maxima is seen under high alkaline and acid conditions (pH 12 and 2, respectively). Of particular interest is pH 2–3 (i.e., most common pH of commercial casing gels), which also demonstrate maximal gel viscosity, a firmer and more translucent gel.

It is important to note that native collagen shows a denaturation transition point at about 60°C ([Bernal and Stanley, 1986](#)). After liming and acidification, the denaturation point goes down to about 34°C ([Table 1](#)). This is a very important point to understand when using collagen for coextrusion because later the collagen (on the sausage) goes through other modifications while being exposed to the brining process (saturated salt solution) and crosslinking by the aldehydes found in liquid smoke. Overall, crosslinking is an essential part of the process and currently liquid smoke which contains aldehydes is used as the chemical linker. This results in the denaturation point doubling and reaching about 62°C ([Table 1](#)). It should also be mentioned that collagen from commercial sources (C1 to 5, see [Table 1](#)) exhibit different tensile strength after being crosslinked. For example, the tensile strength of C1 is significantly greater than C3 (0.67 vs 0.38 MPa), while the corresponding percent elongation is 24.8% versus 18.8%, respectively ([Barbut and Ioi, 2019](#)). [Suurs et al. \(2022\)](#) also reported that the elastic modulus (G') curves of coextruded collagen films exposed to heating (5°C–60°C) show a big drop at about 35°C. The exact temperature depended on the source of poultry collagen evaluated (i.e., obtained from young chickens of fast- and slow-growing rates, and older laying hens or broiler breeders). Pretty similar observations were also reported for different sources of cattle collagen (American calves, heavy Dutch veal, ox/heifer, and heavy German cows. [Suurs et al., 2023](#)).

3.3 Work on improving collagen gels

Only a few academic labs around the world are working on this topic (e.g., Hohenheim University, Wageningen University, University of Guelph) as well as the very few collagen companies involved in the business (their data is confidential). The current source of collagen demonstrates pretty good functionality but is obtained from a very limited group of beef animals. Over the past decade there have been attempts to use other sources such as corium layer from other beef animals, chicken skins, and pork bladder. It should be mentioned that currently there is a limited source of poultry collagen on the market, but the goal is to be able to obtain large amounts of collagen from different species (e.g., overcome religious concerns) and upgrade byproducts of the meat industry, currently going to low-cost streams. [Oechsle et al. \(2017\)](#) reported on the possible modification of extruded chicken skin collagen films and telopeptide-poor collagen from bovine hide by adding salt (0.05 mol/kg) and/or partial substitution by 1.25% soy isolate. Salt addition allowed forming beef and chicken collagen films with high tensile strength and elasticity. In contrast, substitution with soy proteins decreased gel and film strength. This weakening could be compensated by adding salt and leading to more homogenous gels yielding films with higher storage moduli. The compensating salt effect was more pronounced for chicken skins than for beef hides, suggesting differences in the molecular interactions and networks forming between the two collagen types. Later, [Suurs et al. \(2022\)](#) looked at different poultry skin sources (young and old broilers) as potential raw materials. Collagen transition temperatures analysis and SDS-page showed little difference in these parameters among the different sources. However, after exposure to the saturated salt solution, forming films from older broilers (breeders and laying hens) was very poor. The authors concluded that chicken skin collagen from fast and slow growing young broilers has the potential of being a suitable source for co-extrusion. [Suurs et al. \(2023\)](#) also evaluated different cattle skin collagens and reported that American calves, Dutch heavy veal, and Danish ox breeds are potential suitable alternative collagen sources while the German cow breed is not.

3.4 Work on new production systems

Currently, only large collagen production systems are offered to the industry. However, some equipment manufacturers are considering supplying smaller systems that can be much more versatile in terms of changing product lines in a fast and non-complicated manner. Those systems should be able to produce a few hundred to thousand kg per hour, be much less costly and allow meat companies to quickly change various parameters (e.g., nozzle diameter, gel application rate). Such systems can potentially open the market for medium and small processors to adopt the co-extrusion technology while not having to invest large sums for the infrastructure. One of the ideas is to also offer modular systems that can be expanded later on.

4 Summary

Overall, the co-extrusion collagen concept has been a game changer in the industry, allowing fully automated small diameter sausage production. When comparing to, for example, a natural casing stuffing operation which requires a substantial amount of manual labor, the co-extrusion system presents a major advantage in cost-savings and waste-reduction (natural casing operations require initial labor-intensive cleaning of the casings, dealing with rupture of casings, and discarding products' ends). The concept is also a major step in improving food safety as cook-in-the package technology can be used to prevent post-cooking contamination, and also increase shelf life while reducing waste (collagen is an edible material as opposed to the large amount of cellulose casings used to process the product and then removed after 2–3 h). However, currently using the technology requires a big investment in equipment and employing a certain number of highly skilled people. It is expected that a new smaller system will be available on the market and open the way for small/medium size companies to also adopt the technology.

Data availability statement

The original contributions presented in the study are included in the article/Supplementary material, further inquiries can be directed to the corresponding author.

Author contributions

SB: Conceptualization, Resources, Writing—original draft, Writing—review and editing.

Funding

The author(s) declare financial support was received for the research, authorship, and/or publication of this article. No special funding was awarded for this perspective article. The author is a faculty member at the University of Guelph.

Acknowledgments

The author would like to thank his previous students working in this area, and the organizers of the excellent first Soft Matter Conference: Drs. Ali Gilles, Alejandro Marangoni, Frank Alexis, and Mezzenga Raffaele.

Conflict of interest

The author declares that the research was conducted in the absence of any commercial or financial relationships that could be construed as a potential conflict of interest.

Publisher's note

All claims expressed in this article are solely those of the authors and do not necessarily represent those of their affiliated

organizations, or those of the publisher, the editors and the reviewers. Any product that may be evaluated in this article, or claim that may be made by its manufacturer, is not guaranteed or endorsed by the publisher.

References

- Anonymous, (1990). Some taste recipes for a Babylonian feast; national geographic. *Geographica* 178.
- Bakker, W. A. M., Houben, J. H., Koolmees, P. A., Bindrich, U., and Sprehe, L. (1999). Effect of initial mild curing, with additives, of hog and sheep sausage casings on their microbial quality and mechanical properties after storage at difference temperatures. *Meat Sci.* 51 (2), 163–174. doi:10.1016/s0309-1740(98)00118-1
- Barbut, S., and Ioi, M. (2019). An investigation of the mechanical, microstructural and thermo-mechanical properties of collagen films cross-linked with smoke condensate and glutaraldehyde. *Italian J. Food Sci.* 31 (3), 644–660.
- Barbut, S. M., Ioi, M., and Marcone, M. (2020). Co-extrusion of collagen casings - effects of preparation, brining, and heating on the strength, rheology, and microstructure. *Italian J. Food Sci.* 32 (1), 91–106.
- Bernal, V. M., and Stanley, D. W. (1986). Changes in the melting characteristics of bovine tendon collagen induced by a bacterial collagenase. *J. Food Sci.* 51, 834–835. doi:10.1111/j.1365-2621.1986.tb13944.x
- Burke, N. I. (1980). Use of corium layer in edible casings. *J. Am. Leather Chem. Assoc.* 75, 459.
- Harper, B. A., Barbut, S., Smith, A., and Marcone, M. F. (2015). Mechanical and microstructural properties of “wet” alginate and composite films containing various carbohydrates. *J. Food Sci.* 80, E84–E92. doi:10.1111/1750-3841.12716
- Hilbig, J., Hartlieb, K., Gibis, M., Herrmann, K., and Weiss, J. (2020). Rheological and mechanical properties of alginate gels and films containing different chelators. *Food Hydrocoll.* 101, 105487. doi:10.1016/j.foodhyd.2019.105487
- Hood, L. L. (1987). “Collagen in sausage casings,” in *Advances in meat research - vols.* (New York, NY, USA: AVI Books -Van Nostrand Reinhold Company Inc).
- Hoogenkamp, H. R., Bakker, G.-J., Wolf, L., Suurs, P., Dunnewind, B., and Barbut, S., (2015). Directing collagen fibers using counter-rotating cone extrusion. *Acta Biomater.* 12, 113–121. doi:10.1016/j.actbio.2014.10.012
- Howell, G. V. J., and Miller, R. (2010). Maple leaf foods: crisis and containment case study. *PCR* 1, 47. doi:10.5130/pcr.v1i1.1297
- Kobussen, J., Kobussen, M., and Alexander, D. (2000). *Brine formulation for curing extruded sausage strand.* (United States Patent 6054155). Available at: <https://www.freepatentsonline.com/6054155.html>.
- Kurpas, M., Wiczorek, K., and Osek, J. (2018). Ready-to-eat meat products as a source of *Listeria monocytogenes*. *J. Veterinary Res.* 62, 49–55. doi:10.2478/jvetres-2018-0007
- Oechsle, A. M., Akgün, D., Krause, F., Maier, C., Gibis, M., and Kohlus, R., (2016). Microstructure and physical-chemical properties of chicken collagen. *Food Struct.* 7, 29–37. doi:10.1016/j.fostr.2016.02.001
- Oechsle, A. M., Bugbee, T. J., Gibis, M., Kohlus, R., and Weiss, J. (2017). Modification of extruded chicken collagen films by addition of co-gelling protein and sodium chloride. *J. Food Eng.* 207, 46–55. doi:10.1016/j.jfoodeng.2017.03.017
- Savic, Z., and Savic, J. (2016). *Sausage casings.* 2nd. Victus International GmbH, Vienna, Austria. Available at: <https://search.worldcat.org/title/sausage-casings/oclc/961939942?referer=di&ht=edition>.
- Suurs, P., and Barbut, S. (2020). Collagen use for co-extruded sausage casings – a review. *Trends Food Sci. Technol.* 102, 91–101. doi:10.1016/j.tifs.2020.06.011
- Suurs, P., Van Den Brand, H., Daamen, W. F., and Barbut, S. (2022). Properties of different poultry skins sources in relation to co-extruded sausage casings. *Food Hydrocoll.* 125, 107434. doi:10.1016/j.foodhyd.2021.107434
- Suurs, P., Van Den Brand, H., Ten Have, R., Daamen, W. F., and Barbut, S. (2023). Evaluation of cattle skin collagen for producing co-extrusion sausage casing. *Food Hydrocoll.* 140, 108595. doi:10.1016/j.foodhyd.2023.108595



OPEN ACCESS

EDITED BY

Frank Alexis,
Universidad San Francisco de Quito, Ecuador

REVIEWED BY

Luca Lanotte,
INRA Centre Bretagne-Normandie, France
Alejandro D. Rey,
McGill University, Canada
Matthew Harrington,
McGill University, Canada

*CORRESPONDENCE

Konstantin G. Kornev,
✉ kornev@clemson.edu

†These authors have contributed equally to
this work

RECEIVED 19 November 2023

ACCEPTED 13 February 2024

PUBLISHED 27 March 2024

CITATION

Aprelev P, Brasovs A, Bruce TF, Beard CE,
Adler PH and Kornev KG (2024), To seal a
wound, caterpillars transform blood from a
viscous to a viscoelastic fluid in a few seconds.
Front. Soft Matter 4:1341129.
doi: 10.3389/frsfm.2024.1341129

COPYRIGHT

© 2024 Aprelev, Brasovs, Bruce, Beard, Adler
and Kornev. This is an open-access article
distributed under the terms of the [Creative
Commons Attribution License \(CC BY\)](#). The use,
distribution or reproduction in other forums is
permitted, provided the original author(s) and
the copyright owner(s) are credited and that the
original publication in this journal is cited, in
accordance with accepted academic practice.
No use, distribution or reproduction is
permitted which does not comply with these
terms.

To seal a wound, caterpillars transform blood from a viscous to a viscoelastic fluid in a few seconds

Pavel Aprelev^{1†}, Artis Brasovs^{1†}, Terri F. Bruce², Charles E. Beard³,
Peter H. Adler³ and Konstantin G. Kornev^{1*}

¹Department of Materials Science and Engineering, Clemson University, Clemson, SC, United States,

²Light Imaging Facility, Clemson University, Clemson, SC, United States, ³Department of Plant and
Environmental Sciences, Clemson University, Clemson, SC, United States

In insects vulnerable to dehydration, the mechanistic reaction of blood after wounding is rapid. It allows insects to minimize blood loss by sealing the wound and forming primary clots that provide scaffolding for the formation of new tissue. Using nano-rheological magnetic rotational spectroscopy with nickel nanorods and extensional rheology, we studied the properties of blood dripping from the wound of caterpillars of the Carolina sphinx moth (*Manduca sexta*) with a high concentration of blood cells. We discovered that wound sealing followed a two-step scenario. First, in a few seconds, the Newtonian low-viscosity blood turns into a non-Newtonian viscoelastic fluid that minimizes blood loss by retracting the dripping blood back into the wound. Next, blood cells aggregate, starting from the interfaces and propagating inward. We studied these processes using optical phase-contrast and polarized microscopy, X-ray imaging, and modeling. Comparative analyses of the cell-rich and cell-poor blood of different insects revealed common features of blood behavior. These discoveries can help design fast-working thickeners for vertebrate blood, including human blood.

KEYWORDS

cell aggregation, hemolymph, hemocytes, clotting kinetics, Lepidoptera, rheology

1 Introduction

Insects have developed special strategies to deal with wounding and potential infection (Salt, 1970; Wigglesworth and Gupta, 1979; Gillespie et al., 1997; Theopold et al., 2002; Strand, 2008; Dushay, 2009; Jiang et al., 2010; Hillyer and Strand, 2014; Eleftherianos et al., 2021). Wounding triggers humoral and cellular reactions associated with insect blood (hemolymph) (Salt, 1970; Gregoire and Rockstein, 1974; Wigglesworth and Gupta, 1979; Bohn and Brehelin, 1986; Gillespie et al., 1997; Theopold et al., 2002; Strand, 2008; Dushay, 2009; Jiang et al., 2010; Hillyer and Strand, 2014; Eleftherianos et al., 2021). These reactions span spatial scales, from the nanometer to microscopic level, and time scales, from microseconds to hours. At the wound site, a primary clot nucleates within minutes after wounding (Salt, 1970; Wigglesworth and Gupta, 1979), while the formation of a scab and new epidermal tissue happen on a time scale more than two orders of magnitude greater (Salt, 1970; Wigglesworth and Gupta, 1979; Parle et al., 2016). The physical features of primary clot formation in the first minutes of hemolymph leakage from the wound are

not sufficiently detailed, and a quantitative analysis of the kinetics of clot nucleation in cell-rich hemolymph was only recently reported (Aprelev et al., 2019).

The concentration of cells (hemocytes) in the blood of different insect species varies significantly; hence, insects developed various strategies for wound sealing. In the hemocyte-poor hemolymph, as in butterflies and moths, the humoral reactions in the plasma cause the self-assembly of lipoproteins (Bohn and Brehelin, 1986; Zdybicka-Barabas and Cytrynska, 2013; Ling et al., 2018; Miserez et al., 2023). Lipoproteins, with their surfactant-like action, recognize the foreign interface and immediately engage hemocytes or other large proteins, such as hemocytin (molecular weights of hemocytin in the moth *Bombyx mori* and the fly *Drosophila melanogaster* are ~260 and ~300 kDa, respectively) (Hu et al., 2024), to aggregate into filamentary threads consisting of more complex biopolymer subunits (Mulnix et al., 1995) and then into gel-like wound covers (Gregoire and Rockstein, 1974; Bohn and Brehelin, 1986). The gel tightening of the hemocytes at the wound surface renders the complex mesh impermeable to microorganisms and hinders water evaporation.

Lipoproteins are also found in the primary clots of the hemocyte-rich hemolymph (Brehelin, 1979; Boman and Hultmark, 1987; Chino et al., 1987; Mulnix et al., 1995; Theopold et al., 2004; Dushay, 2009; Jiang et al., 2010; Maravilla et al., 2020), such as exchangeable apolipoprotein-III in the cockroach *Periplaneta americana* (Coodin and Caveney, 1992; Dushay, 2009). In contrast to the hemocyte-poor blood of butterflies and moths (Lepidoptera), the hemolymph of their larvae (i.e., caterpillars) is hemocyte-rich. The comparative biomolecular studies of clotting in lepidopteran larvae and adults and in other insects suggest that the hemocytin and lipoproteins common in adults and larvae could be among the first to respond and trigger complex immune reactions, resulting in the formation of filamentary structures and primary clots (Boman and Hultmark, 1987; Mulnix et al., 1995; Theopold et al., 2004; Rahman et al., 2006; Jiang et al., 2010; Zdybicka-Barabas and Cytrynska, 2013; Staczek et al., 2018; Maravilla et al., 2020; Hu et al., 2024).

The limiting step for primary clot formation in the larvae of the Carolina sphinx moth (*Manduca sexta*) is the aggregation of hemolymph cells (hemocytes), assisted by pseudopodia, the thread-like extensions of hemocytes (Gregoire, 1955). In the larvae of *M. sexta*, the cells aggregate in approximately 3–5 min. Within a few minutes, the cells consolidate, and the aggregate stiffens, as manifested by a weak elastic reaction (Aprelev et al., 2019) approximately 4–5 min from the moment of aggregation. The primary clot remains soft relative to the repaired wound (Parle et al., 2016) not only in Lepidoptera, such as *M. sexta*, but also in other insects. In *Drosophila*, for example, primary clots are initially soft and can be pulled from the hemolymph using a metal needle (Bidla et al., 2005). The biomechanics of primary clot nucleation, consolidation, and stiffening remain poorly understood.

In view of these knowledge gaps, we investigated the material properties of clotting hemolymph to reveal the physical determinants that stop the bleeding. The hemocyte-rich blood of the fifth-instar (i.e., mature) larvae of *M. sexta* was chosen as our model system.

We first studied the time needed for the insect to react to wounding and to stop the loss of hemocyte-rich hemolymph. For

the caterpillars of *M. sexta*, the time to change the rheological properties of the hemolymph is surprisingly short, i.e., only a few seconds. This fast reaction and the small volume of the available droplets present a challenge to the investigation of the material properties of the hemolymph. Therefore, we developed new approaches to study the rheological and surface properties of the droplets. The comparative analysis of the short-time clotting phenomena associated with the preliminary sealing of the insect wound revealed a general strategy for wound healing: first, the insect turns the Newtonian, almost inviscid hemolymph into a viscoelastic fluid. The acquired elasticity prevents the hemolymph from escaping from the wound. The fluid film or a drop covering the wound surface then forms a crust prepared from a gel-like biopolymer mesh (in hemocyte-poor hemolymph) or a composite hemocyte-polymer mesh (in hemocyte-rich hemolymph).

2 Results

2.1 The time to stop the bleeding from the wound

To evaluate the relevant time scale of the formation of a primary clot, we used a setup (Figure 1A) in which the wound was oriented downward and the hemolymph dripped on its own. Caterpillars of 9–10 g and 1–2 days before pre-pupation were used. Each caterpillar was constrained in a tube, and the hemolymph was extracted via a 1–2-mm incision in the third proleg.

This setup allowed us to probe the dripping hemolymph several seconds after making the incision. Filming the features of the drop and liquid bridge formation had a success rate of approximately 5%, because shortly after the incision, the caterpillar moved vigorously, causing difficulties in focusing the camera. Nonetheless, our naked-eye observations and filming confirmed that in the first several seconds after the incision, the detachment of the falling drop from the wound followed the scenario common for simple fluids, such as water (Eggers, 1997; Montanero and Ponce-Torres, 2020); the drop formed a liquid bridge connecting it with the wound (Figure 2A), and then, the bridge necked (Figures 2B, C) and broke, producing satellites (Figures 2D, E). This behavior suggested that in the first seconds, a mostly water-like, low-viscosity hemolymph dripped from the wound.

During the next 5–10 s (i.e., ~10–15 s after incision), drop detachment showed a different scenario (Figure 3). The necking stage, shown in Figures 2B, C, proceeded similarly (Figures 3A, B), but after that, instead of breaking up the bridge, as shown in Figure 2D, the hemolymph formed filaments of uniform radii (Figure 3C). Before the breakup, the straight filament formed a bulge in the middle (Figure 3D), and the bulge grew to form a second drop (Figures 3E, F). The droplets moved toward the menisci pulled by the connecting filaments. The filaments that formed 10–15 s after the incision broke up in ~20–40 ms (Figure 3G).

During the next 50–60 s (i.e., ~75 s after incision), drop detachment followed the scenario shown in Figure 3 (Supplementary Video S1). However, the lifetime of these late filaments increased significantly by approximately one order of magnitude to ~240 μ s.

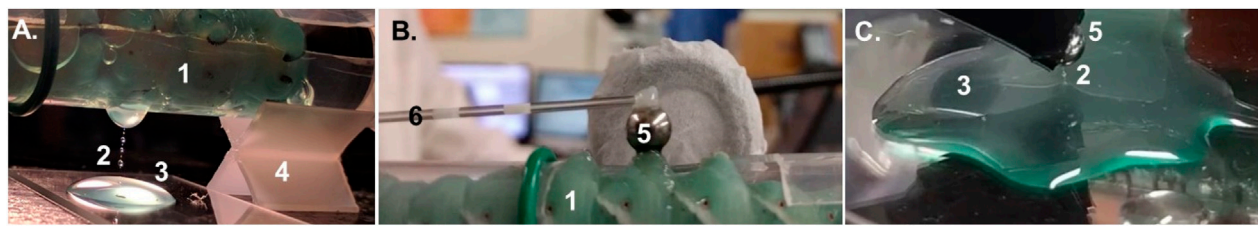


FIGURE 1

(A) Cylindrical plastic sleeve (1) supported by an X-shaped holder (4). The plastic sleeve has a window exposing a portion of the side of the mid-abdomen of a larva of *Manduca sexta* with a wounded proleg. The dripping hemolymph formed long filaments (2) with droplets. The hemolymph is collected in a Petri dish (3). (B) The sleeve (1) with the caterpillar is flipped upside down, and a metal ball (5) is brought in contact with the wound to form a hemolymph meniscus. The glass rod (6) with the ball (5) is controlled by a manipulator that allows the ball to be lifted to a prescribed height and to form a liquid bridge. (C) Hemolymph filament can be obtained from a pool of hemolymph, using either the same ball (5) as in (B) or by applying a rod (6).

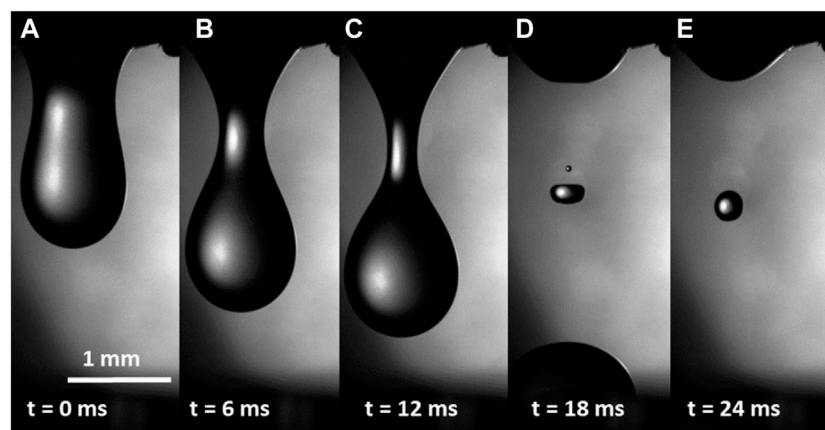


FIGURE 2

(A–E) Hemolymph dripping from the wound of a caterpillar several seconds after the wound was made. No filaments were observed, indicating that the hemolymph at this time scale was not highly viscous or elastic.

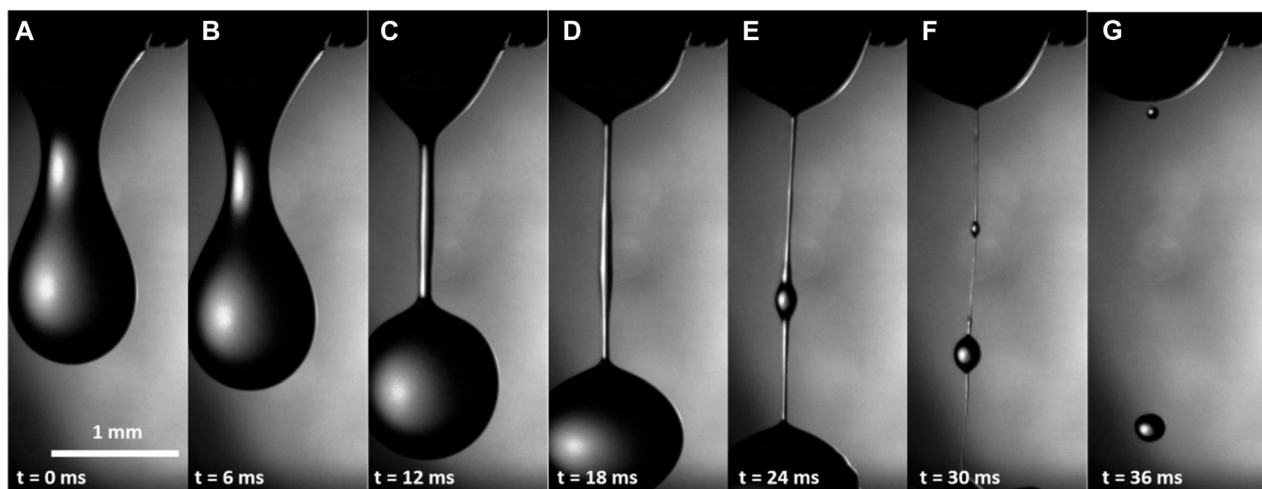


FIGURE 3

(A–G) Hemolymph dripping from the wound of a caterpillar within 10–15 s after wounding. A straight filament in (D) indicates that the hemolymph either increased its viscosity or became viscoelastic.

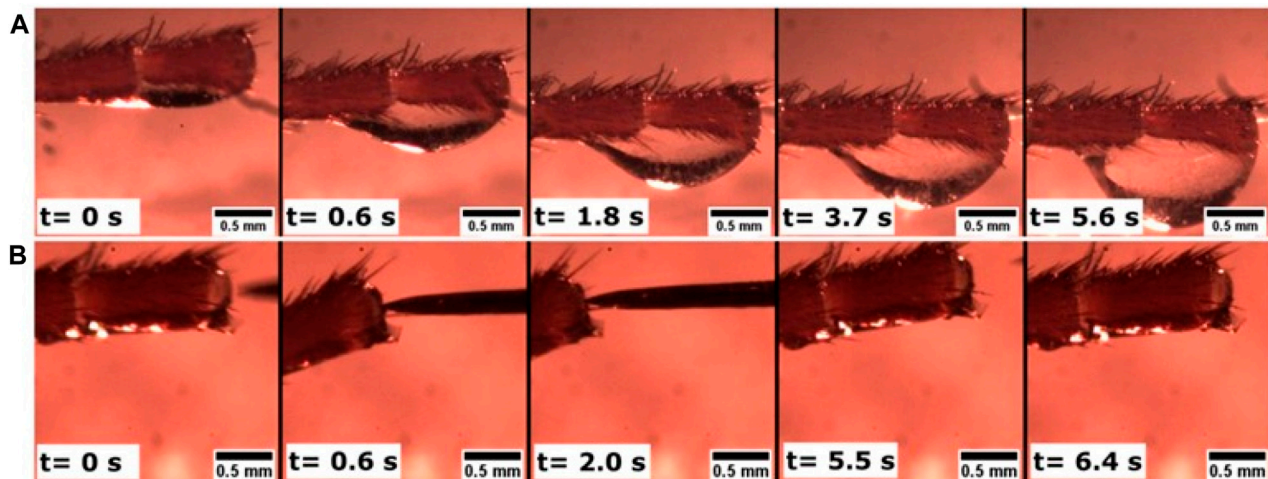


FIGURE 4

Hemolymph dripping from the severed antenna of the cockroach *Periplaneta americana*. The head (not pictured) is to the left. (A) After cutting off the end of the antenna, the hemolymph continued flowing to this end. Over approximately 6 s, a drop formed. After $t = 5.6$ s, the drop fell, and no other drops appeared. (B) After ~10 min, the wound was completely sealed by a rigid crust: a tungsten needle was not able to penetrate the crust. When the needle was applied ($t = 0.6$ s) to a cantilevered antenna, the antenna bent, tilting its end as shown in the figure. When the needle was removed ($t = 5.5$ s and $t = 6.4$ s), the antenna returned to its original state, and the sealed end appeared undeformed.

These results indicate that the properties of the hemolymph change quickly; the hemolymph starts dripping as an almost inviscid water-like fluid and then quickly changes its rheological properties. Typically, bleeding stopped after 60–90 s.

The scenario of wound sealing in the larvae of *M. sexta* was validated with that of the cockroach *P. americana* (Figure 4). Although the hemolymph composition of cockroaches could be somewhat different, both the insects have hemocyte-rich hemolymph (Chapman, 2013), and, as shown below, the plasma viscosity for both species is similar. After the detachment of an antennal flagellomere (i.e., an individual unit of the last antennal segment), a drop of hemolymph appeared at the cut end. The drop fell, and the remaining hemolymph moved back into the antennal lumen. No other drops appeared, and after approximately 10 min, the wound had sealed with a rigid crust.

The almost constant radius of the cylindrical filaments indicated that the hemolymph had either thickened by increasing its shear viscosity or had become elastic (McKinley and Sridhar, 2002; Montanero and Ponce-Torres, 2020). In other words, one could think of the filaments as being similar to those either produced by thick honey-like fluids or thin dog saliva-like fluids. To obtain honey-like filaments, the shear viscosity of the hemolymph must increase significantly. We, therefore, measured the shear viscosity by magnetic rotational spectroscopy (MRS) with nickel (Ni) nanorods.

2.2 Characterization of shear viscosity using magnetic rotational spectroscopy with nickel nanorods

Ferromagnetic nickel nanorods coated with poly(vinylpyrrolidone) were dispersed in a hemolymph drop and were continuously rotated by applying a rotating magnetic field and changing their rotating frequency ω_B (Gu and Kornev, 2016; Kornev et al., 2016; Aprelev et al., 2019;

Brasovs et al., 2023). When an applied rotating magnetic field B acts on a nanorod of magnetization M and volume V , it exerts a torque, $T_B = VMB\sin(\omega_B t - \theta)$, forcing the nanorod to turn in the B -plane. The angle $\psi = \omega_B t - \theta$ specifies the angle that the magnetic moment forms with the magnetic field at time moment t . The magnetic moment is aligned with the nanorod axis, forming angle θ with a stationary reference axis (Figure 5).

When a nanorod rotates, it experiences resistance from the surrounding hemolymph. The MRS theory uses the Jeffery (Jeffery, 1922) model of rotation of an ellipsoid in a Newtonian fluid of viscosity η . Therefore, this technique provides the fluid viscosity at the zero shear rate. The torque on the nanorod of length L_0 and diameter d is $T_\eta = \Gamma\eta d\theta/dt$, where $\Gamma = \frac{\pi L_0^3}{3\ln(L_0/d)-2.4}$ is the nanorod form factor (Doi and Edwards, 1988). For nanorods, the inertial forces at the given frequencies are insignificant; thus, by balancing the mechanical and magnetic torques, $T_\eta = T_B$, we model and interpret the observed behavior and the rotational dynamics of the nanorods in different drops of the hemolymph.

The nanorods were tracked using a camera (Figures 5A–C), and the videos were post-processed to fit the nanorod angle versus time, using this model. Two distinguishable scenarios of nanorod rotation are shown in Figures 5D, E.

At low-driving frequencies, ω_B , the nanorod rotated synchronously, lagging behind the field by a constant angle ψ . When the frequency ω_B increased above a certain critical value $\omega_c = VMB/(\Gamma\eta)$, the nanorod began to tumble (Figures 6A, B). By measuring ω_c , as explained by Kornev et al. (1999); Gu and Kornev (2016); Aprelev et al. (2017); and Brasovs et al. (2023), we measured the shear viscosity of the hemolymph (Table 1). The hemolymph of all probed species showed Newtonian behavior. The shear viscosity of the probed hemolymph did not change over the first few minutes (Figures 6C, D). When probed using a cone-and-plate viscometer at a greater load, the *M. sexta* hemolymph showed Newtonian behavior as well (Kenny et al., 2018).

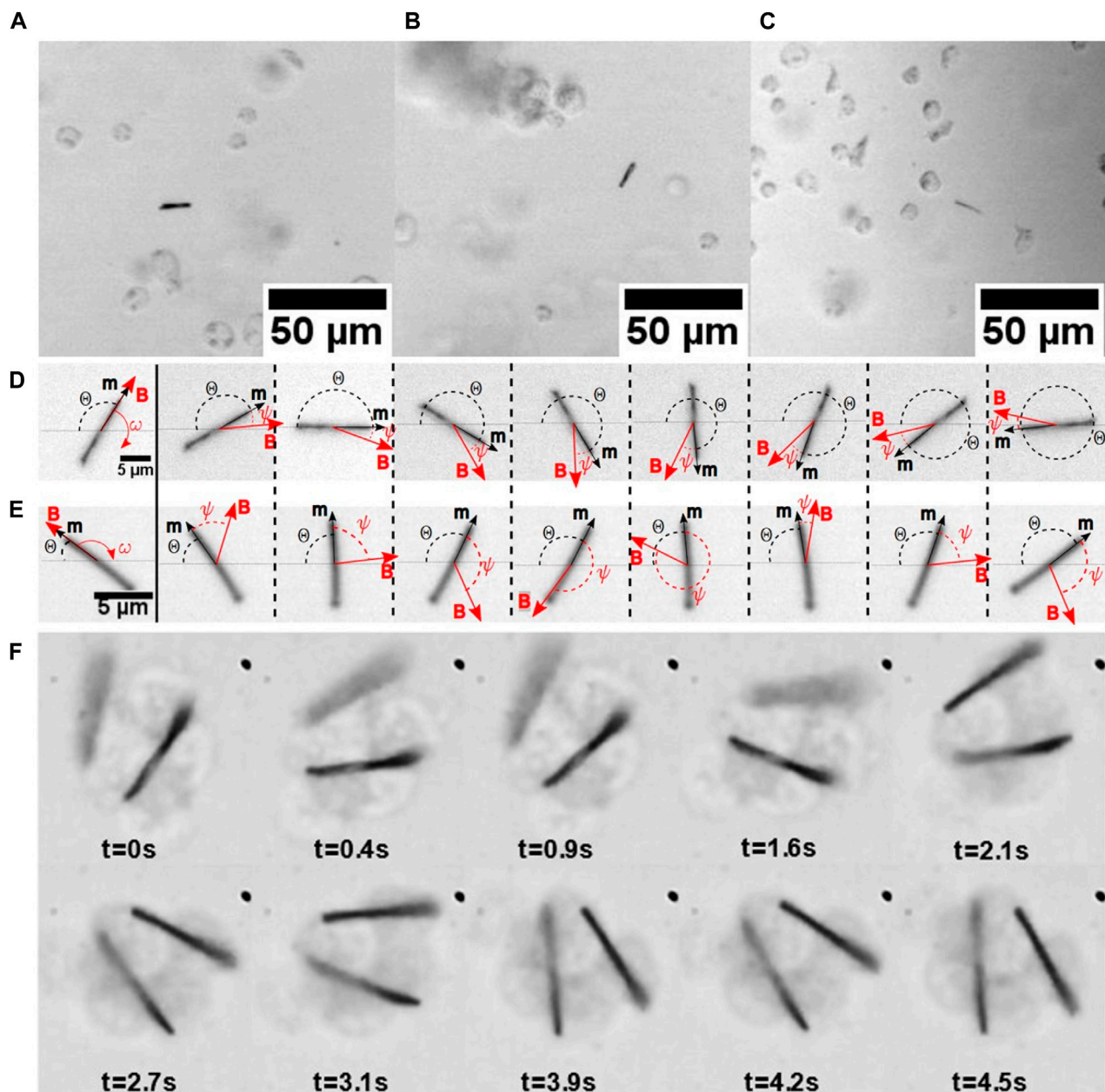


FIGURE 5

(A) Nickel nanorods in a hemolymph drop from the larvae of *M. sexta*. The different nanorods were imaged using a $\times 10$ Olympus BX51 objective. The nanorods were observed through the hemolymph–air interface, and the images were taken at (A) $t = 5$ minutes, (B) 11 minutes, and (C) 16 minutes after drop placement on the glass slide. (D) Synchronous rotation of a nanorod with the applied rotating field. The angle ψ that the magnetic moment \mathbf{m} forms with the field \mathbf{B} is constant. (E) Asynchronous rotation of a nanorod with the applied rotating field. When the nanorod follows the applied magnetic field, it oscillates so that the angle ψ periodically changes with time. (F) Hemocytes attach themselves to the nanorods. Applying a rotating magnetic field, the aggregate can rotate in an asynchronous regime.

This analysis of the shear viscosity suggests that the hemolymph dripping from the wound does not behave as a thick honey-like fluid. Furthermore, the hemocytes had no time to aggregate. Therefore, the appearance of cylindrical filaments when the hemolymph drips from the wound cannot be explained by the significant increase in its shear viscosity.

Thus, we hypothesized that as the first step in primary clot formation, the hemolymph has to be turned into a viscoelastic fluid.

2.3 Extensional rheology of hemolymph

To evaluate the rheological properties of hemolymph filaments, we used the setup shown in Figure 1B. The wound can be probed for only a few minutes after an incision. That is, the time for experimental preparation was long, and when we applied the probe, no dripping occurred. Thus, the wound was partially sealed by the primary clot. Upon placing the probe on the

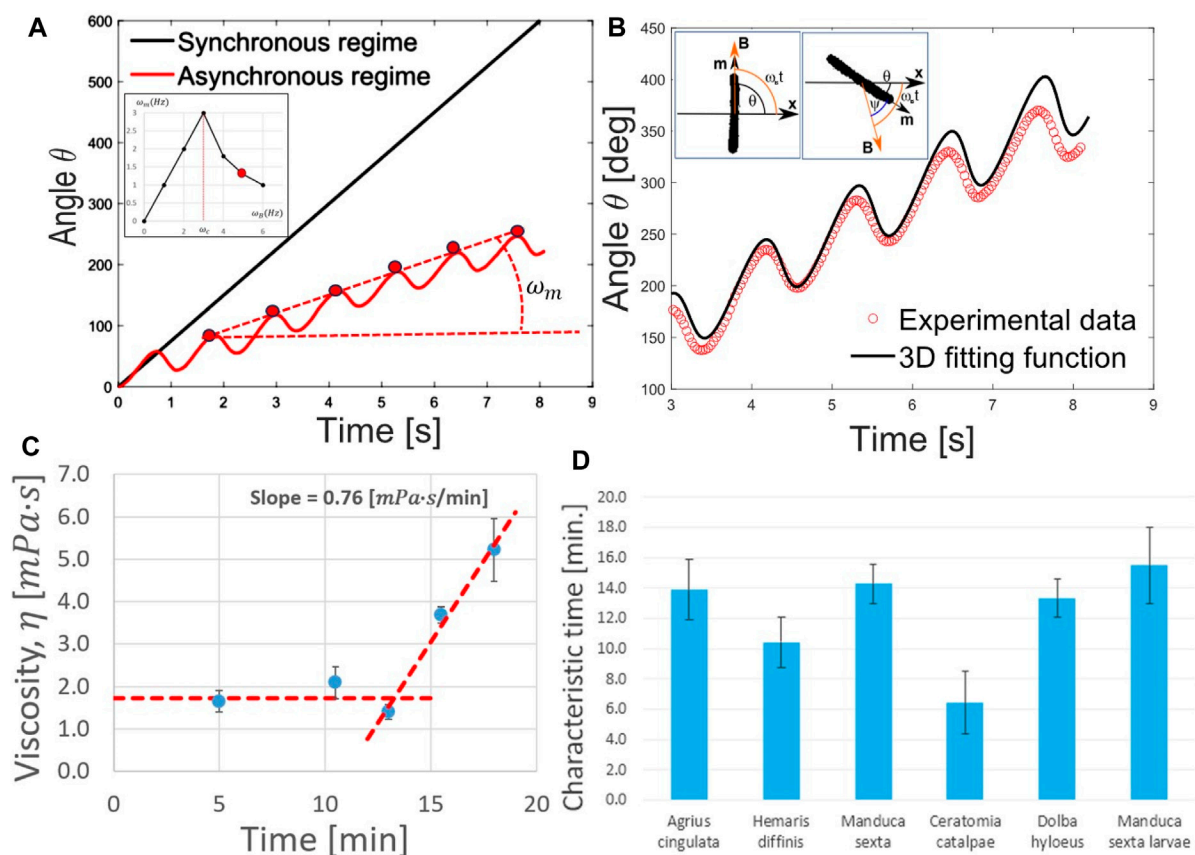


FIGURE 6

(A) Angular dependence of $\theta(t)$ on time for the synchronous (black) and asynchronous (red) rotation of the nanorod. The slope of the dashed line provides the average rate of nanorod revolution ω_m in the asynchronous regime of rotation. The inset illustrates the characteristic master curve used in magnetic rotational spectroscopy. The rate ω_m of rotation of the nanorod is measured as a function of the frequency of the rotating field ω_B . When the driving frequency is small, $\omega_B < \omega_c$, the nanorod rotates synchronously with the field, $\omega_m = \omega_B$. When the driving frequency reaches a critical frequency $\omega_B = \omega_c$ and increases further, the nanorod rotation changes to asynchronous mode. The descending curve illustrates the effect of enhanced energy dissipation during the asynchronous rotation of the nanorod. The peak value ω_c is easy to detect in experiments. The red dot in the inset corresponds to this slope of the dashed line. (B) In experiments, the magnetic moment \mathbf{m} of a nanorod is always directed along the nanorod axis. Aligning the moment (and hence, the nanorod) parallel to the field \mathbf{B} , the reference axis x is set perpendicular to the nanorod axis. Then, rotating the field with frequency ω_B , one tracks the angle θ that the nanorod axis forms with the x -axis. During nanorod rotation, the angle ψ that the magnetic moment \mathbf{m} forms with the applied field \mathbf{B} is not visible. The observed angle θ is then analyzed with the model to evaluate the fluid viscosity. In this example, the experimental data on nanorod rotation in hemolymph were satisfactorily explained by modeling hemolymph as a Newtonian fluid with constant viscosity. (C) Viscosity remained constant over minutes. In this example, showing the dependence of the hemolymph viscosity of *M. sexta* larvae, viscosity stayed constant for more than 10 min and then steeply increased. (D) Measurements of the time when the viscosity of different lepidopterans (hawkmoths) increased twice the initial value indicated that the shear viscosity remained constant for at least 5 min.

wound and lifting the probe (Figure 1B), we formed the first filament connecting the ball with the wound (Figure 7A). This filament was quite stable; despite the caterpillar's movements, the meniscus that formed at the filament foot slid across the drop surface and did not break (Figures 7B, C). When the wounded proleg was moved up or down, the filament stretched or contracted, respectively (Figures 7E, H). The first filament took 1–20 s to become thin and break up (Figures 7I, J). We call these liquid bridges “long-lived filaments” (LLFs), indicating that their lifetime exceeded 1 s. These long-lived filaments sometimes developed single or multiple droplets, which remained on the filament until its breakup or moved to the ends. The droplet that moved to the wound was re-absorbed by the wound, and the droplet that moved to the ball was re-absorbed by the film on the ball.

When the probe was applied for the second time, the filament was less stable and broke in less than 1 s (Figure 8). We called these

filaments “short-lived filaments” (SLFs). They behaved like those dripping from the wound (Figure 3).

After the second trial, when the probe touched the wound and was then raised, the liquid bridges broke in less than 10 ms, following the breakup stages shown in Figure 2. These observations suggested that the hemolymph behaved as a simple low-viscosity Newtonian liquid, like water, that does not form cylindrical filaments (Eggers, 1997; Montanero and Ponce-Torres, 2020) (see an example in Supplementary Video S2).

Using short-lived filaments as representatives of those dripping from the wound and assuming that they would reflect the properties of the dripping filaments, we characterized their rheological properties. The rheological properties of the hemolymph were evaluated by tracking the radius of the short-lived filaments with time. By analyzing the kinetics of liquid-bridge thinning, we discovered that the bridge radius followed the exponential law

TABLE 1 Hemolymph viscosity, body length, body width, and sample size for 19 insect species.

Common names	Latin names	Hemolymph viscosity, mPa*s	Body length, cm	Body width, cm	Forewing length, cm	Number of individuals	Number of nanorods	Number of measurements
Lepidoptera species (adults)	Lepidoptera species (adults)							
Painted lady butterfly	<i>Vanessa cardui</i>	1.34 ± 0.24	2.11 ± 0.08	0.50 ± 0.10	3.01 ± 0.10	14	43	190
Monarch butterfly	<i>Danaus plexippus</i>	1.44 ± 0.39	3.18 ± 0.13	0.57 ± 0.11	5.16 ± 0.10	9	16	106
Pawpaw sphinx moth	<i>Dolba hyloeus</i>	1.48 ± 0.11	3.40 ± 0.14	0.96 ± 0.08	2.83 ± 0.29	5	15	85
Plebeian sphinx moth	<i>Paratrea plebeja</i>	1.51 ± 0.17	3.43 ± 0.35	0.99 ± 0.10	3.13 ± 0.24	5	11	63
Rustic sphinx moth	<i>Manduca rustica</i>	1.47 ± 0.16	5.47 ± 0.27	1.55 ± 0.15	5.99 ± 0.10	5	16	95
Five-spotted hawkmoth	<i>Manduca quinquemaculata</i>	1.70 ± 0.24	5.31 ± 0.44	1.23 ± 0.13	5.40 ± 0.30	7	26	168
Carolina sphinx moth	<i>Manduca sexta</i>	2.17 ± 0.50	4.55 ± 0.49	1.10 ± 0.06	5.28 ± 0.52	19	49	315
Catalpa sphinx moth	<i>Ceratomia catalpae</i>	2.07 ± 0.33	3.40 ± 0.40	0.91 ± 0.10	4.38 ± 0.48	6	13	72
Pink-spotted hawkmoth	<i>Agrius cingulata</i>	1.85 ± 0.29	5.37 ± 0.50	1.28 ± 0.07	4.80 ± 0.40	5	21	110
Tersa sphinx moth	<i>Xylophanes tersa</i>	1.77 ± 0.29	4.01 ± 0.21	0.85 ± 0.06	3.40 ± 0.20	4	18	99
Pandora sphinx moth	<i>Eumorpha pandorus</i>	1.61 ± 0.14	4.86 ± 0.28	1.10 ± 0.09	4.60 ± 0.50	5	19	123
White-lined sphinx moth	<i>Hyles lineata</i>	1.55 ± 0.28	3.87 ± 0.66	1.02 ± 0.17	3.10 ± 0.20	6	31	174
Snowberry clearwing moth	<i>Hemaris diffinis</i>	1.81 ± 0.12	2.72 ± 0.30	1.04 ± 0.18	2.95 ± 0.06	5	19	104
Mournful sphinx moth	<i>Enyo lugubris</i>	1.83 ± 0.22	3.45 ± 0.19	0.96 ± 0.11	3.67 ± 0.10	5	18	103
Nessus sphinx moth	<i>Amphion floridensis</i>	1.87 ± 0.22	2.4 ± 0.1	0.5 ± 0.1	2.3 ± 0.1	2	6	26
Laurel sphinx moth	<i>Sphinx kalmiae</i>	1.43 ± 0.29	4.0 ± 0.1	0.8 ± 0.1	0.9 ± 0.1	2	4	21
Banded sphinx moth	<i>Eumorpha fasciatus</i>	1.36 ± 0.14	3.85 ± .50	0.82 ± 0.1	4.3 ± 0.1	3	8	41
Lepidoptera species (larvae)	Lepidoptera species (larvae)							
Tobacco hornworm	<i>Manduca sexta</i>	1.66 ± 0.37	7.8 ± 0.3	1.3 ± 0.1	—	6	11	63
Blattodea species	Blattodea species							
American cockroach	<i>Periplaneta americana</i>	1.83 ± 0.41	3.5 ± 0.7	1 ± 0.2	2.7 ± 0.3	9	27	135

with relaxation time θ . These kinetics are typically expected for a viscoelastic fluid following the Oldroyd-B constitutive equation (Bazilevsky et al., 1990; Bazilevskii et al., 2001; McKinley and Sridhar, 2002; Rodd et al., 2005; Kojic et al., 2006; Bazilevsky et al., 2011). The Oldroyd-B fluid is characterized by two constants: its shear viscosity η and relaxation time θ . The

$$R = R_0 \exp\left(\frac{-t}{3\theta}\right), \tag{1}$$

measured relaxation time of this viscoelastic hemolymph ranges between 2 and 4 ms (Figure 9). Figure 3 shows that this estimate of the relaxation time is reasonable. Specifically, three filaments were filmed after the drop fell to the substrate, and the filaments thinned in the same manner as that shown in Figure 8 due to capillary action. The analysis of those filaments yielded an average relaxation time of $\theta \sim 5$ ms. Thus, filament stabilization in the dripping hemolymph can be explained by its viscoelasticity (Larson, 1999; Bazilevskii et al., 2005).

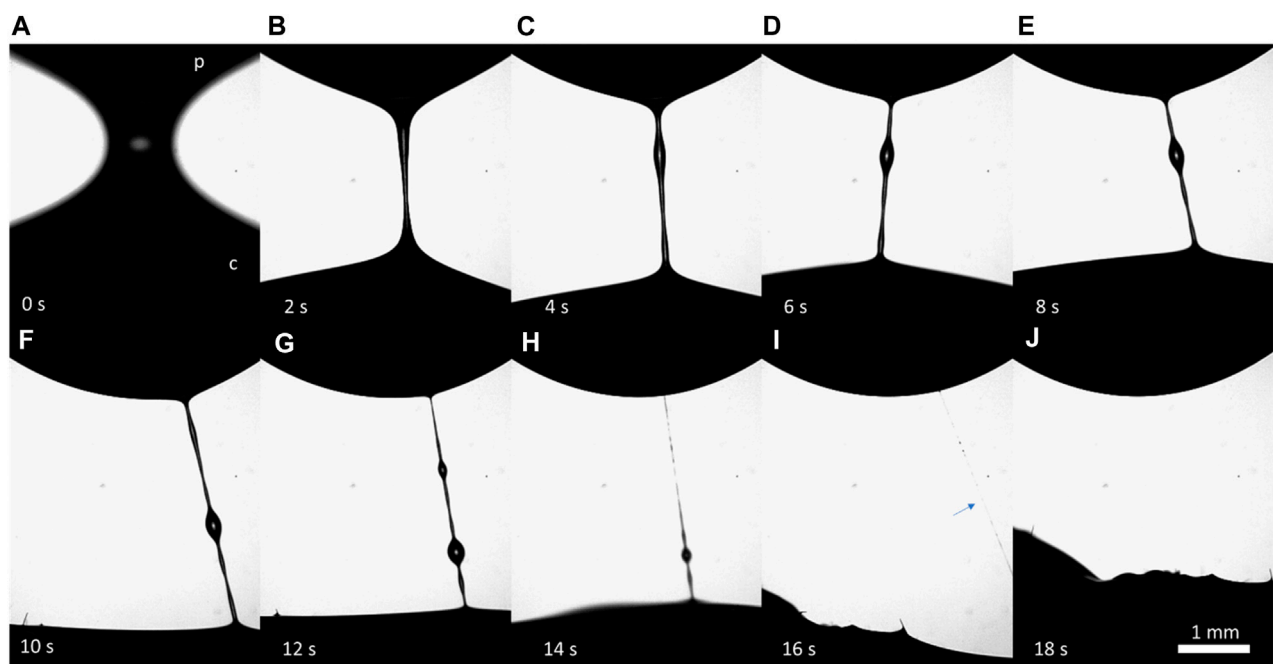


FIGURE 7
(A–J) Series of frames illustrating the features of the formation and breakup of a long-lived filament (LLF). The filament formed between a stainless-steel probe (p) at the top and a wound of the *M. sexta* caterpillar (c) at the bottom. The camera was focused on the filament, and the wound was not visible. The caterpillar constantly moved, causing the filament to move.

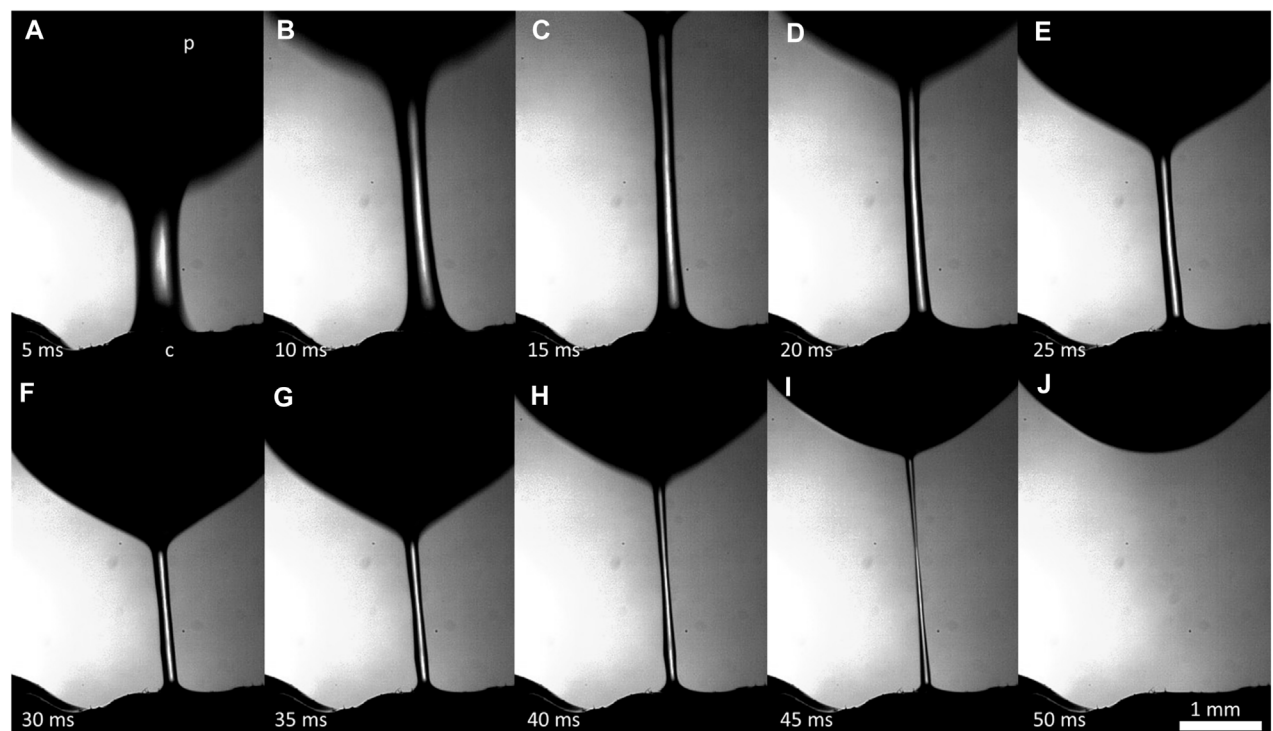


FIGURE 8
(A–J) Series of frames illustrating the features of the formation and breakup of a short-lived filament (SLF); (p) is a stainless-steel probe, and (c) is the wound of the *M. sexta* caterpillar. It takes approximately 45 ms for the SLF to break up and disappear.

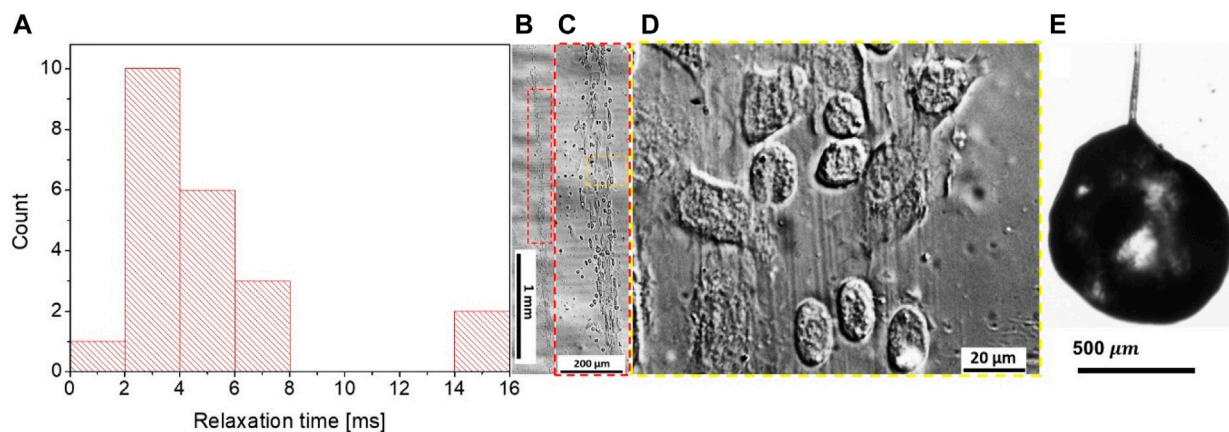


FIGURE 9

(A) Relaxation time θ measured for four *M. sexta* caterpillars with 22 liquid bridges. The short-lived filaments appeared to be viscoelastic, and the majority had a relaxation time θ of between 2 and 4 ms. (B–D) Phase-contrast optical microscopy of the filamentous core in long-lived filaments. The boxed region in (B) is magnified in (C), and the box in (C) is magnified in (D). The core of the long-lived filament consisted of a network of micron- and submicron-diameter filaments with embedded hemocytes. (E) The hanging drop remained on a long-lived filament after forming this filament from the pool of hemolymph, as shown in Figure 1C. The lower filament connecting the drop with the hemolymph pool was naturally broken following the scenario shown in Figure 8, but the weight of the remaining liquid drop was balanced by the stress on the supporting filament. Water naturally evaporated from the filament, while the surface of the drop formed a crust that contained the interior as the liquid hemolymph.

To evaluate the cause of the distinct kinetics of the SLF and LLF thinning, we turned to the structural analysis of their composition. When we probed the wound with the ball in the first 3 min, long-lived filaments were formed 13 times, short-lived filaments were formed 18 times, and 22 trials produced no filaments. For wounds older than 8 min, we observed a long-lived filament only once, while short-lived filaments were observed 11 times, and 52 trials produced no filaments. The long-lived filaments did not necessarily follow the Oldroyd-B model or have a broad dispersion of the relaxation times ranging from milliseconds to seconds. This scattering of the material parameters led us to hypothesize that because of the caterpillar's movements, the ball might have probed the hemolymph from different depths of ball immersion. We suspected that the ball forming the long-lived filaments might have probed the primary clot together with the layer of hemocytes covering the wound surface. Sometimes, the flowing hemocytes can be observed inside the LLF (Supplementary Video S4).

By collecting long-lived filaments on a glass slide and studying them using phase-contrast microscopy, we discovered filamentous cores made up of polymeric filaments with embedded hemocytes (Figures 9B–D). These filaments were long and bundled, even without hemocytes. When a long-lived filament was broken at one end, some droplets sometimes remained on a dried filament and formed a crusted surface, while the interior of the drop remained full of liquid hemolymph (Figure 9E).

These observations confirm that LLFs contain primary clots, and hence, their thinning kinetics is controlled by the deformation and flow of the highly inhomogeneous composite structure of primary clots. The more mature the primary clot is, the slimmer it is, and the slower the filament breaks up.

2.4 Clotting starts with the interfaces

To further investigate the phenomenon of crust formation, we examined the behavior of hemolymph drops using X-ray micro-CT and SEM imaging. X-ray imaging is attractive because it distinguishes between the structure of the multiphase and multicomponent materials (Andrews et al., 2011; Maire and Withers, 2014). Before submitting the hemolymph drop for X-ray imaging, we rapidly froze the drop on a metal substrate and slowly sublimated the water (as explained in Materials and methods). Then, a freeze-dried drop was imaged using an X-ray microscope (Bruker SkyScan 1176). The images were reconstructed (Figures 10A, B), and we schematically show how the cross-sections parallel and perpendicular to the substrate were taken (Figure 10C). These images show the density distribution of primary aggregates or clots through the drop thickness. The material closer to the air/hemolymph and hemolymph/substrate interfaces had a greater density.

To evaluate the microstructure of this interfacial layer, the frozen drop was broken and removed from the substrate. The remaining material that adhered to the substrate was examined by scanning electron microscopy. Figures 10D–F show residues on the substrate from the droplet sitting on it for longer than 20 min before freezing. Chain-like aggregates are observed attached to the substrate. These aggregates are much larger than the individual hemocytes, suggesting that the hemocytes were already assembled into chain-like primary clots. The possible building blocks of these chain-like aggregates are shown in Figure 10E, where solitary aggregates of approximately $30\mu\text{m}$ in diameter were found. Filamentary residues covered the boundaries of larger primary clots (Figure 10F). These filaments were like those described by Geng and Dunn (1988) and Geng (1990). No visible filaments were found in the droplets incubated for less than 20 min.

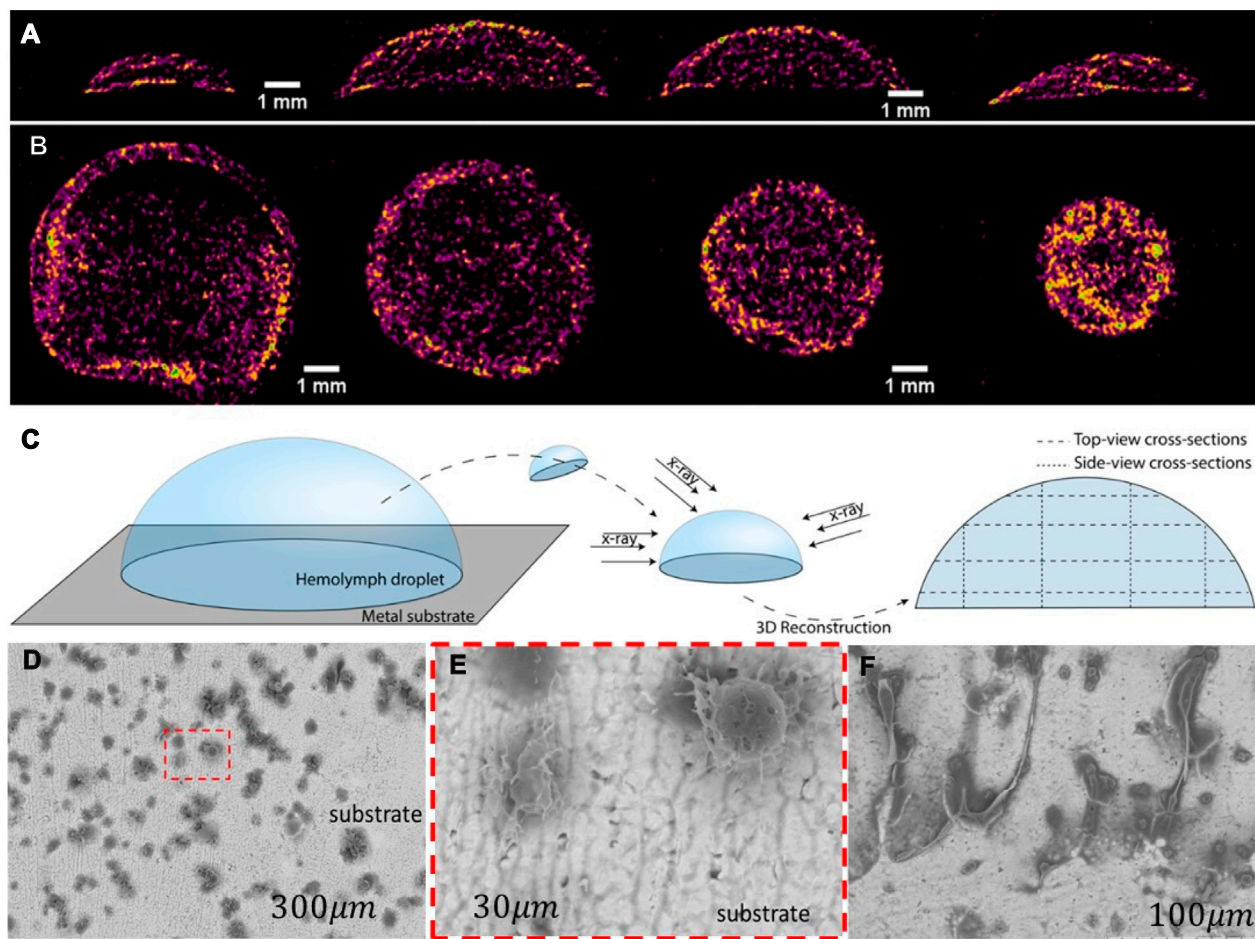


FIGURE 10

Micro-CT scans of a freeze-dried hemolymph drop. Yellow represents a high-density material, and purple represents a low-density material. (A) Series of drop cross-sections was taken perpendicular to the substrate, as specified in (C). The cross-sectional area increased from the drop edge to the center. (B) Series of drop cross-sections was taken parallel to the substrate, as specified in (C). The cross-sectional area decreased from the substrate to the droplet top. The interfacial layer of the hemolymph appears to have a high-density material. (C) Diagram depicting the sample preparation procedure and the locations of the four parallel and perpendicular sections. (D) SEM micrographs of hemolymph residues attached to the substrate. Small dark spots form either chain-like or solitary aggregates. (E) Solitary aggregates appeared in the framed area in (D). (F) Filamentary residues sticking out from the aggregate are also common for larger aggregates.

All these findings favor the hypothesis that in larval *Lepidoptera*, the primary clots first nucleate at the interfaces and form a crust-like shell preventing water evaporation. The shell propagates inward to occupy the entire drop.

2.5 Interfacial interactions between hemocytes in the hemocyte-rich hemolymph

Hemocytes interact with one another closer to the surface. It has long been hypothesized that some hemocytes extrude thread-like projections (i.e., pseudopodia) in response to foreign surfaces; then, other hemocytes adhere to the formed network (Salt, 1970; Gregoire and Rockstein, 1974). This hypothesis implicitly assumes that the hemocyte density is high enough to allow the connection of two neighboring hemocytes by pseudopodia (Wigglesworth, 1937; Salt, 1970).

We investigated this hypothesis by observing the hemocyte behavior in the droplets released from the wound. Within approximately 3 min from the moment of drop formation, the hemocytes from the larvae of *M. sexta* began adhering to each other. When a magnetic nanorod was introduced to the drop, the pseudopodia anchored the nanorods to the hemocyte aggregates (Figure 5F); the nanorods never broke the hemocytes. In contrast to the free nanorods, the nanorods attached to hemocyte aggregates did not make full revolutions (Aprelev et al., 2019). Instead, they beat in response to the applied rotating field around an equilibrium direction, revealing hidden interconnections between hemocytes (Supplementary Video S3). During these oscillations, the surrounding cells moved in unison with the nanorod. Thus, the hemocytes with the attached nanorods mechanically communicated with the neighboring hemocytes that were not visibly connected to one another. A hidden biopolymer network provides a far-field reaction to a local perturbation, engaging hemocytes in the movement. This local perturbation of an oscillating nanorod

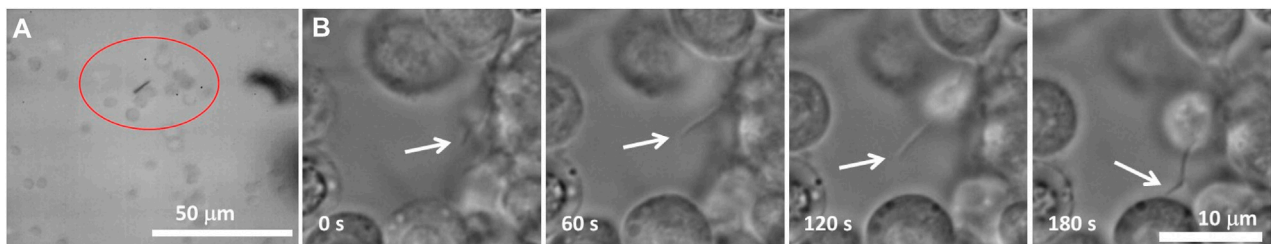


FIGURE 11

(A) Image of a nanorod surrounded by a network of cells. The encircled hemocytes are engaged in the movement of the nanorod. As the nanorod attempts to rotate, the hemocytes inside a circled aggregate move together. The hemocytes outside the circle do not respond to the motion of the nanoprobe, indicating that the hemocytes form an aggregate shielding a foreign object from the surrounding hemocytes. (B) Phase-contrast image of a growing pseudopodium (arrows). After ~180 s, the two hemocytes become connected through a pseudopodial bridge [adapted from Aprelev et al., 2019].

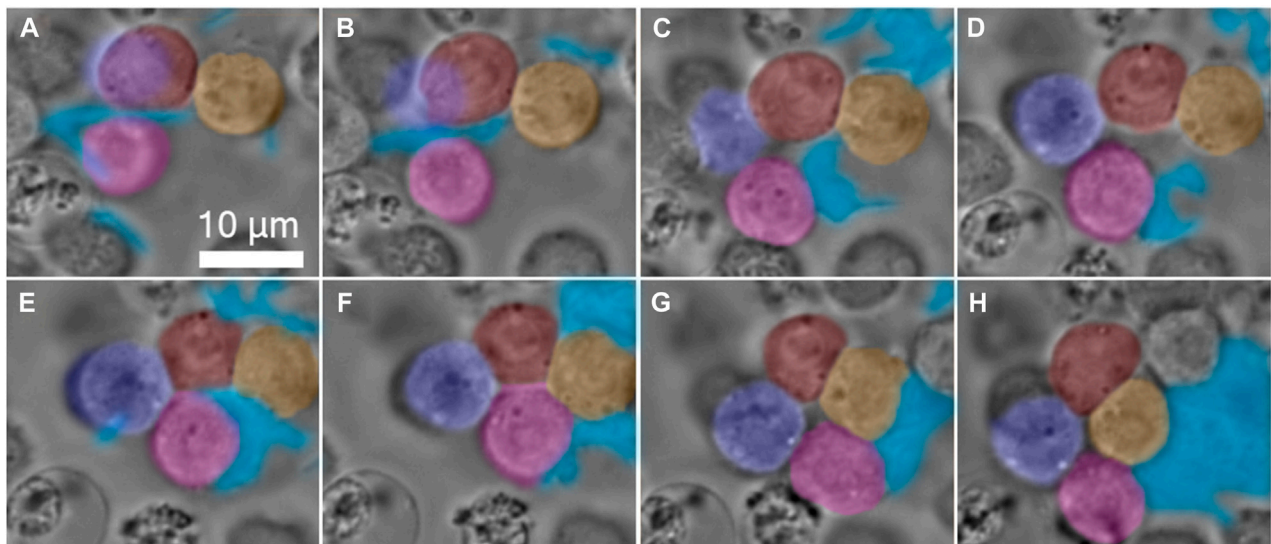


FIGURE 12

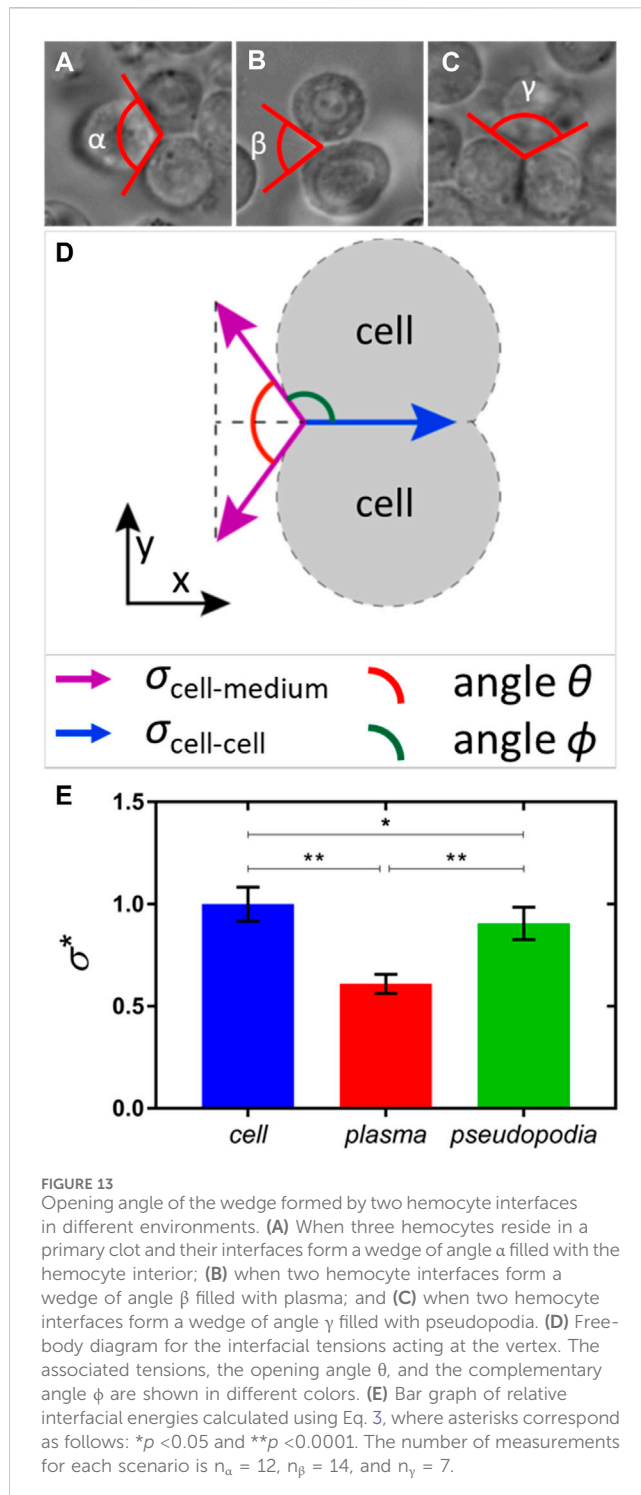
Gallery of time-lapse frames, depicting a four-hemocyte aggregate in a primary clot of the hemolymph of a larva of *M. sexta*. The pseudopodia are formed by hemocytes first deforming the interface in finger-like extensions. Each extension could deform and propagate over long distances searching for a target. The hemocytes are artificially colored in red, yellow, purple, and pink, and the aggregate-involved pseudopodia are in blue. (A) Initially, the red and yellow hemocytes touch weakly, and the pink hemocyte is free near the extending pseudopodia. (B,C) With time, the interface between the red and yellow hemocytes increases, while the pseudopodium attaches to the pink hemocyte and drags it to the right. (D) The purple hemocyte, which is attached to both red and pink hemocytes, comes into focus, while the pseudopodium continues to drag the pink hemocyte to the right. (E) The red/purple and the pink/purple interfaces grow, and the pink hemocyte, which is half-engulfed in pseudopodia, first touches the red hemocyte. (F) The pink hemocyte disconnects from the pseudopodia and attaches to the red and yellow hemocytes. (G) The red and pink hemocytes disconnect, and the four-hemocyte aggregate forms a hole in the center. (H) The purple and yellow hemocytes form an interface, and the four hemocytes remain in this configuration until the end of the observation [images were extracted from the video in the study by Aprelev et al., 2019].

propagates through an area with a radius of ~5–8 nanorod lengths from the probing nanorod (Figure 11). The analysis of nanorod oscillations in these aggregates suggested that the aggregates with a hidden network that connects them behaved as a viscoelastic material with temporary cross-links (Aprelev et al., 2019), as described by the Green–Tobolsky theory of gels (Green and Tobolsky, 1946).

The high density of hemocytes can only be expected in the neighborhood of the wounded tissue; otherwise, the hemocyte density in a healthy caterpillar is insufficient for hemocyte bridging. We illustrated this statement by showing that after ~3 min of being close to one another in a large population of

hemocytes, only two of them were bridged by a pseudopodium; the other hemocytes remained mobile (Figure 11B).

An illustrative scenario of hemocytes gathering in a primary clot during the first 10 min of hemolymph coagulation is presented in Figure 12 (Aprelev et al., 2019). A pseudopodium extends from the originating mother hemocyte, stretches further, and bends on its way, targeting another hemocyte, to which it later adheres. The pseudopodium functions as a hydraulic spring; on its way to finding the target, it stretches the constituent material. After contact, the pseudopodium tends to spread along the hemocyte surface. The tension generated in the hemocyte during stretching tends to relax, squeezing the



constituent material back to the mother hemocyte and dragging the targeted hemocyte with it. As the pseudopodium contracts toward the mother hemocyte, it may encounter another hemocyte, attach to it, and bring it to the mother hemocyte. The process repeats, and the aggregates grow larger and change their shape, leading to the formation of a primary clot (Salt, 1970; Gregoire and Rockstein, 1974; Aprelev et al., 2019).

The mechanism of hemocyte adhesion by pseudopodia can be understood from the analysis of the strength of adhesive bonds

between hemocytes in the aggregate. The interfacial tensions and the associated interfacial energies of films separating the adjacent hemocytes offer quantitative metrics for the analysis of aggregation phenomena (Figure 13). These interfacial tensions control the opening angle θ , introduced as the angle of the wedge that the two hemocyte interfaces form at contact (Figure 13D). We distinguish the wedges filled with different media of interest. At least three types of wedges could be formed by the two hemocyte interfaces in the primary aggregate when hemocytes contacted each other (Figures 13A–C). When the wedge is filled with the hemocyte interior, and two interfaces in the wedge separate three different hemocytes, the wedge angle is given as $\theta = \alpha$. When the wedge is filled with plasma, and two interfaces separate hemocytes from the plasma, the wedge angle is given as $\theta = \beta$. When the wedge is filled with pseudopodia, and two interfaces separate hemocytes from the pseudopodia, the wedge angle is given as $\theta = \gamma$.

We introduce the interfacial tension $\vec{\sigma}_{cell-cell}$ between two identical hemocytes that share a common interface and their interfacial tension $\vec{\sigma}_{cell-medium}$ separating a hemocyte from the surrounding medium (Figure 13D). These vectors are parallel to interfaces and perpendicular to the contact line that runs perpendicular to the figure. In the introduced Cartesian system of coordinates, the x -axis is parallel to vector $\vec{\sigma}_{cell-cell}$. Setting up a free-body diagram at the vertex, where three interfaces meet (Figure 13D), we have

$$\vec{\sigma}_{cell-medium} + \vec{\sigma}_{cell-medium} + \vec{\sigma}_{cell-cell} = 0. \quad (2)$$

Balancing the x -components of forces, we obtain

$$\sigma_{cell-medium} \cos\left(\frac{\theta}{2}\right) + \sigma_{cell-medium} \cos\left(\frac{\theta}{2}\right) = \sigma_{cell-cell}. \quad (3)$$

The measured angle $\alpha = 120^\circ \pm 5^\circ$ is close to $\alpha = 120^\circ$, as predicted by Plateau's law (Plateau, 1873) for the bubble and droplet aggregates with the same interfacial tension $\sigma_{cell-cell}$. Therefore, we conclude that these aggregates are formed by the same hemocytes with the same interfacial energy $\sigma_{cell-cell}$. This interfacial energy $\sigma_{cell-cell}$ is assigned for the interfacial energy of hemocytes in the preliminary clot. The relative change in the interfacial energy referenced to $\sigma_{cell-cell}$ is introduced as follows:

$$\sigma_{medium}^* = \sigma_{cell-medium} / \sigma_{cell-cell} = \left[2 \cos\left(\frac{\theta}{2}\right) \right]^{-1}. \quad (4)$$

Using the measured angles $\alpha = 120^\circ \pm 5^\circ$, $\beta = 70^\circ \pm 11^\circ$, and $\gamma = 113^\circ \pm 6^\circ$, the relative interfacial energies of hemocytes in a primary clot (σ_{cell}^*), the two-hemocyte aggregate in the plasma (σ_{plasma}^*), and the two-hemocyte aggregate in pseudopodia ($\sigma_{pseudopodia}^*$) were calculated as $\sigma_{cell}^* = 1.00 \pm 0.08$, $\sigma_{plasma}^* = 0.61 \pm 0.05$, and $\sigma_{pseudopodia}^* = 0.91 \pm 0.08$, respectively (Figure 13E). These estimates confirm that pseudopodia form a landing bed for incoming hemocytes, and only ~10% of extra bonds are required to lock the hemocyte in the aggregate.

This analysis emphasizes the importance of interfacial forces in gathering and holding hemocytes together during the development of primary clots.

3 Discussion and conclusion

In recent years, the fruitful analogy between the cell aggregates of developing tissues and liquids with a viscoelastic rheology has offered new perspectives in biological soft matter (Steinberg, 2007; Janmey et al., 2009; Gonzalez-Rodriguez et al., 2012; Foty and Steinberg, 2013; Beaune et al., 2014; Beris et al., 2021; Patteson et al., 2022). Although the mainstream research in this direction is focused on vertebrate and human blood, little is known about the material properties of insect blood. We, therefore, investigated the hemolymph clotting phenomena using materials science approaches. The main question that we asked was, “What are the material determinants of fast wound sealing in insects?” By evaluating the rheological properties of the hemolymph over short periods of time, we investigated the mechanisms leading to the arrest of bleeding and to the nucleation and formation of primary clots in insects with hemocyte-rich hemolymph.

Our experiments were triggered by observations of the hemolymph extracted directly from a wound. When a metal pin is dipped in a hemolymph drop with primary clots and then immediately pulled back, one observes a liquid filament bridging the droplet surface using the pin. The hemolymph filament does not break as quickly as a water bridge formed with the same pin drawn from a water droplet. This feature of hemolymph stringing (Gregoire, 1955; Chino et al., 1987; Scherfer et al., 2004; Aprelev et al., 2019) is the first indication of clotting. It can be used for screening different clot inhibitors or promoters, as demonstrated in the hemolymph of fruit fly larvae (*D. melanogaster*) (Bidla et al., 2005; Lesch and Theopold, 2008). Bidla et al. (2005) and Lesch and Theopold (2008) studied the effect of the protein phenoloxidase (PO) on clot tenacity by measuring the maximum pull-out length of the filament in the hemolymph droplets with and without PO. This protein is thought to facilitate the cross-linking and hardening of the primary clot. One would expect that the greater the PO concentration, the harder the clot, and the shorter the pull-out length of the filament before it breaks. This prediction is correct (Bidla et al., 2005; Lesch and Theopold, 2008). Although these observations are useful, no quantitative data on the material properties of the hemolymph have been provided. The most challenging biological question regarding the mechanism of fast wound sealing remain enigmatic.

We found that the larvae of *M. sexta*, which have hemocyte-rich hemolymph, stopped bleeding after 60–90 s. At this time scale, the hemolymph viscosity is low (Table 1), and high-speed videography is needed to film the filament breakup (Figures 2, 3, 8). The appearance of a long cylindrical filament in the dripping hemolymph points to its possible viscoelasticity (Macosko, 1994; Larson, 1999). Many low-shear viscosity biofluids demonstrate viscoelasticity (Bazilevsky et al., 2011; Haward et al., 2011). The hemolymph could behave like saliva dripping from a dog’s mouth, with water-level low-shear viscosity, which would still be capable of producing long filaments. Making an aqueous fluid elastic allows an animal to stabilize the flow of blood through the circulatory system or prevent the breakup of liquid bodies, as in the case of dripping hemolymph.

The kinetics of the breakup of a cylindrical filament allows one to evaluate the rheological properties of fluids and distinguish between the specifics of the viscoelastic non-Newtonian behavior

of the material (Bazilevsky et al., 1990; Entov and Hinch, 1997; McKinley and Sridhar, 2002). We, therefore, analyzed the kinetics of the filament breakup and observed that before the arrest of bleeding, the hemolymph became viscoelastic with relaxation time 2 ms (Figure 9A).

Knowing the relaxation time and shear viscosity (Table 1), $\eta = 1.66 \text{ mPa} \cdot \text{s}$, the elastic modulus $G \sim \eta/\theta$ of the elastic additives in the filament can be estimated as $G \sim 2 \text{ Pa}$. At least two possible elastic contributors are present in the hemolymph: biopolymers and hemocytes. Collecting the short-lived filaments of interest during bleeding and analyzing them under the microscope, we found no hemocytes. Therefore, the hemolymph elasticity might only come from biopolymers in the hemolymph. Assuming that biopolymers form a weak network, and using the rubber elasticity theory $G \sim \nu k_B T$ (Doi and Edwards, 1988; Larson, 1999), where k_B is the Boltzmann constant and T is the absolute temperature, we can estimate the density ν of cross-links. At room temperature, $k_B T \approx 10^{-21} \text{ J}$, the 2-Pa network should contain $\nu \sim 10^{21} \text{ m}^{-3} = 1000 \mu\text{m}^{-3}$, that is, a single cross-link is expected per cube with 100-nm sides. Thus, the distance between cross-links is greater than the typical radius of gyration of proteins, suggesting that to self-assemble into bundles, proteins should unfold from their globular state (Erickson, 2009).

Typically, hemolymph plasma contains 0.01–0.1 % w/w of different proteins, some with large molecular weights of up to 500 kDa (He et al., 2016). Geng and Dunn (Geng and Dunn, 1988; Geng, 1990) hypothesized that an insect’s immune response causes some fibrous proteins to self-assemble into a network. Among a variety of insect proteins, lipoproteins are known for their ability to self-assemble into chain-like aggregates of more complex biopolymer subunits (Brehelin, 1979; Boman and Hultmark, 1987; Chino et al., 1987; Coodin and Caveney, 1992; Mulnix et al., 1995; Arakawa et al., 1996; Theopold et al., 2004; Rahman et al., 2006; Dushay, 2009; Jiang et al., 2010; Maravilla et al., 2020). Many other fibrous proteins can do the same (Ling et al., 2018; Miserez et al., 2023). Even a minute concentration of chains makes the fluid elastic. For example, even dilute polymer solutions, where polymeric coils are far apart, can stabilize liquid bridges and jets and turn them into constant-radius cylinders (Bazilevskii et al., 2005; Yan et al., 2011; Hoath et al., 2014; Zhang et al., 2022). Therefore, making the hemolymph viscoelastic is critical to stop the bleeding.

Even after the arrest of bleeding, wound closure must be fast to prevent water and solute loss, maintain hydrostatic pressure, and form a barrier against infection. At this step, the viscoelasticity of the low-viscosity hemolymph does not help much, and the insect develops a new strategy by forming a clot that spreads to form a stiff wound seal. The hemocyte-rich hemolymph contains adhesive and non-adhesive hemocytes (Salt, 1970; Lavine and Strand, 2002; Ribeiro and Brehelin, 2006). One scenario of clot nucleation assumes that adhesive cells aggregate at the wound surface or any other surface (Gregoire, 1953; Lai-Fook, 1966; Wigglesworth and Gupta, 1979; Brodland, 2002; Steinberg, 2007; Gonzalez-Rodriguez et al., 2012; Mattix et al., 2014) and are involved in wound healing, phagocytosis (Gregoire, 1955; Salt, 1970; Arnold and Rockstein, 1974; Rowley and Ratcliffe, 1976; Pech and Strand, 1996; Gillespie et al., 1997; Pech and Strand, 2000; Lavine and Strand, 2002; Ribeiro and Brehelin, 2006), and the regrowth of epidermal cells

(Wigglesworth, 1937; Godt and Tepass, 1998; Hayashi and Carthew, 2004; Carthew, 2005; Bulgakova et al., 2012). In this scenario, primary clots are formed at the wound surface or any other foreign surface. We showed that in the larvae of *M. sexta*, primary clots are formed at the interfaces (Figure 10), which propagate from the damaged surface toward the hemolymph interior. This scenario has also been observed for other insects (Gregoire, 1955; Salt, 1970; Wigglesworth and Gupta, 1979; Theopold et al., 2004).

Hemocytes spread over and embed in a fibrous network of primary clots, as shown by the analysis of the core of long-lived filaments (Figure 9). The importance of interfacial forces in gathering and holding hemocytes together during the development of primary clots is shown in Figures 11, 12 and by the theoretical analysis in Section 2.5.

The Ni-nanorod experiments and phase-contrast imaging of these primary clots showed that fibrous connectors are essential for holding hemocytes inside the aggregate and to form connections between the aggregates. We showed that approximately 90% of the adhesion energy between hemocytes comes from the surrounding fibrous bed. To permanently lock the hemocytes in the aggregate, only ~10% of it needs to be added to the adhesion energy. These additional bonds are formed later in clot development during the consolidation of the aggregates (Aprelev et al., 2019).

In summary, we observed that insects with hemocyte-rich hemolymph develop a two-step strategy to form clots. In the first step, the Newtonian plasma of the hemolymph turns into a non-Newtonian viscoelastic fluid, remaining at very-low viscosity. This transformation allows the retraction of the dripping hemolymph to the wound. In the second step, primary clots nucleate and form a crust at the air–hemolymph and hemolymph–substrate interfaces. The clots propagate from the interface toward the droplet center.

Given the adaptive value of viscous-to-viscoelastic fluid conversion, we expect this physical phenomenon to be widespread in insects and other organisms with hemocyte-rich hemolymph. In addition to insects, for example, hemocyte-rich fluids are present in some mollusks (e.g., snails), where they promote wound healing (Machalowski and Jesionowski, 2021). As the hemocyte density changes with age and the infection level in some insects (Stoepler et al., 2013), we also expect the physical behavior of the hemolymph to change. Intriguing experimental subjects include insects that partition hemocyte-rich and hemocyte-poor hemolymph in the same body. The larvae of at least some mosquito species, for instance, are hemocyte-rich at specific body sites, such as the openings into the heart, where they rapidly mobilize to fight infection (League and Hillyer, 2016).

The period from the initiation of the immune cascade reaction to the first microscopically visual detection of a rheological response of the hemolymph remains the unquantified bridge between molecular biology and materials science. Since the last century (Gregoire, 1953), biologists have known that vertebrate red blood cells can initiate an immune cascade reaction in the hemolymph of insects. The material manifestation of viscous-to-viscoelastic conversion of insect hemolymph in a few seconds is attractive for biomedical applications. We hope that our findings will trigger the interest of biochemists and molecular biologists to design fast-working thickeners for vertebrate blood, including human blood.

4 Materials and methods

4.1 Larval maintenance

The larvae of *M. sexta* were obtained from Carolina Biological Supply (<https://www.carolina.com>) or were reared in-house on food from Great Lakes Hornworm (<https://www.greatlakeshornworm.com/>), with some feeding *ad libitum* on hornworm food obtained from Carolina Biological Supply. The deposited eggs were obtained from adults that emerged in a net enclosure (ca. 27°C and relative humidity ca. 65%). Rearing containers were wide-mouthed 1-L glass jars with strips (ca. 3 × 15 cm) of plastic gutter guard (Frost King Model VX620) as a climbing substrate and food support. Larvae were maintained at controlled room temperature (approximately 25°C) and 24 h of artificial light. To provide gas exchange, the jar lids were replaced with aluminum window screens. Food (ca. 10 mL) was added in the first three instars as needed. In later instars, larvae were removed from jars and placed in clean jars with more food added as needed. The number of larvae per jar was reduced as they grew, with 10 or fewer per jar in the last instars. Larvae entering pre-pupation (i.e., those with a more yellowish thorax, no longer eating, and in a wandering phase) were not used as a source of hemolymph.

4.2 Hemolymph extraction

The larvae of *M. sexta*, which were 1–2 days before pre-pupation and weighed more than 8.5 g, were used. The caterpillars were washed free of contaminants with DI water and dried using a paper towel. To minimize the movement of larvae, they were placed in specially designed containers (Figure 1) that gripped the larva along the length of the body while exposing the second and third prolegs. Hemolymph was extracted via a 1–2-mm incision made using a razor blade in the third proleg. The hemolymph exiting the wound was collected on a glass slide or probed directly on the body. All experiments were conducted at 20°C–22°C.

4.3 Phase-contrast imaging

To investigate the LLF structure, a liquid bridge was created between a hemolymph drop and the metal ball (Figure 1C). A glass slide was placed next to the ball perpendicular to the drop surface so that the slide touched the ball's side. Pulling the ball parallel to the glass slide above the slide edge stretched the liquid bridge and formed a filament. By moving the ball with the filament toward the glass surface, we deposited the filament on the slide. The deposited filament was covered with a cover slip to prevent evaporation during phase-contrast imaging.

To study cell aggregation, drops of blood were placed under an inverted transmitted-light phase-enhanced microscope (Nikon Eclipse Ti; ×40 Oil Objective, S Fluor, NA = 1.30, DIC H/N2; Photometrics CoolSNAP HQ2 camera, 272-ms exposure, time interval = 1 s), and the cell behavior was recorded. Cellular aggregation during the first 10 min of coagulation was observed under high magnification.

4.4 X-ray micro-CT and SEM imaging

A drop of hemolymph was rapidly frozen on a metal block in liquid nitrogen, freeze-dried under vacuum, detached from the metal block, mounted on a low-density Styrofoam block, and imaged using X-ray micro-CT (Bruker SkyScan 1176). The image was digitally reconstructed, and the cross-sections were studied. The methodology can be summarized as follows: an X-ray source in tandem with a detector was rotated around the sample, and projection images of the sample were taken. The images were digitally reconstructed into a three-dimensional structure. The cross-sections of the three-dimensional structure could then be visualized. The resolution of the instrument was $9\ \mu\text{m}$ per pixel, which was inadequate to observe the internal structure of the freeze-dried clots but was sufficient to determine the internal distribution of the material density.

4.5 Magnetic rotational spectroscopy

Nickel nanorods of diameter $d \sim 200\ \text{nm} - 400\ \text{nm}$ and length $L_0 \sim 7\ \mu\text{m} - 13\ \mu\text{m}$, with a remanent magnetization of $M_r = 224\ \text{kA/m}$ (Aprelev et al., 2017), were dispersed in methanol through sonication. A droplet of the nanorod-methanol suspension was placed on a glass slide and allowed to dry at $23 \pm 1^\circ\text{C}$ and $50 \pm 20\%$ humidity. The hemolymph was placed on the dried nanorod-methanol residue and stirred with a glass rod to disperse the nanorods. The hemolymph droplets were directly exposed to air ($21\text{--}23^\circ\text{C}$). To eliminate any effects of the hemolymph-substrate and hemolymph-air interfaces on viscosity, only nanorods inside the drop ($6\ \mu\text{m}$ below the air-hemolymph interface and $\sim 6\ \mu\text{m}$ above the substrate) were used. The nanorod rotation was filmed, and the videos were processed using LabVIEW and MATLAB algorithms, as explained by Brasovs et al. (2023).

4.6 Analysis of the filament rheology

The SLF and LLF breakup was filmed using an IDT Technologies MotionPro X3 camera at 200–900 fps with a resolution of 512–640 pixels and a Grasshopper Point Gray camera at 100–140 fps with a resolution of 1,920–1,200 pixels. The time dependence of the filament radius was obtained with a specially developed LabVIEW Vision Development Module that allowed us to extract and analyze the profile of the liquid bridge for each frame of the videos (Sun et al., 2022; Sun et al., 2023). The module used the IMAQ Extract Contour algorithm to provide the filament profile. Then, the radius of the cylindrical neck of the filament was fit by Eq. 1, and the goodness of fit was evaluated as discussed by Sun et al. (2022) and Sun et al. (2023). The procedure was repeated for each filament, and the average relaxation time for the series was reported.

The LLF hemolymph puddles from 10 caterpillars were tested using the setup shown in Figure 1C. The method required approximately 1.0–1.5 min to collect the hemolymph from the bleeding caterpillar and to prepare the experimental setup. Liquid

bridges were formed from the same $5\ \text{mm} \times 5\ \text{mm}$ area of the central spot of the puddles.

Data availability statement

The original contributions presented in the study are included in the article/Supplementary Material; further inquiries can be directed to the corresponding author.

Ethics statement

Ethical approval was not required for the study involving animals in accordance with the local legislation and institutional requirements because research on insect blood does not require approval.

Author contributions

PaA: data curation, formal analysis, investigation, methodology, software, validation, visualization, and writing-review and editing. AB: data curation, formal analysis, investigation, software, validation, visualization, and writing-review and editing. TB: visualization and writing-review and editing. CB: investigation, resources, and writing-review and editing. PeA: formal analysis, funding acquisition, investigation, supervision, and writing-review and editing. KK: conceptualization, formal analysis, funding acquisition, investigation, methodology, project administration, resources, writing-original draft, and writing-review and editing.

Funding

The author(s) declare that financial support was received for the research, authorship, and/or publication of this article. This work was partially supported by the NSF grant IOS 2014664, by the Clemson University Creative Inquiry project to KK, and by the SC BioCRAFT facilities supported by the National Institute of General Medical Sciences (NIGMS) of the National Institutes of Health under award number P30GM131959 through the voucher program to KK. The work of PeA was also partially supported by the NIFA/USDA, under project number SC-1700527, with technical contribution no. 7237 of the Clemson University Experiment Station. The work of PaA was partly supported by NASA through the SC Space Grant Consortium Graduate Assistantship, NASA grant: NNX15AL49H.

Acknowledgments

The authors thank Guzeliya Korneva and Bryan Wiggers for helping with the optical imaging and characterization of hemolymph properties and Ahva Zadeh for helping them collect the MRS data on the hemolymph of cockroaches.

Conflict of interest

The authors declare that the research was conducted in the absence of any commercial or financial relationships that could be construed as a potential conflict of interest.

Publisher's note

All claims expressed in this article are solely those of the authors and do not necessarily represent those of their affiliated

organizations, or those of the publisher, the editors, and the reviewers. Any product that may be evaluated in this article, or claim that may be made by its manufacturer, is not guaranteed or endorsed by the publisher.

Supplementary material

The Supplementary Material for this article can be found online at: <https://www.frontiersin.org/articles/10.3389/frsfm.2024.1341129/full#supplementary-material>

References

- Andrews, J. C., Meirer, F., Liu, Y. J., Mester, Z., and Pianetta, P. (2011). Transmission X-ray microscopy for full-field nano imaging of biomaterials. *Microsc. Res. Tech.* 74 (7), 671–681. PubMed PMID: WOS:000292570900011. doi:10.1002/jemt.20907
- Aprelev, P., Bruce, T. F., Beard, C. E., Adler, P. H., and Kornev, K. G. (2019). Nucleation and formation of a primary clot in insect blood. *Sci. Rep.* 9, 3451. doi:10.1038/s41598-019-40129-0
- Aprelev, P., McKinney, B., Walls, C., and Kornev, K. G. (2017). Magnetic stage with environmental control for optical microscopy and high-speed nano- and microrheology. *Phys. Fluids* 29 (7), 072001. PubMed PMID: WOS:000406765200003. doi:10.1063/1.4989548
- Arakawa, T., Kato, Y., Hattori, M., and Yamakawa, M. (1996). Lipophorin: a carrier for lipids in insects participates in superoxide production in the haemolymph plasma. *Insect Biochem. Mol. Biol.* 26 (4), 403–409. PubMed PMID: WOS:A1996UQ42100011. doi:10.1016/0965-1748(95)00110-7
- Arnold, J. W. (1974). "The hemocytes of insects," in *The physiology of insecta* 5 Editor M Rockstein. 2nd ed. (New York: Academic Press), 201–254.
- Bazilevskii, A. V., Entov, V. M., and Rozhkov, A. N. (2001). Breakup of an Oldroyd liquid bridge as a method for testing the rheological properties of polymer solutions. *Polym. Sci. Ser. A* 43 (7), 716–726. PubMed PMID: WOS:000170282300008.
- Bazilevskii, A. V., Meyer, J. D., and Rozhkov, A. N. (2005). Dynamics and breakup of pulse microjets of polymeric liquids. *Fluid Dyn.* 40 (3), 376–392. PubMed PMID: WOS:000207870400005. doi:10.1007/s10697-005-0078-4
- Bazilevsky, A. V., Entov, V. M., and Rozhkov, A. N. (1990). *Liquid filament microrheometer and some of its applications* (Edinburgh, UK: The Golden Jubilee Meeting of the British Society of Rheology and Third European Rheology Conference).
- Bazilevsky, A. V., Entov, V. M., and Rozhkov, A. N. (2011). Breakup of a liquid bridge as a method of rheological testing of biological fluids. *Fluid Dyn.* 46 (4), 613–622. PubMed PMID: WOS:000294174000011. doi:10.1134/s0015462811040119
- Beaune, G., Stirbat, T. V., Khalifat, N., Cochet-Escartin, O., Garcia, S., Gurchenkov, V. V., et al. (2014). How cells flow in the spreading of cellular aggregates. *Proc. Natl. Acad. Sci. U. S. A.* 111 (22), 8055–8060. PubMed PMID: WOS:000336687900051. doi:10.1073/pnas.1323788111
- Beris, A. N., Horner, J. S., Jariwala, S., Armstrong, M. J., and Wagner, N. J. (2021). Recent advances in blood rheology: a review. *Soft Matter* 17 (47), 10591–10613. PubMed PMID: WOS:000719451600001. doi:10.1039/d1sm01212f
- Bidla, G., Lindgren, M., Theopold, U., and Dushay, M. S. (2005). Hemolymph coagulation and phenoloxidase in hawkmoths and its implications for hovering flight. *Dev. Comp. Immunol.* 29, 669–679. PubMed PMID: 15854679. doi:10.1016/j.dci.2004.11.007
- Bohn, H. (1986). "Hemolymph clotting in insects," in *Immunity in invertebrates, cells, molecules and defense reactions*. Editor M. Brehelin (Heidelberg: Springer), 188–207.
- Boman, H. G., and Hultmark, D. (1987). Cell-free immunity in insects. *Annu. Rev. Microbiol.* 41, 103–126. PubMed PMID: WOS:A1987K194900005. doi:10.1146/annurev.mi.41.100187.000535
- Brasovs, A., Palaoro, A. V., Aprelev, P., Beard, C. E., Adler, P. H., and Kornev, K. G. (2023). Haemolymph viscosity in hawkmoths and its implications for hovering flight. *Proc. R. Soc. B* 290, 20222185. doi:10.1098/rspb.2022.2185
- Brehelin, M. (1979). Hemolymph coagulation in *Locusta-migratoria* - evidence for a functional equivalent of fibrinogen. *Comp. Biochem. Physiol. B-Biochem. Mol. Biol.* 62 (4), 329–334. PubMed PMID: WOS:A1979GS50300007. doi:10.1016/0305-0491(79)90098-1
- Brodland, G. W. (2002). The differential interfacial tension hypothesis (DITH): a comprehensive theory for the self-rearrangement of embryonic cells and tissues. *J. Biomech. Eng-Trans ASME* 124 (2), 188–197. PubMed PMID: WOS:000175343800006. doi:10.1115/1.1449491
- Bulgakova, N. A., Klapholz, B., and Brown, N. H. (2012). Cell adhesion in *Drosophila*: versatility of cadherin and integrin complexes during development. *Curr. Opin. Cell Biol.* 24 (5), 702–712. PubMed PMID: WOS:000310943300019. doi:10.1016/j.celb.2012.07.006
- Carthew, R. W. (2005). Adhesion proteins and the control of cell shape. *Curr. Opin. Genet. Dev.* 15 (4), 358–363. PubMed PMID: WOS:000231205400002. doi:10.1016/j.gde.2005.06.002
- Chapman, R. F. (2013). *The insects: structure and function*. Cambridge, UK: Cambridge University Press.
- Chino, H., Hirayama, Y., Kiyomoto, Y., Downer, R. G. H., and Takahashi, K. (1987). Spontaneous aggregation of locust lipophorin during hemolymph collection. *Insect Biochem.* 17 (1), 89–97. PubMed PMID: WOS:A1987E892900013. doi:10.1016/0020-1790(87)90148-x
- Coodin, S., and Caveney, S. (1992). Lipophorin inhibits the adhesion of cockroach (*Periplaneta americana*) hemocytes *in vitro*. *J. Insect Physiology* 38 (11), 853–862. PubMed PMID: WOS:A1992JZ89400005. doi:10.1016/0022-1910(92)90096-v
- Doi, M., and Edwards, S. F. (1988). *The theory of polymer dynamics*. (Oxford: Clarendon Press), 391.
- Dushay, M. S. (2009). Insect hemolymph clotting. *Cell. Mol. Life Sci.* 66, 2643–2650. PubMed PMID: 19418022. doi:10.1007/s00018-009-0036-0
- Eggers, J. (1997). Nonlinear dynamics and breakup of free-surface flows. *Rev. Mod. Phys.* 69 (3), 865–930. PubMed PMID: WOS:A1997XL66500009. doi:10.1103/RevModPhys.69.865
- Eleftherianos, I., Heryanto, C., Bassal, T., Zhang, W., Tettamanti, G., and Mohamed, A. (2021). Haemocyte-mediated immunity in insects: cells, processes and associated components in the fight against pathogens and parasites. *Immunology* 164 (3), 401–432. PubMed PMID: WOS:000679933500001. doi:10.1111/imm.13390
- Entov, V. M., and Hinch, E. J. (1997). Effect of a spectrum of relaxation times on the capillary thinning of a filament of elastic liquid. *J. Newt. Fluid Mech.* 72 (1), 31–53. PubMed PMID: WOS:A1997XP64400002. doi:10.1016/s0377-0257(97)00022-0
- Erickson, H. P. (2009). Size and shape of protein molecules at the nanometer level determined by sedimentation, gel filtration, and electron microscopy. *Biol. Proced. Online* 11, 32–51. PubMed PMID: 19495910. doi:10.1007/s12575-009-9008-x
- Foty, R. A., and Steinberg, M. S. (2013). Differential adhesion in model systems. *Wires Dev. Biol.* 2 (5), 631–645. PubMed PMID: WOS:000323306600004. doi:10.1002/wdev.104
- Geng, C. (1990). *Studies of hemolymph coagulation in Manduca sexta*. Ph.D. dissertation. West Lafayette, IN: Purdue University Proquest Dissertation Publishers.
- Geng, C. X., and Dunn, P. E. (1988). Hemostasis in larvae of *Manduca sexta*: formation of a fibrous coagulum by hemolymph proteins. *Biochem. Biophys. Res. Commun.* 155 (2), 1060–1065. PubMed PMID: WOS:A1988Q050400077. doi:10.1016/s0006-291x(88)80604-1
- Gillespie, J. P., Kanost, M. R., and Trenczek, T. (1997). Biological mediators of insect immunity. *Annu. Rev. Entomology* 42, 611–643. PubMed PMID: WOS:A1997WD49500025. doi:10.1146/annurev.ento.42.1.611
- Godt, D., and Tepass, U. (1998). *Drosophila* oocyte localization is mediated by differential cadherin-based adhesion. *Nature* 395 (6700), 387–391. PubMed PMID: WOS:000076083800055. doi:10.1038/26493
- Gonzalez-Rodriguez, D., Guevorkian, K., Douezan, S., and Brochard-Wyart, F. (2012). Soft matter models of developing tissues and tumors. *Science* 338 (6109), 910–917. PubMed PMID: WOS:000311083600035. doi:10.1126/science.1226418
- Green, S. M., and Tobolsky, A. V. (1946). A new approach to the theory of relaxing polymeric media. *J. Chem. Phys.* 14, 80–92. doi:10.1063/1.1724109
- Gregoire, C. (1974). "Hemolymph coagulation," in *The physiology of insecta*. 5. Editor M. Rockstein (New York: Academic Press), 309–360.
- Gregoire, C. H. (1953). Blood coagulation in Arthropods. HI. Reactions of insect hemolymph to coagulation inhibitors of vertebrate blood. *Biol. Bull.* 104 (3), 372–393. PubMed PMID: BCI:19532700027216. doi:10.2307/1538491

- Gregoire, C. H. (1955). Blood coagulation in arthropods. V. Studies on hemolymph coagulation in 420 species of insects. *Arch. Biol.* 66 (1), 103–148. PubMed PMID: BCI:BCI1956300004464.
- Gu, Y., and Kornev, K. G. (2016). Ferromagnetic nanorods in applications to control of the in-plane anisotropy of composite films and for *in situ* characterization of the film rheology. *Adv. Funct. Mater.* 26 (22), 3796–3808. PubMed PMID: WOS:000379128700004. doi:10.1002/adfm.201504205
- Haward, S. J., Sharma, V., and Odell, J. A. (2011). Extensional opto-rheometry with biofluids and ultra-dilute polymer solutions. *Soft Matter* 7 (21), 9908–9921. PubMed PMID: WOS:000296026700017. doi:10.1039/c1sm05493g
- Hayashi, T., and Carthew, R. W. (2004). Surface mechanics mediate pattern formation in the developing retina. *Nature* 431 (7009), 647–652. PubMed PMID: WOS:000224993000030. doi:10.1038/nature02952
- He, Y., Cao, X. L., Zhang, S. G., Rogers, J., Hartson, S., and Jiang, H. B. (2016). Changes in the plasma proteome of *Manduca sexta* larvae in relation to the transcriptome variations after an immune challenge: evidence for high molecular weight immune complex formation. *Mol. Cell. Proteomics* 15 (4), 1176–1187. PubMed PMID: WOS:000373992600001. doi:10.1074/mcp.M115.054296
- Hillyer, J. F., and Strand, M. R. (2014). Mosquito hemocyte-mediated immune responses. *Curr. Opin. Insect Sci.* 3, 14–21. PubMed PMID: WOS:000209578700004. doi:10.1016/j.cois.2014.07.002
- Hoath, S. D., Vadiello, D. C., Harlen, O. G., McIlroy, C., Morrison, N. F., Hsiao, W. K., et al. (2014). Inkjet printing of weakly elastic polymer solutions. *J. Newt. Fluid Mech.* 205, 1–10. PubMed PMID: WOS:000333857000001. doi:10.1016/j.jnnfm.2014.01.002
- Hu, H. W., Hu, Q. B., Weng, Q. F., and Wang, J. J. (2024). Hemocytin, the special aggregation factor connecting insect hemolymph immunity, a potential target of insecticidal immunosuppressant. *Pesticide Biochem. Physiology* 198, 105704. PubMed PMID: WOS:001135149200001. doi:10.1016/j.pestbp.2023.105704
- Janmey, P. A., Winer, J. P., and Weisel, J. W. (2009). Fibrin gels and their clinical and bioengineering applications. *J. R. Soc. Interface* 6 (30), 1–10. PubMed PMID: WOS:000262756800001. doi:10.1098/rsif.2008.0327
- Jeffery, G. B. (1922). The motion of ellipsoidal particles in a viscous fluid. *Proc. R. Soc. Lond. Ser. A-Containing Pap. a Math. Phys. Character* 102 (715), 161–179. PubMed PMID: WOS:000202801300004. doi:10.1098/rspa.1922.0078
- Jiang, H., Vilcinskis, A., and Kanost, M. R. (2010). “Immunity in Lepidopteran insects,” in *Invertebrate immunity. Advances in experimental medicine and biology*. 708. Editor K. Soderhall (Berlin: Springer-Verlag Berlin), 181–204.
- Kenny, M. C., Giarrà, M. N., Granata, E., and Socha, J. J. (2018). How temperature influences the viscosity of hornworm hemolymph. *J. Exp. Biol.* 221 (21), jeb186338. PubMed PMID: WOS:000449824800016. doi:10.1242/jeb.186338
- Kojic, N., Bico, J., Clasen, C., and McKinley, G. H. (2006). *Ex vivo* rheology of spider silk. *J. Exp. Biol.* 209 (21), 4355–4362. PubMed PMID: WOS:000242132500027. doi:10.1242/jeb.02516
- Kornev, K. G., Gu, Y., Aprelev, P., and Tokarev, A. (2016). “Magnetic rotational spectroscopy for probing rheology of nanoliter droplets and thin films,” in *Springer book series on characterization tools for nanoscience and nanotechnology*. 6. Editor CSSR Kumar (New York: Springer), 51–83.
- Kornev, K. G., Neimark, A. V., and Rozhkov, A. N. (1999). Physical mechanisms of foam flow in porous media. *Rheol. Ser.* 8, 1151–1182. doi:10.1016/s0169-3107(99)80016-1
- Lai-Fook, J. (1966). The repair of wounds in the integument of insects. *J. insect physiology* 12, 195–226. doi:10.1016/0022-1910(66)90136-3
- Larson, R. G. (1999). *The structure and rheology of complex fluids*. New York: Oxford University Press, 663.
- Lavine, M. D., and Strand, M. R. (2002). Insect hemocytes and their role in immunity. *Insect Biochem. Mol. Biol.* 32, 1295–1309. PubMed PMID: 12225920. doi:10.1016/s0965-1748(02)00092-9
- League, G. P., and Hillyer, J. F. (2016). Functional integration of the circulatory, immune, and respiratory systems in mosquito larvae: pathogen killing in the hemocyte-rich tracheal tufts. *Bmc Biol.* 14, 78. PubMed PMID: WOS:000383839100001. doi:10.1186/s12915-016-0305-y
- Lesch, C., and Theopold, U. (2008). “Methods to study hemolymph clotting in insects,” in *Insect Immunology*. Editor N. E. Beckage (Academic Press), 1–12.
- Ling, S. J., Kaplan, D. L., and Buehler, M. J. (2018). Nanofibrils in nature and materials engineering. *Nat. Rev. Mater.* 3 (4), 18016. PubMed PMID: WOS:000430173500002. doi:10.1038/natrevmats.2018.16
- Machalowski, T., and Jesionowski, T. (2021). Hemolymph of molluscan origin: from biochemistry to modern biomaterials science. *Appl. Phys. A-Materials Sci. Process.* 127 (1), 3. PubMed PMID: WOS:000597637300001. doi:10.1007/s00339-020-04166-1
- Macosko, C. W. (1994). *Rheology: principles, measurements, and applications*. New York: Wiley VCH.
- Maire, E., and Withers, P. J. (2014). Quantitative X-ray tomography. *Int. Mater. Rev.* 59 (1), 1–43. PubMed PMID: WOS:000330498000001. doi:10.1179/1743280413y.0000000023
- Maravilla, E., Le, D. P., Tran, J. J., Chiu, M. H., Prenner, E. J., and Weers, P. M. M. (2020). Apolipoprotein III interaction with phosphatidylglycerol and lipopolysaccharide: a potential mechanism for antimicrobial activity. *Chem. Phys. Lipids* 229, 104909. PubMed PMID: WOS:000531098600005. doi:10.1016/j.chemphyslip.2020.104909
- Mattix, B., Olsen, T. R., Gu, Y., Casco, M., Herbst, A., Simionescu, D. T., et al. (2014). Biological magnetic cellular spheroids as building blocks for tissue engineering. *Acta Biomater.* 10 (2), 623–629. PubMed PMID: WOS:000330921700006. doi:10.1016/j.actbio.2013.10.021
- McKinley, G. H., and Sridhar, T. (2002). Filament-stretching rheometry of complex fluids. *Annu. Rev. Fluid Mech.* 34, 375–415. PubMed PMID: WOS:000174038400017. doi:10.1146/annurev.fluid.34.083001.125207
- Miserez, A., Yu, J., and Mohammadi, P. (2023). Protein-Based biological materials: molecular design and artificial production. *Chem. Rev.* 123, 2049–2111. PubMed PMID: WOS:000925857700001. doi:10.1021/acs.chemrev.2c00621
- Montanero, J. M., and Ponce-Torres, A. (2020). Review on the dynamics of isothermal liquid bridges. *Appl. Mech. Rev.* 72 (1). PubMed PMID: WOS:000525416400003. doi:10.1115/1.4044467
- Mulnix, A. B., and Dunn, P. E. (1995). “Molecular biology of immune response,” in *Molecular model systems in the Lepidoptera*. Editors M. R. Goldsmith and A. S. Wilkins (Cambridge, UK: Cambridge University Press), 369–396.
- Parle, E., Dirks, J. H., and Taylor, D. (2016). Bridging the gap: wound healing in insects restores mechanical strength by targeted cuticle deposition. *J. R. Soc. Interface* 13 (117), 20150984. PubMed PMID: WOS:000378311800003. doi:10.1098/rsif.2015.0984
- Patteson, A. E., Asp, M. E., and Janmey, P. A. (2022). Materials science and mechanosensitivity of living matter. *Appl. Phys. Rev.* 9 (1), 011320. PubMed PMID: WOS:000783171000001. doi:10.1063/5.0071648
- Pech, L. L., and Strand, M. R. (1996). Granular cells are required for encapsulation of foreign targets by insect haemocytes. *J. Cell Sci.* 109, 2053–2060. PubMed PMID: WOS:A1996VC21500009. doi:10.1242/jcs.109.8.2053
- Pech, L. L., and Strand, M. R. (2000). Plasmotocytes from the moth *Pseudoplusia includens* induce apoptosis of granular cells. *J. Insect Physiology* 46 (12), 1565–1573. PubMed PMID: WOS:000090079400007. doi:10.1016/s0022-1910(00)00083-4
- Plateau, J. (1873). *Statique Experimentale et The'orique des Liquides Soumis aux Seules Forces Mole'culaires*. Paris: Gauthier-Villars.
- Rahman, M. M., Ma, G., Roberts, H. L. S., and Schmidt, O. (2006). Cell-free immune reactions in insects. *J. Insect Physiology* 52 (7), 754–762. PubMed PMID: WOS:000239081500012. doi:10.1016/j.jinsphys.2006.04.003
- Ribeiro, C., and Brehélin, M. (2006). Insect haemocytes: what type of cell is that? *J. Insect Physiology* 52, 417–429. PubMed PMID: 16527302. doi:10.1016/j.jinsphys.2006.01.005
- Rodd, L. E., Scott, T. P., Cooper-White, J. J., and McKinley, G. H. (2005). Capillary break-up rheometry of low-viscosity elastic fluids. *Appl. Rheol.* 15 (1), 12–27. PubMed PMID: WOS:000233116600004. doi:10.1515/arh-2005-0001
- Rowley, A. F., and Ratcliffe, N. A. (1976). The granular cells of *Galleria mellonella* during clotting and phagocytic reactions *in vitro*. *Tissue Cell* 8, 437–446. doi:10.1016/0040-8166(76)90004-5
- Salt, G. W. (1970). *The cellular defence reactions of insects*. Cambridge: Cambridge University Press.
- Scherfer, C., Karlsson, C., Loseva, O., Bidla, G., Goto, A., Havemann, J., et al. (2004). Isolation and characterization of hemolymph clotting factors in *Drosophila melanogaster* by a pullout method. *Curr. Biol.* 14 (7), 625–629. PubMed PMID: WOS:000220809900030. doi:10.1016/j.cub.2004.03.030
- Staczek, S., Zdybicka-Barabas, A., Mak, P., Sowa-Jasilek, A., Kedracka-Krok, S., Jankowska, U., et al. (2018). Studies on localization and protein ligands of *Galleria mellonella* apolipoprotein III during immune response against different pathogens. *J. Insect Physiology* 105, 18–27. PubMed PMID: WOS:000427218000003. doi:10.1016/j.jinsphys.2017.12.009
- Steinberg, M. S. (2007). Differential adhesion in morphogenesis: a modern view. *Curr. Opin. Genet. Dev.* 17 (4), 281–286. PubMed PMID: WOS:000249366400004. doi:10.1016/j.gde.2007.05.002
- Stoepler, T. M., Castillo, J. C., Lill, J. T., and Eleftherianos, I. (2013). Hemocyte density increases with developmental stage in an immune-challenged forest caterpillar. *Plos One* 8 (8), e70978. PubMed PMID: WOS:000324401500055. doi:10.1371/journal.pone.0070978
- Strand, M. R. (2008). The insect cellular immune response. *Insect Sci.* 15 (1), 1–14. PubMed PMID: WOS:000252587700001. doi:10.1111/j.1744-7917.2008.00183.x
- Sun, Y., Ma, J., Peng, F., and Kornev, K. G. (2022). Making droplets from highly viscous liquids by pushing a wire through a tube. *Phys. Fluids* 34 (3), 032119. doi:10.1063/5.0082003

Sun, Y. M., Bazilevsky, A. V., and Kornev, K. G. (2023). Classification of axisymmetric shapes of droplets on fibers. Could non-wettable fibers support axisymmetric droplets? *Phys. Fluids* 35 (7), 072004. PubMed PMID: WOS:001025235200004. doi:10.1063/5.0151950

Theopold, U., Li, D., Fabbri, M., Scherfer, C., and Schmidt, O. (2002). The coagulation of insect hemolymph. *Cell. Mol. Life Sci.* 59, 363–372. PubMed PMID: 11915949. doi:10.1007/s00018-002-8428-4

Theopold, U., Schmidt, O., Soderhall, K., and Dushay, M. S. (2004). Coagulation in arthropods: defence, wound closure and healing. *Trends Immunol.* 25 (6), 289–294. PubMed PMID: WOS:000222302100004. doi:10.1016/j.it.2004.03.004

Wigglesworth, V. B. (1937). Wound healing in an insect (*Rhodnius prolixus*, Hemiptera). *J. Exp. Biol.* 14 (3), 364–381. PubMed PMID: WOS:000200577900010. doi:10.1242/jeb.14.3.364

Wigglesworth, V. B. (1979). “Hemocytes and growth in insects,” in *Insect hemocytes: development, forms, functions, and techniques*. Editor A. P. Gupta (Cambridge, UK: Cambridge University Press), 303–318.

Yan, X. J., Carr, W. W., and Dong, H. M. (2011). Drop-on-demand drop formation of polyethylene oxide solutions. *Phys. Fluids* 23 (10), 107101. PubMed PMID: WOS:000296528000029. doi:10.1063/1.3643269

Zdybicka-Barabas, A., and Cytrynska, M. (2013). Apolipophorins and insects immune response. *Isj-Invertebrate Surviv. J.* 10 (1), 58–68. PubMed PMID: WOS:000328155800001.

Zhang, Z., Peng, F., and Kornev, K. G. (2022). The thickness and structure of dip-coated polymer films in the liquid and solid states. *Micromachines* 13 (7), 982. PubMed PMID: doi:10.3390/mi13070982



OPEN ACCESS

EDITED BY

Frank Alexis,
Universidad San Francisco de Quito, Ecuador

REVIEWED BY

Anne-laure Fameau,
Institut National de recherche pour l'agriculture,
l'alimentation et l'environnement (INRAE),
France
Konstantin Kornev,
Clemson University, United States

*CORRESPONDENCE

Alejandro D. Rey,
✉ alejandro.rey@mcgill.ca

RECEIVED 20 December 2023

ACCEPTED 16 April 2024

PUBLISHED 21 May 2024

CITATION

Zamora Cisneros DU, Wang Z,
Dorval Courchesne N-M, Harrington MJ and
Rey AD (2024), Geometric modeling of phase
ordering for the isotropic–smectic A
phase transition.
Front. Soft Matter 4:1359128.
doi: 10.3389/frsfm.2024.1359128

COPYRIGHT

© 2024 Zamora Cisneros, Wang, Dorval
Courchesne, Harrington and Rey. This is an
open-access article distributed under the terms
of the [Creative Commons Attribution License](#)
(CC BY). The use, distribution or reproduction in
other forums is permitted, provided the original
author(s) and the copyright owner(s) are
credited and that the original publication in this
journal is cited, in accordance with accepted
academic practice. No use, distribution or
reproduction is permitted which does not
comply with these terms.

Geometric modeling of phase ordering for the isotropic–smectic A phase transition

David Uriel Zamora Cisneros¹, Ziheng Wang¹,
Noémie-Manuelle Dorval Courchesne¹, Matthew J. Harrington²
and Alejandro D. Rey^{1*}

¹Department of Chemical Engineering, McGill University, Montreal, QC, Canada, ²Department of Chemistry, McGill University, Montreal, QC, Canada

Background: Liquid crystal (LC) mesophases have an orientational and positional order that can be found in both synthetic and biological materials. These orders are maintained until some parameter, mainly the temperature or concentration, is changed, inducing a phase transition. Among these transitions, a special sequence of mesophases has been observed, in which priority is given to the direct smectic liquid crystal transition. The description of these transitions is carried out using the Landau–de Gennes (LdG) model, which correlates the free energy of the system with the orientational and positional order.

Methodology: This work explored the direct isotropic-to-smectic A transition studying the free energy landscape constructed with the LdG model and its relation to three curve families: (I) level-set curves, steepest descent, and critical points; (II) lines of curvature (LOC) and geodesics, which are directly connected to the principal curvatures; and (III) the Casorati curvature and shape coefficient that describe the local surface geometries resemblance (sphere, cylinder, and saddle).

Results: The experimental data on 12-cyanobiphenyl were used to study the three curve families. The presence of unstable nematic and metastable plastic crystal information was found to add information to the already developed smectic A phase diagram. The lines of curvature and geodesics were calculated and laid out on the energy landscape, which highlighted the energetic pathways connecting critical points. The Casorati curvature and shape coefficient were computed, and in addition to the previous family, they framed a geometric region that describes the phase transition zone.

Conclusion and significance: A direct link between the energy landscape's topological geometry, phase transitions, and relevant critical points was established. The shape coefficient delineates a stability zone in which the phase transition develops. The methodology significantly reduces the impact of unknown parametric data. Symmetry breaking with two order parameters (OPs) may lead to novel phase transformation kinetics and droplets with partially ordered surface structures.

KEYWORDS

liquid crystals, smectic A, phase transition, energy landscape, shape coefficient, free energy, Landau–de Gennes

1 Introduction

Synthetic and biological liquid crystals (LCs) are anisotropic soft materials with partial degrees of orientational and positional order, conveying fluidity as viscous liquids and anisotropy as in the crystalline order (Rey and Denn, 2002; Donald et al., 2006; Rey, 2010; Sonnet and Virga, 2012; Petrov, 2013; Lagerwall, 2016; Selinger, 2016; Collings and Goodby, 2019; Stewart, 2019; Zannoni, 2022). Importantly, possible LC mesogens include rod-, board-, disk-, and screw-like molecules with flexibilities ranging from semi-flexible to rigid, involving monomers or main/side-chain polymers and colloids (Donald et al., 2006; Demus et al., 2008b; Demus et al., 2011). The synthesis and formation of these mesophase materials follow equilibrium self-assembly processes driven by temperature (thermotropic), concentration (lyotropic), or both (Bowick et al., 2017; Wang et al., 2023b). The presence of multiple components, as in nanoparticle-loaded mesophases, gives rise to couplings between self-assembly and phase separation with states that can combine the crystallinity (positional order) of one component with the liquid crystallinity (various degrees of positional and orientational order) of the other (Soulé et al., 2012a; Soulé et al., 2012b; Soulé et al., 2012c; Soule and Rey, 2012; Milette et al., 2013; Gurevich et al., 2014). Various external fields (flow, electromagnetic, and thermal) can be used to generate self-organized structures not seen in purely equilibrium self-assembly. The natural setting to describe self-assembly starts with the energy landscape and its geometrical properties (curvatures, cusps, domes, *etc.*), while for non-equilibrium organization, the natural setting will include the entropy production landscape and its defining geometric measures. In this paper, we present a widely applicable geometry-based methodology for describing self-assembly in anisotropic soft matter and target one specific transition that exhibits complex ordering processes. Without ambiguity, for convenience and brevity, below we refer to self-assembly as phase ordering and/or phase transition, as we do not include phase separation and conserved quantities. In addition, we refer to the degree of quench as the equivalent of the thermodynamic driving force for phase ordering.

The spectrum of self-assembly processes is significantly enriched when considering the sequence of phase transformations. This progression follows an increase in order as the magnitude of the thermodynamic driving force is increased, corresponding to a decrease in temperature for thermotropes or an increase in concentration for lyotropes. The sequence then goes from a high-symmetry isotropic state to an orientationally ordered (nematic) state. This state is then followed by the addition of the positional order (smectic). Then, the crystalline organization is reached with a further increase in the driving force. The usual sequence of isotropic–orientational–positional phase ordering (Oswald and Pieranski, 2005a; Jáklí and Saupe, 2006; Blinov, 2011) is sometimes reordered to a direct isotropic–positional/orientational ordering, as observed in monomeric thermotropes (certain cyanobiphenyls (CB) and oxy-cyanobiphenyls (OCB)) (Oh, 1977; Idziak et al., 1996; Oswald and Pieranski, 2005b; Donald et al., 2006; Abukhdeir and Rey, 2008; Chahine et al., 2010; Gudimalla et al., 2021; Nesrullajev, 2022) and biological liquid crystals (BLCs) such as collagen mesophase precursors in the mussel byssus (Knight and Vollrath, 1999; Viney, 2004; Donald et al., 2006; Rey, 2010; Rey and

Herrera-Valencia, 2012; Rey et al., 2013; Renner-Rao et al., 2019; Manolakis and Azhar, 2020; Harrington and Fratzl, 2021; Berent et al., 2022). This important and non-classical behavior is the focus of this paper: the direct isotropic-to-smectic A (I-SmA) LC phase transition, where SmA denotes the simplest smectic phase. A collection of compounds exhibiting this scheme can be found (Hawkins and April 1983; Idziak et al., 1996; Lenoble et al., 2007; Abukhdeir and Rey, 2008; Mohieddin Abukhdeir and Rey, 2008a; Li et al., 2009; Wojcik et al., 2009; Chahine et al., 2010; Pouget et al., 2011; Salamonczyk et al., 2016; Bradley, 2019; Renner-Rao et al., 2019; Gudimalla et al., 2021; Jackson et al., 2021; Jehle et al., 2021; Khadem and Rey, 2021; Nesrullajev, 2022), which is largely driven by attractive forces in thermotropic LCs [e.g., cyanobiphenyl family (n -CB, $n > 10$) (Bellini et al., 2002)] and excluded volume interactions in BLCs (e.g., collagen in mussel byssus and Ff phages). In both cases, a common geometric feature is the presence of rigid or semi-rigid rod-like cores and sufficiently long semi-flexible ends. Currently, the best-characterized materials that follow the direct I-SmA are low-molar mass thermotropic LCs, such as 10CB and 12CB (Collings, 1997; Urban et al., 2005; Demus et al., 2008a; Li et al., 2009; Chahine et al., 2010; Gudimalla et al., 2021; Zaluzhnyy et al., 2022). To avoid introducing a plethora of unknown parameters and material data, we focus on them as model systems. In the future, our ultimate goal is to expand the findings to lyotropic polymeric and colloidal smectics that are found in collagen precursors of the mussel byssus (Renner-Rao et al., 2019; Jehle et al., 2021; Waite and Harrington, 2022). It is noted that even though we only consider thermotropic LCs in the current manuscript, using correspondence principles such as those provided in the following references (Picken, 1990; Soule and Rey, 2011; Golmohammadi and Rey, 2009; Doi, 1981), we can, in the future, use the current findings for collagen-based LCs.

A key feature of the I-SmA transition is the strong coupling of the positional and orientational order parameters (OPs) (Pikin, 1991; Gorkunov et al., 2007; Blinov, 2011; Turek et al., 2020; Gurin et al., 2021), which results in the enhancement of the orientational OP over and above what a nematic phase could show at these conditions of temperature or concentration. A practical consequence of this, as we know from synthetic liquid crystal polymers (LCPs), is that in the solid state, the enhanced orientational order parameter has a strong impact on the mechanical properties (e.g., Young modulus) that can be seen in LCP fibers (Ward, 1993; Ziabicki, 1993; Donald et al., 2006; Turek et al., 2020; Bunsell et al., 2021). This order parameter coupling decreases the free energy of the system to result in a smectic A phase at minimal quenches from the stable disordered state. Polymeric and biological liquid-crystalline materials, being part of the lyo/thermotropic spectrum, also share the preferred native mode of fiber-formation, as seen in their *in vivo* and *in vitro* states (Matthews et al., 2002; Viney, 2004; Dierking and Al-Zangana, 2017; Renner-Rao et al., 2019; Deng et al., 2021; Harrington and Fratzl, 2021; Tortora and Jost, 2021; Cai et al., 2023; Zhang et al., 2023), which reinforces the hypothesis of smecticity enhancing the material's mechanical properties through increased alignment.

The computational liquid crystal phase-field methodology used in this paper, largely based on the Landau–de Gennes (LdG) models and their many generalizations, has been widely used to simulate and predict self-assembly, self-organization, rheology, bulk,

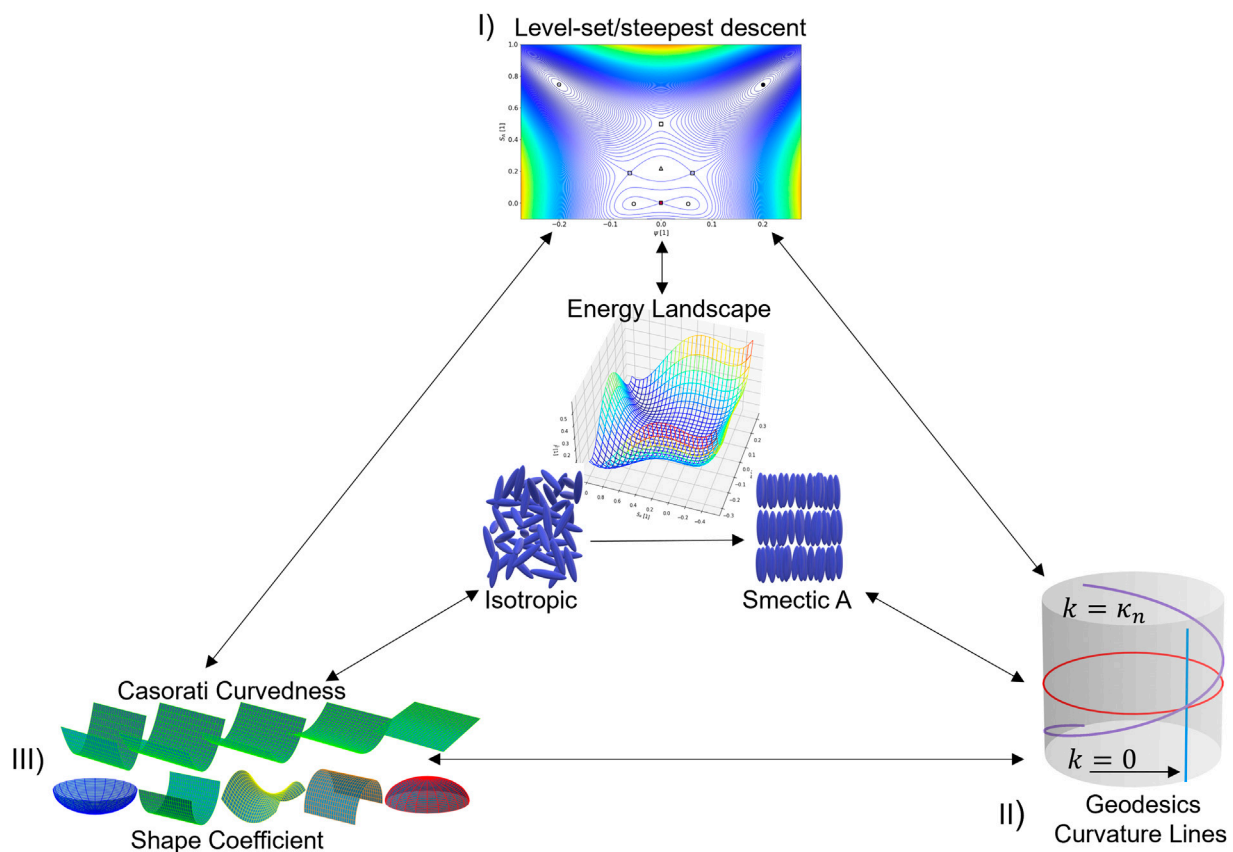


FIGURE 1
Methodology of the geometric-thermodynamics formulated (Section 2) and implemented (Section 3) in this paper. The central energy landscape corresponding to the direct I-SmA transition is characterized using three geometric methods (I) level sets/steepest descent/critical points, (II) geodesics and curvature lines, and (III) shape and Casorati curvedness analysis; the bottom left shows changes in shape from cup (left), to rut, saddle, ridge, and cap (right) and changes in the degree of curvedness for a rut patch (left) into a flat plane. The outer arrows show the connection and integration of the three calculations.

interfacial transport phenomena, and more for both thermotropic and lyotropic LCs (Biscari et al., 2007; Hormann and Zimmer, 2007; Popa-Nita and Sluckin, 2007; Saunders et al., 2007; Mohieddin Abukhdeir and Rey, 2008b; Rey, 2010; Coles and Strazielle, 2011; Garti et al., 2012; Mukherjee, 2014; Han et al., 2015; Selinger, 2016; Collings and Hird, 2017; Vitral et al., 2019; Copic and Mertelj, 2020; Vitral et al., 2020; Schimming et al., 2021; Bukharina et al., 2022; Paget et al., 2022; Zaluzhnyy et al., 2022). As in other coupled OP transitions, the challenges for a given energy landscape include the following issues:

- What is the total number of local maxima, minima, and saddles in the energy surface for a given quench?
- Where are the local minima and maxima located for a given quench?
- When do we find bi-stability?
- What states exist when one of the OPs is zero (e.g., nematic and plastic crystal)?
- What are the shortest path directions connecting minima?

Previous works have excellently characterized these mesophases and phase transitions, including phase diagrams, orientation distribution function profiles, bifurcation analysis, and the use of

imaging techniques, calorimetry characterization, and dynamic simulations, accentuating the thermodynamic I-SmA phase transition perspective (Palfy-Muhoray, 1999; Dogic and Fraden, 2001; Mukherjee et al., 2001; Larin, 2004; Urban et al., 2005; Biscari et al., 2007; Das and Mukherjee, 2009; Chahine et al., 2010; Nandi et al., 2012; Izzo and De Oliveira, 2019; Gudimalla et al., 2021; Khan and Mukherjee, 2021; Mukherjee, 2021). Given that the first four key issues are essentially anchored in the spatial features of the energy landscape, we develop, implement, and validate a novel geometric methodology. The use of geometric methods to characterize thermodynamics, phase transitions, and energy landscapes has been widely recognized as a useful and complementary set of tools (Miller, 1925; Hormann and Zimmer, 2007; Quevedo et al., 2011; Wales, 2018; Wang et al., 2020; Demirci and Holland, 2022; Liu et al., 2022; Quevedo et al., 2022). These approaches rely on establishing a proper thermodynamic surface in terms of variables such as pressure, temperature, and chemical potential. Here, we extend and generalize these geometric-thermodynamic methods for self-assembly in anisotropic soft matter in general and phase ordering in the I-SmA transition. The methodology is summarized in Figure 1. The triangle's center is the key focus of this paper, the direct isotropic-SmA transition, as characterized by an energy landscape given by the Landau free energy $F(\psi, S_A)$ as a

function of the positional (ψ) and orientational (S_A) order parameters for a given temperature T . Importantly, the surface parametrization is explicit and known as Monge parameterization, and it is the starting point for the geometric methodology developed in this paper.

In (I), at the upper vertex from Figure 1, the critical points (dots) of the surface (maxima, minima, and saddles) are determined as a function of changes in temperature using level-set curves and curves of the steepest descent. The closed loops in the former allow the detection of minima/maxima and saddles, and the signs of the gradient curves differentiate the stable from the unstable. In addition, saddles in the level sets are unstable points. These calculations are guided and validated using the powerful index theorem of polynomials, yielding a conservation equation for the number of maxima N_{maxima} , the number of minima N_{minima} , and the number of saddles N_{saddles} . At a high temperature for a stable isotropic phase, the landscape is simple and $N_{\text{maxima}} = N_{\text{saddles}} = 0$, but for low quenches with a stable SmA phase, the landscape is complex, as we find $N_{\text{minima}} = N_{\text{saddles}} = 4$ and $N_{\text{maxima}} = 1$. In (II), at the lower right vertex, the geodesic lines of the energy landscape are found using accurate ordinary differential equation (ODE) solvers. Importantly, the lack of torsion in the geodesic lines correlates with the energy heights of the maxima and minima. In (II), we also compute the lines of curvature (LOC) that define an orthogonal grid on the energy surface and indicate the maximum or minimum directional curvature flow. In (III), the shape coefficient, or shape index S , relates a given value with a shape that comes from the spectrum $S = \pm 1$ for up/down half-spheres (cup and cap, respectively), $S = \pm 1/2$ for up/down cylinders (rut and ridge, respectively), and $S = 0$ for saddle-like shapes; the positive scalar curvedness Casorati curvature C (surface deviation from planarity) of the energy landscape and its critical points are identified to determine aspects of the minima and maxima, such as anisotropy, the presence or absence of umbilic $S = \pm 1$ points, and the degree of curvedness (magnitude of Casorati curvature), and detect maxima/minima/saddles in a fast and efficient way.

Describing the shape using the dimensionless normalized shape coefficient (S) avoids co-mingling properties associated with shape with those associated with curvedness, such as when using the classical differential geometry descriptions based on Gaussian (K), mean (H), and deviatoric (D) curvatures. The shape coefficient–Casorati curvedness (S, C) method has been successfully applied to several soft-matter materials and equilibrium and dissipative processes (Wang et al., 2020; Wang et al., 2022b; Wang et al., 2022a; Wang et al., 2023b). For example, for a saddle point, the classical approach yields $K = -D^2$. On the other hand, the (S, C) method detects a saddle simply when $S = 0$ and its curvedness is $C = D = \sqrt{-K}$. Finally, the arrows on the triangle side and toward the center denote the integration of the methods to shed new light on the I-SmA transition.

This work builds on the fundamental studies on the self-assembled smectic phase transition (Pleiner et al., 2000; Mukherjee et al., 2001; Abukhdeir, 2009; Abukhdeir and Rey, 2009b; Mukherjee, 2021). The particular objectives of this paper are the following:

- Characterize the energy landscape using a simple Monge parametrization in terms of nematic and smectic order parameters, including the number and type of critical

points and characteristic trajectories between stable, metastable, and unstable isotropic, nematic, and smectic states as a function of the changing degrees of quenching from the isotropic state.

- Use classical curvatures (Gaussian and mean) and new soft matter geometric methods (shape coefficient and Casorati curvedness) to shed light on where saddles and cusps are located and their curvedness, thus providing a broad picture of the energy landscape.
- Integrate thermodynamic stability, polynomial-based charge conservation methods, and geometric methods.
- Detect and characterize unstable nematic and metastable plastic crystal states that emerge at medium and large degrees of quenching.

The remainder of this paper is organized as follows: Section 2 presents the OPs, Landau free energy (Section 2.1), geometric thermodynamics (Section 2.2), and computational methods (Section 2.3). Section 3 presents the results and discussion. Section 4 summarizes the key findings, their significance, and the novelty of the geometric approach.

2 Methodology

2.1 Order parameters and Landau model

2.1.1 Nematic and smectic A phases: orientational and positional order parameters

The SmA LC phase has partial 1D positional and orientational order. Two order parameters, the orientational order parameter Q and the positional order parameter Ψ , are used for this mesophase characterization. These parameters capture the average molecular order by the establishment of distinctive moduli at the transition, with the moduli (S_A, P) for the orientation and ψ for the position (Oswald and Pieranski, 2005b; Rey, 2010; Mukherjee, 2014; Vitral et al., 2020).

The theoretical characterization of the partial orientational alignment in LCs is described by an orientation distribution function, the tensor order parameter Q (De Gennes and Prost, 1993), which is as follows:

$$Q = S_A \left(\mathbf{nn} - \frac{\mathbf{I}}{3} \right) + \frac{1}{3} P (\mathbf{mm} - \mathbf{II}), \quad (2.1)$$

where \mathbf{n} , \mathbf{m} , and \mathbf{l} are the molecular unit vectors and \mathbf{I} is the unit tensor. The Q tensor is expressed in terms of the orthonormal director triad (\mathbf{n} , \mathbf{m} , and \mathbf{l}), which are the eigenvectors of Q that describe the molecular axes and the scalar moduli (S_A, P) that measure the magnitude of the average molecular orientation (De Luca and Rey, 2006; Coles and Strazielle, 2011). The Q tensor is symmetric and traceless, i.e., $Q = Q^T$ and $Q : \mathbf{I} = 0$, and it has five independent components. It is comprised of uniaxial (S_A and \mathbf{n}) and biaxial (P and \mathbf{m}, \mathbf{l}) contributions. The uniaxial contribution $S_A = \frac{3}{2} (\mathbf{nn} : Q)$ corresponds to the major eigenvalue/eigenvector, and the biaxial contribution $P = \frac{3}{2} (\mathbf{mm} - \mathbf{II}) : Q$ corresponds to the minor eigenvalues/eigenvectors. A free-energy expansion near the nematic transition, as per the Landau formalism, was defined, yielding an LdG free-energy expression for nematic orientational alignment F_N

(de Gennes and Prost, 1993), truncated up to the fourth-order term with respect to S_A as follows:

$$F_N = F_0 + \frac{1}{2}a(\mathbf{Q}:\mathbf{Q}) - \frac{1}{3}b(\mathbf{Q}:\mathbf{Q})^2 + \frac{1}{4}c(\mathbf{Q}:\mathbf{Q})^3 + \dots, \quad (2.2)$$

where F_0 is the energy of the isotropic state, $a = a_0(T - T_{NI}^*)$, T_{NI}^* is the critical nematic phase transition temperature, and a_0 , b , and c are experimentally measured material parameters.

In addition to the orientational organization, due to its lamellar configuration and the periodic structure of the uniaxial SmA phase, a one-dimensional positional order parameter is required, and the complex wave vector Ψ has been widely used for this purpose (Mukherjee et al., 2001; Abukhdeir and Rey, 2009c; Vitral et al., 2020). It is typified by the phase ϕ , and its modulus ψ characterizes a one-dimensional density wave used to describe such a layered nature as follows:

$$\Psi = \psi e^{i\phi}. \quad (2.3)$$

Then, a free-energy functional of the smectic positional order, F_S , is introduced, accounting for positional ordering, and the material-dependent parameters are $\alpha = \alpha_0(T - T_{AI}^*)$ and β around the critical smectic transition temperature T_{AI}^* .

$$F_S = \alpha|\Psi|^2 + \beta|\Psi|^4 + \dots. \quad (2.4)$$

In the simplest case, the I-SmA transition is captured by the free-energy contributions of the form $F = F_N + F_S + F_{NS}$, where F_{NS} is the coupling free-energy term, which is given as follows:

$$F_{NS} = -\delta|\Psi|(\mathbf{Q}:\mathbf{Q}) - \frac{1}{2}e\mathbf{Q}:(\nabla\Psi\nabla\Psi) + \frac{1}{2}b_1|\nabla\Psi|^2 + \frac{1}{4}b_2|\nabla^2\Psi|^2. \quad (2.5)$$

2.1.2 Landau model for the isotropic–smectic A transition

The well-established models have been formulated and used to describe the I-SmA transition, including non-direct transitions (Pleiner et al., 2000; Abukhdeir and Rey, 2009b; Nandi et al., 2012; Pevnyi et al., 2014; Izzo and De Oliveira, 2019; Mukherjee, 2021; Paget et al., 2022). These models include the nematic and smectic contributions (Eqs. 2.2, 2.4, and 2.5) and consolidate the final total free-energy density using coupling terms (δ, e) that favor one phase over the other and terms that account for the energy cost from the coexistence of the positional ordering (b_1, b_2):

$$\text{Total Energy} = \int F dV$$

$$F = F_0 + \frac{1}{2}a(\mathbf{Q}:\mathbf{Q}) - \frac{1}{3}b(\mathbf{Q}:\mathbf{Q})^2 + \frac{1}{4}c(\mathbf{Q}:\mathbf{Q})^3 + \alpha|\Psi|^2 + \beta|\Psi|^4 - \delta|\Psi|(\mathbf{Q}:\mathbf{Q}) - \frac{1}{2}e\mathbf{Q}:(\nabla\Psi\nabla\Psi) + \frac{1}{2}b_1|\nabla\Psi|^2 + \frac{1}{4}b_2|\nabla^2\Psi|^2. \quad (2.6)$$

Considering Equation 2.6, assuming a spatially homogenous system, and performing reparameterization (see Supplementary Appendix A1), we find the following governing free energy density $F(\psi, S_A)$:

$$F(\psi, S_A) = \underbrace{\frac{1}{3}aS_A^2 - \frac{2}{27}bS_A^3 + \frac{1}{9}cS_A^4}_{F_N} + \underbrace{\frac{1}{2}\left(\alpha - \frac{b_1^2}{2b_2}\right)\psi^2 + \frac{1}{4}\beta\psi^4}_{F_S} - \underbrace{\left(\frac{e^2 + 3\delta b_2}{9b_2}\right)\left[S_A^2\psi^2 - \left(\frac{3eb_1}{(e^2 + 3\delta b_2)}\right)S_A\psi^2\right]}_{F_{NS}}, \quad (2.7)$$

where F_N is the nematic contribution, F_S is the smectic contribution, and F_{NS} is the crucial coupling contribution between the positional and orientational OPs that are in their expanded form. In this paper, we evaluate the OPs in their extended domain of dependence $F(\psi, S_A): [-1, 1] \times [-1/2, 1] \rightarrow [-F_0, \infty)$ to fully capture the important phenomena at the nematic axis ($\psi = 0$) and the smectic axis ($S_A = 0$); we note that negative nematic OP states (molecular alignment normal to the director orientation) are usually considered in nematostatics (Golmohammadi and Rey, 2010), but in the particular equilibrium spatially homogeneous I-SmA transitions considered in this study, these orientation states play no role.

The possible states are obtained by the minimization of the homogeneous free energy in Equation 2.7 concerning the two non-conserved OPs (ψ, S_A). This yields a system of ODEs (see Supplementary Appendix A1). Then, at a given temperature T , different phases arise according to the ordering contributions. As mentioned in the introduction, positional and orientational ordering define an LC state, which varies in accordance with the combination of these order parameters. In this paper, we consider the following:

$$\begin{aligned} \text{Isotropic (Iso): } S_A &= \psi = 0. \\ \text{Nematic (N): } S_A &> 0, \psi = 0. \\ \text{Plastic crystal (P}_c\text{): } S_A &= 0, \psi > 0. \\ \text{Smectic - A (SmA): } S_A &> 0, \psi > 0. \end{aligned} \quad (2.8)$$

The isotropic-liquid state is characterized by the absence of positional and orientational orders, the nematic LC possesses only average molecular orientation, the plastic crystal phase (characterized by the density wave) describes a material with positional order and very small-to-none orientational order, and the smectic A LC exhibits positional and orientational orders (Oswald and Pieranski, 2005a; Oswald and Pieranski, 2005b; De Gennes, 2007; Demus et al., 2008a; DiLisi, 2019; Mukherjee, 2021). We note that the density wave behavior, designated as the plastic crystal state in this study, has been reported even for some rod-like systems (Kyrylyuk et al., 2011; Liu et al., 2014; Sato et al., 2023). In this work, the metastable plastic crystal emerges at deep quenches when the isotropic state becomes unstable, the nematic and coupling energies vanish, and the stable phase is SmA. Similarly, since $(e^2 + 3\delta b_2)/9b_2 > 0$ and $[S_A^2\psi^2 - (3eb_1/(e^2 + 3\delta b_2))S_A\psi^2] > 0$ for the SmA state in Equation 2.7, the important coupling term F_{NS} promotes the emergence of SmA with the positional and orientational order.

2.2 Geometric thermodynamics for phase ordering in the isotropic–smectic A transition

In this section, we investigate the surface geometry of the energy landscape $F(\psi, S_A)$, with a particular emphasis on understanding and characterizing the essential nature of all the critical points.

These critical points, derived from Equation 2.7, include the local maxima, local minima, and saddle points. As mentioned at the end of the introduction, their significance extends across many research fields in liquid crystals, such as self-assembly, kinematics, and thermodynamics of these systems.

Next, we briefly mention the basic argument to keep all critical points, forgoing complex mathematical details. For instance, the time-dependent Ginzburg–Landau model (Popa-Nita, 1999) provides a quantitative study of the spatiotemporal evolution of thermodynamic behaviors on a non-conserved OPs vector \mathbf{p} .

$$\frac{\partial \mathbf{p}}{\partial t} \propto \frac{\partial (f + f_e)}{\partial \mathbf{p}} = \frac{\partial (F + F_e)}{\partial \mathbf{p}} - \nabla \cdot \frac{\partial (F + F_e)}{\partial \nabla \mathbf{p}}, \mathbf{p} = \begin{bmatrix} \psi \\ S_A \end{bmatrix}, \quad (2.9)$$

where $F_e \propto \nabla \mathbf{p}$: $\nabla \mathbf{p}$ is the elastic energy dependent on the deformation; note that \mathbf{p} is the OP vector for the smectic A phase. A special solution of Equation 2.9 describes a front propagation that could describe growing smectic droplets in an isotropic matrix. For example, the wave-like property has been intensively studied by De Luca and Rey (2004) for the case of chiral nematic fronts propagating into an unstable isotropic phase. In our present smectic model, the wave-like solution $\mathbf{p} = \mathbf{p}(\mathbf{x} - \mathbf{v}t) = \mathbf{p}(\tilde{\mathbf{x}})$; $\tilde{\mathbf{x}} = \mathbf{x} - \mathbf{v}t$ with constant velocity \mathbf{v} simplifies Eq. 2.9 to a more compact form, $\frac{\partial F}{\partial \mathbf{p}} = (\mathbf{v} \cdot \tilde{\nabla} + \tilde{\nabla}^2) \mathbf{p}$, where all the coefficients are not included for clarity. At $\frac{\partial F}{\partial \mathbf{p}} = 0$, the critical points lay inside the kernel of the linear map defined by the velocity $(\mathbf{v} \cdot \tilde{\nabla} + \tilde{\nabla}^2)$. The polynomial decomposition of $F(\psi, S_A)$ (see Eq. 2.7 for the quartic polynomial expression in two variables (ψ, S_A)) then gives the governing equation for phase transformation, $(\mathbf{v} \cdot \tilde{\nabla} + \tilde{\nabla}^2) \mathbf{p} = \prod_i (\mathbf{p} - \hat{\mathbf{p}}_i)$, where $\hat{\mathbf{p}}_i$ are the critical points at critical points $(\partial_\psi F = \partial_{S_A} F = 0)$ and $\prod_i (\mathbf{p} - \hat{\mathbf{p}}_i)$ is the product function that expresses the polynomial $F(\psi, S_A)$. The phase transformation depends on the polynomial decomposition of the free energy involving all the critical points. Given the significance of all the critical points on growth, kinematics, and interfaces, we explore their behavior in this section.

2.2.1 Polynomial index theorem and critical points of the $F(\psi, S_A)$ -energy landscape

Since the two-OP model considered in this study is of quartic order in each of the parameters, a proliferation of critical points and a complex energy landscape are expected. Hence, tools that set upper limits on the number and type of critical points are essential to achieving or enhancing tractability. In this section, we formulate an approach tailored to the I-SmA transition, keeping the complex mathematics to a minimum.

Let $f(x, y)$ be a polynomial of degree $d > 1$. Then, f has a critical point (x_0, y_0) , if $\partial_k f(x_0, y_0) = 0$, where the following notation (∂_k) is adopted for partial derivatives of a given function with respect to k . The number of critical points N_{cp} is then defined by $(d-1)^2$. In general, for a given polynomial h in two variables x, y of degree d_x and d_y , respectively, we expect at most $d_x d_y$ critical points (Durfee et al., 1993). Thus, the computation of ψ and S_A from the solution of the ODEs (see Supplementary Appendix A2) that minimize the free energy F will yield at most $N_{cp} = 9$ critical points and at least one critical point $N_{cp} = 1$. These points include the degenerate and

nondegenerate points that follow the well-known nondegeneracy criteria, which are as follows:

$$\partial_{\psi\psi}(F(\psi, S_A)) > 0, \quad \partial_{SS}(F(\psi, S_A)) > 0, \quad (2.10)$$

$$\det \begin{bmatrix} \partial_{\psi\psi}(F(\psi, S_A)) & \partial_{\psi S}(F(\psi, S_A)) \\ \partial_{S\psi}(F(\psi, S_A)) & \partial_{SS}(F(\psi, S_A)) \end{bmatrix} \neq 0. \quad (2.11)$$

The number of critical points N_{cp} is bound by the Poincaré–Hopf index theorem (Knill, 2012). The index i_f of the gradient vector ∇f is computed based on the nondegeneracy of all critical points of f , which assigns a value of $(+1)$ to a maximum or minimum and a value of (-1) to a saddle (Durfee et al., 1993) in the following definition:

$$i_f = N_{\text{maxima}} \times (+1) + N_{\text{minima}} \times (+1) + N_{\text{saddles}} \times (-1) \\ = N_{\text{maxima}} + N_{\text{minima}} - N_{\text{saddles}}. \quad (2.12)$$

Here, the index of the free-energy polynomial of Equation 2.7 was computed as $i_F = +1$ in an area homeomorphic to a disk, which importantly puts a cap on the number of saddles N_{saddles} . Thus, from the index theorem, we conclude that saddles play a crucial role in this transformation across various temperature ranges.

2.2.2 Level-set and steepest descent

In addition to the index $i_F = +1$, the gradient vector ∇f stores the information required to compute the directional derivative of $f(x, y)$ for any direction at any point (x_i, y_i) , which provides the rate of change in f as it approaches (x_i, y_i) . This directional derivative is just the inner product of the gradient and the direction of a certain vector \mathbf{u} :

$$D_{\mathbf{u}} f(x, y) = \nabla f(x, y) \cdot \mathbf{u}(i, j). \quad (2.13)$$

The gradient then contains the direction of the greatest change of f , known as the steepest descent, or ascent, as the opposite direction that may be computed with $-\nabla f$. Contrary to this, a vector orthogonal to ∇f will point toward a zero change in f . These are vectors that lie on the tangent plane and are normal to a surface that can be constructed by the level set of the scalar-valued function $f: \mathbb{R}^n \rightarrow \mathbb{R}$. These are cross-sections of the (x, y) -frame, individually representing its different levels c and containing any real solution of $f(x, y)$.

$$\{(x, y) \in \mathbb{R}^2 \mid f(x, y) = c\}. \quad (2.14)$$

The energy landscape $F(\psi, S_A)$ is a surface whose main features are characterized by the shape of the level-set curves, the direction of the steepest descent curves, and the location and nature of the critical points. For a given set of critical point locations, the level sets and steepest descent indicate how and if local minima can be reached. For example, local minima (maxima) on the energy surface are characterized by ellipses, and the steepest descent curves are converging (diverging) splay curves (see Figure 2). This is similar to the minimum energy path (MEP) approach (Massi and Straub, 2001; Liu et al., 2022), which seeks to locate and characterize the conformation changes between chemical states based on their relationship with their characteristic energy hypersurface (Fischer and Karplus, 1992; Wang et al., 1996; Liu et al., 2022) that describes the thermodynamic equilibrium and self-assembly process.

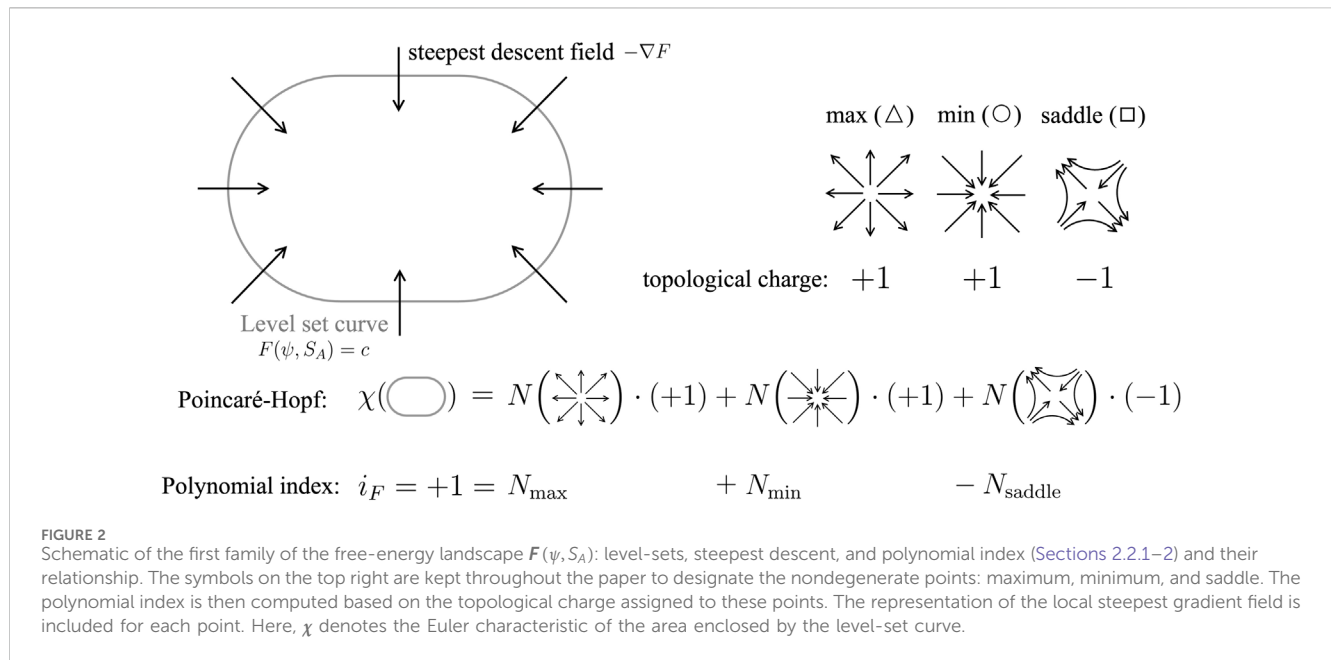


Figure 2 presents the connection between the polynomial index and the level set and steepest descent curves. By assigning topological charges to the critical points based on their nondegeneracy, the polynomial index is constructed. Each nondegenerate point is then linked to the expected local behavior of the gradient vector.

2.2.3 Lines of curvature and geodesics

The lines of curvature are computed by solving a set of equations defined by the coefficients of the first (g) and second (b) fundamental forms, as shown in Supplementary Appendix A2 (Maekawa, 1996; Farouki, 1998). The LOC have been used to describe the relationship between entropy production in membranes and interfaces (Wang et al., 2020) and the curvature of isotropic–smectic interfaces under self-organization (equilibrium) and self-assembly (dynamic) states (Vital et al., 2019) using an orthonormal network. These LOC applied to the free-energy landscape describe the change in the order parameters with respect to the arc-length s , following the principal direction of the tangent vectors (Eq. A.6) along γ : $dy/ds = \mathbf{r}_k / \|\mathbf{r}_k\|$, where γ is a line of curvature. Thus,

$$\frac{d\psi}{ds} = \eta(M - \kappa A) \quad \text{and} \quad \frac{dS_A}{ds} = -\eta(L - \kappa E), \quad (2.15)$$

or

$$\frac{d\psi}{ds} = \mu(N - \kappa G) \quad \text{and} \quad \frac{dS_A}{ds} = -\mu(M - \kappa A), \quad (2.16)$$

where κ represents the principal curvatures (κ_1, κ_2), (E, A, G), and (L, M, N) are the coefficients of the first and second fundamental forms (see Supplementary Appendix A2) and (η, μ) are non-zero coefficients defined by

$$\begin{aligned} \eta &= (E(M - \kappa A)^2 - 2A(M - \kappa A)(L - \kappa E) + G(L - \kappa E)^2)^{-1/2}, \\ \mu &= (E(N - \kappa G)^2 - 2A(M - \kappa A)(N - \kappa G) + G(M - \kappa A)^2)^{-1/2}, \end{aligned} \quad (2.17)$$

$$ds = \sqrt{E(d\psi)^2 + 2Ad\psi dS_A + G(dS_A)^2}. \quad (2.18)$$

Under our free-energy framework $F(\psi, S_A)$, the geodesic lines indicate the shortest path between two points in the thermodynamic equilibrium state (Do Carmo, 2016; Wang et al., 2020), which can also show the self-assembly path connecting the phases expected in the I-SmA energy landscape. This is similar to what is found in the analysis of the geometry of thermodynamic stable states of ideal gases (Quevedo et al., 2008). This is described by a curve with the smallest arc length connecting two points on a given surface, and it is given by the following equation (Do Carmo, 2016; Wang et al., 2020):

$$\frac{d^2 y^k}{ds^2} + \Gamma_{ij}^k \frac{dy^i}{ds} \frac{dy^j}{ds} = 0, \quad (2.19)$$

where E, A , and G are the first fundamental form coefficients, Γ_{ij}^k are the Christoffel symbols, and the geodesic curve is y^i for the i th component of the quantities that define the free-energy parametrized surface (ψ, S_A) (see Supplementary Appendix A3).

2.2.4 Casorati curvature and shape coefficient

In this section, we provide details of the Casorati curvature (C) and shape coefficient (S) given in the introduction and Figure 1 (lower left vertex). A method presented by Wang et al. (2020) redefines a thermodynamic hypersurface into a Monge shape-curvedness surface patch for the characterization of entropy production in LC membranes and interfaces. As mentioned above, in this paper, we use this methodology to describe the local geometry of the I-SmA phase transition energy landscape using a normalized shape coefficient (S) that distinguishes between three primary shapes: cup/cap (spherical), rut/ridge (cylindrical), and saddle, and the Casorati curvature (C) for the curvature magnitude measurement (Koenderink and van Doorn, 1992; Aguilar Gutierrez and Rey, 2018). This requires the reparameterization of the energy landscape $F(\psi, S_A)$ into a

Monge patch (Abbena et al., 2017) comprised of the shape coefficient (S) and Casorati curvature (C).

Classical curvature concepts, in addition to the Casorati curvature (C) and shape coefficient (S) (Wang et al., 2023a), are used in the description of the curvedness and shape, such as the (i) mean (H), (ii) deviatoric (D), and (iii) Gaussian (K) curvature (see Supplementary Appendix A2), whose information is stored in the surface gradient of the surface unit normal $-\nabla_s \mathbf{k}$, where $\nabla_s = (\mathbf{I} - \mathbf{k}\mathbf{k}) \cdot \nabla$ is the surface gradient and ∇ is the gradient operator. From this, the symmetric curvature tensor is defined as $\mathbf{b} = -\nabla_s \mathbf{k} = \kappa_1 \mathbf{e}_1 \mathbf{e}_1 + \kappa_2 \mathbf{e}_2 \mathbf{e}_2$, where (κ_1, κ_2) are its eigenvalues (see Figure 1II) characterizing the principal curvatures (Aguilar Gutierrez and Rey, 2018). The Casorati curvature is defined by $C = \sqrt{(\kappa_1^2 + \kappa_2^2)/2}$, the mean curvature by $H = (\kappa_1 + \kappa_2)/2$, the deviatoric curvature by $D = (\kappa_1 - \kappa_2)/2$, and the Gaussian curvature by $K = \kappa_1 \kappa_2$, for which the principal curvatures are assumed to follow $\kappa_1 \geq \kappa_2$ (Wang et al., 2020).

The non-dimensionality of the shape coefficient condenses information that allows it to classify the local shape into simple geometries within the normalized range $S \in [-1, +1]$. The Casorati curvature, however, quantifies how curved a surface is (Aguilar Gutierrez and Rey, 2018; Wang et al., 2020) (see Supplementary Appendix A2)

$$S = \frac{2}{\pi} \arctan\left(\frac{H}{D}\right) \quad \text{and} \quad C = \sqrt{2H^2 - K}. \quad (2.20)$$

The primary fundamental shapes are then generalized with $S = \{0, \pm 1/2, \pm 1\}$, assigning the values to a saddle (0), a rut ($-1/2$), a ridge ($+1/2$), a cup (-1), and a cap ($+1$), where the \pm sign defines if it is a concave-up (negative) or concave-down (positive) patch (see Figure 1.III). It is important to notice that these are primary shapes and a continuous spectrum is contained within the normalized parameter interval. The Casorati curvature varies within $C = [0, +\infty)$, defining a flat surface with no curvature ($C = 0$) and a curved surface ($C > 0$), respectively. Figure 1 (III) shows a schematic representation of the Casorati curvature (upper set) and the shape coefficient spectrum (lower set).

2.3 Computational methods

In this work, we sought detailed information of the phase ordering as the quenching degree increases from the highest possible temperature for the existence of the SmA phase. We found that it is possible to classify the ordering and geometry by defining three quenching regimes: shallow quench, middle quench, and deep quench (with three temperatures corresponding to each of them, as listed in Table 2). As the degree of quenching increased, the isotropic phase lost stability, while the SmA gained stability, and a number of saddle nodes and supercritical bifurcations emerged at the boundaries of these quench regimes. Given the nonlinearities and OP couplings in the energy density and the differential geometry quantities, high-performance computational techniques were developed, applied, and tested when exact data were available, and high fidelity was demonstrated. Stability, accuracy, and dispersion criteria were implemented according to the standard numerical methods. The validation of our results was established using previous studies (Urban et al., 2005; Abukhdeir and Rey, 2008;

Coles and Strazielle, 2011). As mentioned in the introduction, a well-characterized member of the n-cyanobiphenyl family (12CB) has been chosen as the study case for its I-SmA transition behavior (see Supplementary Appendix A4).

The calculation sequence was as follows: (1) level sets and steepest descent curves were obtained with (i) the complete solution of Equation 2.7 at different temperatures for the phases in Equation 2.8 using the stability criteria in Section 2.2.1, which categorizes the critical points that are bound by the number N_{cp} and the I-SmA LdG free-energy index i_F in Equation 2.12 and (ii) the orthogonal pair of steepest descent and level-set curves from Section 2.2.2. (2) Geodesics/LOC calculations in Section 2.2.3 involved coupled nonlinear second-order stiff ODEs, which are numerically unstable depending on the step size taken, especially the system of equations defined by the discretization of the geodesics (Equation 2.19) (see Supplementary Appendix A2). Boundary conditions must be provided to solve the geodesic. We used the shooting method, which requires the definition of a starting point, chosen in our case study to be the stable isotropic/smectic A phases. In addition to equation stiffness, it is also worth noting that the model is arc-length parametrized, meaning that the arc length was computed for every step. In the LOC case, the sets of Equations 2.15–2.16 while seeming analogous, are in reality distinct instances of the principal directions that depend on the arc length. The sign of the proceeding direction at a given point $(\psi_n, S_{A,n})$ must be adjusted according to the local surface geometry, meaning that the system solved was switched from one to another depending on the maximum and minimum principal curvatures (κ_1, κ_2) (Farouki, 1998; Wang et al., 2020). For this, we followed a very robust algorithm developed for computing LOC (Maekawa, 1996; Farouki, 1998), which generates a pair of orthogonal curves at $(\psi_n, S_{A,n})$ following the criterion: Equation 2.15 is solved if $|L - \kappa E| \geq |N - \kappa G|$, and Equation 2.16 is used otherwise. Then, a curvature network was constructed with the orthogonal LOC by solving the ODE system at a point $(\psi_n, S_{A,n})$ along the length defined by the energy landscape for a sufficiently small step-size that balances out resolution, solution stability, and computational time. (3) For obtaining the Casorati and shape coefficient in Section 2.2.4, we computed the first fundamental forms and the principal curvatures of the free-energy landscape (see Supplementary Appendix A2).

3 Results and discussion

In this paper, we present a complete description and characterization of the energy landscape of the isotropic–smectic A transition using a two-non-conserved order parameter version of the Landau–de Gennes model for the following reasons: (i) the kinetics of phase transformations for non-conserved order parameters is dependent on stable, metastable, and unstable critical points of free energy (Tuckerman and Bechhoefer, 1992; De Luca and Rey, 2003; De Luca and Rey, 2004); this point is briefly elaborated at the beginning of Section 2.2; (ii) in the case of phase transformation by propagating fronts, where a stable phase replaces an unstable phase, non-monotonic ordering structures appear at the interface due to the presence of various critical points (Tuckerman and Bechhoefer, 1992); (iii) in the case of drop formation of a stable

phase in a metastable matrix, one can expect thin film-like layers with intermediate degrees of order between the droplet phase and matrix (Abukhdeir and Rey, 2009a); (iv) interfacial processes as in a LC drop couple shape-bulk and surface structure-size due to orientational order (Rey, 2000; Rey and Denn, 2002; Rey, 2004a; Rey, 2004b; Rey, 2006). In view of these phenomena, we do not neglect metastable and unstable ordering states, such as nematic or plastic (density wave) phases, as previously suggested (Saunders et al., 2007). How exactly they will manifest themselves under nucleation and growth and spinodal transformation of the isotropic phase into the SmA phase will be examined in future work and is outside the scope of this paper.

3.1 Quench zones and critical points and their stability

Figure 3 presents the orientational and positional order phase diagram as a function of temperature T obtained by solving Equation 2.7 with 12CB material parameters (Supplementary Appendix A4). Subscripts on the OPs denote stable (s), unstable (u), and metastable (m); superscripts denote larger (+) and smaller (−) values. The line style (full, dashed, and dotted) identifies the phase (see Eq. 2.8). The figure frames the three quenches (see Table 2) delimited by key temperatures: the deep quench for $T < T_{SD}$ (light blue), the middle quench for $T_{SD} < T < T_{NG}$ (light purple), and the shallow quench for $T < T_{IL}$ (light red). Here, T_{SD} is the spinodal decomposition temperature, T_{NG} is the nucleation and growth temperature, and T_{IL} is the maximum temperature for the existence of any smectic order phase, as explained below. Using quenching measures, we can characterize the critical point features and determine whether they are stable, unstable, or metastable, depending on the quench zone. To fully characterize the nature of all the sources and sinks at the nematic axis ($S_A > 0, \psi = 0$), we include $\psi < 0$ solutions. These non-physical solutions ($S_A > 0, \psi < 0$) arise from the mirror symmetry of the free energy $F(S_A, \psi) = F(S_A, -\psi)$ but assist in characterizing transitions and bifurcations that occur at the $S_A = 0$ axis. In describing and classifying results, we focus on the I-SmA transition, and the quench depth refers to a temperature decrease from the highest temperature (T_{IL}) at which the metastable SmA arises. Thus, reference to nucleation and growth mode, NG, indicates the temperature interval in which the isotropic (SmA) phase is metastable (stable), and when referring to spinodal decomposition, SD, the isotropic (SmA) phase is unstable (stable). The challenges regarding the location of the critical points at a given quench, their stability, and the other possible states when considering the entirety of the points, which were introduced at the beginning of the paper, are addressed below.

The phases in the deep quench (light blue region in Figure 2) to the spinodal decomposition region are the following:

- $S_{A,s}^+, \psi_s^+$ stable SmA black, continuous lines.
- Iso_u unstable isotropic, red-dotted line.
- $S_{A,u}^-, \psi_u^-$ unstable nematic/smectic, black, dashed lines.
- N_u^+, N_u^- unstable nematic, blue, dashed lines.
- ψ_u^+, ψ_u^- unstable smectic, gray, dash-dotted lines.

- P_m^+, P_m^- metastable plastic crystal, purple, dash-dotted lines.

Here, the SD region exhibits an unstable isotropic state and a stable SmA. In addition, we find a metastable plastic region. This region exists for $T < T_{SD} = 330.6$ K. Thus, we expect that quenching an isotropic phase into the spinodal region will transform the phase into a stable SmA phase, but the presence of unstable smectic and metastable plastic crystal states introduces complexities to the energy landscape.

The phases in the middle quench (light purple region in Figure 2) to the nucleation and growth region are the following:

- $S_{A,s}^+, \psi_s^+$ stable SmA, black, continuous lines.
- Iso_m metastable isotropic, red-dotted line.
- $S_{A,u}^-, \psi_u^-$ unstable nematic/smectic, black, dashed lines.
- N_u^+, N_u^- unstable nematic, blue, dashed line.
- ψ_u^+, ψ_u^- unstable smectic, gray, dash-dotted line.

In the ND region, the isotropic state is metastable and SmA is stable, as in the SD region, in addition to the unstable smectic and nematic phases. However, the density wave is no longer present as it vanishes at the temperature T_{SD} , and the isotropic phase becomes metastable. This region exists $T_{SD} = 330.6$ K $< T < T_{NG} = 331.3$ K. Thus, we expect that quenching an isotropic phase into the NG region will transform the phase into a stable SmA phase by droplet growth.

The phases in the shallow quench (light red region in Figure 2) are the following:

- $S_{A,m}^+, \psi_m^+$ metastable SmA, black, continuous lines
- Iso_s stable isotropic, red-dotted line.
- $S_{A,u}^-, \psi_u^-$ unstable nematic, black, dashed line.
- ψ_u^+, ψ_u^- unstable smectic, gray, dash-dotted line.

At shallow quenches, the isotropic phase is now stable, while SmA is only metastable. In addition, the unstable smectic state remains, but the nematic loop closes and vanishes at the temperature T_{NG} . This region is then defined by $T_{NG} = 331.3$ K $< T < T_{IL} = 331.85$ K. Quenching from the NG triggers a phase transition at temperature T_I , as obtained with the solution of Equation 2.7 for a temperature at which $F = F_0$; thus, a temperature higher than the isotropic limit T_{IL} will lead to a disordered state.

The deep quench is characterized by the strong stability and presence of the expected smectic A phase and by a supercritical bifurcation (Oswald and Pieranski, 2005a) or plastic loop since it belongs to the metastable plastic crystal phase, where mirror symmetry is broken at the temperature T_{SD} . The nematic order effect is seen in the orientational order parameter diagram, with the presence of the nematic loop in the deep- and middle-quench zones. This marks the entrance of the shallow quench and the stability change of the SmA phase. A summary of these key temperatures and regions is given in Table 1.

The computed energy landscape has a critical root population that decreases exactly as predicted by the polynomial index theorem (Eq. 2.12; Figure 2) as the temperature increases. This is summarized in Table 2, where the number of nondegenerate points is included along with their type and the index value for each quench zone (see (2.12)).

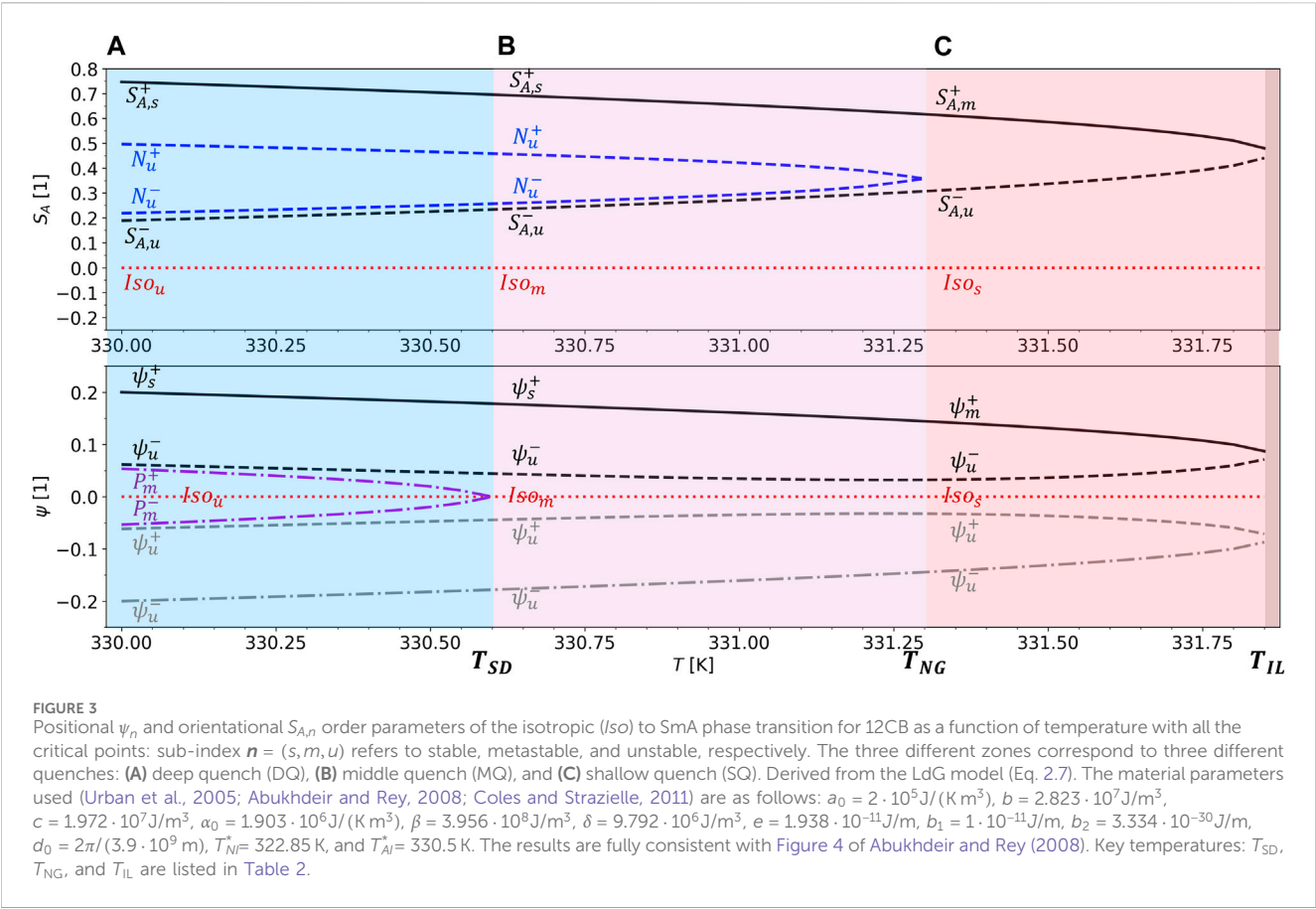
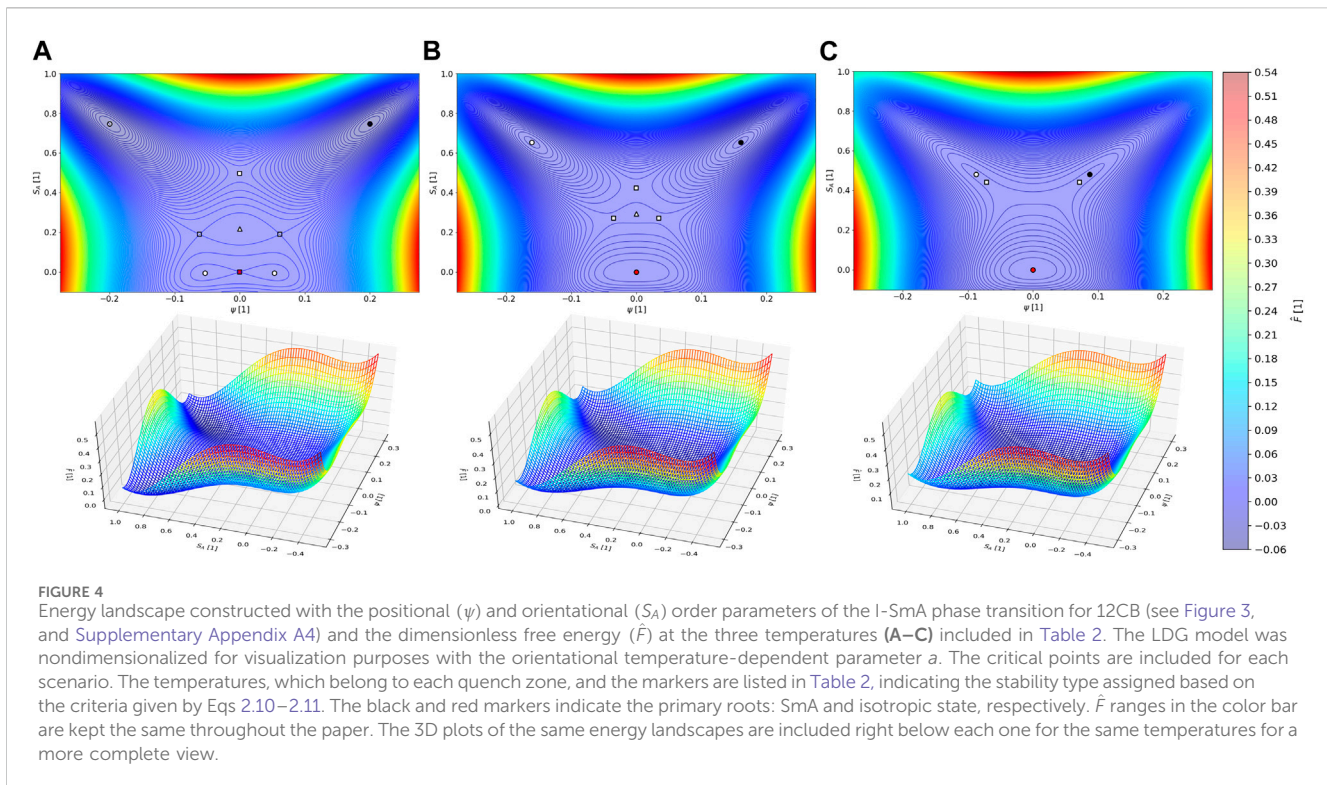


TABLE 1 Summary of stable, unstable, and metastable states in each quench zone and their key temperatures as presented in Figure 2.

	Deep Quench (DQ): Spinodal Decomposition for the Isotropic phase.	Middle Quench (MQ): Nucleation and Growth for the Isotropic phase.	Shallow Quench (SQ): Limit for the Isotropic phase.	Zero quench
Primary roots	Stable smectic A Unstable isotropic	Stable smectic A Metastable isotropic	Metastable smectic A Stable isotropic	Stable isotropic
Secondary roots	Metastable plastic crystal Unstable nematic Unstable smectic A	Unstable nematic	NA	NA
Transition temperature	$T_{SD} = 330.6\text{ K}$	$T_{NG} = T_t = 331.3\text{ K}$	$T_{IL} = 331.85\text{ K}$	

TABLE 2 Number and types of critical points on the phase diagram for different temperatures and their indexes; the three cases presented in Figure 2 correspond to the three quench zones; and one for the complete isotropic phase transition. The symbol style used for each of them is kept constant throughout the paper. Numerical results are in exact agreement with the polynomial index theorem (Eq. 2.12).

T [K]	Maxima	Minima	Number of saddles	Index i_F	Zone
A-330	1	4	4	1	Deep quench (spinodal decomposition, SD)
B-331	1	3	3	1	Middle quench (nucleation and growth, NG)
C-331.85	0	3	2	1	Shallow quench
$T > T_{IL}$	0	1	0	1	
Symbol in Figure 3	Δ	\bigcirc	\square		



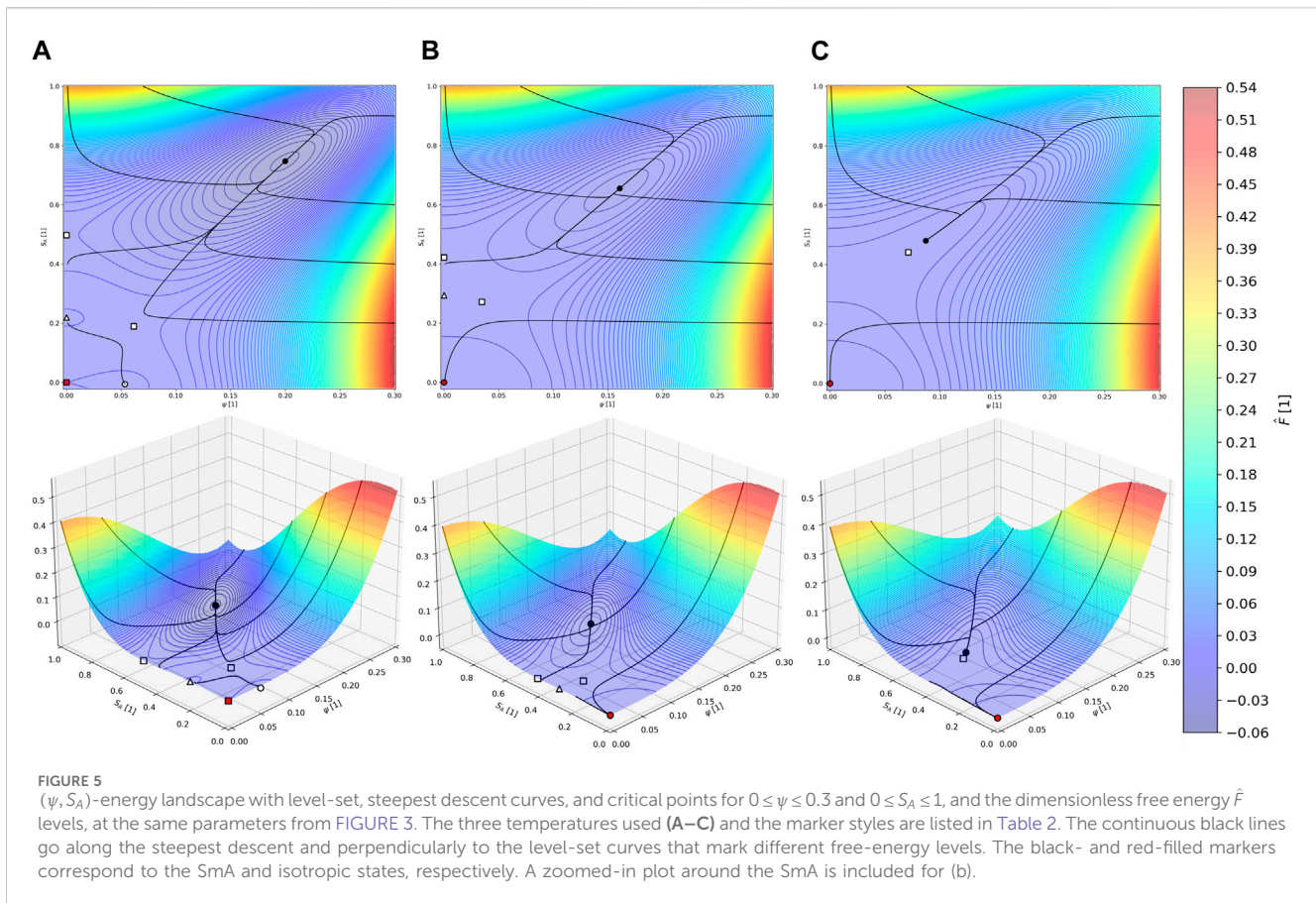
The bounds in Equations 2.10–2.11 provide stability boundaries that do not necessarily mean a phase transition line but present the possible real physical phases that can be displayed within that range given the first-order nature of this transition (Mukherjee et al., 2001). Thus, the phase transition line was found by looking for a metastability–stability exchange of the I-SmA phases using level sets and computing the temperature at which both phases present the same energy level. This temperature, T_t , happened to be around the limit at which the nematic unstable loop vanished, going from deep quench (DQ) to middle quench (MQ), as seen in Figure 2, agreeing with the experimental transition temperature of 331.3 K (Coles and Strazielle, 2011).

Figure 4 represents the $\hat{F}(\psi, S_A)$ dimensionless free-energy landscape 2D projection for the LdG model using the parameters in Figure 2, with its corresponding 3D energy landscape at a given temperature. We have expanded the x-axis to negative values to emphasize the mirror symmetry along the positional order. The level-set curves have been included with all the critical points at three different temperatures in Table 2, which are representative of each quench zone. As quench depth decreases (temperature increases), the critical point population density decreases ($N_{cp} \downarrow$), which corresponds to the merging and vanishing of the nondegenerate points, as seen in Figure 2. Increasing T from the spinodal region, the plastic loop eventually converges at a supercritical bifurcation (Han and Rey, 1993; Rey, 1995) at T_{SD} , which is a process that replaces two minima (+2) and one saddle (−1) with a single minimum (+1). Entering the NG quench region with three saddles and four nodes (i.e., maximum or minimum), a further increase in T eventually leads to saddle-node bifurcation (Rey, 1995), with the elimination of a nematic

saddle and a node. The shallow quench now has three minima and two saddles, which, after another saddle-node bifurcation of smectic phases, eventually leads to a planar surface with no order. It is noteworthy that the sequence of saddle number elimination as T increases and order decreases is multi-stepwise: $4 \rightarrow 3 \rightarrow 2 \rightarrow 0$. Likewise, the sequence of local minima elimination as T increases and order multi-stepwise decreases is $4 \rightarrow 3 \rightarrow 3 \rightarrow 1$. On the other hand, the elimination of the maxima follows a single step: $1 \rightarrow 1 \rightarrow 0 \rightarrow 0$. This shows that for shallow quench, local maxima play no role, and for deep quench, saddles and minima are equal in number.

3.2 Level-set curves and steepest descent lines

Figure 5 presents the level-set curves and the steepest descent lines (see Section 2.2.2), including the critical points projected on the dimensionless energy surface $\hat{F}(\psi, S_A)$ for the three quench regimes listed in Table 1. The blue (red) region corresponds to lower (higher) energy. It is seen that the steepest descent and level-set curves are members of an orthogonal family, where the level-set curves indicate a constant free-energy value and the steepest descent presents a path leading to primary roots that come from the minimization of the LdG model. The pair of roots (isotropic and smectic A phases) are divided by a set of maximums, minima, and saddles that discretely disappear as the quench depth decreases. In the deep-quench region, (A) the main feature is the family of elliptical rings around the stable SmA state (black dot), whose largest axes are oriented toward the



unstable phases. The level sets identify the nematic saddle and nematic maximum as well as the metastable plastic root. The principal steepest descent line connects the unstable smectic (white square) with the stable isotropic state (black dot) and defines a collecting manifold with nearly horizontal, constant S_A values. In the middle quench, nucleation, and growth, (B) the region of elliptical trajectories surrounding the SmA phase moves toward the isotropic state, causing the horizontal band of steepest descent lines to narrow. Furthermore, the steepest descent inverted L shows how energy states near the energetically high region end at the isotropic state (red dot). In (C), the metastability of SmA is shown by a lack of elliptical trajectories and the stability of the isotropic state.

In partial summary, the level-sets/steepest descent lines show the main features of the energy landscape; the number, location, and type of critical points; and the basin of attraction of SmA under spinodal and nucleation and growth conditions.

3.3 Lines of curvature and geodesics

[Figure 6](#) shows the 2D projection and 3D plot of the LOC network on the energy landscape $\hat{F}(\psi, S_A)$ generated with the algorithm described in [Section 2](#). It consists of orthogonal curve pairs that follow the minimum and maximum curvatures (cyan and magenta, respectively) at a given point on the surface. It also includes the primary roots shown in [Table 1](#).

The maximum curvature (magenta) lines on the top left and bottom right closely follow the energy contours, corresponding to high S_A –low ψ and *vice versa*, while along the downward diagonal, they funnel out consistently in accordance with the energy landscape. The minimum curvature (cyan) lines form a set of nearly parallel L -lines, which are nearly vertical along the nematic axis and nearly horizontal close to the smectic axis. This is consistent with the fact that most critical points are around the diagonal region, as shown in [Figure 5](#). Furthermore, since the energy surface envelope is roughly a concave-up expanding cylinder with flat edges, it follows that we must find circular curvature lines (as in the circular lines of a cylinder) and diverging straight lines (like in an expanding cone).

[Figure 7](#) shows the projected geodesic lines of the energy landscape, computed by solving [Equation 2.19](#) for the temperatures belonging to the three quench zones listed in [Table 1](#) with the method provided in [Supplementary Appendix A2](#). The geodesic family origin is the isotropic state that changes stability from unstable (A) to metastable (B) to stable (C), as seen in [Figure 4](#). The lines minimize the path length and are therefore significant directions for phase changes. These lines show an expanding funnel whose centerline (purple) connects the two primary I-SmA phases. This line, which resembles the MEP introduced in [Section 2.2.2](#), follows the minimum-curvature tendency designated in [Figure 6](#) by the magenta lines. In addition, this phase-connecting geodesic becomes straighter as the depth quench is increased, achieving essentially a straight line

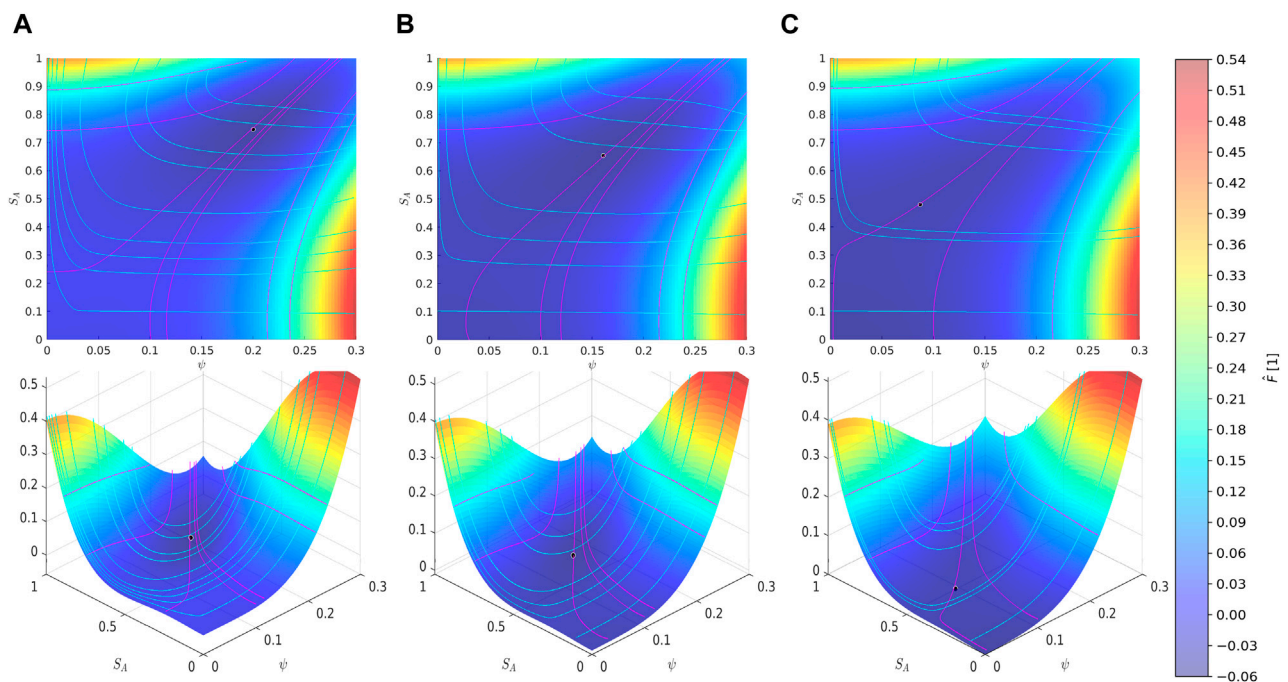


FIGURE 6

Lines of curvature projected on the (ψ, S_A) -energy landscape at the same three temperatures (A–C) and with the marker styles listed in Table 2. The parameters used are listed in Figure 3. The circular marker presents the SmA state at those temperatures. The cyan and magenta orthogonal network of LOC corresponds to the minimum κ_1 and maximum κ_2 curvatures, respectively.

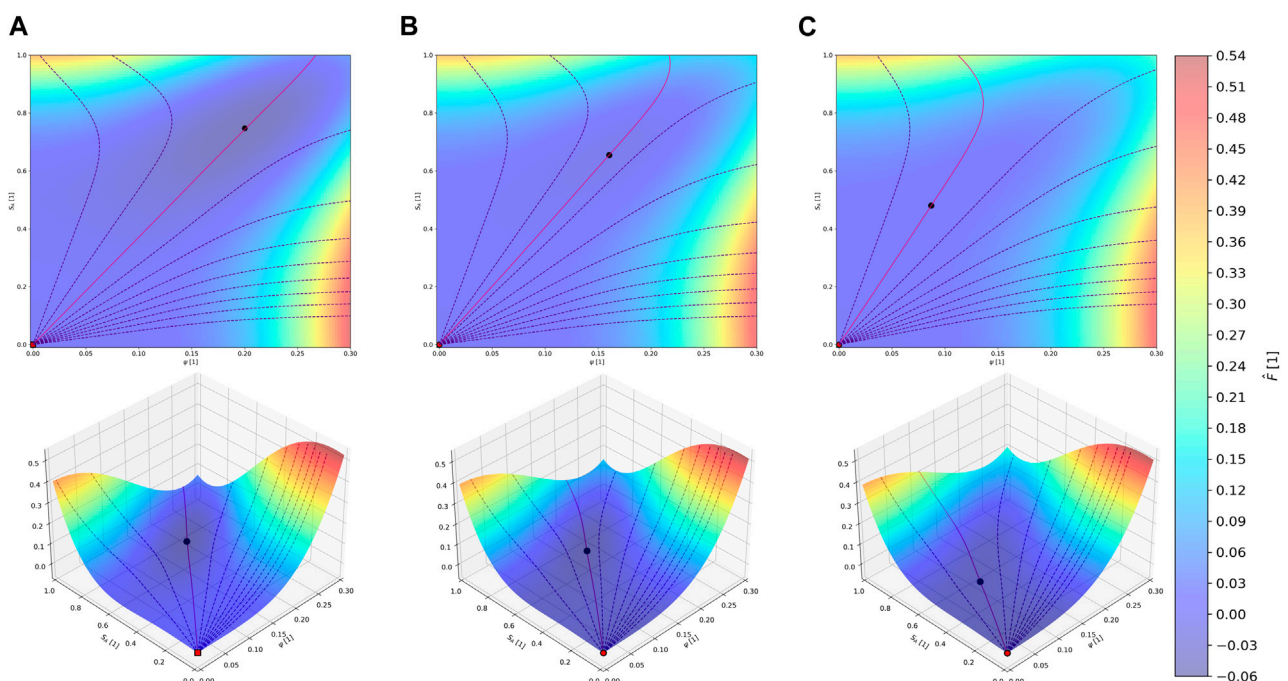


FIGURE 7

Geodesics superimposed on the (ψ, S_A) -energy landscape at the same three temperatures (A–C) and with the marker styles listed in Table 2. The parameters used are listed in Figure 3. The circular marker presents the SmA state at those temperatures. All lines, dashed and continuous, are geodesics; however, the continuous line connects both the isotropic and SmA primary roots.

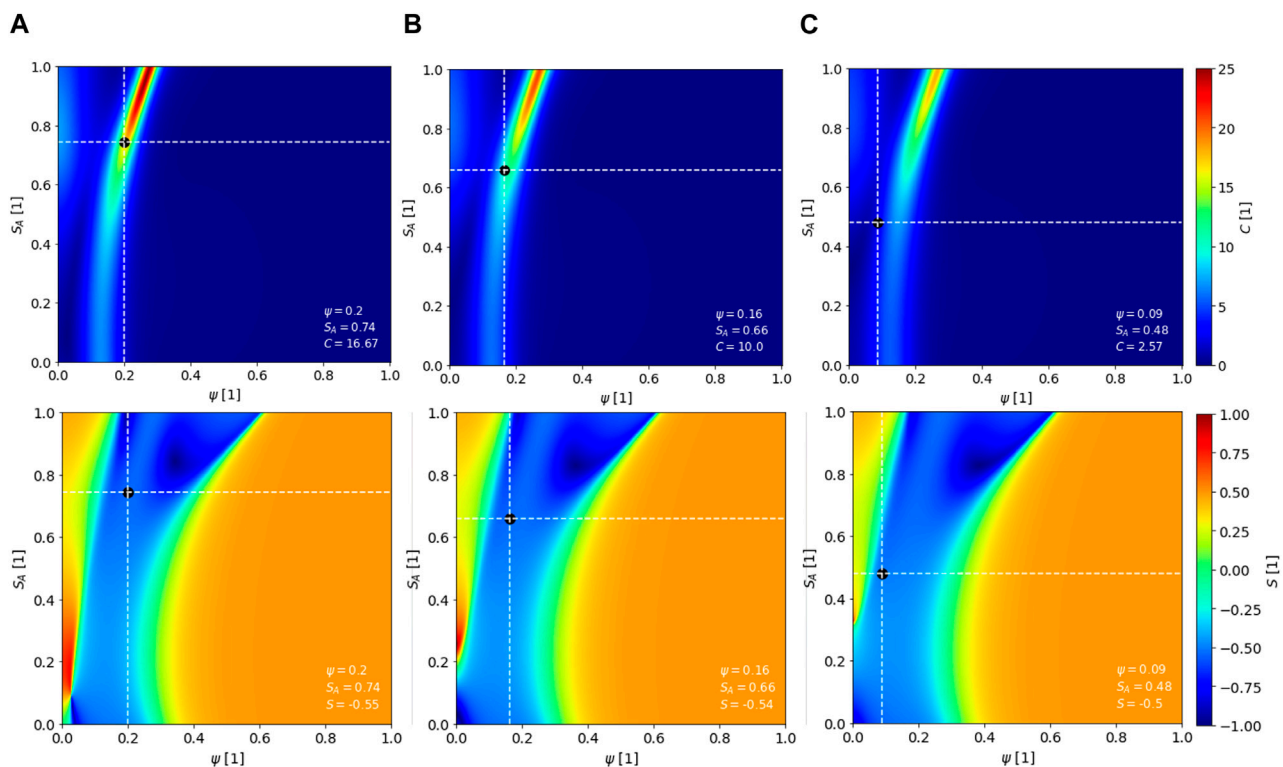


FIGURE 8

Casorati curvature C (upper set) and shape S coefficient (lower set) heatmaps as a function of ψ and S_A at the same three temperatures (A–C) and with the marker styles listed in Table 2. The parameters used are listed in Figure 3. The coordinates on the bottom-right corner correspond to the SmA phase (black dot) with their Casorati and shape coefficient values at each temperature.

in (A), and it starts to bend in the direction of a greater change in energy as the shallow quench (C) is reached. Another important observation is that the change in shape, direction, and bending are reflected in the LOC as the quench regime changes, as opposed to what the geodesics show in this figure.

3.4 Shape coefficient and Casorati curvature

Figure 8 shows the Casorati (C) curvature (top) and shape (S) coefficient (bottom) heatmaps as a function of the OPs (ψ, S_A) coordinates. The Casorati curvature and shape coefficient were computed using Equation 2.20 and the definitions in Supplementary Appendix A2 at the temperatures listed in Table 1 for the three representative quench zones. The primary root that corresponds to the most stable phase at each temperature was included in the bottom-right corner of each plot containing the Casorati curvature and shape coefficient values at those coordinates.

The Casorati curvature presents major activity along the zone where the critical points move as the temperature varies. It can be noted that the Casorati curvature decreases as the quench depth decreases, which follows a trend toward the isotropic transition, where both order parameters are zero and the energy surface is planar and, hence, $C = 0$. The crucial feature of the computed $C = C(\psi, S_A)$ is the presence of a bent vertical tubular region of higher C values in a matrix of low C . Within this high C tube, the curvedness increases as we move toward and beyond the SmA phase in the SD

and NG zones. In the shallow quench, the increase is attenuated as the energy surface evolves toward planarity. Interestingly, an approximate scaling for the high C tube is a power law $S_A \approx (\psi - 0.1)^n$; $n \approx 0.01$; more accurate fittings require parameters, but the important point is that smectic ordering produces a large increase in orientational ordering along the high C tube. Furthermore, if we compare Figure 8A (top right) with the energy landscape of Figure 5 (bottom left) in the spinodal mode, we see that the axis of the high C tube follows the steepest descent line that starts at the metastable plastic crystal and traverses the stable SmA phase to end at the higher energy states ($\psi \approx 0.3, S_A \approx 1$). Hence, the C tube is another distinguishing feature of the energy landscape.

We now search for the distinguished feature(s) of the shape S coefficient. Figure 8 (bottom) shows that the shape coefficient associated with the local minima at each temperature does not reach $S = -1$ or a perfect ideal cup shape, as previously observed from the findings of Wang et al. (2020). The reason behind this is the energy surface anisotropy that originates from the LdG polynomial structure (Eq. 2.7), as observed already in non-circular level-set curves (see elliptical curves surrounding minima in Figure 4). In addition, we noticed that for stability, the shape coefficient follows a trend, assigning the local minima to a surface lying between a cup (-1) and a rut (-0.5) shape; for completeness, we note that the intermediate value ($S = -0.75$) is usually denoted as a trough. This shape condition of local minima ($-1 < S < -0.5$) corresponds to a shape with small and large principal curvatures. This behavior is also

supported by the LOC network seen in Figure 6. In more quantitative detail, Figure 8 shows that the correspondence between the OPs of the local minimum and the energy surface shape is as follows:

- Spinodal decomposition mode: $S(\psi = 0.2, S_A = 0.74) = -0.55$, and the shape is between a rut and a trough.
- Nucleation and growth mode: $S(\psi = 0.16, S_A = 0.66) = -0.54$, and the shape is between a rut and a trough.
- Shallow quench mode: $S(\psi = 0, S_A = 0) = -0.84$, and the shape is between a trough and a cup.

Figure 8 (bottom) shows another distinguishing feature of the shape index, with the blue concave-up (ridge) domain describing a bent channel that narrows and widens as the order increases. The outer red domains indicate unstable or concave-down (cap) states, and the green boundaries are saddle-like shapes. Hence, the shape landscape for smectic phases follows the previously established rules (Wang et al., 2020) of shape coexistence, where moving from left to right in each panel from Figure 8 (bottom), we find the following:

$$S = 0.75 \rightarrow S = 0.5 \rightarrow S = 0 \rightarrow S = -0.5 \rightarrow S = -0.75 \rightarrow S = -0.5 \rightarrow S = 0 \rightarrow S = 0.5 \rightarrow S = 0.75,$$

concave down
saddle
concave-up
saddle
concave down

where saddles are needed to separate minima from maxima, which is in agreement with the polynomial theorem for critical point index $i_F = +1$ given in Table 2 and Equation 2.12.

Figure 9 takes the geodesics presented in Figure 7 and projects them on the Casorati and shape coefficient heatmaps from Figure 8 for each temperature according to the three quenching zones listed in Table 1.

The main features gleaned from the Casorati-I-SmA geodesic correlations from Figure 9 (top) are the following:

- The intersection of the geodesic with the high curvedness Casorati tube occurs at high S_A values but is eventually lost because the slope of the geodesic increases with T , while the Casorati tube bends to the right. For the intersection of the geodesic and tube, we need a geodesic slope m given by the following equation:

$$S_{A,C} \approx (\psi - 0.1)^{0.01};$$

$$S_{A,G} \approx m(T)\psi \rightarrow S_{A,C} = S_{A,G} \rightarrow (\psi - 0.1)^{0.01}$$

$$= m(T)\psi \rightarrow m(T) = \frac{(\psi - 0.1)^{0.01}}{\psi},$$

where the subscripts (C, G) denote the Casorati and geodesics. This is only possible in the deep and intermediate quenches.

- The I-SmA geodesics for NG and SD modes largely avoid the higher Casorati curvatures, indicating paths of lower curvatures.

The main features gleaned from shape coefficient-I-SmA geodesic correlations from Figure 9 (bottom) are as follows:

- The geodesic path remains well-contained in the shape index channel comprehending ruts and trough concave-up shapes, except at low OP and low-temperature values, where saddle-like (green areas close to the origin) and concave-down (red areas close to the origin) shapes arise.
- The development of SmA droplets that may form from an intermediate quench into the NG mode starts with a $S \approx -0.54$ in the smectic phase and ends with $S \approx -0.84$ in the isotropic state; therefore, the geodesic path to drop formation involves relatively modest shape configurational changes.

Figure 10 integrates the curve families on the energy landscape corresponding to the SD quench regime ($T = 330$ K), the stable SmA phase (black dot), and an unstable isotropic phase. It presents the steepest descent lines, LOC, and geodesics on the (ψ, S_A) -energy landscape. The linear diagonal geodesic connecting the isotropic (unstable)-to-smectic A (stable) phases partitions the rut and trough region and serves as an attracting manifold for maximal LOC and curves of the steepest descent; the congruence of these three lines indicates why, at this temperature, SmA is the attractor. On the bottom right high-energy area, the congruence is now between minimal LOC, curves of steepest descent, and curved geodesics, indicating a repelling landscape.

4 Conclusion

In this paper, we developed, implemented, and tested a novel computational geometrical method that complements classical liquid crystal phase transition modeling for the complex case of two-order-parameter symmetry breaking. This approach uses complementary geometric schemes to link the thermodynamic energy landscape of the isotropic-to-smectic A liquid crystal direct phase transition with novel soft-matter geometric metrics such as the Casorati curvature and shape coefficient. We summarize the results and their significance as follows:

1. A previously presented and comprehensive study of the Landau-de Gennes free-energy model (De Gennes and Prost, 1993; Pleiner et al., 2000; Larin, 2004; Oswald and Pieranski, 2005b; Donald et al., 2006; Biscari et al., 2007; Abukhdeir and Rey, 2009b; Nandi et al., 2012; Izzo and De Oliveira, 2019) for the direct isotropic-to-smectic A transition with well-known material properties (Urban et al., 2005; Abukhdeir and Rey, 2008; Coles and Strazielle, 2011) formed the basis of the theory and computational modeling characterization of phase ordering with two non-conserved order parameters.
2. The Landau free-energy landscape was obtained using explicit Monge surface parametrization as a function of orientational and positional orders, allowing the deployment of, in a simple manner, differential geometry calculations (Eq. 2.7)
3. The index polynomial theorem (Eq. 2.12) for the number of critical roots as a function of quench depth revealed the importance of saddle roots in the spinodal and nucleation and growth region; without the knowledge of parametric free-energy coefficient data, the theorem shows that the maximum number of critical roots is 3×3 since the free energy is a quartic polynomial in the two order parameters.

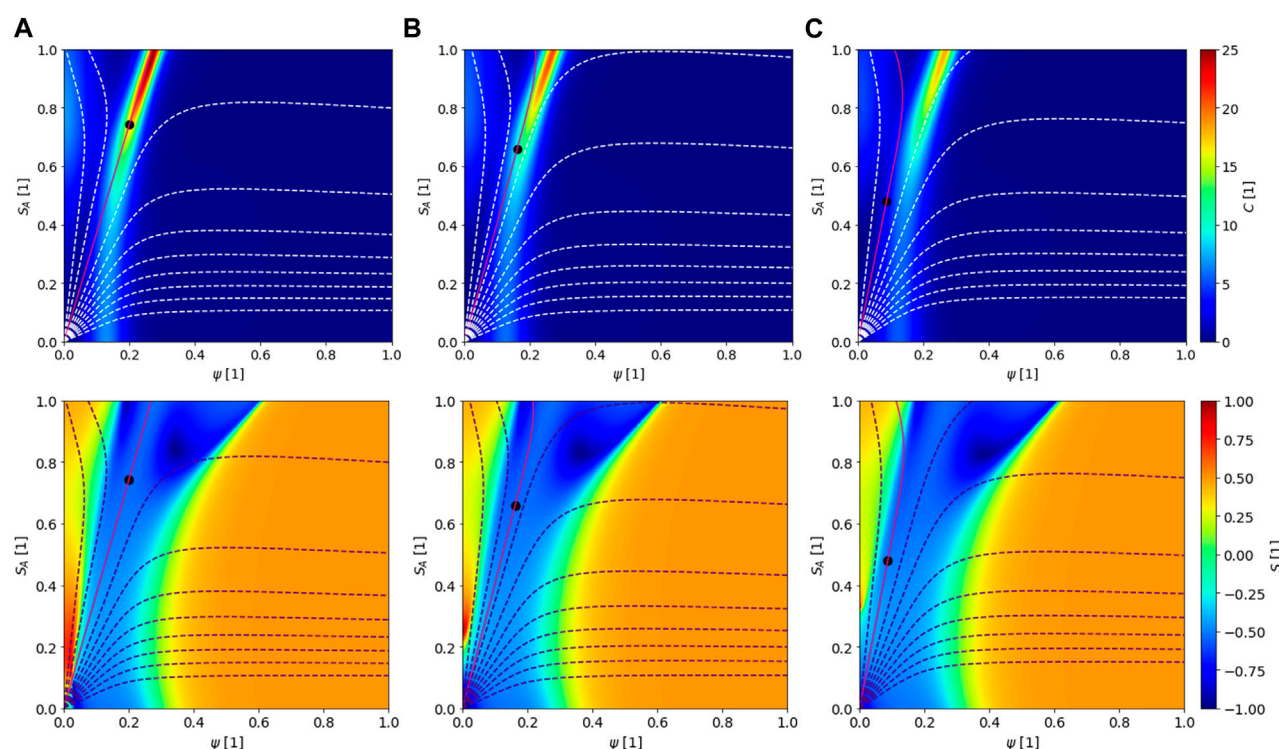


FIGURE 9

Geodesics projected on the Casorati curvature C (upper set) and shape S coefficient (lower set) heatmaps from Figure 8 as a function of ψ and S_A at the same three temperatures (A–C) and with the marker styles listed in Table 2. The parameters used are listed in Figure 3. The circular marker presents the SmA phase at those temperatures. The geodesics are the same from Figure 7, with different color scheme for visualization purposes. The continuous purple lines are geodesics that connect both the isotropic and SmA phases.

- Using high-performance computing and high-fidelity numerical methods for nonlinear algebraic and differential equations, the following curve families were calculated (Sections 3.2 and 3.3): level-set-steepest descent and geodesic-principal curvatures. These special curves revealed the location of critical points already predicted by the index theorem, directions of small and large curvatures, and minimal length connections between isotropic and smectic roots. In particular, linear geodesics joining isotropic and smectic states in nucleation and growth and spinodal quenches revealed phase transformation paths. The level-set curves around stable roots were elliptical, indicating anisotropy originating from the Landau free-energy polynomial.
- The emergence of metastable plastic crystals at deep quenches and unstable nematic states at deep and intermediate quenches was characterized, and their annihilation through supercritical and saddle-node bifurcation was captured, re-emphasizing results from the index polynomial theorem. The relevance of the nematic or plastic order at the interfaces of smectic A drops in an isotropic matrix was pointed out.
- Previously presented measures of shape and curvedness (Casorati) in soft-matter materials were used (Section 3.4) to characterize the energy landscape with purely geometric measures instead of order parameter coordinates. The calculations were integrated with the curve families, showing consistency and revealing that the Casorati landscape is a bent, higher-curved tube embedded in

a low-curvedness matrix; the tube is well-fitted with a power law function. The smectic A root resides inside this tube and moves downward as the temperature increases. The shape coefficient landscape is characterized by a wide channel of concave-up shapes separated from an area of concave-down shapes by saddle-like interfaces, which is in agreement with shape coexistence phenomena.

- Plotting all the curve families (point 4 above) in the energy landscape, we find that at large quench, the isotropic-to-smectic A geodesic is an attractor for maximal lines of curvature and curves of the steepest descent, explaining the stability of the smectic A state.

The combination of parameter-free predictions from polynomial theorems with the computational geometry of the free-energy landscape contributes to the evolving understanding and characterization of the isotropic-to-smectic A transition, which is of high interest to biological colloidal liquid crystals, such as in the precursors to the mussel byssus (Renner-Rao et al., 2019; Harrington and Fratzl, 2021; Jehle et al., 2021) through droplet nucleation/growth and colloidal impingement. We demonstrated that the presence of two non-conserved order parameters creates challenges in equilibrium spatially homogeneous simulations, but how time-dependent processes such as droplet growth resolve the couplings of shape–size–structure–interface remains to be elucidated in future work by building on the present results and methods.

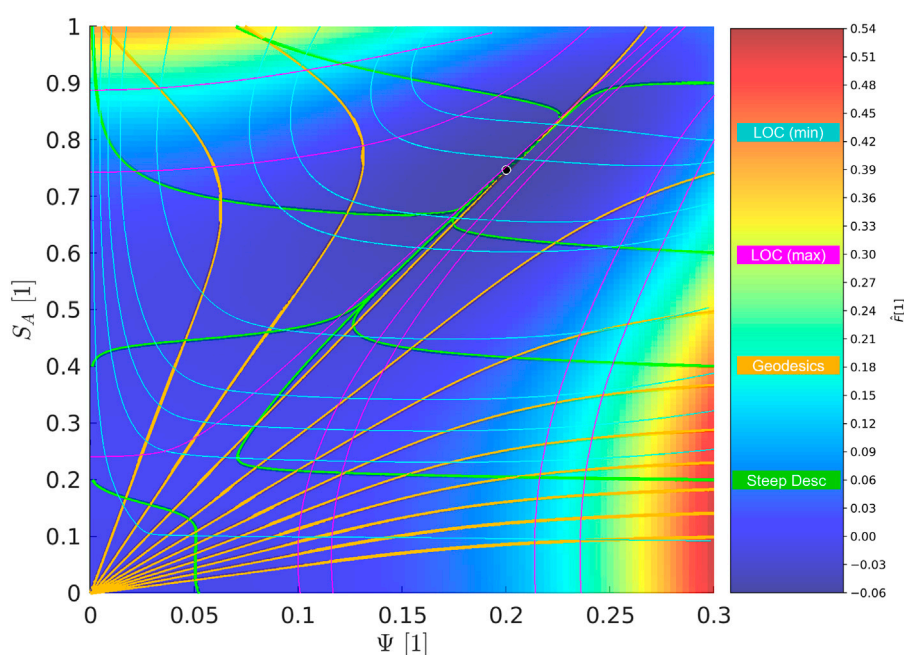


FIGURE 10

(ψ, S_A)-energy landscape for temperature (A) as listed in Table 2, integrating the steepest descent lines (green), LOC (cyan-min and magenta-max), and geodesics (orange) curves. The black dot represents the stable primary root, SmA phase.

Data availability statement

Data related to this work will be made available by request to the authors. Requests to access the datasets should be directed to ADR, alejandro.rey@mcgill.ca.

Author contributions

DZ: writing–original draft, conceptualization, data curation, formal analysis, investigation, methodology, software, validation, visualization, and writing–review and editing. ZW: conceptualization, writing–review and editing, validation, and methodology. ND: conceptualization, supervision, and writing–review and editing. MH: conceptualization, supervision, and writing–review and editing. AR: conceptualization, validation, writing–review and editing, formal analysis, funding acquisition, project administration, resources, and supervision.

Funding

The author(s) declare that financial support was received for the research, authorship, and/or publication of this article. This work was supported by the Fonds de Recherche du Québec (FRQNT) (2021-PR-284991) and the Natural Science and Engineering Research Council of Canada (NSERC) (#223086). Author DUZC thanks Consejo Nacional de Humanidades, Ciencia y Tecnología (CONAHCYT) (853563), and McGill Engineering Doctoral Award (MEDA) scholarships for financial support.

Acknowledgments

The authors acknowledge Digital Research Alliance of Canada (ID 4700) for computational resources and technical support.

Conflict of interest

The authors declare that the research was conducted in the absence of any commercial or financial relationships that could be construed as a potential conflict of interest.

Publisher's note

All claims expressed in this article are solely those of the authors and do not necessarily represent those of their affiliated organizations, or those of the publisher, the editors, and the reviewers. Any product that may be evaluated in this article, or claim that may be made by its manufacturer, is not guaranteed or endorsed by the publisher.

Supplementary material

The Supplementary Material for this article can be found online at: <https://www.frontiersin.org/articles/10.3389/frsfm.2024.1359128/full#supplementary-material>

References

- Abbena, E., Salamon, S., and Gray, A. (2017). *Modern differential geometry of curves and surfaces with Mathematica*. China: CRC Press.
- Abukhdeir, N. M. (2009). Growth, dynamics, and texture modeling of the lamellar smectic-A liquid crystalline transition. *Doctor of Philosophy*. Canada: McGill University.
- Abukhdeir, N. M., and Rey, A. D. (2008). Simulation of spherulite growth using a comprehensive approach to modeling the first-order isotropic/smectic-A mesophase transition. *arXiv Prepr. arXiv:0807.4525*. doi:10.48550/arXiv.0807.4525
- Abukhdeir, N. M., and Rey, A. D. (2009a). Metastable nematic preordering in smectic liquid crystalline phase transitions. *Macromolecules* 42, 3841–3844. doi:10.1021/ma900796b
- Abukhdeir, N. M., and Rey, A. D. (2009b). Nonisothermal model for the direct isotropic/smectic-A liquid-crystalline transition. *Langmuir* 25, 11923–11929. doi:10.1021/la9015965
- Abukhdeir, N. M., and Rey, A. D. (2009c). Shape-dynamic growth, structure, and elasticity of homogeneously oriented spherulites in an isotropic/smectic-A mesophase transition. *Liq. Cryst.* 36, 1125–1137. doi:10.1080/02678290902878754
- Aguilar Gutierrez, O. F., and Rey, A. D. (2018). Extracting shape from curvature evolution in moving surfaces. *Soft Matter* 14, 1465–1473. doi:10.1039/c7sm02409f
- Bellini, T., Clark, N. A., and Link, D. R. (2002). Isotropic to smectic A phase transitions in a porous matrix: a case of multiporous phase coexistence. *J. Phys. Condens. Matter* 15, S175–S182. doi:10.1088/0953-8984/15/1/322
- Berent, K., Cartwright, J. H. E., Checa, A. G., Pimentel, C., Ramos-Silva, P., and Sainz-Diaz, C. I. (2022). Helical microstructures in molluscan biomineralization are a biological example of close packed helices that may form from a colloidal liquid crystal precursor in a twist-bend nematic phase. *Phys. Rev. Mater.* 6, 105601. doi:10.1103/physrevmaterials.6.105601
- Biscari, P., Calderer, M. C., and Terentjev, E. M. (2007). Landau-de Gennes theory of isotropic-nematic-smectic liquid crystal transitions. *Phys. Rev. E Stat. Nonlin Soft Matter Phys.* 75, 051707. doi:10.1103/physreve.75.051707
- Blinov, L. M. (2011). *Structure and properties of liquid crystals*. Dordrecht: Springer.
- Bowick, M. J., Kinderlehrer, D., Menon, G., and Radin, C. (2017). Mathematics and materials, *American mathematical soc.*
- Bradley, P. A. (2019). On the physicochemical control of collagen fibrillogenesis and biomineralization. *Doctor of Philosophy*. USA: Northeastern University.
- Bukharina, D., Kim, M., Han, M. J., and Tsukruk, V. V. (2022). Cellulose nanocrystals' assembly under ionic strength variation: from high orientation ordering to a random orientation. *Langmuir* 38, 6363–6375. doi:10.1021/acs.langmuir.2c00293
- Bunsell, A. R., Joannès, S., and Thionnet, A. (2021). *Fundamentals of fibre reinforced composite materials*. Germany: CRC Press.
- Cai, A., Abdali, Z., Saldanha, D. J., Aminzare, M., and Dorval Courchesne, N.-M. (2023). Endowing textiles with self-repairing ability through the fabrication of composites with a bacterial biofilm. *Sci. Rep.* 13, 11389. doi:10.1038/s41598-023-38501-2
- Chahine, G., Kityk, A. V., Démarest, N., Jean, F., Knorr, K., Huber, P., et al. (2010). Collective molecular reorientation of a calamitic liquid crystal (12CB) confined in alumina nanochannels. *Phys. Rev. E* 82, 011706. doi:10.1103/physreve.82.011706
- Coles, H. J., and Strazielle, C. (2011). The order-disorder phase transition in liquid crystals as a function of molecular structure. I. The alkyl cyanobiphenyls. *Mol. Cryst. Liq. Cryst.* 55, 237–250. doi:10.1080/00268947908069805
- Collings, P. J. (1997). *Phase structures and transitions in thermotropic liquid crystals handbook of liquid crystal research*.
- Collings, P. J., and Goodby, J. W. (2019). *Introduction to liquid crystals: chemistry and physics*. Germany: Crc Press.
- Collings, P. J., and Hird, M. (2017). *Introduction to liquid crystals chemistry and physics*. Germany: CRC Press.
- Copic, M., and Mertelj, A. (2020). Q-tensor model of twist-bend and splay nematic phases. *Phys. Rev. E* 101, 022704. doi:10.1103/physreve.101.022704
- Das, A. K., and Mukherjee, P. K. (2009). Phenomenological theory of the direct isotropic to hexatic-B phase transition. *J. Chem. Phys.* 130, 054901. doi:10.1063/1.3067425
- de Gennes, P. G. (2007). Some remarks on the polymorphism of smectics. *Mol. Cryst. Liq. Cryst.* 21, 49–76. doi:10.1080/15421407308083313
- de Gennes, P.-G., and Prost, J. (1993). *The physics of liquid crystals*. Oxford: Oxford University Press.
- de Luca, G., and Rey, A. D. (2004). Chiral front propagation in liquid-crystalline materials: formation of the planar monodomain twisted plywood architecture of biological fibrous composites. *Phys. Rev. E* 69, 011706. doi:10.1103/physreve.69.011706
- de Luca, G., and Rey, A. D. (2006). Dynamic interactions between nematic point defects in the spinning extrusion duct of spiders. *J. Chem. Phys.* 124, 144904. doi:10.1063/1.2186640
- de Luca, G., and Rey, A. (2003). Monodomain and polydomain helicoids in chiral liquid-crystalline phases and their biological analogues. *Eur. Phys. J. E* 12, 291–302. doi:10.1140/epje/i2002-10164-3
- Demirci, N., and Holland, M. A. (2022). Cortical thickness systematically varies with curvature and depth in healthy human brains. *Hum. Brain Mapp.* 43, 2064–2084. doi:10.1002/hbm.25776
- Demus, D., Goodby, J. W., Gray, G. W., Spiess, H. W., and Vill, V. (2008a). *Handbook of liquid crystals*.
- Demus, D., Goodby, J. W., Gray, G. W., Spiess, H. W., and Vill, V. (2008b). *Handbook of liquid crystals, volume 3: high molecular weight liquid crystals*. USA: John Wiley and Sons.
- Demus, D., Goodby, J. W., Gray, G. W., Spiess, H. W., and Vill, V. (2011). *Handbook of liquid crystals, volume 2A: low molecular weight liquid crystals I: calamitic liquid crystals*. USA: John Wiley and Sons.
- Deng, F., Dang, Y., Tang, L., Hu, T., Ding, C., Hu, X., et al. (2021). Tendon-inspired fibers from liquid crystalline collagen as the pre-oriented bioink. *Int. J. Biol. Macromol.* 185, 739–749. doi:10.1016/j.ijbiomac.2021.06.173
- Dierking, I., and al-Zangana, S. (2017). Lyotropic liquid crystal phases from anisotropic nanomaterials. *Nanomater. (Basel)* 7, 305. doi:10.3390/nano7100305
- Dilisi, G. A. (2019). In *An introduction to liquid crystals*. Editor J. J. DELUCA (New York: Morgan and Claypool Publishers).
- Do Carmo, M. P. (2016). *Differential geometry of curves and surfaces: revised and updated*. second edition. New York: Courier Dover Publications.
- Dogic, Z., and Fraden, S. (2001). Development of model colloidal liquid crystals and the kinetics of the isotropic-smectic transition. *Philosophical Trans. R. Soc. a-Mathematical Phys. Eng. Sci.* 359, 997–1015. DOI, M. 1981. doi:10.1098/rsta.2000.0814
- Doi, M. 2022 Molecular dynamics and rheological properties of concentrated solutions of rodlike polymers in isotropic and liquid crystalline phases. *J. Polym. Sci. Polym. Phys. Ed.* 19, 229–243. doi:10.1002/pol.1981.180190205
- Donald, A. M., Windle, A. H., and Hanna, S. (2006). *Liquid crystalline polymers*. Cambridge: Cambridge University Press.
- Durfee, A., Kronenfeld, N., Munson, H., Roy, J., and Westby, I. (1993). Counting critical points of real polynomials in two variables. *Am. Math. Mon.* 100, 255–271. doi:10.2307/2324459
- Farouki, R. T. (1998). On integrating lines of curvature. *Comput. Aided Geom. Des.* 15, 187–192. doi:10.1016/s0167-8396(97)00022-8
- Fischer, S., and Karplus, M. (1992). Conjugate peak refinement: an algorithm for finding reaction paths and accurate transition states in systems with many degrees of freedom. *Chem. Phys. Lett.* 194, 252–261. doi:10.1016/0009-2614(92)85543-j
- Garti, N., Somasundaran, P., and Mezzenga, R. (2012). *Self-assembled supramolecular architectures: lyotropic liquid crystals*. USA: John Wiley and Sons.
- Golmohammadi, M., and Rey, A. D. (2009). Thermodynamic modelling of carbonaceous mesophase mixtures. *Liq. Cryst.* 36, 75–92. doi:10.1080/02678290802666218
- Golmohammadi, M., and Rey, A. D. (2010). Structural modeling of carbonaceous mesophase amphotropic mixtures under uniaxial extensional flow. *J. Chem. Phys.* 133, 034903. doi:10.1063/1.3455505
- Gorkunov, M., Osipov, M., Lagerwall, J., and Giesselmann, F. (2007). Order-disorder molecular model of the smectic-A–smectic-C phase transition in materials with conventional and anomalously weak layer contraction. *Phys. Rev. E* 76, 051706. doi:10.1103/physreve.76.051706
- Gudimalla, A., Thomas, S., and Zidanšek, A. (2021). Phase behaviour of n-CB liquid crystals confined to controlled pore glasses. *J. Mol. Struct.* 1235, 130217. doi:10.1016/j.molstruc.2021.130217
- Gurevich, S., Soule, E., Rey, A., Reven, L., and Provatas, N. (2014). Self-assembly via branching morphologies in nematic liquid-crystal nanocomposites. *Phys. Rev. E* 90, 020501. doi:10.1103/physreve.90.020501
- Gurin, P., Odriozola, G., and Varga, S. (2021). Enhanced two-dimensional nematic order in slit-like pores. *New J. Phys.* 23, 063053. doi:10.1088/1367-2630/ac05e1
- Han, J. Q., Luo, Y., Wang, W., Zhang, P. W., and Zhang, Z. F. (2015). From microscopic theory to macroscopic theory: a systematic study on modeling for liquid crystals. *Archive Ration. Mech. Analysis* 215, 741–809. doi:10.1007/s00205-014-0792-3
- Han, W., and Rey, A. (1993). Supercritical bifurcations in simple shear flow of a non-aligning nematic: reactive parameter and director anchoring effects. *J. Newt. fluid Mech.* 48, 181–210. doi:10.1016/0377-0257(93)80070-r
- Harrington, M. J., and Fratzl, P. (2021). Natural load-bearing protein materials. *Prog. Mater. Sci.* 120, 100767. doi:10.1016/j.pmatsci.2020.100767
- Hawkins, R. J., and April, E. W. (1983). “Liquid crystals in living tissues,” in *Advances in liquid crystals*. Editor G. H. BROWN (Germany: Elsevier).

- Hormann, K., and Zimmer, J. (2007). On Landau theory and symmetric energy landscapes for phase transitions. *J. Mech. Phys. Solids* 55, 1385–1409. doi:10.1016/j.jmps.2007.01.004
- Idziak, S. H. J., Koltover, I., Davidson, P., Ruths, M., Li, Y., Israelachvili, J. N., et al. (1996). Structure under confinement in a smectic-A and lyotropic surfactant hexagonal phase. *Phys. B Condens. Matter* 221, 289–295. doi:10.1016/0921-4526(95)00939-6
- Izzo, D., and de Oliveira, M. J. (2019). Landau theory for isotropic, nematic, smectic-A, and smectic-C phases. *Liq. Cryst.* 47, 99–105. doi:10.1080/02678292.2019.1631968
- Jackson, K., Peivandi, A., Fogal, M., Tian, L., and Hosseinioust, Z. (2021). Filamentous phases as building blocks for bioactive hydrogels. *ACS Appl. Bio Mater.* 4, 2262–2273. doi:10.1021/acsabm.0c01557
- Jákli, A., and Saupe, A. (2006). *One-and two-dimensional fluids: properties of smectic, lamellar and columnar liquid crystals*. New York: CRC Press.
- Jehle, F., Priemel, T., Strauss, M., Fratzl, P., Bertinetti, L., and Harrington, M. J. (2021). Collagen pentablock copolymers form smectic liquid crystals as precursors for mussel byssus fabrication. *ACS Nano* 15, 6829–6838. doi:10.1021/acsnano.0c10457
- Khadem, S. A., and Rey, A. D. (2021). Nucleation and growth of cholesteric collagen tactoids: a time-series statistical analysis based on integration of direct numerical simulation (DNS) and long short-term memory recurrent neural network (LSTM-RNN). *J. Colloid Interface Sci.* 582, 859–873. doi:10.1016/j.jcis.2020.08.052
- Khan, B. C., and Mukherjee, P. K. (2021). Isotropic to smectic-A phase transition in taper-shaped liquid crystal. *J. Mol. Liq.* 329, 115539. doi:10.1016/j.molliq.2021.115539
- Knight, D., and Vollrath, F. (1999). Hexagonal columnar liquid crystal in the cells secreting spider silk. *Tissue Cell* 31, 617–620. doi:10.1054/tice.1999.0076
- Knill, O. (2012). A graph theoretical Poincaré-Hopf theorem. *arXiv Prepr. arXiv:1201.1162*. doi:10.48550/arXiv.1201.1162
- Koenderink, J. J., and van Doorn, A. J. (1992). Surface shape and curvature scales. *Image Vis. Comput.* 10, 557–564. doi:10.1016/0262-8856(92)90076-f
- Kyrylyuk, A. V., Anne van de Haar, M., Rossi, L., Wouterse, A., and Philipse, A. P. (2011). Isochoric ideality in jammed random packings of non-spherical granular matter. *Soft Matter* 7, 1671–1674. doi:10.1039/c0sm00754d
- Lagerwall, J. P. (2016). An introduction to the physics of liquid crystals. *Fluids, Colloids Soft Mater. Introd. Soft Matter Phys.*, 307–340. doi:10.1002/9781119220510.ch16
- Larin, E. S. (2004). Phase diagram of transitions from an isotropic phase to nematic and smectic (uniaxial, biaxial) phases in liquid crystals with achiral molecules. *Phys. Solid State* 46, 1560–1568. doi:10.1134/1.1788795
- Lenoble, J., Campidelli, S., Maringa, N., Donnio, B., Guillon, D., Yevlampieva, N., et al. (2007). Liquid–crystalline Janus-type fullerodendrimers displaying tunable smectic–columnar mesomorphism. *J. Am. Chem. Soc.* 129, 9941–9952. doi:10.1021/ja071012o
- Li, C.-Z., Matsuo, Y., and Nakamura, E. (2009). Luminescent bow-tie-shaped decaaryl[60]fullerene mesogens. *J. Am. Chem. Soc.* 131, 17058–17059. doi:10.1021/ja907908m
- Liu, B., Besseling, T. H., Hermes, M., Demirörs, A. F., Imhof, A., and van Blaaderen, A. (2014). Switching plastic crystals of colloidal rods with electric fields. *Nat. Commun.* 5, 3092. doi:10.1038/ncomms4092
- Liu, X., Chen, H., and Ortner, C. (2022). Stability of the minimum energy path. *arXiv Prepr. arXiv:2204.00984*. doi:10.1007/s00211-023-01391-7
- Maekawa, T. (1996). *Computation of shortest paths on free-form parametric surfaces*.
- Manolakis, I., and Azhar, U. (2020). Recent advances in mussel-inspired synthetic polymers as marine antifouling coatings. *Coatings* 10, 653. doi:10.3390/coatings10070653
- Massi, F., and Straub, J. E. (2001). Energy landscape theory for Alzheimer's amyloid β -peptide fibril elongation. *Proteins Struct. Funct. Bioinforma.* 42, 217–229. doi:10.1002/1097-0134(20010201)42:2<217::aid-prot90>3.0.co;2-n
- Matthews, J. A., Wnek, G. E., Simpson, D. G., and Bowlin, G. L. (2002). Electrospinning of collagen nanofibers. *Biomacromolecules* 3, 232–238. doi:10.1021/bm015533u
- Milette, J., Toader, V., Soulé, E. R., Lennox, R. B., Rey, A. D., and Reven, L. (2013). A molecular and thermodynamic view of the assembly of gold nanoparticles in nematic liquid crystal. *Langmuir* 29, 1258–1263. doi:10.1021/la304189n
- Miller, W. L. (1925). The method of willard gibbs in chemical thermodynamics. *Chem. Rev.* 1, 293–344. doi:10.1021/cr60004a001
- Mohieddin Abukhdeir, N., and Rey, A. D. (2008a). Defect kinetics and dynamics of pattern coarsening in a two-dimensional smectic-A system. *New J. Phys.* 10, 063025. doi:10.1088/1367-2630/10/6/063025
- Mohieddin Abukhdeir, N., and Rey, A. D. (2008b). Modeling the isotropic/smectic-C tilted lamellar liquid crystalline transition.
- Mukherjee, P. K. (2014). Isotropic to smectic-A phase transition: a review. *J. Mol. Liq.* 190, 99–111. doi:10.1016/j.molliq.2013.11.001
- Mukherjee, P. K. (2021). Advances of isotropic to smectic phase transitions. *J. Mol. Liq.* 340, 117227. doi:10.1016/j.molliq.2021.117227
- Mukherjee, P. K., Pleiner, H., and Brand, H. R. (2001). Simple Landau model of the smectic-A-isotropic phase transition. *Eur. Phys. J. E* 4, 293–297. doi:10.1007/s101890170111
- Nandi, B., Saha, M., and Mukherjee, P. K. (2012). Landau theory of the direct smectic-A to isotropic phase transition. *Int. J. Mod. Phys. B* 11, 2425–2432. doi:10.1142/s0217979297001234
- Nesrullajev, A. (2022). Optical refracting properties, birefringence and order parameter in mixtures of liquid crystals: direct smectic A – Isotropic and reverse isotropic – smectic A phase transitions. *J. Mol. Liq.* 345, 117716. doi:10.1016/j.molliq.2021.117716
- Oh, C. S. (1977). Induced smectic mesomorphism by incompatible nematogens. *Mol. Cryst. Liq. Cryst.* 42, 1–14. doi:10.1080/15421407708084491
- Oswald, P., and Pieranski, P. (2005a). *Nematic and cholesteric liquid crystals: concepts and physical properties illustrated by experiments*. China: CRC Press.
- Oswald, P., and Pieranski, P. (2005b). *Smectic and columnar liquid crystals*.
- Paget, J., Alberti, U., Mazza, M. G., Archer, A. J., and Shendruk, T. N. (2022). Smectic layering: Landau theory for a complex-tensor order parameter. *J. Phys. A Math. Theor.* 55, 354001. doi:10.1088/1751-8121/ac80df
- Palfy-Muhoray, P. (1999). Dynamics of filaments during the isotropic-smectic A phase transition. *J. Nonlinear Sci.* 9, 417–437. doi:10.1007/s003329900075
- Petrov, A. G. (2013). Flexoelectricity in lyotropics and in living liquid crystals. *Flexoelectricity Liq. Cryst. theory, Exp. Appl. World Sci.* doi:10.1142/9781848168008_0007
- Pevnyi, M. Y., Selinger, J. V., and Sluckin, T. J. (2014). Modeling smectic layers in confined geometries: order parameter and defects. *Phys. Rev. E Stat. Nonlin Soft Matter Phys.* 90, 032507. doi:10.1103/physrev.90.032507
- Picken, S. J. (1990). Orientational order in aramid solutions determined by diamagnetic susceptibility and birefringence measurements. *Macromolecules* 23, 464–470. doi:10.1021/ma00204a019
- Pikin, S. A. (1991). *Structural transformations in liquid crystals*.
- Pleiner, H., Mukherjee, P. K., and Brand, H. R. (2000). Direct transitions from isotropic to smectic phases. *Proc. Freiburger Arbeitstagung Flüssigkristalle*, P59.
- Popa-Nita, V. (1999). Statics and kinetics at the nematic-isotropic interface in porous media. *Eur. Phys. J. B-Condensed Matter Complex Syst.* 12, 83–90. doi:10.1007/s100510050981
- Popa-Nita, V., and Sluckin, T. J. (2007). *Waves at the nematic-isotropic interface: nematic-non-nematic and polymer-nematic mixtures*. Netherlands: Springer, 253–267.
- Pouget, E., Grelet, E., and Lettinga, M. P. (2011). Dynamics in the smectic phase of stiff viral rods. *Phys. Rev. E Stat. Nonlin Soft Matter Phys.* 84, 041704. doi:10.1103/physrev.84.041704
- Quevedo, H., Quevedo, M. N., and Sánchez, A. (2022). Geometrothermodynamics of van der Waals systems. *J. Geometry Phys.* 176, 104495. doi:10.1016/j.geomphys.2022.104495
- Quevedo, H., Sánchez, A., Taj, S., and Vázquez, A. (2011). Phase transitions in geometrothermodynamics. *General Relativ. Gravit.* 43, 1153–1165. doi:10.1007/s10714-010-0996-2
- Quevedo, H., Sánchez, A., and Vázquez, A. (2008). Invariant geometry of the ideal gas. *arXiv Prepr. arXiv:0811.0222*.
- Renner-Rao, M., Clark, M., and Harrington, M. J. (2019). Fiber Formation from liquid crystalline collagen vesicles isolated from mussels. *Langmuir* 35, 15992–16001. doi:10.1021/acs.langmuir.9b01932
- Rey, A. D. (1995). Bifurcational analysis of the isotropic-discotic nematic phase transition in the presence of extensional flow. *Liq. Cryst.* 19, 325–331. doi:10.1080/02678299508031988
- Rey, A. D. (2000). Viscoelastic theory for nematic interfaces. *Phys. Rev. E* 61, 1540–1549. doi:10.1103/physrev.61.1540
- Rey, A. D. (2004a). Interfacial thermodynamics of polymeric mesophases. *Macromol. theory simulations* 13, 686–696. doi:10.1002/mats.200400030
- Rey, A. D. (2004b). Thermodynamics of soft anisotropic interfaces. *J. Chem. Phys.* 120, 2010–2019. doi:10.1063/1.1635357
- Rey, A. D. (2006). Mechanical model for anisotropic curved interfaces with applications to surfactant-laden Liquid–liquid crystal interfaces. *Langmuir* 22, 219–228. doi:10.1021/la051974d
- Rey, A. D. (2010). Liquid crystal models of biological materials and processes. *Soft Matter* 6, 3402–3429. doi:10.1039/b921576j
- Rey, A. D., and Denn, M. M. (2002). Dynamical phenomena in liquid-crystalline materials. *Annu. Rev. Fluid Mech.* 34, 233–266. doi:10.1146/annurev.fluid.34.082401.191847
- Rey, A. D., and Herrera-Valencia, E. E. (2012). Liquid crystal models of biological materials and silk spinning. *Biopolymers* 97, 374–396. doi:10.1002/bip.21723

- Rey, A. D., Herrera-Valencia, E. E., and Murugesan, Y. K. (2013). Structure and dynamics of biological liquid crystals. *Liq. Cryst.* 41, 430–451. doi:10.1080/02678292.2013.845698
- Salamonczyk, M., Zhang, J., Portale, G., Zhu, C., Kentzinger, E., Gleeson, J. T., et al. (2016). Smectic phase in suspensions of gapped DNA duplexes. *Nat. Commun.* 7, 13358. doi:10.1038/ncomms13358
- Sato, C., Takeda, T., Dekura, S., Suzuki, Y., Kawamata, J., and Akutagawa, T. (2023). Chiral plastic crystal of solid-state dual rotators. *Cryst. Growth and Des.* 23, 5889–5898. doi:10.1021/acs.cgd.3c00495
- Saunders, K., Hernandez, D., Pearson, S., and Toner, J. (2007). Disorder to order: de Vries behavior from a Landau theory for smectic phases. *Phys. Rev. Lett.* 98, 197801. doi:10.1103/physrevlett.98.197801
- Schimming, C. D., Viñals, J., and Walker, S. W. (2021). Numerical method for the equilibrium configurations of a Maier-Saupe bulk potential in a Q-tensor model of an anisotropic nematic liquid crystal. *J. Comput. Phys.* 441, 110441. doi:10.1016/j.jcp.2021.110441
- Selinger, J. V. (2016). *Introduction to the theory of soft matter: from ideal gases to liquid crystals*. Germany: Springer.
- Sonnet, A. M., and Virga, E. G. (2012). *Dissipative ordered fluids: theories for liquid crystals*. Germany: Springer Science and Business Media.
- Soulé, E. R., Lavigne, C., Reven, L., and Rey, A. D. (2012a). Multiple interfaces in diffusional phase transitions in binary mesogen-nonmesogen mixtures undergoing metastable phase separations. *Phys. Rev. E* 86, 011605. doi:10.1103/physreve.86.011605
- Soulé, E. R., Millette, J., Reven, L., and Rey, A. D. (2012b). Phase equilibrium and structure formation in gold nanoparticles—nematic liquid crystal composites: experiments and theory. *Soft Matter* 8, 2860–2866. doi:10.1039/c2sm07091j
- Soulé, E. R., Reven, L., and Rey, A. D. (2012c). Thermodynamic modelling of phase equilibrium in nanoparticles—nematic liquid crystals composites. *Mol. Cryst. Liq. Cryst.* 553, 118–126. doi:10.1080/15421406.2011.609447
- Soule, E. R., and Rey, A. D. (2011). A good and computationally efficient polynomial approximation to the Maier-Saupe nematic free energy. *Liq. Cryst.* 38, 201–205. doi:10.1080/02678292.2010.539303
- Soule, E. R., and Rey, A. D. (2012). Modelling complex liquid crystal mixtures: from polymer dispersed mesophase to nematic nanocolloids. *Mol. Simul.* 38, 735–750. doi:10.1080/08927022.2012.669478
- Stewart, I. W. (2019). *The static and dynamic continuum theory of liquid crystals: a mathematical introduction*. Germany: Crc Press.
- Tortora, M., and Jost, D. (2021). Morphogenesis and self-organization of persistent filaments confined within flexible biopolymeric shells. *arXiv Prepr.* doi:10.48550/arXiv.2107.02598
- Tuckerman, L. S., and Bechhoefer, J. (1992). Dynamical mechanism for the formation of metastable phases: the case of two nonconserved order parameters. *Phys. Rev. A* 46, 3178–3192. doi:10.1103/physreva.46.3178
- Turek, D. E., Simon, G. P., and Tiu, C. (2020). “Relationships among rheology, morphology, and solid-state properties in thermotropic liquid-crystalline polymers,” in *Handbook of applied polymer processing technology* (Germany: CRC Press).
- Urban, S., Przedmojski, J., and Czub, J. (2005). X-ray studies of the layer thickness in smectic phases. *Liq. Cryst.* 32, 619–624. doi:10.1080/02678290500116920
- Viney, C. (2004). Self-assembly as a route to fibrous materials: concepts, opportunities and challenges. *Curr. Opin. Solid State and Mater. Sci.* 8, 95–101. doi:10.1016/j.cossms.2004.04.001
- Vitral, E., Leo, P. H., and Vinals, J. (2019). Role of Gaussian curvature on local equilibrium and dynamics of smectic-isotropic interfaces. *Phys. Rev. E* 100, 032805. doi:10.1103/physreve.100.032805
- Vitral, E., Leo, P. H., and Vinals, J. (2020). Model of the dynamics of an interface between a smectic phase and an isotropic phase of different density. *Phys. Rev. Fluids* 5, 073302. doi:10.1103/physrevfluids.5.073302
- Waite, J. H., and Harrington, M. J. (2022). Following the thread: Mytilus mussel byssus as an inspired multi-functional biomaterial. *Can. J. Chem.* 100, 197–211. doi:10.1139/cjc-2021-0191
- Wales, D. J. (2018). Exploring energy landscapes. *Annu. Rev. Phys. Chem.* 69, 401–425. doi:10.1146/annurev-physchem-050317-021219
- Wang, H. Y., Wang, Y. Z., Tsakalakos, T., Semenovskaya, S., and Khachatryan, A. G. (1996). Indirect nucleation in phase transformations with symmetry reduction. *Philosophical Mag. a-Physics Condens. Matter Struct. Defects Mech. Prop.* 74, 1407–1420. doi:10.1080/01418619608240732
- Wang, Z., Servio, P., and Rey, A. D. (2020). Rate of entropy production in evolving interfaces and membranes under astigmatic kinematics: shape evolution in geometric-dissipation landscapes. *Entropy* 22, 909. doi:10.3390/e22090909
- Wang, Z., Servio, P., and Rey, A. D. (2022a). Complex nanowrinkling in chiral liquid crystal surfaces: from shaping mechanisms to geometric statistics. *Nanomaterials* 12, 1555. doi:10.3390/nano12091555
- Wang, Z., Servio, P., and Rey, A. D. (2023a). Geometry-structure models for liquid crystal interfaces, drops and membranes: wrinkling, shape selection and dissipative shape evolution. *Soft Matter* 19, 9344–9364. doi:10.1039/d3sm01164j
- Wang, Z., Servio, P., and Rey, A. D. (2023b). Pattern formation, structure and functionalities of wrinkled liquid crystal surfaces: a soft matter biomimicry platform. *Front. Soft Matter* 3, 1123324. doi:10.3389/frsfrm.2023.1123324
- Wang, Z., Servio, P., and Rey, A. D. (2022b). Wrinkling pattern formation with periodic nematic orientation: from egg cartons to corrugated surfaces. *Phys. Rev. E* 105, 034702. doi:10.1103/physreve.105.034702
- Ward, I. (1993). *New developments in the production of high modulus and high strength flexible polymers. Orientational Phenomena in Polymers*. Germany: Springer, 103–110.
- Wojcik, M., Lewandowski, W., Matraszek, J., Mieczkowski, J., Borysiuk, J., Pocięcha, D., et al. (2009). Liquid-crystalline phases made of gold nanoparticles. *Angew. Chem. Int. Ed.* 48, 5167–5169. doi:10.1002/anie.200901206
- Zaluzhnyy, I. A., Kurta, R., Sprung, M., Vartanyants, I. A., and Ostrovskii, B. I. (2022). Angular structure factor of the hexatic-B liquid crystals: bridging theory and experiment. *Soft Matter* 18, 783–792. doi:10.1039/d1sm01446c
- Zannoni, C. (2022). *Liquid crystals and their computer simulations*. Germany: Cambridge University Press.
- Zhang, Z., Yang, X., Zhao, Y., Ye, F., and Shang, L. (2023). Liquid crystal materials for biomedical applications. *Adv. Mater.* 35, 2300220. doi:10.1002/adma.202300220
- Ziabicki, A. (1993). *Orientation mechanisms in the development of high-performance fibers Orientational Phenomena in Polymers*. Germany: Springer, 1–7.



OPEN ACCESS

EDITED BY

Ali Miserez,
Nanyang Technological University, Singapore

REVIEWED BY

Animesh Pan,
University of Rhode Island, United States
Frank Alexis,
Universidad San Francisco de Quito, Ecuador

*CORRESPONDENCE

Horst A. von Recum,
✉ horst.vonrecum@case.edu

[†]These authors have contributed equally to this work and share first authorship

RECEIVED 18 March 2024

ACCEPTED 20 June 2024

PUBLISHED 29 July 2024

CITATION

Xin AW, Rivera-Delgado E and von Recum HA (2024), Using QSAR to predict polymer-drug interactions for drug delivery.
Front. Soft Matter 4:1402702.
doi: 10.3389/frsfm.2024.1402702

COPYRIGHT

© 2024 Xin, Rivera-Delgado and von Recum. This is an open-access article distributed under the terms of the [Creative Commons Attribution License \(CC BY\)](https://creativecommons.org/licenses/by/4.0/). The use, distribution or reproduction in other forums is permitted, provided the original author(s) and the copyright owner(s) are credited and that the original publication in this journal is cited, in accordance with accepted academic practice. No use, distribution or reproduction is permitted which does not comply with these terms.

Using QSAR to predict polymer-drug interactions for drug delivery

Alison W. Xin^{1†}, Edgardo Rivera-Delgado^{2†} and Horst A. von Recum^{2*}

¹Hathaway Brown High School, Case Western Reserve University, Cleveland, OH, United States,

²Department of Biomedical Engineering, Case Western Reserve University, Cleveland, OH, United States

Affinity-mediated drug delivery utilizes electrostatic, hydrophobic, or other non-covalent interactions between molecules and a polymer to extend the timeframe of drug release. Cyclodextrin polymers exhibit affinity interaction, however, experimentally testing drug candidates for affinity is time-consuming, making computational predictions more effective. One option, docking programs, provide predictions of affinity, but lack reliability, as their accuracy with cyclodextrin remains unverified experimentally. Alternatively, quantitative structure-activity relationship models (QSARs), which analyze statistical relationships between molecular properties, appear more promising. Previously constructed QSARs for cyclodextrin are not publicly available, necessitating an openly accessible model. Around 600 experimental affinities between cyclodextrin and guest molecules were cleaned and imported from published research. The software PaDEL-Descriptor calculated over 1,000 chemical descriptors for each molecule, which were then analyzed with R to create several QSARs with different statistical methods. These QSARs proved highly time efficient, calculating in minutes what docking programs could accomplish in hours. Additionally, on test sets, QSARs reached R^2 values of around 0.7–0.8. The speed, accuracy, and accessibility of these QSARs improve evaluation of individual drugs and facilitate screening of large datasets for potential candidates in cyclodextrin affinity-based delivery systems. An app was built to rapidly access model predictions for end users using the Shiny library. To demonstrate the usability for drug release planning, the QSAR predictions were coupled with a mechanistic model of diffusion within the app. Integrating new modules should provide an accessible approach to use other cheminformatic tools in the field of drug delivery.

KEYWORDS

QSPR (quantitative structure properties relationship), drug delivery, cyclodextrin, machine learning (ML), small molecules, ODE (ordinary differential equation)

1 Introduction

Affinity delivery, which relies on interactions between a drug delivery system and drug molecules, improves effectiveness of medication by extending the duration of drug release and thereby lengthening the duration of the treatment (Rivera-Delgado et al., 2016). Mathematical modeling of these affinity systems has shown that the strength of the affinity interaction, the ratio of host binding sites to guest ligands, and the molecular path length of diffusion influence the transport of molecules out of the system. Of these physical forces, the

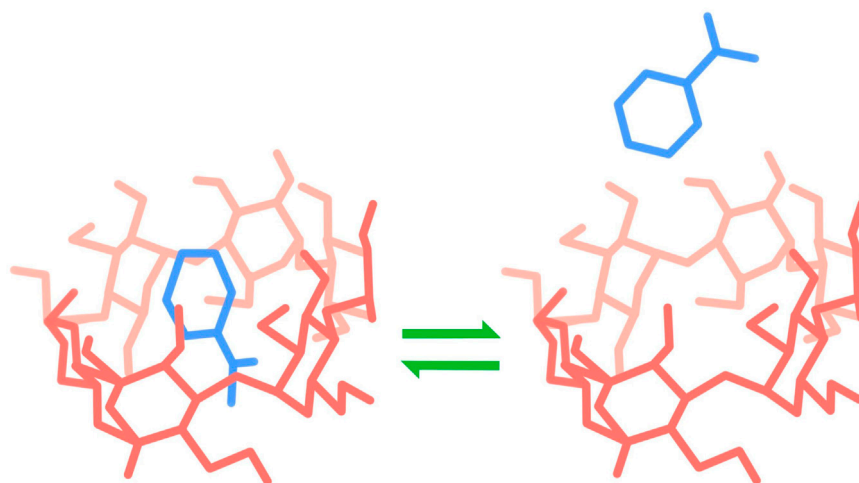


FIGURE 1
Cyclodextrin complexation.

affinity strength plays an important role in the classification of the system and the timescale of drug release (Fu et al., 2011). Affinity interaction can be associated with a variety of physical properties, including charge, hydrophobicity, Van der Waals forces, etc. In the fields of biomaterials and drug delivery, affinity delivery has been used with small molecule drugs (Wang and von Recum, 2011), proteins (Rivera-Delgado et al., 2016), cytokines, and antibodies (Ortiz et al., 2011).

Our lab tests rings of glucose molecules as affinity hosts called cyclodextrins, which are particularly promising affinity drug delivery hosts due to their structural properties, biocompatibility and versatility. The most common cyclodextrin are composed of a ring 6, 7, or 8 glucose molecules (α , β , and γ -cyclodextrin, respectively), and the conformation of the hydroxyl groups of the ring create a basket-like structure with a hydrophobic interior and hydrophilic exterior, allowing for complexation with drug molecules (Figure 1). Additionally, cyclodextrin can be polymerized into a variety of materials, including microparticles, viscous gels, and solid films. Unfortunately, experiments to confirm sustained release from the affinity guest-host system often takes weeks, making testing large numbers of potential candidates for cyclodextrin release systems impractical.

As an alternative to experimental testing, candidate molecules can be analyzed computationally. Predicting the binding affinity between cyclodextrin and drug molecules allows for the processing of molecules on the scale of minutes rather than weeks. There are two major methods for predicting molecular interaction: docking models and QSARs. Docking models use molecular force fields, which simulate interactions and potential energy between atoms. Force field parameters may be derived from experiments, calculations from quantum mechanics, or both (Jacob et al., 2012). In addition to providing a numeric estimate for binding affinity, docking programs produce visualizations of how molecules interact. QSARs, or Quantitative Structure-Activity Relationship models, statistically predict molecular interactions using molecular descriptors. Molecular descriptors are certain physical or chemical characteristics of molecules that can be evaluated numerically (for example, the number of hydrogen atoms or the

length of the longest bond chain). Many different types of regression models and statistical learning methods can be used as QSARs, ranging in complexity from linear models to artificial neural networks (Dehmer et al., 2012).

Previous investigations have been made on the accuracy of both docking and QSARs in predicting cyclodextrin affinity, but examining a sample of these papers reveals several concerns (Table 1). Notably, all of the investigated models used software hidden behind a paywall or only available with a license (Pérez-Garrido et al., 2009; Prakasvudhisarn et al., 2009; Ghasemi et al., 2011; Merzlikine et al., 2011; Ahmadi and Ghasemi, 2014; Veselinović et al., 2015; Xu et al., 2015; Mirrahimi et al., 2016). Additionally, many models lacked proper verification. Following Tropsha's publication detailing best practices for QSAR development, a completely verified model should undergo leave-one-out cross-validation (LOO-CV) (reported as Q^2), y-randomization, pass a variety of internal accuracy tests, and be analyzed for applicability domain. Additionally, models should be evaluated on multiple test sets as well as a hold-out external validation set (Tropsha, 2010). Of the papers investigated, none contained the full set of verification strategies.

In this study, the accuracy and usability of docking and QSARs were compared in order to establish an appropriate framework for the computational design of cyclodextrin based affinity delivery devices. Autodock VINA, an open-source docking program developed by Trott, was used to investigate docking methods (Trott and Olson, 2010). A variety of statistical methods presented in previous cyclodextrin QSARs were also investigated. The performance of QSARs was evaluated on both a standard test set as well as an external validation set to confirm accuracy. Properly evaluating the use of docking and QSARs should improve selection of possible guests for cyclodextrin, reducing the rejection of good candidates (Type II error) and limiting experimental investigation of bad candidates (Type I error).

Finally, though the coded models could be made freely available, understanding the raw script remained a significant obstacle for new users. Additionally, users would have to download multiple files and programs to their own computers, creating potential issues with device compatibility, storage restrictions, processor limitations, etc.

TABLE 1 Results of previous cyclodextrin QSARs.

QSAR	R2	Descriptors	Feature selection	Validation			
				Q2	y-rand	AD	EV
Cubist (Ghasemi et al., 2011)	0.945	Pfizer*	**	**	**	Yes	Yes
Random forest (Ghasemi et al., 2011)	0.912	Pfizer*	**	**	**	Yes	Yes
Partial least squares (PLS) (Veselinović et al., 2015)	0.68	ChemOffice, SYBYL, Pentacle*	Genetic algorithm	0.64	**	Yes	**
PLS (Pérez-Garrido et al., 2009)	0.74	SYBYL, Pentacle*	Fractional factorial design	0.75	Yes	Yes	**
Multiple linear regression (MLR) (Xu et al., 2015)	0.943	ISIS/Draw, CODESSA*	Forward selection	0.848			**
MLR (Mirrahimi et al., 2016)	0.841	ISIS/Draw, MOPAC, Web-DRAGON*	Genetic algorithm	0.821	Yes	Yes	**
MLR (Prakasvudhisarn et al., 2009)	0.833	HyperChem, DRAGON*	Forward selection	0.826	Yes	Yes	**
MLR (Tropsha, 2010)	0.78	SYBYL, MOE, AutoDock Tools, BINANA	Genetic algorithm	0.82	**	Yes	**
Artificial neural network (Prakasvudhisarn et al., 2009)	0.957	HyperChem, DRAGON*	Forward selection	0.955	Yes	Yes	**
Support vector machine (Trott and Olson, 2010)	0.971	HyperChem, MOE*	Particle swarm	**	**	**	**

*Presence of a paywall, usually due to specialized software that requires a license.

**Insufficient verification. None of the models investigated were both fully validated and openly accessible.

To overcome these obstacles and improve accessibility, the models were then integrated into a web application built with the R library “shiny” and then uploaded online. To demonstrate the ease of extendability of the app and its value in planning drug delivery strategies the results from the QSAR studies were then integrated into a mechanistic model of drug release.

2 Materials and methods

In order to be accessible, the models use only open-source software. Importing experimental data, cleaning data, and creating QSAR models were performed using R in RStudio. Both the coding language and the IDE are freely downloadable and easily accessible on Windows, Mac OS, and Linux. Descriptors were generated with PaDEL, also freely downloadable and open-source. Only the original observations of cyclodextrin complexation energies remain inaccessible to the public, but this does not have any effect on using the models for new predictions.

2.1 Dataset

Many of the models in Table 1 work from the same data source, a compilation of α - and β -CD affinities published by Suzuki in 2001 (Suzuki, 2001) [additionally, the sources that cite a different paper by Katritzky ultimately use this same data, as the Katritzky paper cites Suzuki for observations (Katritzky et al., 2004)]. In addition to Suzuki, we also compiled complexes of α - and β -CD Rekharsky and Inoue and Suzuki (Rekharsky and Inoue, 1998). Complexes of γ -CD, missing from the Suzuki dataset and sparse in the Rekharsky and Inoue data, were collected from Connors (Connors, 1995). Once compiled, the data were cleaned for reliable information, one-to-one cyclodextrin complexes, a temperature of 298 ± 2 K, and a solvent of water with pH 7. To obtain structure-data files (SDFs) of the ligands, the names of the guest molecules were passed through the Chemical Identifier Resolver, a web interface provided by the

National Cancer Institute’s Computer-Aided Drug Design Group (NCI/CADD). To handle the data, the R packages tidyverse, data.table, XML, RCurl, and Matrix were used (Bates et al., 2017; Dowle et al., 2017; Wickham, 2017; Duncan Temple Lang and the CRAN T and eam, 2018a; Duncan Temple Lang and the CRAN Team, 2018b).

Dataset splitting was performed using the R package caret (Kuhn and Quinlan, 2018). First, the cleaned data was split between α -, β -, and γ -CD. Structural and activity outliers in each category were removed. Structural outliers were detected using a statistical method relying on standard deviations of molecular descriptors (Roy et al., 2015). For activity outliers, molecules with reported ΔG values greater than 2.5 standard deviations from the mean were removed. Though traditional practice advises classifies outliers as values more than only two standard deviations away, in this case, retaining data points remained a priority and a larger margin was allowed. There were 9, 21, and 11 α -, β -, and γ -CD outliers, respectively. After removal, around 200, 250, and 100 α -, β -, and γ -CD observations remained.

The data was then split into training, testing data and external validation. For each separate cyclodextrin, an external validation set was created from a random 15% subset of the data. To create multiple training and test sets, the remaining modeling data was split with representative resampling of ΔG values into ten different 75:25 train to test data partitions. Though not as advanced as maximum dissimilarity algorithms, this method proved more practical due to the large number of descriptors (over 1,000) generated for each guest molecule. Furthermore, maximum dissimilarity algorithms, when implemented in this instance, had the unfortunate tendency to select highly similar training and test sets, defeating the purpose of creating multiple sets in the first place.

2.2 Docking calculations

The process of docking is based on two processes: sampling and scoring (Jacob et al., 2012). Sampling refers to the capacity to search

an active site on a protein, macromolecule or, in this case, affinity host. This can be performed with distance matrices, matching algorithms or incremental construction, multiple copy simultaneous searching, stochastic methods, or any combination of the aforementioned strategies. Scoring calculates the final binding affinity between the guest and host and can be dependent on force-field, empirical, or knowledge-based calculations. Docking generally involves the use of a host and a guest molecule which can be either rigid or flexible. Three types of conformation exist: rigid-rigid, rigid-flexible and flexible-flexible. In this paper we use AutoDock Vina, a version of AutoDock that uses Monte Carlo stochastic sampling coupled with a force field based scoring function from a resample of a drug like database to derive its weighted parameters. Vina in particular uses a flexible drug guest and a rigid cyclodextrin host, although it allows side chain mobility when docking ligands onto proteins.

The PyRx Virtual Screening Tool provides a variety of services, including molecular energy minimization, docking calculation, and visualization of molecules. PyRx version 0.8 was used here, as further editions require purchase (Dallakyan and J, 2015). Ostensibly, the source code of newer versions of PyRx is freely available, but actually implementing the code requires fairly advanced knowledge of Python, making public usage difficult. To begin, all guest molecules went through energy minimization to determine the most likely atomic configurations. AutoDock Vina, integrated within PyRx, calculated the change in Gibbs free energy (kcal/mol). We tested the effect on the docking process of changes in the search space, search exhaustiveness, and scoring force field type.

2.3 Descriptor generation

The open source software PaDEL-Descriptor calculated over 1,000 descriptors for the remaining molecules, including fingerprints, structural details, and physical properties (Yap, 2011). Additionally, PaDEL-Descriptor removed salts and minimized the energy of inputted files using an MM2 force field. To improve model interpretability, more abstract predictors, such as those related to eigenvalues for molecular matrices or autocorrelation, were excluded from calculation. The elimination of these descriptors did not produce any noticeable effect on final model accuracy and made feature selection less resource intensive.

2.4 Feature selection

Recursive feature elimination (RFE), implemented with caret, was used to subset the predictors used for model-building (Kuhn 2018). Using this method, a random forest model is created using all available descriptors. Once trained, the relative importances of the predictors are calculated and differently sized subsets (defined by the user) of variables are selected to create and evaluate new models. The best combination of predictors is then returned by the model. RFE was performed on each of the ten train-test splits. The predictors determined to be useful for all folds were saved and used for tuning and training the models. This resulted in 13 variables for α -CD, 16 variables for β -CD, and 39 variables for γ -CD.

2.5 QSAR development

We investigated the accuracy of several models that appeared in previous attempts at cyclodextrin QSARS (Table 1), including Cubist models, generalized linear models (GLM or GLMNet), random forests, partial least squares models, and support vector machines. Additionally, two QSAR methods not previously published for cyclodextrin—multivariate adaptive regression splines (MARS) and gradient-boosted models—were created and evaluated. Model building was accomplished with R-packages Cubist, glmnet, randomForest, pls, e1071, earth, and gbm, respectively (Cutler and Wiener, 2015; Mevik and Liland, 2016; Friedman et al., 2017; Kuhn et al., 2017; Meyer et al., 2017).

Cross-validation was used to determine ideal tuning parameters for each QSAR. For faster QSARs—such as generalized linear models (GLM) and partial least squares (PLS)—tuning was performed using 10-fold cross validation. For more resource-intensive models or models with large parameter spaces—such as random forests, Cubist and support vector machines (SVM)—only five folds were used. Optimized models, QSARs built with the tuned parameters and trained on the entire training set, were used to predict the test for each combination of test and training set. Further fine tuning was also performed at this step. The model that produced the lowest root-mean square error (RMSE) and highest R^2 (or an otherwise most ideal combination) on all the test sets became the final model, i.e., the model saved for future use. Furthermore, the models were evaluated according to Tropsha and Golbraikh standards for QSARs (Golbraikh and Tropsha, 2002). Although R^2 and RMSE can be useful for generalizing predictive capacity, they may be misleading in certain cases, necessitating stricter additional standards of evaluation. As an additional test of reproducibility, the final models were used in ensemble to predict the values of the external validation set. Because this dataset was withheld from the entire model training process, the external validation set served to simulate model performance on new data.

2.6 Applicability domain

Applicability domain describes the range of molecules where the model can be expected to generate reliable predictions. A new molecule outside of the applicability domain is structurally quite different from the set of data the model was trained on, and thus a prediction will rely on extrapolation and may not be accurate. The applicability domain of the models was determined with the same method used to detect outliers when cleaning the dataset (Roy et al., 2015).

2.7 Y-randomization

Y-randomization was used to further verify the significance of the results. Many advanced QSAR methods are powerful enough to model data off of noise, so y-randomization ensures that the modelling process produces results significantly more accurate than what could be obtained by chance. Randomization can be achieved by permutation (randomly changing the positions of observed values) or random number generation (replacing

observed values with completely new data). Different combinations of permutation and/or random generation yields five different modes of γ -randomization to investigate: 1) original ΔG values vs randomly generated descriptors, 2) permuted ΔG vs original descriptors, 3) random ΔG vs original descriptors, 4) random ΔG vs random descriptors, and 5) permuted ΔG vs random descriptors. (Combinations including permutation of descriptors are not included because the large number of predictors in QSARs renders the effects of such a process virtually indistinguishable from random number generation.) However, because the γ -randomization process is extremely resource-intensive (as each mode requires that several randomized iterations undergo the modeling process), only mode 1, the most common interpretation of γ -randomization, was investigated (Rücker et al., 2007). The observed ΔG values were randomly assigned to guest molecules, and the entire model refitting process was re-done, from feature selection to external validation.

2.8 Creating an app

Using R's "shiny" package, most of the process of running the QSAR could be implemented in a web app. The app was split into three main pages: Download, Upload, and Explore. "Download" accesses Chemical Identifier Resolver and obtain SDFs. The page also draws the obtained molecule using the package "ChemmineR," allowing the user to check that the SDF is accurate. "Upload" implements the QSARs after the user provides the app with a CSV of the descriptors from PaDEL-descriptor. After calculating the affinity and analyzing the applicability domain of the molecules, the user is provided with both a graph and a table of the results. The third page "Explore," stores the results of using the ensemble on FDA-approved drugs, as obtained from the annual publication "Orange Book: Approved Drug Products with Therapeutic Equivalence Evaluations." (Food and Drug Administration, 2019)

2.9 Modeling release curves

Partial differential equations that model drug diffusion were solved using the R package deSolve (Soetaert et al., 2018) using the method of lines as previously done by Fu et al. (2011). In the model, the release media was assumed to be water and the delivery system was assumed to be flat, thin circular cyclodextrin disc. The boundary condition between the polymer and the media was approached as described by Wang and von Recum (2011). Diffusivities of drug molecules were calculated from molecular weight and viscosity using a modified Stokes-Einstein-Sutherland equation, as done by Vulic et al. (2015).

3 Results and discussion

3.1 Performance of docking

When predicting on the entire cleaned dataset (all modeling data, which includes the training, testing, and external validation set), AutoDock Vina yielded an R^2 of 0.18 and a RMSE of 5.00 kJ/mol (Figure 2). Of the 547 cleaned complexes, docking provided calculations

for 458, failing to provide data on 89 complexes. Adjusting settings in Vina, such as the minimization algorithm size of the steps in the calculation, did not yield significant differences in accuracy. In comparison, the affinity of only around 40 cleaned molecules could not be obtained by the ensemble QSAR. In these cases, the withheld molecules were determined to be outliers, and the actual QSAR model could still be used to predict a value.

3.2 Performance of QSARs

The results of predicting on the test data for each QSAR and cyclodextrin type are markedly higher than docking (with the exception of γ -CD), reaching an R^2 of around 0.5 to 0.7, as seen in Table 2 and Figure 3. The reported R^2 for each QSAR type is calculated from an average of the performance of the model on all test splits. Additionally, Table 2 contains information on verification of all the QSAR types (3-VII Validation methods). Of the types investigated, only PLS and GLMNet failed to pass the salvo of verification criteria, both falling short of attaining an R^2 of 0.6.

In terms of reliability, most models were able to handle the available data well, providing calculations for all provided molecules. Only the Random Forest and Cubist models failed to calculate the affinity of some molecules, possibly due to being based around decision-trees. The algorithm underlying both models attempts to draw predictions by categorizing entries based on their features. If they encounter a molecules entirely different from the data they trained on, the models may fail to create a prediction. Advantageously for our approach, the failure to calculate some values becomes less important where models are combined in an ensemble where the final prediction is averaged over many models.

The results of ensemble prediction (averaging the results of many different QSARs) can be seen in Figure 4. While α - and β -CD models managed to reach moderately high predictive performance metrics, unfortunately, all γ -CD models lacked useable predictive power.

The models passing the verification in Table 2 were further verified using γ -randomization. To ensure accuracy was not the result of the models building off of noise, 25 different permutations of ΔG values were created. All Q^2 values of the models created from the original data were calculated to lie well outside 3 standard deviations of the mean Q^2 of the randomized data. Additionally, the R^2 values of the ensemble QSARs were significantly greater than the R^2 values obtained from the ensemble models created from permuted data (means of 0.021 and 0.027 and standard deviations of 0.011 and 0.016 for α - and β -CD, respectively).

3.3 Variable importance

Interpretability of a model provides a rough check if a model is calculating off of random noise or if the model is drawing logical calculations from physical properties to molecular behavior. Each model, due to differences in statistical algorithms and approaches, has differing levels of interpretability. GLM, being similar to linear models, have easily accessible coefficients associated with each predictor, so the relative impact of each factor can be compared with reasonable confidence. Cubist models, on the other hand, tend

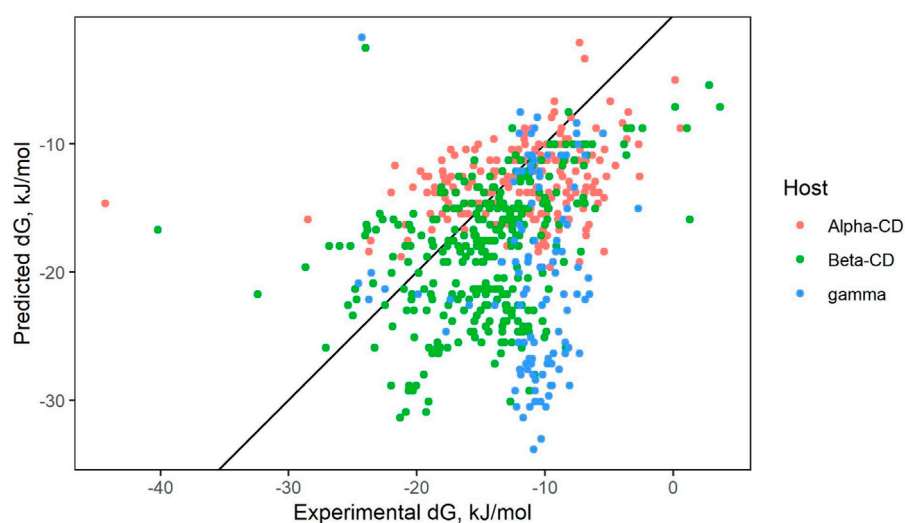


FIGURE 2
Results of PyRx docking.

TABLE 2 Evaluation of QSARs on test sets.

QSAR	α -CD				β -CD				γ -CD			
	A	B	C	D	A	B	C	D	A	B	C	D
Cubist	0.63	0.56	0.07	0.93	0.75	0.59	0.02	0.97	0.08*	-0.19*	0	0.98
GBM	0.78	0.5	0.05	0.95	0.83	0.73	0.02	0.98	0.35*	0.03*	0.68*	0.96
GLMNet	0.53*	0.54	0	0.94	0.52*	0.45	0.03	0.95	0.36*	-0.26*	0.17*	0.97
MARS	0.65	0.58	0.03	0.99	0.73	0.58	0	0.98	0.40*	-0.33*	0.33*	0.97
PLS	0.55*	0.47	0.05	0.93	0.55*	0.47	0.02	0.95	0.16*	-0.1*	0.28*	0.97
Polynomial SVM	0.65	0.55	0	0.98	0.74	0.56	0	0.98	0.45*	-0.28*	0.05	1
Random Forest	0.76	0.63	0.02	0.96	0.84	0.67	0.03	0.98	0.69	0.28*	0.24*	0.98
RBF SVM	0.74	0.64	0.02	0.96	0.85	0.61	0	0.98	0.35*	-0.19*	0.05	0.98
Sigmoid SVM	0.51*	0.52	0.05	0.93	0.50*	0.56	0.27	0.92	0.32*	-0.11*	0	0.98

The columns labeled A-D indicate the four conditions outlined by Golbraikh and Tropsha. A: $R^2 > 0.6$; B: $q^2 > 0.5$, where q^2 is the result from leave one out cross-validation on the training set; C: $|R^2 - R^2_0|/R^2 < 0.1$, indicating that the R^2 when the axes are flipped (R^2_0) is close to the original R^2 ; D: $0.85 < k < 1.15$, where k , the slope of the regression line through the points is close to 1.

*Model failed condition.

to be difficult to interpret as variables are processed through multiple levels of decision trees.

Evaluation for the relative importance of variables are shown in Figure 5. Random forest was the only QSAR type with a pre-packaged importance function for variable analysis. PLS variables were analyzed using a function obtainable from Mevik et al. (2007). Max Kuhn's caret package was used to evaluate GLMNet, the two SVM kernels, and Cubist. Unfortunately, caret was unable to process the final models for GLMNet and SVM, and the reported variable importance values were actually derived from models created within caret's "train" function, and are thus slightly different from the models saved in the ensemble. To determine importance, the "train" function removes a variable, rebuilds the model, and analyzes the

effect on accuracy. The more important a variable, the larger the drop in accuracy. After each variable has been tested, the function can then rank the importance of the descriptors.

For β -CD, XLogP, a measure of lipophilicity, appears to be important for all models, consistent with how the structure of cyclodextrin allows for easier complexation with small hydrophobic drugs. The same reasoning can be extended to LipoAffinityIndex and MLogP, additional approaches to quantifying lipophilicity. The number of carbons, nC, is also consistently important, possibly due to a relationship with molecule size. WTPT-2 is the PaDEL weighted path descriptor divided by the number of atoms, and also may be important due to encoding information on molecular size.

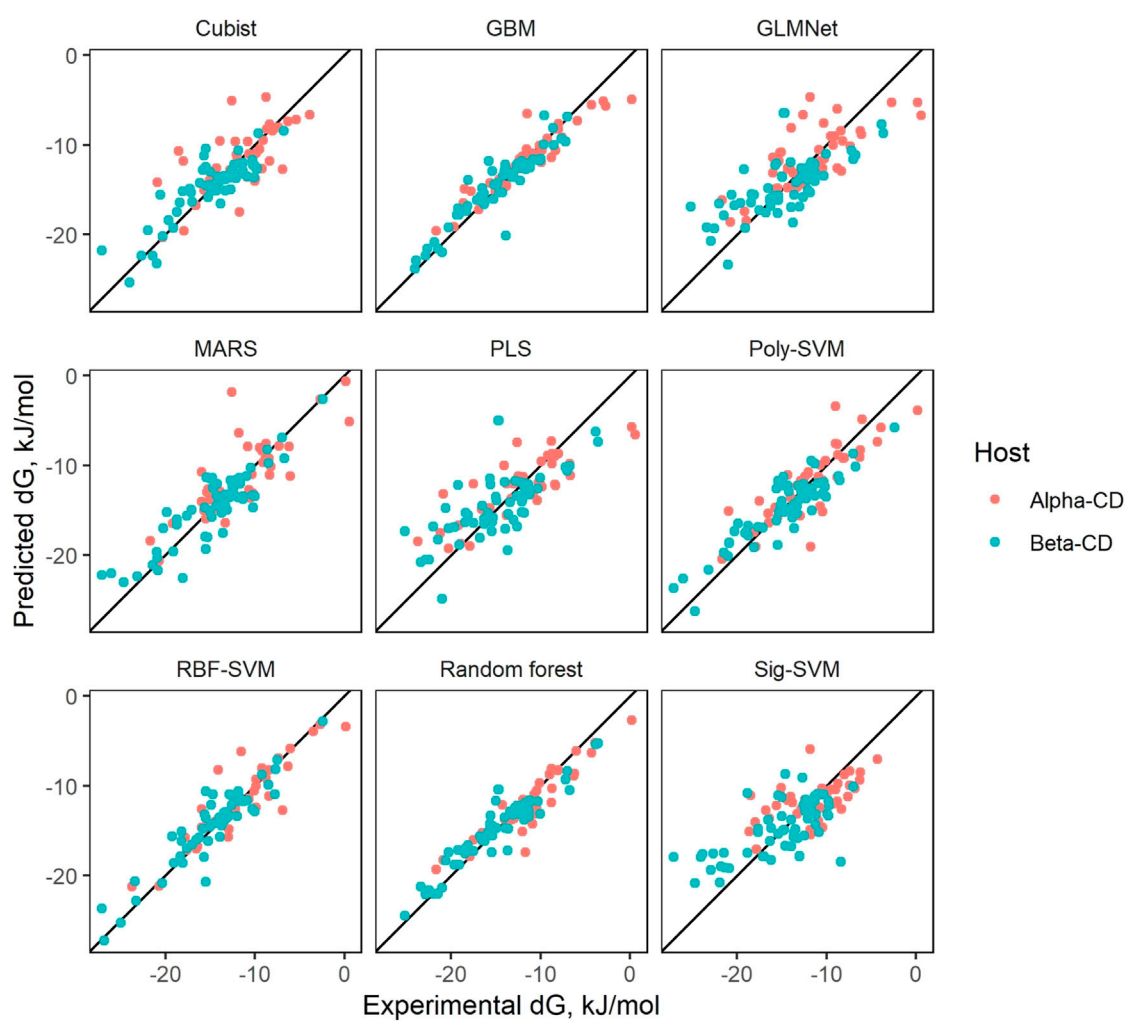


FIGURE 3
Results of QSARs on test sets.

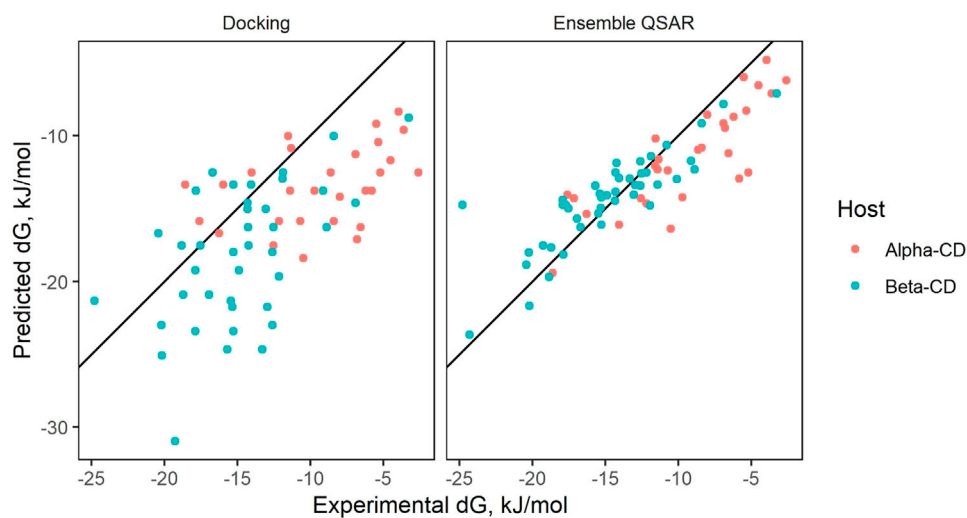


FIGURE 4
QSAR ensemble prediction.

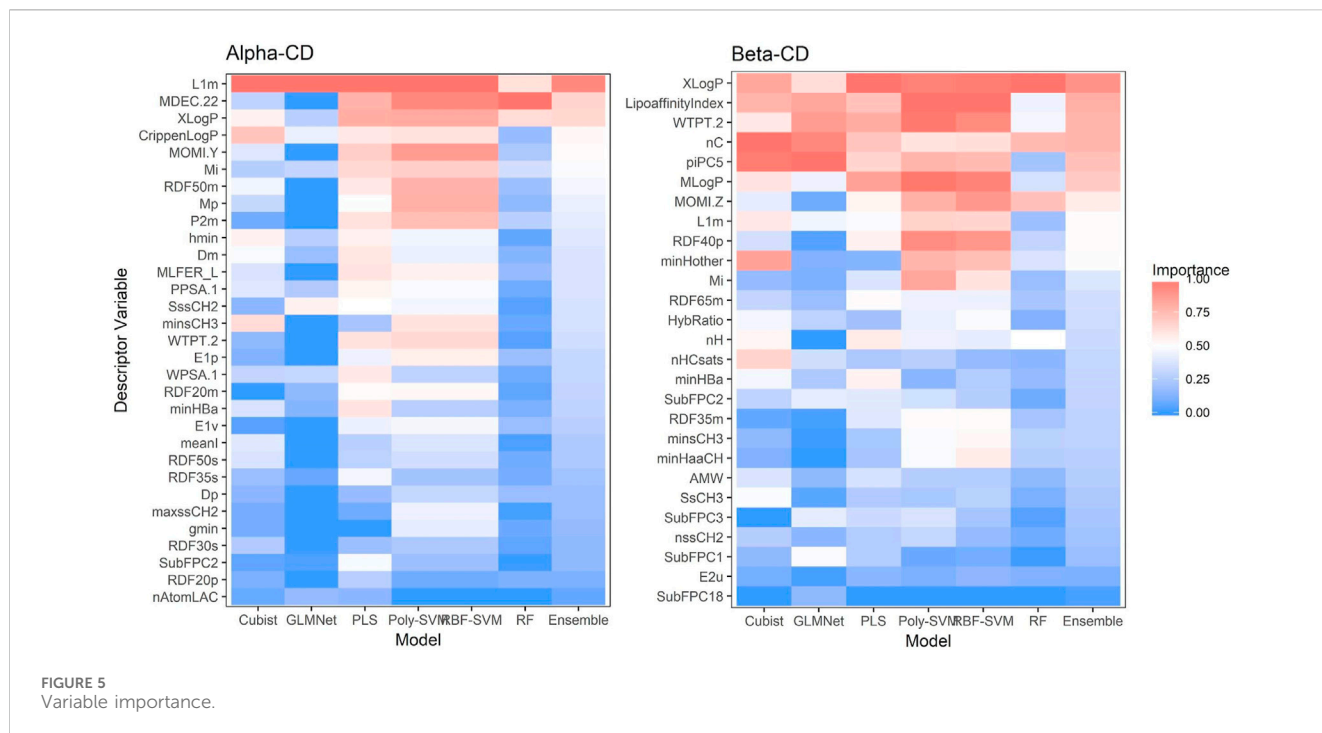


FIGURE 5
Variable importance.

However, not all the variables can be linked to set chemical properties. SpMax and SpMin relates to eigenvalues of a modified connectivity matrix, a numerical representation of atomic and molecular bonds, and may not be associated with any interpretable physical property (the same analysis can also be used for GATS predictors). To aid interpretability, building a model with predictors easily attributed to physical or chemical properties may be advised. The extent to which interpretability should trade off with accuracy remains in question. Our findings go in accordance to those in the general literature were lipophilicity tends to highly influence model output.

3.4 Web application and FDA database

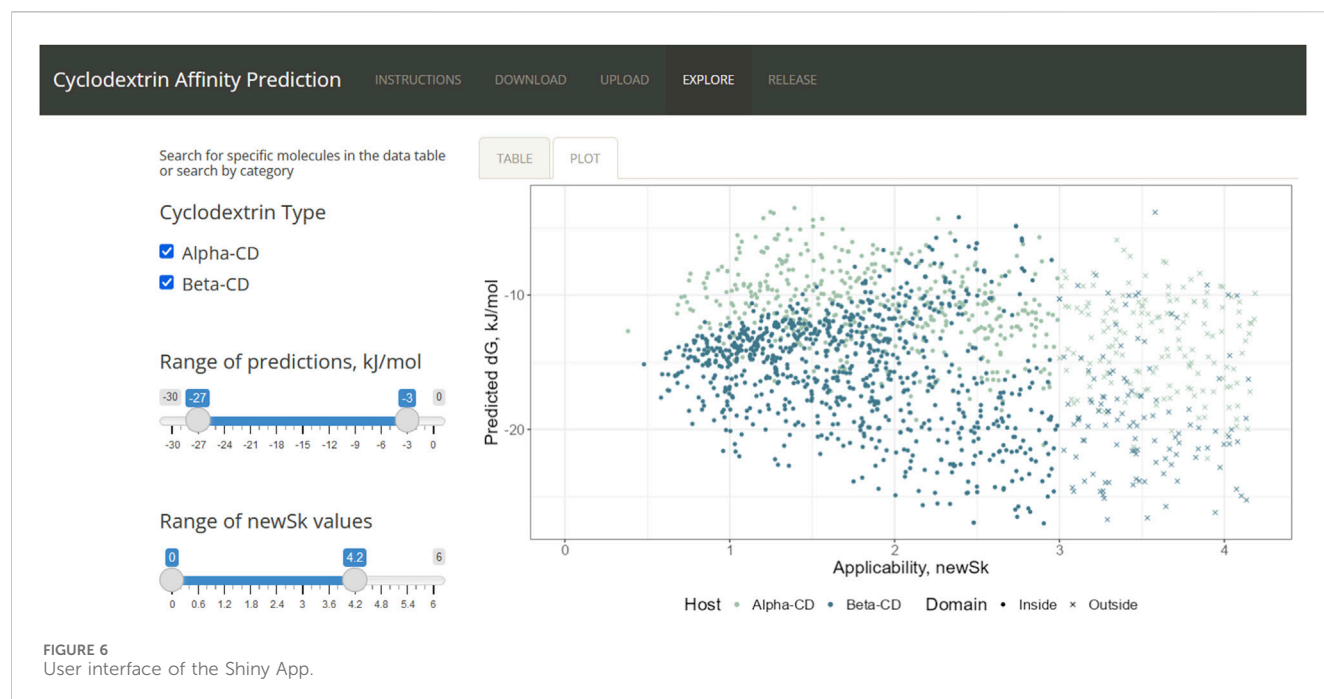
After collecting a list of FDA-approved drugs and drug combinations from the Orange Book, an annual publication listing all approved pharmaceuticals, the names were cleaned for individual active compounds. In total, 1,401 unique molecules could be extracted. Of these, 1,116 could be downloaded from Cactus and 1,031 could be processed by PaDEL. Many of the molecules that could not be analyzed by PaDEL would have proven impractical for cyclodextrin delivery, such as simple ionic salts (e.g., potassium chloride), or large molecules made of more than 100 atoms. Running the remaining guests through applicability domain analysis yielded 638 molecules, 45.5% of the original set. While less than half of FDA-approved drugs could pass through the model, the 600 available guests spans a wide range of properties and uses, allowing the page to be useful for candidate selection (Figure 6).

Though the app could be uploaded online through shinyapps.io, server time limitations on the account hosting the app make it impractical for usage by a large number of individuals simultaneously. In order to run the app for more than a few

hours, such as with screening a large dataset of molecules, the code would have to be downloaded through GitHub. In addition, the user would need to download the R libraries and the IDE RStudio, potentially negating the goal of creating an accessible, intuitive interface. The “Explore” page partially alleviates this obstacle, as it allows the user to perform a quick search of a pre-predicted affinity rather than spend time downloading the structure file, launching PaDEL, and running the QSAR.

3.5 Drug release module

To demonstrate the extensibility of the shiny app and its value in the design of drug delivery strategies the results of the QSAR predictions can be fed into a mechanistic model of drug delivery (Figure 7). The results demonstrate the ranges of values expected from the strongest affinity binding predictions and from the weakest. As expected, strong predictions produce much slower release profiles and weak predictions produce faster release profiles. Conservation of mass was verified as the sum of all mass within the system from the polymer and media compartment across all times as a test of the implementation. Notably, the implementation in R required a modification of the method of lines for appropriate modeling of the polymer to liquid media interface (Linge and Langtangen, 2016). Future efforts in creating new modules could explore substructure searching to identify alternative strategies for weak binders or drugs that demonstrate unsuitable release profiles. It is expected that not all drugs will follow this simplistic model of drug release. For those cases our lab has built a whole suite of approaches to alter elution rates such as a wide range of formulations, supramolecular interactions, Schiff-base formation and multi-arm PEG substitutions.



4 Conclusion

In predicting the binding affinity of cyclodextrin with small drug molecules, QSARS such as Cubist, GBM, MARS, random forest, and SVM models can be created using accessible open-source software. These models outperform available docking software in both accuracy and time consumption and pass statistical verification of reliability. The additional accuracy

afforded by QSARs can be integrated into the previously published mechanistic model for predicting drug release curves for candidate molecules. This would both help narrow down candidates for cyclodextrin affinity-based drug delivery as well as help advise which molecules are most appropriate to tailor the release rate from a delivery system for a given biomedical application. Furthermore, the QSAR models can be used to evaluate existing marketed pharmaceutical

formulations for their small molecule interaction with cyclodextrin to better understand the extent that the strength of binding between the cyclodextrin and the drug is of importance for the marketed product formulation (Braga, 2023; Puskás et al., 2023). Both of these goals can be achieved by any reader interested in the current work by accessing the github repository for this manuscript (<https://github.com/awqx/qsar-app>). The current model is limited to predictions in the experimental space of the training data and applications outside its applicability, for example, at low or very high pH, should be employed with caution and tested experimentally.

The integration of these machine learning models in combination with the mechanistic models of drug delivery all within a web application allows for a novel framework to plan drug delivery strategies. The application allows for a “design before you build” approach where others can bring their library of small molecules and determine which ones make the best candidates for an affinity release strategy. The mechanistic models of other geometries or drug delivery forms such as microparticles and injectable polymers can be readily included in the application to further extend the capabilities for other biomedical applications.

Data availability statement

The datasets presented in this study can be found in online repositories. The names of the repository/repositories and accession number(s) can be found below: QSAR model building package repository <https://github.com/awqx/qsar> Drug Release Module Code https://github.com/eriveradelgado/ODE_Practice/blob/master/09_ODE-drug-release.Rmd QSAR Application <https://github.com/awqx/qsar-app>

References

- Ahmadi, P., and Ghasemi, J. B. (2014). 3D-QSAR and docking studies of the stability constants of different guest molecules with beta-cyclodextrin. *J. Incl. Phenom. Macrocycl. Chem.* 79, 401–413. doi:10.1007/s10847-013-0363-5
- Bates, D., Maechler, M., Davis, T. A., Amd, C., Oehlschlägel, J., Riedy, J., et al. (2017). Matrix: sparse and dense matrix classes and methods. Available at: <https://cran.r-project.org/web/packages/Matrix/index.html>.
- Braga, S. S. (2023). Molecular mind games: the medicinal action of cyclodextrins in neurodegenerative diseases. *Biomolecules* 13 (4), 666. doi:10.3390/biom13040666
- Connors, K. A. (1995). Population characteristics of cyclodextrin complex stabilities in aqueous solution. *J. Pharm. Sci.* 84, 843–848. doi:10.1002/jps.2600840712
- Cutler, F., and Wiener, R. (2015). randomForest: Breiman and Cutler's random forests for classification and regression. Available at: <https://cran.r-project.org/web/packages/randomForest/index.html>.
- Dallakyan, S., and Olson, A. (2015). Small-molecule library screening by docking with PyRx. *Methods Mol. Biol. (Clifton, NJ)* 1263, 243–250. doi:10.1007/978-1-4939-2269-7_19
- Dehmer, M., Varmuza, K., and Bonchev, D. (2012). *Statistical modelling of molecular descriptors in QSAR/QSPR*. John Wiley and Sons.
- Dowle, M., Srinivasan, A., Gorecki, J., Short, T., Lianoglou, S., and Antonyan, E. (2017). data.table: extension of “data.frame”. Available at: <https://cran.r-project.org/web/packages/data.table/index.html>.
- Duncan Temple Lang and the CRAN Team (2018a). *RCurl: general network (HTTP/FTP/...) client interface for R*. Available at: <https://cran.r-project.org/web/packages/RCurl/index.html>.
- Duncan Temple Lang and the CRAN Team (2018b). *XML: tools for parsing and generating XML within R and S-plus*. Available at: <https://cran.r-project.org/web/packages/XML/index.html>.
- Food and Drug Administration (2019). *Approved drug products with therapeutic equivalence evaluations*. Available at: <https://www.fda.gov/media/71474/download> (Accessed May 31, 2019).
- Friedman, J., Hastie, T., Simon, N., Qian, J., and Tibshirani, R. (2017). glmnet: lasso and elastic-net regularized generalized linear models. Available at: <https://cran.r-project.org/web/packages/glmnet/index.html>.
- Fu, A. S., Thatiparti, T. R., Saidel, G. M., and von Recum, H. A. (2011). Experimental studies and modeling of drug release from a tunable affinity-based drug delivery platform. *Ann. Biomed. Eng.* 39, 2466–2475. doi:10.1007/s10439-011-0336-z
- Ghasemi, J. B., Salahinejad, M., and Rofouei, M. K. (2011). An alignment independent 3D-QSAR study for predicting the stability constants of structurally diverse compounds with β -cyclodextrin. *J. Incl. Phenom. Macrocycl. Chem.* 71, 195–206. doi:10.1007/s10847-011-9927-4
- Golbraikh, A., and Tropsha, A. (2002). Beware of q²!. *J. Mol. Graph. Model.* 20, 269–276. doi:10.1016/S1093-3263(01)00123-1
- Jacob, R. B., Andersen, T., and McDougal, O. M. (2012). Accessible high-throughput virtual screening molecular docking software for students and educators. *PLOS Comput. Biol.* 8, e1002499. doi:10.1371/journal.pcbi.1002499
- Katritzky, A. R., Fara, D. C., Yang, H., Karelson, M., Suzuki, T., Solov'ev, V. P., et al. (2004). Quantitative Structure–Property relationship modeling of β -cyclodextrin complexation free energies. *J. Chem. Inf. Comput. Sci.* 44, 529–541. doi:10.1021/ci034190j
- Kuhn, M., and Quinlan, R. (2018). *Caret: classification and regression training*. Available at: <https://CRAN.R-project.org/package=caret>.
- Kuhn, M., Steve, W., Chris, K., Nathan, C., and Quinlan, R. (2017). Cubist: rule- and instance-based regression modeling. Available at: <https://cran.r-project.org/web/packages/Cubist/index.html>.

github.com/awqx/qsar-app Walkthrough on how to use the models <https://github.com/awqx/qsar-app> Enter subfile process. Rmd.

Author contributions

AX: Investigation, Software, Writing—original draft, Data curation. ER-D: Conceptualization, Supervision, Investigation, Software, Writing—original draft. HR: Conceptualization, Funding acquisition, Supervision, Writing—review and editing.

Funding

The author(s) declare that no financial support was received for the research, authorship, and/or publication of this article.

Conflict of interest

The authors declare that the research was conducted in the absence of any commercial or financial relationships that could be construed as a potential conflict of interest.

Publisher's note

All claims expressed in this article are solely those of the authors and do not necessarily represent those of their affiliated organizations, or those of the publisher, the editors and the reviewers. Any product that may be evaluated in this article, or claim that may be made by its manufacturer, is not guaranteed or endorsed by the publisher.

- Linge, S., and Langtangen, H. P. (2016) "Texts in computational science and engineering," in *Programming for computations - Python*. doi:10.1007/978-3-319-32428-9
- Merzlikine, A., Abramov, Y. A., Kowsz, S. J., Thomas, V. H., and Mano, T. (2011). Development of machine learning models of β -cyclodextrin and sulfobutylether- β -cyclodextrin complexation free energies. *Int. J. Pharm.* 418, 207–216. doi:10.1016/j.ijpharm.2011.03.065
- Mevik, B.-H. (2007). VIP.R: implementation of VIP (variable importance in projection) (*) for the "pls" package. Available at: <http://mevik.net/work/software/VIP.R>.
- Mevik, B.-H., and Liland, R. W. (2016). Pls: partial least squares and principal component regression. Available at: <https://cran.r-project.org/web/packages/pls/index.html>.
- Meyer, D., Dimitriadou, E., Hornik, K., Weingessel, A., and Leisch, F. (2017) e1071: Misc Functions of the Department of Statistics, Probability Theory Group (Formerly: E1071) TU Wien. Available at: <https://cran.r-project.org/web/packages/e1071/index.html>.
- Mirrahimi, F., Salahinejad, M., and Ghasemi, J. B. (2016). QSPR approaches to elucidate the stability constants between β -cyclodextrin and some organic compounds: docking based 3D conformer. *J. Mol. Liq.* 219, 1036–1043. doi:10.1016/j.molliq.2016.04.037
- Ortiz, M., Fragoso, A., and O'Sullivan, C. K. (2011). Amperometric detection of antibodies in serum: performance of self-assembled cyclodextrin/cellulose polymer interfaces as antigen carriers. *Org. Biomol. Chem.* 9, 4770–4773. doi:10.1039/C1OB05473B
- Pérez-Garrido, A., Helguera, A. M., Guillén, A. A., Cordeiro, MNDS, and Escudero, A. G. (2009). Convenient QSAR model for predicting the complexation of structurally diverse compounds with β -cyclodextrins. *Bioorg. Med. Chem.* 17, 896–904. doi:10.1016/j.bmc.2008.11.040
- Prakasvudhisarn, C., Wolschann, P., and Lawtrakul, L. (2009). Predicting complexation thermodynamic parameters of β -cyclodextrin with chiral guests by using swarm intelligence and support vector machines. *Int. J. Mol. Sci.* 10, 2107–2121. doi:10.3390/ijms10052107
- Puskás, I., Szente, L., Szócs, L., and Fenyvesi, E. (2023). Recent list of cyclodextrin-containing drug products. *Period. Polytech. Chem. Eng.* 67 (1), 11–17. doi:10.3311/ppch.21222
- Rekharsky, M. V., and Inoue, Y. (1998). Complexation thermodynamics of cyclodextrins. *Chem. Rev.* 98, 1875–1918. doi:10.1021/cr970015o
- Rivera-Delgado, E., Ward, E., and von Recum, H. A. (2016). Providing sustained transgene induction through affinity-based drug delivery. *J. Biomed. Mater. Res.* 104, 1135–1142. doi:10.1002/jbm.a.35643
- Roy, K., Kar, S., and Ambure, P. (2015). On a simple approach for determining applicability domain of QSAR models. *Chemom. Intelligent Laboratory Syst.* 145, 22–29. doi:10.1016/j.chemolab.2015.04.013
- Rücker, C., Rücker, G., and Meringer, M. (2007). γ -Randomization and its Variants in QSPR/QSAR. *J. Chem. Inf. Model* 47, 2345–2357. doi:10.1021/ci700157b
- Soetaert, K., Petzoldt, T., and Setzer, R. W. (2018). deSolve: solvers for initial value problems of differential equations ("ODE", "DAE", "DDE"). Available at: <https://CRAN.R-project.org/package=deSolve>.
- Suzuki, T. (2001). A nonlinear group contribution method for predicting the free energies of inclusion complexation of organic molecules with α - and β -cyclodextrins. *J. Chem. Inf. Comput. Sci.* 41, 1266–1273. doi:10.1021/ci010295f
- Tropsha, A. (2010). Best practices for QSAR model development, validation, and exploitation. *Mol. Inf.* 29, 476–488. doi:10.1002/minf.201000061
- Trott, O., and Olson, A. J. (2010). AutoDock Vina: improving the speed and accuracy of docking with a new scoring function, efficient optimization, and multithreading. *J. Comput. Chem.* 31, 455–461. doi:10.1002/jcc.21334
- Veselinović, A. M., Veselinović, J. B., Toropov, A. A., Toropova, A. P., and Nikolić, G. M. (2015). *In silico* prediction of the β -cyclodextrin complexation based on Monte Carlo method. *Int. J. Pharm.* 495, 404–409. doi:10.1016/j.ijpharm.2015.08.078
- Vulic, K., Pakulska, M. M., Sonthalia, R., Ramachandran, A., and Shoichet, M. S. (2015). Mathematical model accurately predicts protein release from an affinity-based delivery system. *J. Control. Release* 197, 69–77. doi:10.1016/j.jconrel.2014.10.032
- Wang, N. X., and von Recum, H. A. (2011). Affinity-based drug delivery. *Macromol. Biosci.* 11, 321–332. doi:10.1002/mabi.201000206
- Wickham, H. (2017). *Tidyverse: easily install and load tidyverse packages*. R. package version 1.
- Xu, Q., Wei, C., Liu, R., Gu, S., and Xu, J. (2015). Quantitative structure–property relationship study of β -cyclodextrin complexation free energies of organic compounds. *Chemom. Intelligent Laboratory Syst.* 146, 313–321. doi:10.1016/j.chemolab.2015.06.001
- Yap, C. W. (2011). PaDEL-descriptor: an open source software to calculate molecular descriptors and fingerprints. *J. Comput. Chem.* 32, 1466–1474. doi:10.1002/jcc.21707

Frontiers in Soft Matter

Explores substances whose energy is in the order
of few KbT

A multidisciplinary journal which draws on areas
as diverse as physics, chemistry, nanotechnology,
and engineering to describe phenomena
associated with soft matter.

Discover the latest Research Topics

See more →

Frontiers

Avenue du Tribunal-Fédéral 34
1005 Lausanne, Switzerland
frontiersin.org

Contact us

+41 (0)21 510 17 00
frontiersin.org/about/contact



Frontiers in
Soft Matter

